# Characterization of Shear Strengths and Microstructures for Charred Solid Rocket Motor Insulation Materials

**Steven Alan Kyriakides**

Thesis submitted to the faculty of the Virginia Polytechnic Institute and State University
in partial fulfillment of the requirements for the degree of

Master of Science
in
Materials Science and Engineering

*Committee Members:*

Dr. Scott Case, Chair
Dr. Stephen Kampe
Dr. Norman Dowling

November 29, 2007
Blacksburg, Virginia

**Keywords: EPDM, Insulation, Char, Shear Strength, Microstructure**

# Characterization of Shear Strengths and Microstructures for Charred Solid Rocket Motor Insulation Materials

**Steven Alan Kyriakides**

ABSTRACT

As advances in solid rocket technology push rocket motors to more extreme operating speeds and temperatures, it becomes increasingly important to have well-designed material systems capable of surviving these harsh conditions. One common component in these systems is the use of a fiber- and particle-reinforced EPDM insulation layer between the motor casing and the solid fuel to shield the casing from the temperatures of the burning fuel and from the high velocity of gas particles traveling within the motor. This work studies several insulation materials to determine which exhibits the highest shear strength after being charred. Double-notch shear test specimens of three materials, ARI-2718, ARI-2719, and ARI-2750, were charred and tested to measure the failure strength of each charred material. The ARI-2750 showed the highest shear strength when loaded along the material orientation, but the ARI-2719 was strongest when transversely loaded. The strength measurements for ARI-2750 were highly sensitive to loading direction, unlike ARI-2718 and ARI-2719. Extensive scanning electron microscopy to identify correlations between shear strength and microstructure revealed that the amount of fiber orientation and amount of residual matrix material may have significant impacts on charred shear strength in these materials.

## Acknowledgements

I would like to thank the following people for their support and guidance during this project:

**Dr. Scott Case**, for giving me the opportunity to work with him and his research group during my graduate tenure here at Virginia Tech

**Fred Davidson**, **John Sparks**, **Doug McPherson**, and **Kent Hennessey** with Aerojet and **Rusty Blanski** at Edwards Air Force Base, for providing the funding for this project and for all of their input and advice from start to finish

**Mac McCord**, for his help in developing the means to cut the shear test specimens from the initial material panels

**Theo Theophanous**, for helping to set up the initial furnace fixture and the HotDisk fixture, and for always being there to help when needed

**Dave Berry**, for helping design and implement the final furnace fixture, and for helping with anything and everything I brought to him

**Steve McCartney**, for his training and assistance on the SEM

**Darrell Link** and **Dave Simmons**, for machining most of the shear test specimens

**D.J. Pohlit**, for helping me get things started while finishing up his own thesis

**Josh Sole**, for his training and assistance with the Instron fixture

I would especially like to thank:

My parents, **Alan and Danielle Kyriakides** and **Pamela and Patrick De Ridder**, for their love and guidance for the last 23 years or so

My three brothers and two sisters, for being all the best parts of me and for never letting me forget where I came from (especially **D.J.**, for putting up with me sharing his bedroom for the last four months)

**Annie Parsons**, for loving me and always being there to help on my projects and to point me in the right direction for the last four years

All the rest of my family and friends, whether in Blacksburg, Chesterfield, or any other corner of the country, for the beautiful inspirations and welcome distractions they have provided whenever I needed them the most

## Dedication

I would like to dedicate this work to my grandfather, Stavros Achilles Kyriakides, for being my inspiration in engineering and life. I wouldn't be the man I am today without his love and influence, and I hope that this work will be the start of an engineering career that is as successful as his.

Σε αγαπώ πολύ, παππού

# TABLE OF CONTENTS

# List of Figures

# List of Tables

# Chapter 1: Introduction

## *Background*

Throughout the history of rocketry, the performance of rocket-powered devices has depended upon their ability to withstand the high temperatures and loads associated with their use. As the use of rockets has developed to require longer flights, the focus of research has shifted from developing the most efficient pressure vessel to improving the nozzle, insulation, and other time-sensitive materials.[1] Observed temperatures in modern solid rocket motors can reach as high as 4000 °C, putting most structural materials at risk.[2] To allow the use of more standard materials for rocket casings, an effective thermal protection system is important. Typically, several layers of insulation are added between the solid fuel and casing, shielding the casing from the heat produced by the combusting fuel. Figure 1-1 below shows a simple design for a cylindrical casing for a solid rocket motor.

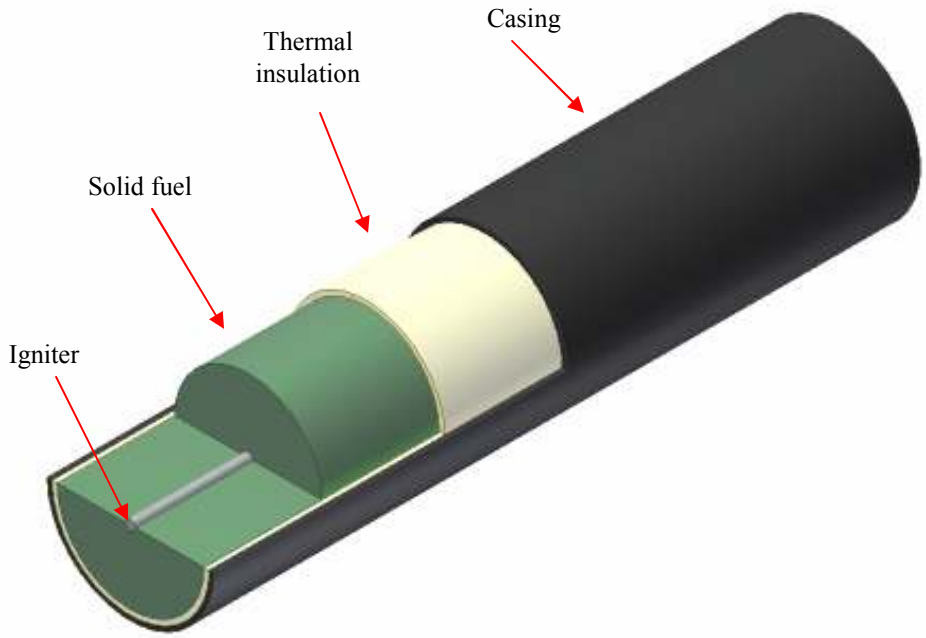


Figure 1-1: Simple Cylindrical Solid Rocket Motor Casing

Because the fuel in this design initially burns from the inside and then works its way outward, the actual insulation will not see its maximum operating temperatures until the final stages of operation.[3] By that point, the insulation must also be able to withstand the ablating forces occurring within the motor. In addition to seeing heat spikes of up to 340 J/cm$^2$-s, particles in the exhaust flow of modern rocket motors can be traveling at over 1000 m/s.[2,4] The mechanical erosion of the insulating layer caused by these particles helps to reduce the layer's surface temperature, but also reduces the amount of material present.[5,6] The amount of erosion actually occurring in service is complicated by the effect of high flight velocities on ablative erosion, as studies have shown significant increases in erosion observed in recovered service motors compared to those tested under static conditions in a lab environment.[7] The material selection and design for these systems attempts to optimize performance in consideration of this tradeoff.

Elastomeric compounds have been researched since the mid-to-late 1960s for applications as ablative insulation for solid rocket motors.[8] Ethylene propylene diene monomer (EPDM) rubber, found in automotive weatherstripping and some tennis shoes, is currently the standard choice for this application.[2,7,9,10] EPDM has good ozone resistance, necessary in the environments often encountered during service, has a good ability to adhere to the propellant within the motor casing, and is able to produce stable char layers during firing.[11,12] Much of the research into EPDM insulation now focuses on altering the additives, which can include Kevlar and other fibers as well as particulates such as alumina, silica, or carbon black.[7,10,12] Nano-fillers such as carbon nanofibers, montmorillonite (MMT) nanoclays, and polyhedral oligomeric silsesquioxane (POSS) are also being considered as performance-enhancing additives to EPDM insulation.[2] Also of

interest is the integrity and strength of the insulation at the interface of the charred and virgin material during operation.[8] Indeed, the strength of the materials in general is crucial to the design of solid rocket motors, as it impacts the amount and placement of insulation within the casing.[13] Effective modeling of these motor designs depends upon the accuracy of the material properties used in those models.

## *Problem Statement*

The design and modeling of elastomeric insulation systems for solid rocket motors is hindered by the lack of clear mechanical properties for the charred insulation. The charring process itself is still very difficult to model, as is its effect on the properties of the virgin material.[14-16] A full characterization of the shear strengths of these materials is necessary to provide more accurate properties for future attempts to model solid rocket motor systems.

## *Project Details*

This investigation took place at Virginia Tech in collaboration with personnel at AFRL and Aerojet. Aerojet donated all four materials tested herein, as well as one sample of material charred in their own insulation screening motor (ISM). To test the shear strengths of these materials, double-notch shear tests were performed using a modified version of the ASTM-D3846-02 test standard. Thermal properties were measured using HotDisk analysis; HotDisk is a trade name for equipment that measures several properties using the transient plane source technique.

## Mechanical Testing

The ASTM-D3846-02 test standard, designed for testing the shear strengths of reinforced plastics, describes placing two offset notches into a specimen and applying a compressive force transverse to the notches, thus creating a shear force between the tips of the notches. Figure 1-2 below shows the basic dimensions for the specimens used for shear strength testing herein.

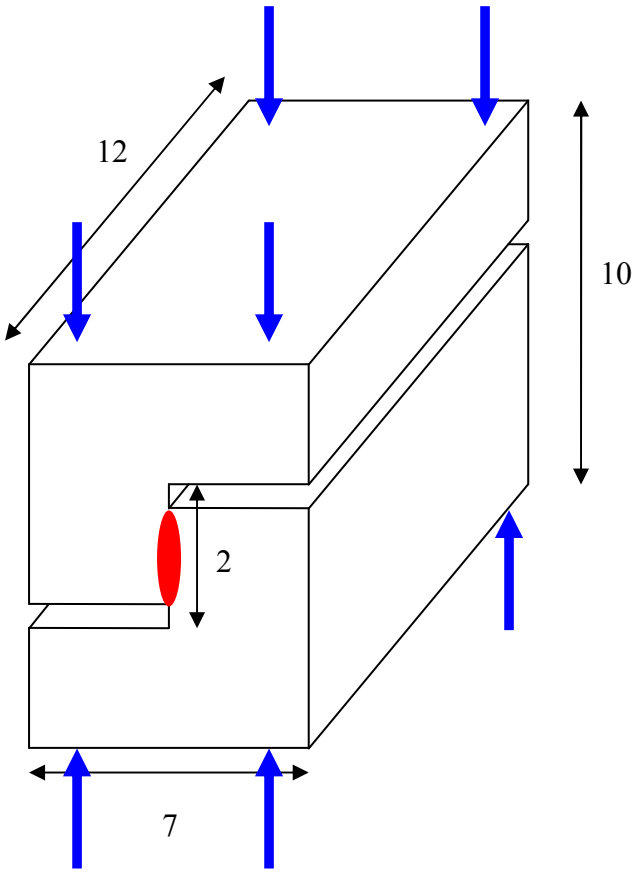


Figure 1-2: Shear Strength Test Specimen Geometry (all dimensions in mm)

These are the nominal dimensions after the shrinking caused during charring; the effect of the char process on specimen dimensions is described in Chapter 2. The application of a compressive force, illustrated by the blue arrows above, causes shearing between the notches, noted by the red oval. The failure load was divided by the planar area between the notch tips to determine the overall shear strength.

### Thermal Property Testing

To further characterize these materials, a HotDisk sensor was used to measure the thermal conductivity, thermal diffusivity, and heat capacity of these materials. Initially, these measurements were to be taken at a variety of temperatures; however, limitations on sample size prevented any elevated-temperature measurements.

The HotDisk fixture makes use of the transient plane source technique to measure these properties. In this technique, a circular sensor is placed between two flat pieces of the material in question. A small electrical current passes through the sensor, which in turn measures the temperature across the sensor area. By recording and analyzing the time-temperature response, the machine's software can accurately calculate the thermal properties. In order for this to be accurate, however, the diameter of the sensor must be smaller than the probing depth, defined as the smallest distance from the sensor to an outer surface of the sample.[17] No elevated-temperature sensors were currently available that were sufficiently small in diameter to test the material on hand.

## *Objectives*

The objectives of this project were as follows:

- Measure the shear strengths of the four materials described above
- Characterize the microstructures of each material
- Compare the microstructure of the charred ARI-2750 to that of the ARI-2750 taken from the ISM sample
- Identify correlations between microstructure and shear strength

## *Material Information*

The four materials donated by Aerojet were designated ARI-2718, ARI-2719, ARI-2732, and ARI-2750. ARI-2718 is the current industry standard for this application, and ARI-2718 and ARI-2719 are basically the same material, though the components of

each come from different suppliers and the processing times at each stage listed below differ somewhat. ARI-2750 is a potential replacement for ARI-2718, and ARI-2732 is essentially the same as ARI-2750 with no fiber material. All consist of an EPDM matrix, and all but ARI-2732 include aramid fiber reinforcements; ARI-2718 and ARI-2719 also have a silicon compound added. Elemental compositions of the virgin materials, as well as more detailed descriptions of these materials, are provided below in Appendix A (ITAR restricted). Table 1-1 below summarizes the basic similarities and differences of each material.

Table 1-1: Material Details

| Material | ARI-2718 | ARI-2719 | ARI-2732 | ARI-2750 |
|---|---|---|---|---|
| Matrix | EPDM | EPDM | EPDM | EPDM |
| Fiber Reinforcement | Yes | Yes | No | Yes |
| Particle Reinforcement | Yes | Yes | Yes | Yes |

The processing of these materials takes place in four basic steps. In the first step, all ingredients (except the curatives) are mixed in a master batch. The second step, referred to as refining, uses two-roll mills and/or calenders to break up and disperse the fiber bundles. Step three places the ingredients back in the mixer, at which point the curatives, based on a clay carrier, are added to the material. Finally, the calender is used to establish the final thickness of the panel.

To machine the shear test specimens, notches were cut with a 0.025-in. thick carbide blade in one of two directions, perpendicular or parallel to the processing orientation. Aluminum plates were used to clamp the panels in place, thereby preventing the material from deforming during cutting. After the notches were cut, strips were cut from the panel; test specimens were then cut from each strip using a box cutter. Figure 1-3 below shows the basic process for machining these specimens.

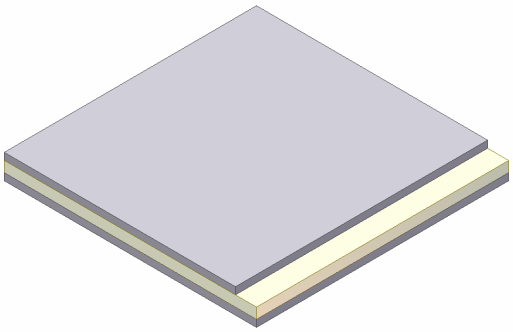

Figure 1-3a: Shear Specimen Preparation – Insulation Panel between Aluminum Plates

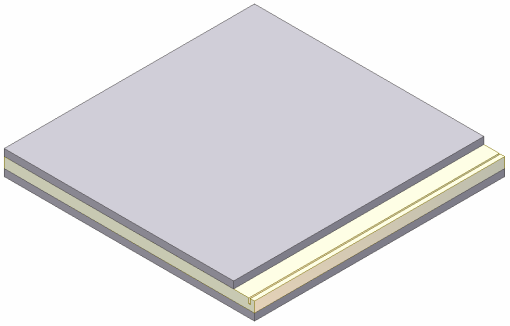

Figure 1-3b: Shear Specimen Preparation – First Notch Machined into Insulation

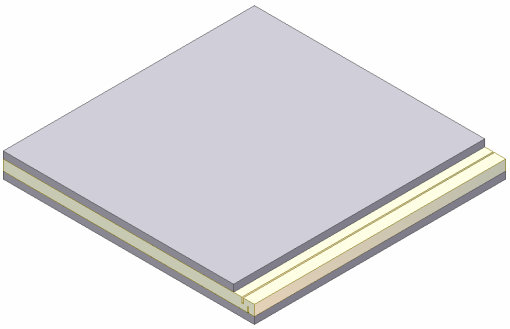

Figure 1-3c: Shear Specimen Preparation – Insulation Inverted; Second Notch Machined

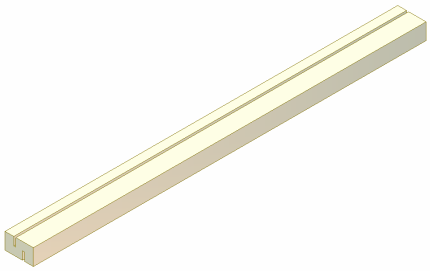

Figure 1-3d: Shear Specimen Preparation – Strip Machined from Panel

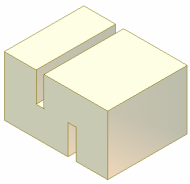

Figure 1-3e: Shear Specimen Preparation – Specimens Cut to Length from Strip

# Chapter 2: Experimental and Results

## *Charring Procedure*

Because of the low oxygen content of the upper atmosphere, the insulation does not presumably oxidize to any significant degree during field operation. To simulate this when charring specimens for this work, all material was to be charred under a predominately inert atmosphere of ultra-high-purity nitrogen gas. Due to the brittle nature observed in the charred material, the notches for the shear specimens were machined prior to charring.

### Process development

Initial attempts to char the shear specimens took place in an open-air Lab-Line / Carbolite tube furnace, so a system had to be developed to maintain a nitrogen atmosphere around the specimens themselves. Two specimens of ARI-2718 were first bound together near the end of a steel nitrogen delivery tube, with ceramic blocks in place to prevent thermal expansion during charring. Stainless steel shims were placed in the notches to hold them open as well. Once the samples were securely fastened to the delivery tube, the entire structure was enclosed in an improvised envelope of stainless steel foil. The ends of this foil were folded several times and clamped together mechanically to prevent any leaks besides the small hole around the delivery tube. Nitrogen was pumped into this envelope throughout the charring, allowing the excess nitrogen to leave from the hole for the delivery tube and prevent oxygen from entering. The furnace's open end was placed under a fume hood for the safety of others in the lab.

This furnace did not have a programmable controller; there was merely a dial to set the final temperature. To reach the charring temperature of 1100 °C, determined

based on consultations with Aerojet, this furnace heated at an average rate of approximately 20 °C/min. After holding for 20 min at 1100 °C, the furnace was switched off, but the nitrogen flow was not yet terminated. The furnace was allowed to cool as fast as possible in the air, and the nitrogen flow was cut off upon reaching 300 °C.

Once the cooling was complete, the steel foil was cut away to examine the specimens. Both ARI-2718 specimens had crumbled, as seen in Figure 2-1 below.

Figure 2-1: Charred ARI-2718 Specimens from Initial Char Procedure

Inspection revealed that there were cracks throughout the specimens, running both parallel and perpendicular to the notch direction. Similar results occurred for a second run, using the same procedure but replacing the ARI-2718 with ARI-2750. Thinking that these cracks may have come from thermal stresses in the constrained material, the next charring run did not include the ceramic spacers mentioned above. These specimens did not crumble, but still showed some cracking and would not have been adequate for shear testing. Places where the foil was close to the specimens caused them to warp to fit the surface of the foil upon expansion during the charring, as shown in Figure 2-2.

Figure 2-2: Charred ARI-2718 Specimen Showing Warping from Foil Surface

In addition to the physical defects in specimens produced this way, there were several other drawbacks. First, the small size of the furnace (75-mm interior diameter) and the difficulty in preparing a steel foil envelope to fit within the tube prevented charring more then 2-4 specimens at a time. Such a small volume inside the envelope may also have had difficulty maintaining a consistent temperature because of the cooler nitrogen gas flowing in. Finally, the time necessary to prepare the samples for charring under this procedure, which was about 90 min, was deemed too long to feasibly produce a large number of test-worthy specimens for this work.

A second tube furnace, manufactured by Lindberg, was located and appeared to address many of the issues with the first furnace. For one, the controller for this furnace was fully programmable. The furnace could also be closed at both ends, allowing nitrogen to fill the entire tube and a greater number of samples to be charred at once, even though the tube diameter was smaller than before (50 mm instead of 75 mm). The aluminum caps were fitted to the ends of the alumina tube and sealed with vacuum tape to prevent nitrogen from leaking into the lab. A small circle of alumina, cut to be slightly smaller than the inner furnace diameter, was placed inside the tube to prevent thermal

damage to the aluminum caps. Figure 2-3 below shows one end of the tube as prepared for this work.

Figure 2-3: Sealed End of Alumina Tube

Initially, one end was more permanently sealed with rubber cement and samples were loaded into the end sealed with the vacuum tape. The tube furnace eventually needed to be shared with another research group, though, so both ends were then sealed with vacuum tape to allow the tube to be easily switched out while remaining uncontaminated. A bubbler was added to the end of the nitrogen system to allow for monitoring of the nitrogen flow throughout the charring process; this again vented to a fume hood.

To mirror the heating profile attempted on the first furnace, the controller was programmed to heat up at a rate of 20 °C per minute until reaching 1100 °C, then to hold for 20 min and cool as fast as possible. Nitrogen flowed from the start until the interior of the furnace cooled to 300 °C. Specimens were placed on a flat piece of alumina, as shown below, and pushed into the center of the furnace.

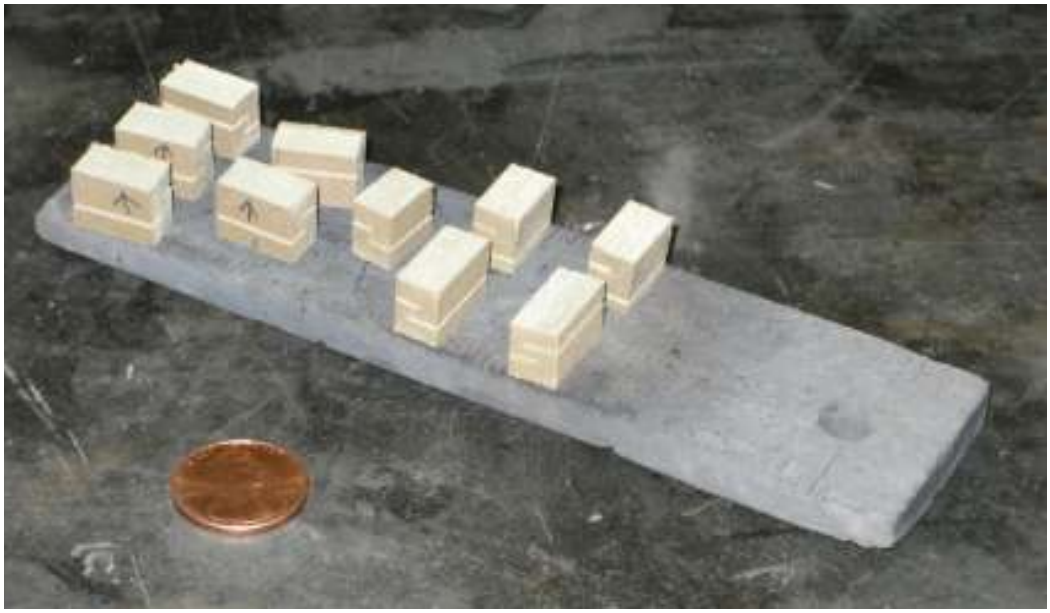

Figure 2-4: Virgin ARI-2718 Specimens on Alumina Platform

Specimens charred in this furnace turned out better than in the other furnace, though there was still some cracking visible in about half the specimens. Many specimens also showed varying amounts of warping, as shown in Figure 2-5 below.

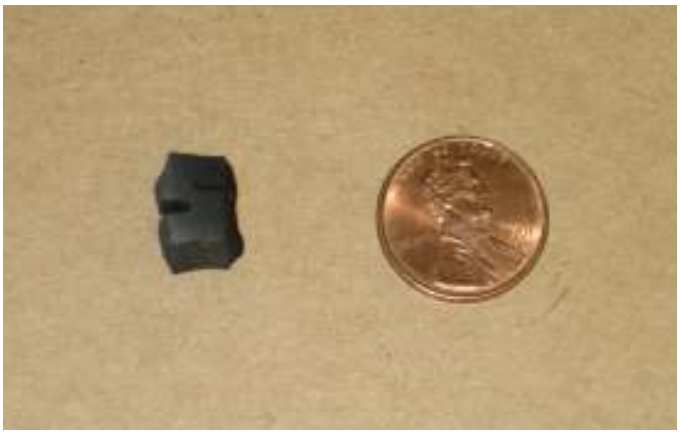

Figure 2-5: Warped Specimen of Charred ARI-2719

Some of the specimens that passed a quick visual inspection were tested on a dynamic mechanical analysis (DMA) compression fixture, but none performed acceptably. The force of the compression exposed cracks within the material that were initially unseen. After contacting lab personnel at Aerojet, it was suggested to try a much lower heating rate, on the order of 1 °C/min, to improve the quality of the test specimens.[18]

The controller was then set to heat at that rate, 1 °C/min instead of 20 °C/min, with the same hold time and cooling rate. This slower heating rate allows volatile compounds in the EPDM to diffuse out of the material before reaching a temperature where they can erupt and damage the material. The cooling rate was not changed because there is no danger of volatile eruption after the material has fully reacted. Nitrogen flowed the same way as before, but because of the long run time of the new heating profile, with nearly 24 hours under gas, the nitrogen regulator had to be periodically adjusted to increase flow as the pressure within the nitrogen cylinder decreased over time. The setup was checked once every 30 minutes for the first 2 hours, once every 2 hours for the next 6 hours, then once every 3 hours for the next 6 hours. At this last inspection, the nitrogen flow was set slightly higher than normal, allowing for some decrease in cylinder pressure over the remainder of the char cycle, and the furnace was not checked again until after cooling had begun. These inspections also proved useful for monitoring the status of the vacuum tape, which, exposed to longer times at the high temperatures involved, would grow soft and occasionally begin to leak through small holes; in these cases, additional tape was placed over the holes to reseal the furnace. After observing that the tape would sometimes lose adhesion and sag away from the tube, steel hose clamps were used to hold the tape in contact with the tube throughout the charring process.

The specimens produced from this charring system were of significantly better quality than the previous specimens. There was much less cracking, with only one or two cracked specimens per run, and the degree of warping observed was also reduced. Very rarely, there were small regions of bubbling or swelling observed in the specimens,

especially ARI-2719. No absolute reason for this was determined, but the issue occurred so infrequently that the charring process was finalized to these parameters, as shown in the following heating profile.

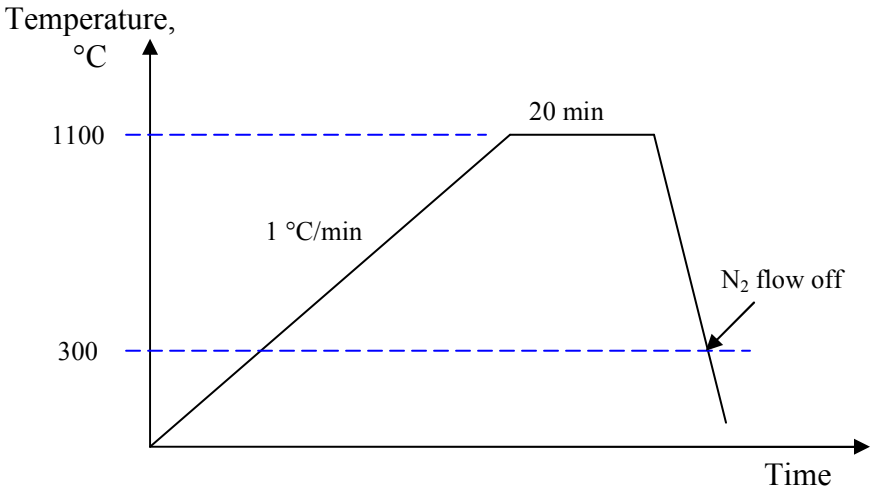


Figure 2-6: Final Heating Profile for Tube Furnace Charring

These char parameters were later applied to ARI-2732, but did not produce any quality specimens. Every specimen had cracked several times perpendicular to and in the direction of the notch cuts, regardless of material processing direction. Because this development was late in the overall project timeframe, these cracked specimens were used for elemental analysis and microscopy, and no further specimens were prepared for shear, thermal, or dimensional analysis.

## Dimensional changes

To characterize and compare the behavior of the materials during char, the specimens were measured before and after charring to determine the volumetric shrinkage. The length, width, and height of each specimen were measured by digital caliper before and after charring, using a basic $V = l*w*h$ method to determine the nominal volume. The change in volume was divided by the virgin volume to determine

the percent volumetric change. The results of these measurements are shown in the figure and table below (the error bars represent one standard deviation).

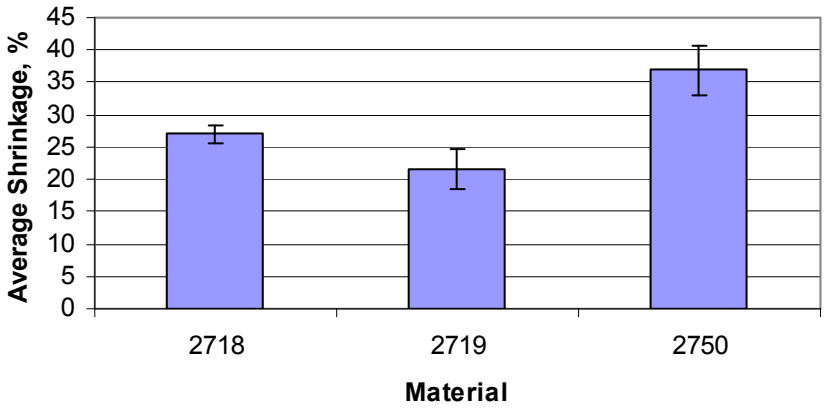


Figure 2-7: Dimensional Changes Observed After Char

Table 2-1: Dimensional Changes Observed After Char

| Material | Average Shrinkage, % | Standard Deviation |
|---|---|---|
| ARI-2718 | 27.0 | 1.4 |
| ARI-2719 | 21.6 | 3.2 |
| ARI-2750 | 37.0 | 3.9 |

## *Microscopy*

Scanning electron microscopy (SEM) was used to characterize the charred microstructures of each material in this study. An FEI Quanta 600 F microscope, fitted with a Bruker AXS energy-dispersive X-ray spectrometer (EDS), was used to collect these images in order to look for any possible correlations between microstructure and strength in each of the materials. All images were taken of fracture surfaces from the shear testing described below, except for the images of ARI-2732, for which no shear testing took place, and the ISM-charred ARI-2750. ARI-2732 micrographs were taken on exposed surfaces from cracking during char, and ISM micrographs were taken from surfaces exposed during failure of the material. Material orientation directions are shown with red arrows when applicable.

## ARI-2718 Micrographs

The following images show representative microstructures observed for the ARI-2718 material.

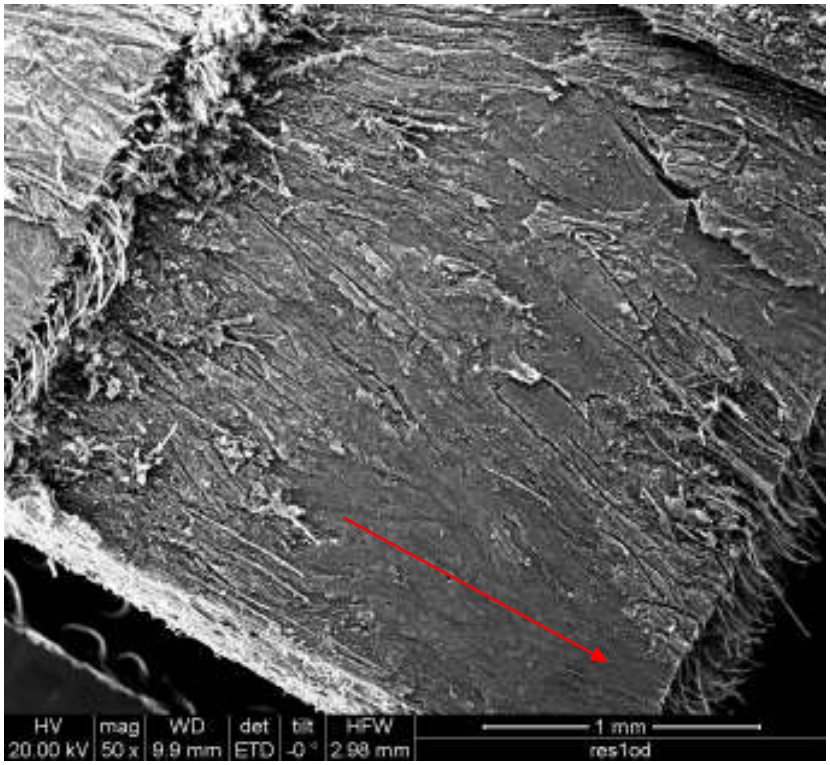


Figure 2-8: Microstructure of ARI-2718 Specimen L20 (50x)

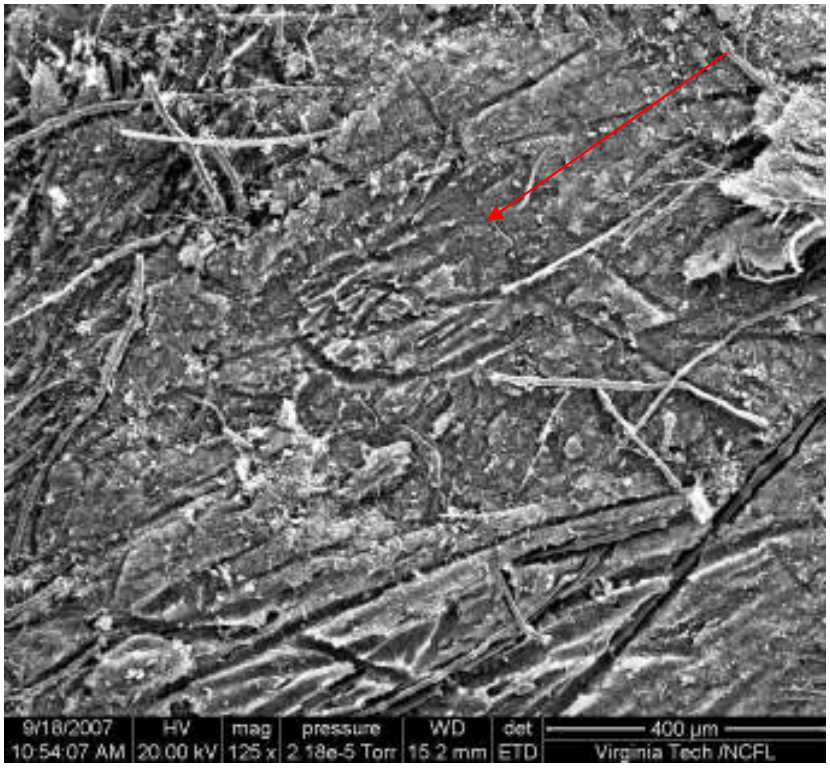

Figure 2-9: Microstructure of ARI-2718 Specimen L4 (125x)

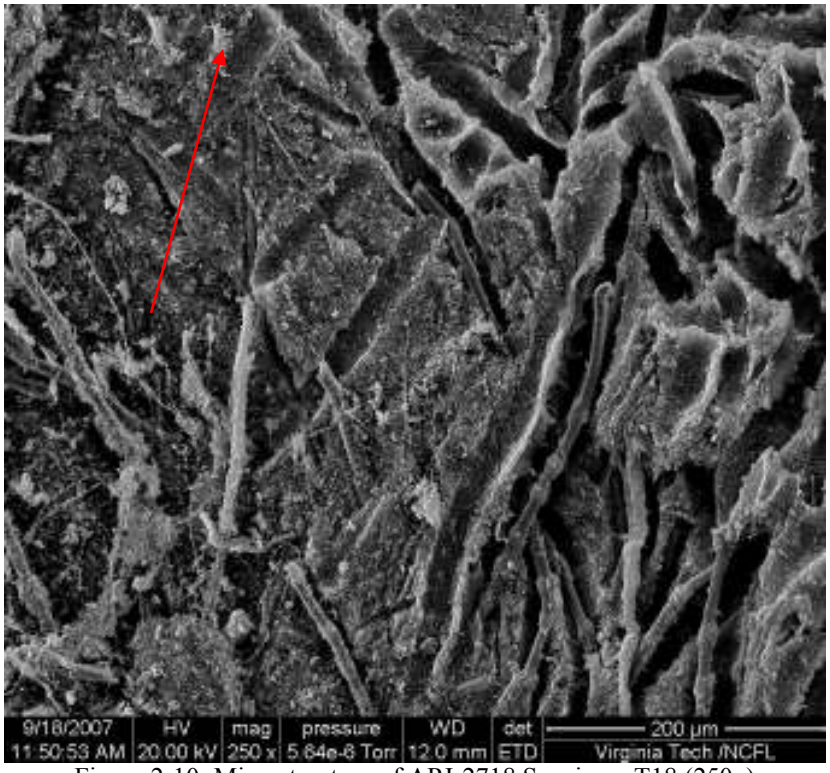

Figure 2-10: Microstructure of ARI-2718 Specimen T18 (250x)

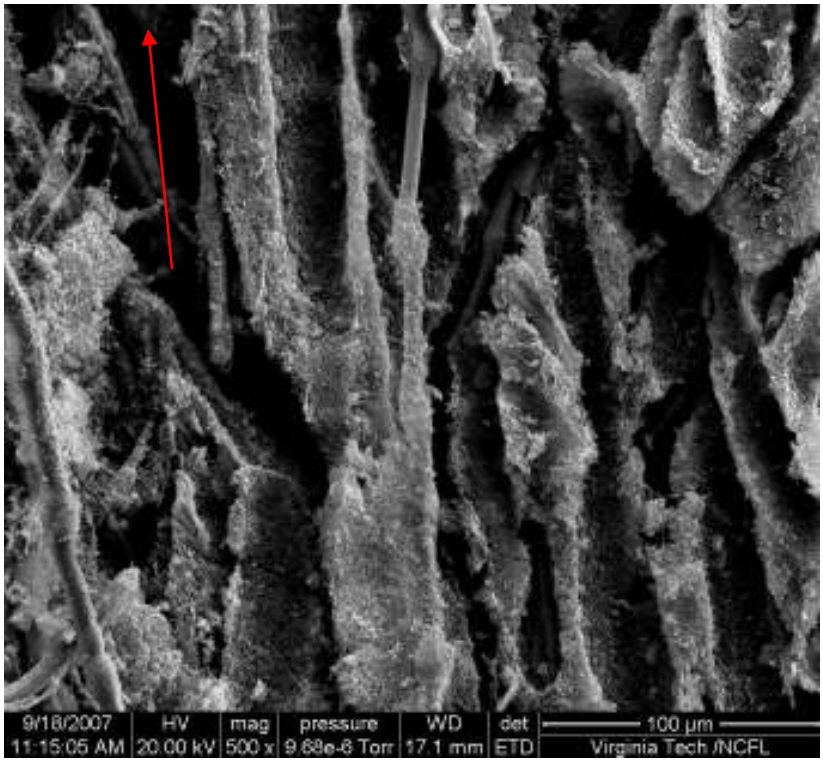

Figure 2-11: Microstructure of ARI-2718 Specimen T11 (500x)

These images show broken fibers, cavities surrounding the fibers, and small clumps of particles dispersed throughout, attached sometimes to fibers and sometimes to the remnants of the matrix. For most of the fibers shown, either the matrix seems to have pulled away from the fiber during char, or the fiber has shrunk during char, leaving gaps between the fiber and matrix.

## ARI-2719 Micrographs

The following images show representative microstructures observed for the ARI-2719 material.

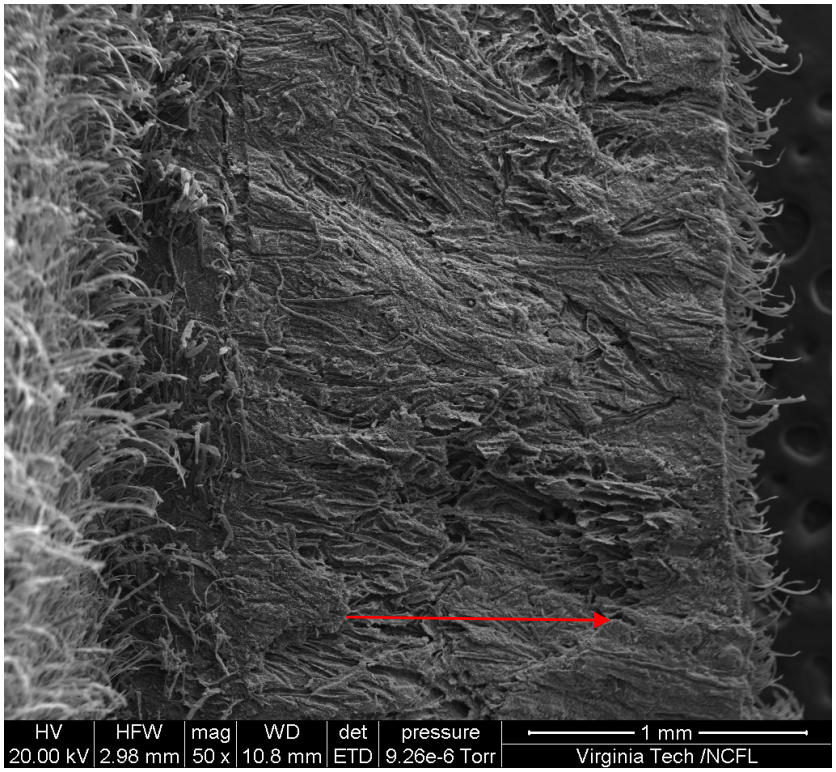

Figure 2-12: Microstructure of ARI-2719 Specimen L10 (50x)

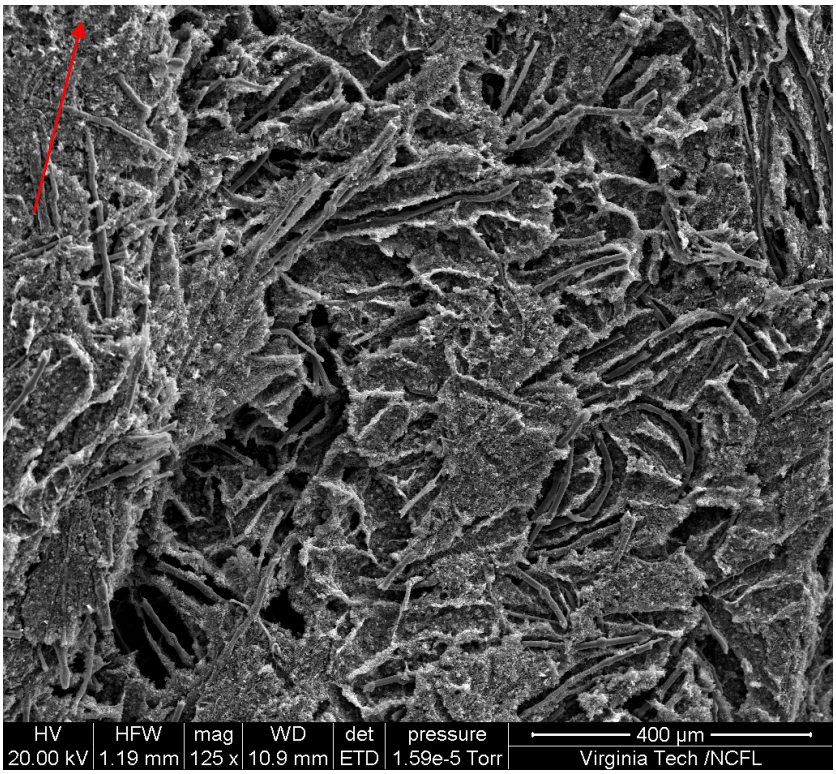

Figure 2-13: Microstructure of ARI-2719 Specimen T11 (125x)

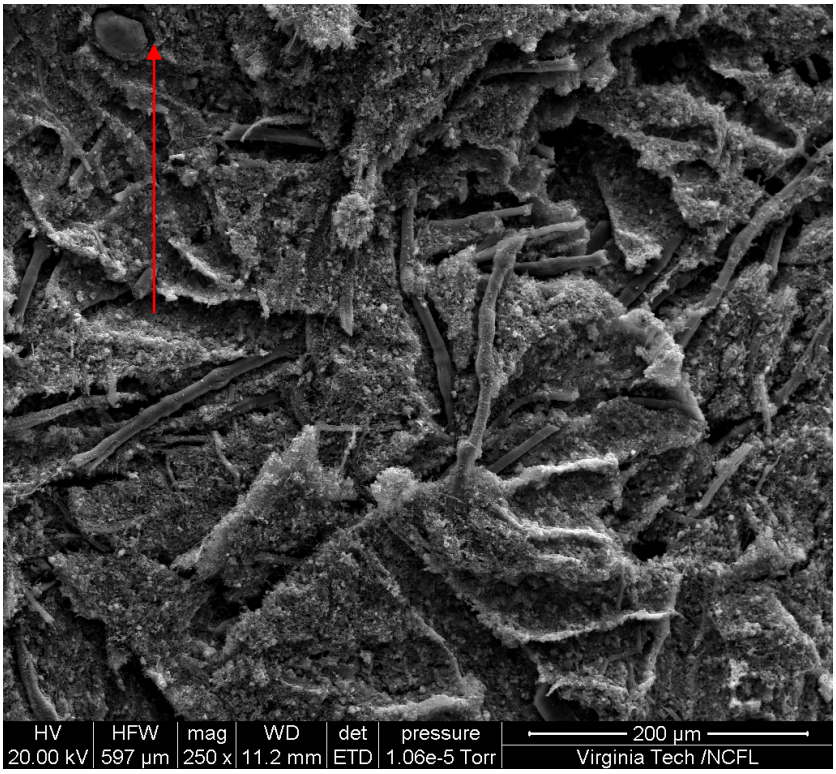

Figure 2-14: Microstructure of ARI-2719 Specimen T15 (250x)

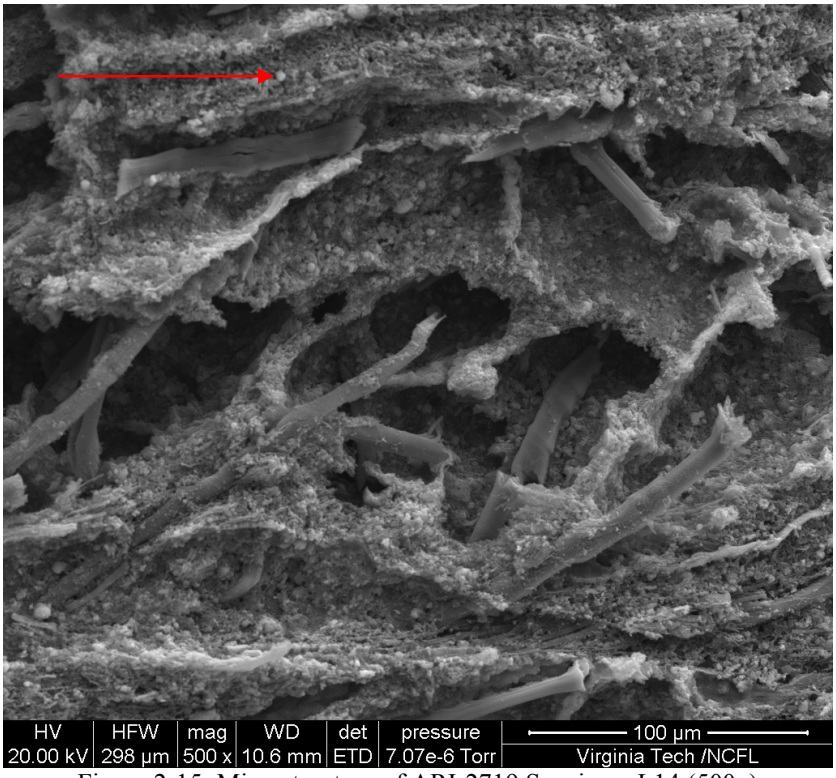

Figure 2-15: Microstructure of ARI-2719 Specimen L14 (500x)

The microstructure for this material is very similar to that of ARI-2718, as was expected. See Chapter 3 for a discussion of the differences observed.

## ARI-2732 Micrographs

The micrographs taken from the exposed surfaces of the cracked specimens of ARI-2732 showed a variety of microstructure types. The following images show several at the same magnification.

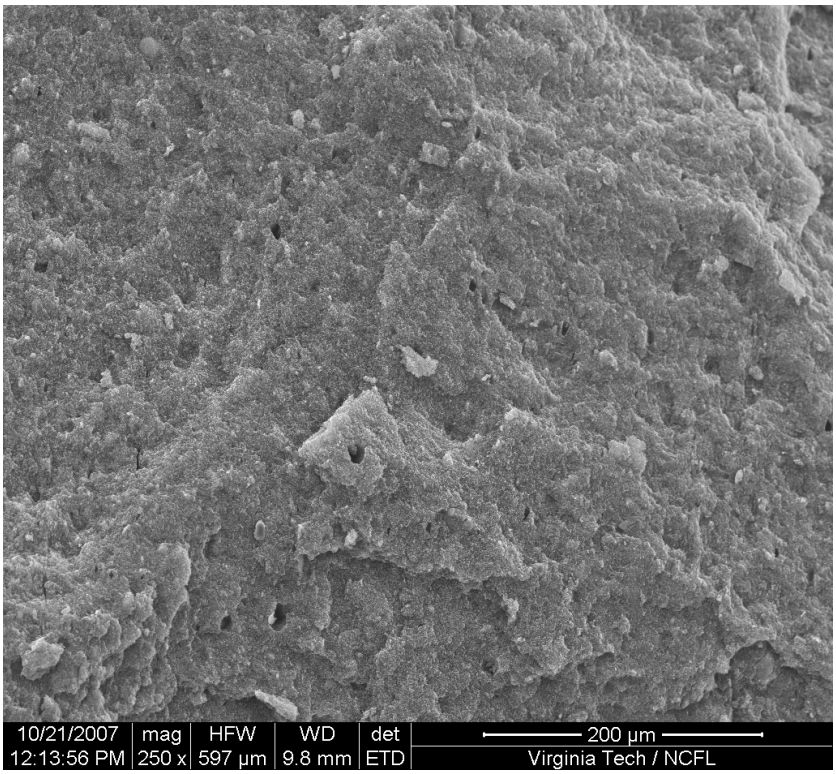

Figure 2-16: Microstructure of ARI-2732 Specimen 1 (250x)

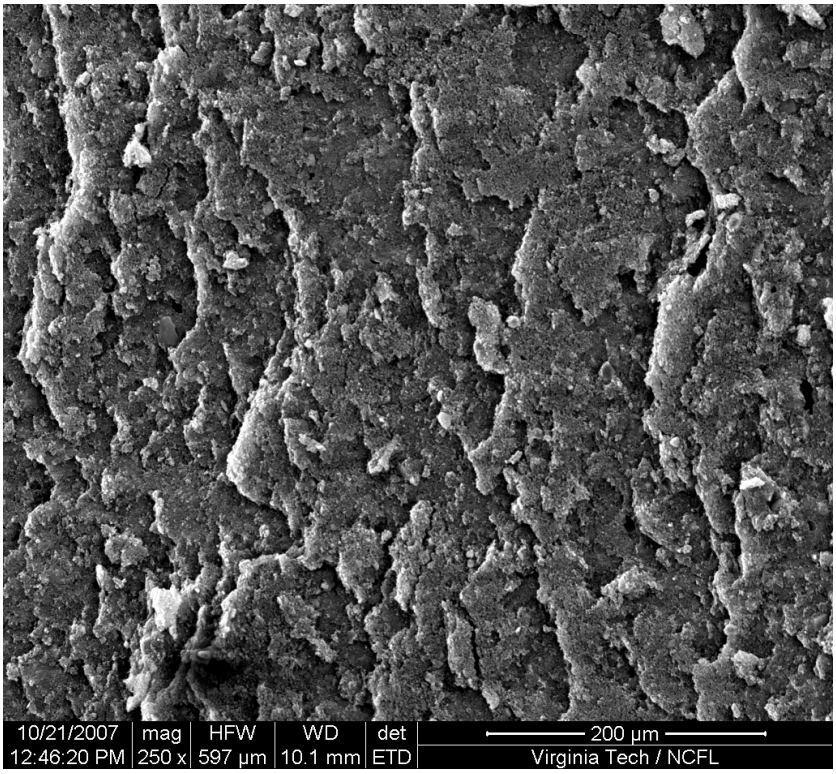

Figure 2-17: Microstructure of ARI-2732 Specimen 3 (250x)

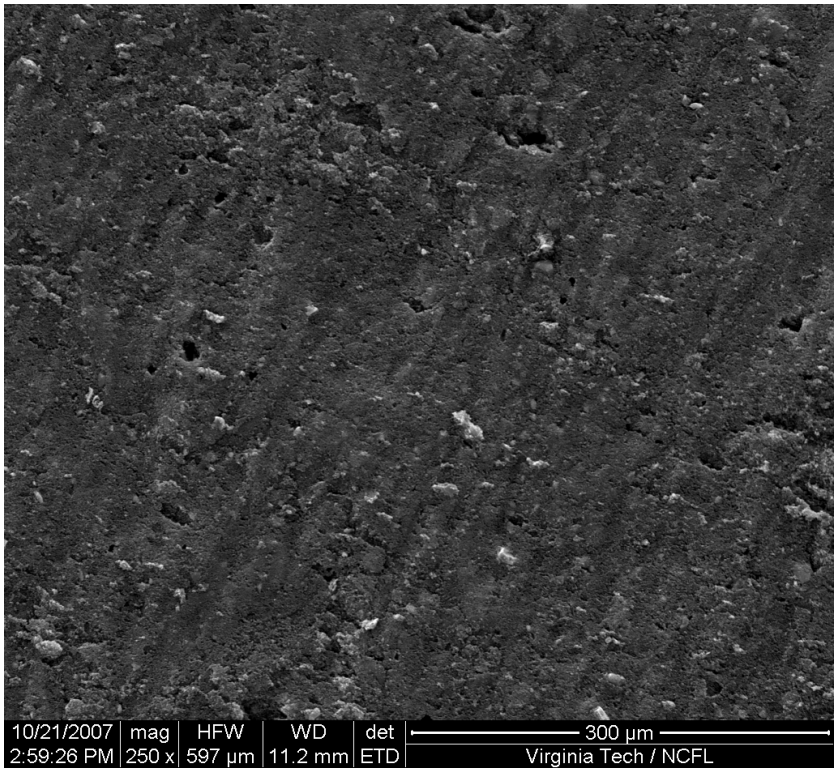

Figure 2-18: Microstructure of ARI-2732 Specimen 5 (250x)

These images are presented only for the sake of completion; since shear testing did not take place, there are no fracture surfaces to compare to the other materials. The variety in the microstructures observed for this material show that there were differing types of failure occurring during char.

## ARI-2750 Micrographs

The following images show representative microstructures observed for the ARI-2750 material.

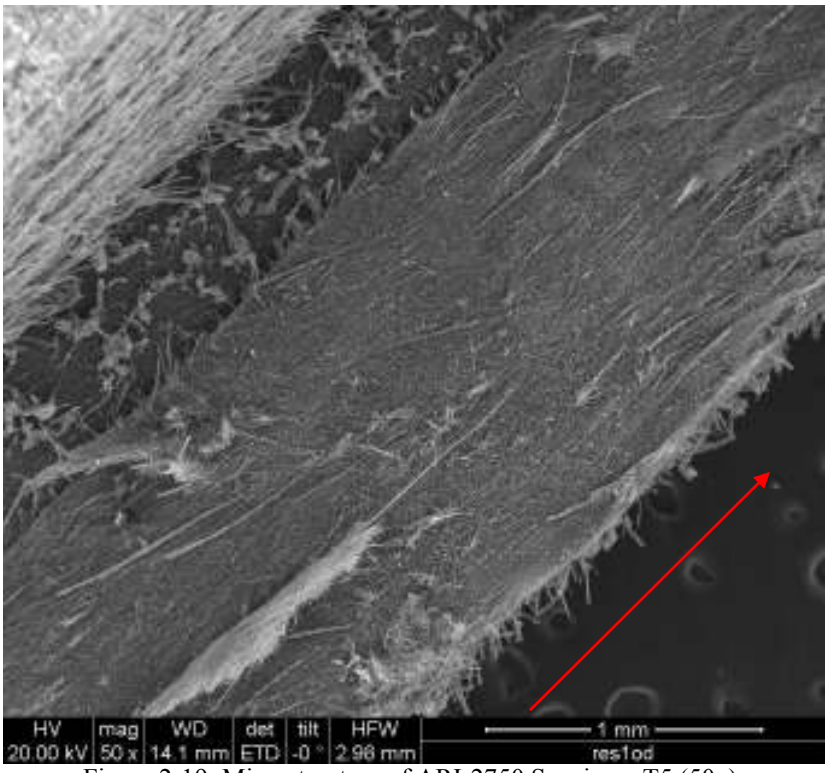

Figure 2-19: Microstructure of ARI-2750 Specimen T5 (50x)

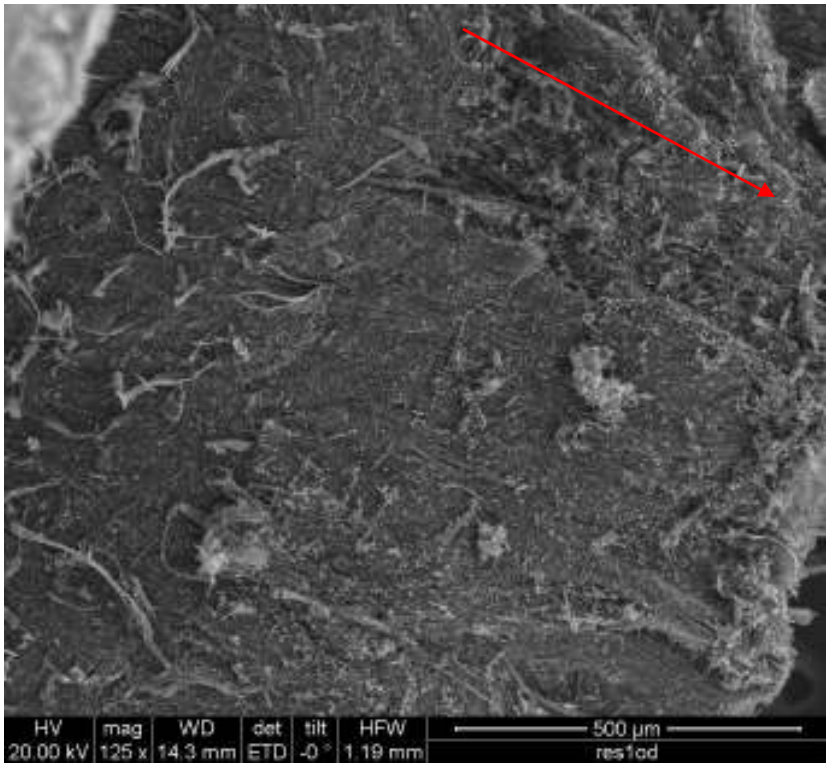

Figure 2-20: Microstructure of ARI-2750 Specimen L6 (125x)

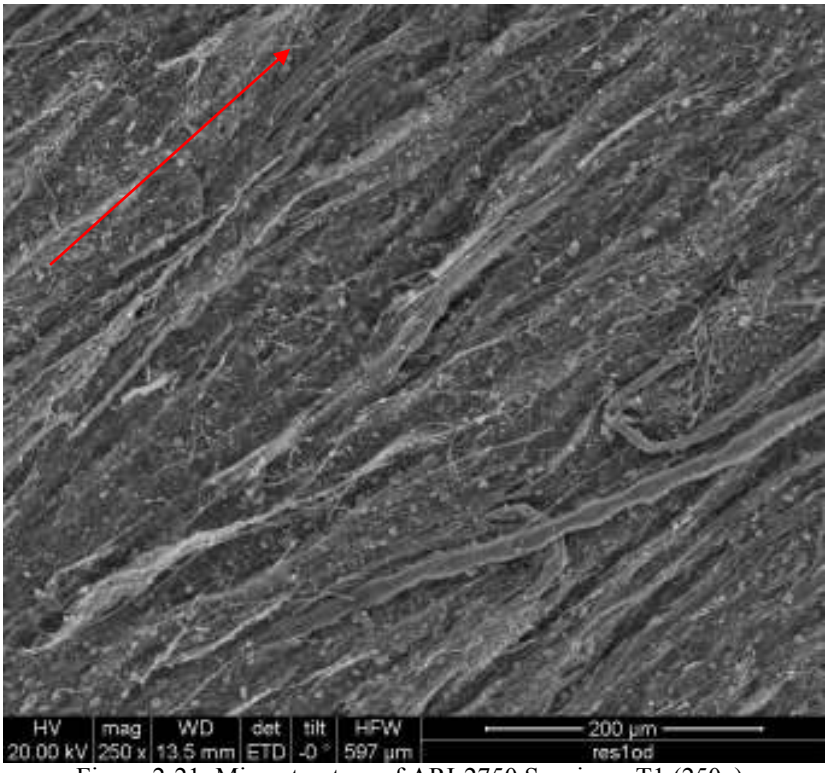

Figure 2-21: Microstructure of ARI-2750 Specimen T1 (250x)

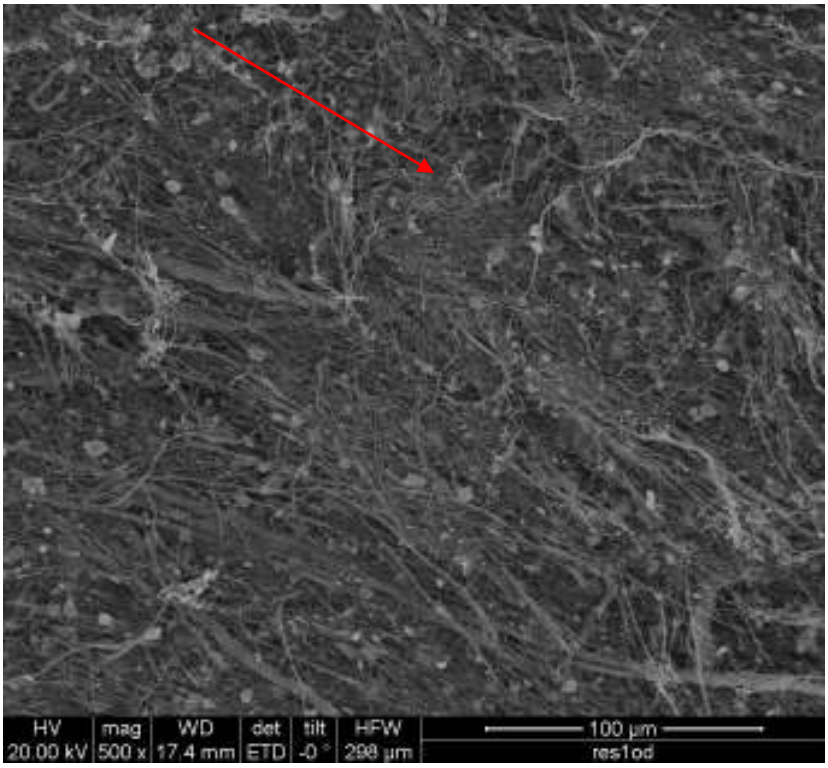

Figure 2-22: Microstructure of ARI-2750 Specimen L1 (500x)

Figure 2-23: Microstructure of ARI-2750 Specimen T13 (1000x)

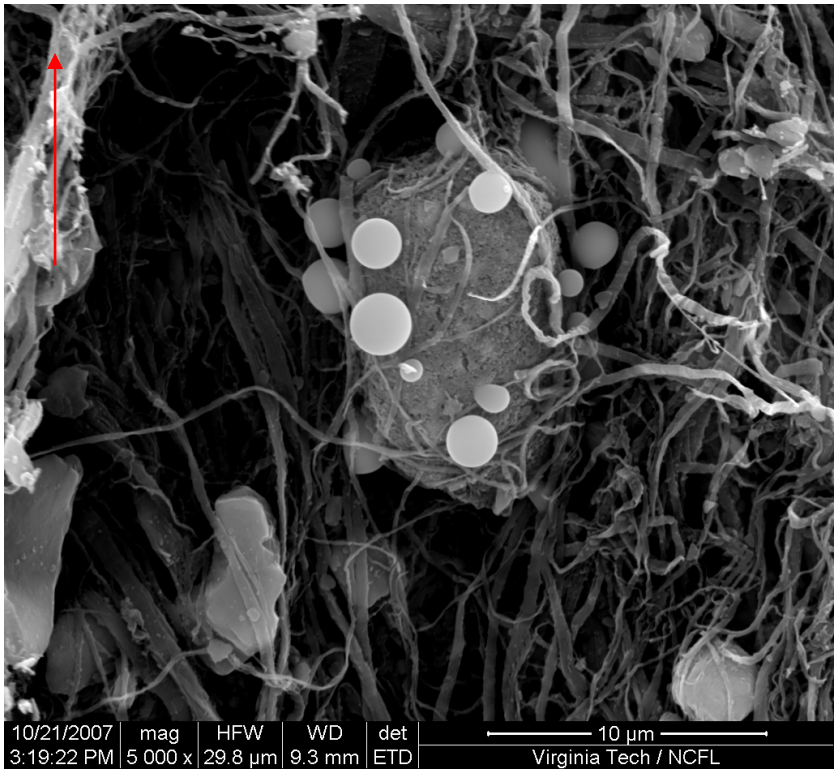

Figure 2-24: Microstructure of ARI-2750 Specimen T13 Showing Particles (5000x)

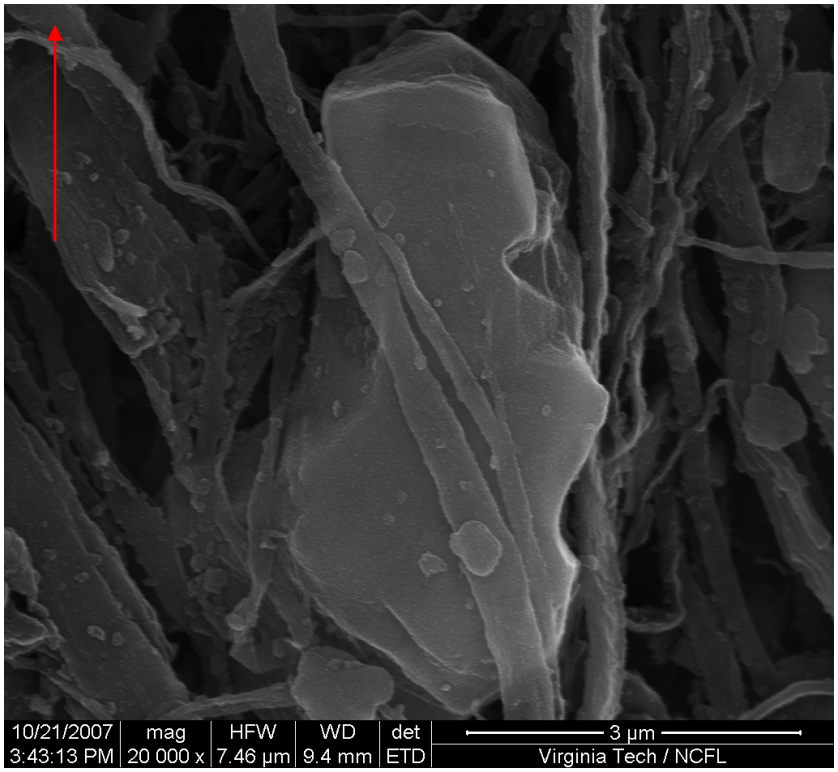

Figure 2-25: Particles from ARI-2750 Specimen T13 (20kx)

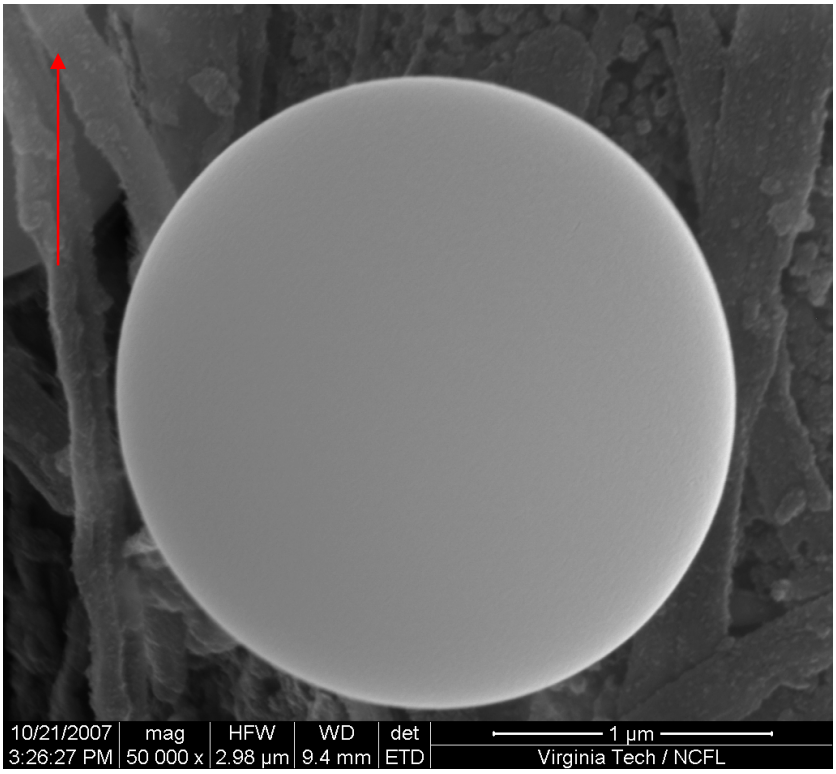

Figure 2-26: Particle from ARI-2750 Specimen T13 (50kx)

These images show the differing fiber sizes used in the fiber blend, a somewhat tangled network of fibers, and at least two types of particles scattered throughout the material, sometimes attached to fibers.

## ISM-Charred ARI-2750 Micrographs

The following images show representative microstructures observed for the ARI-2750 material recovered from Aerojet's insulation screening motor (ISM).

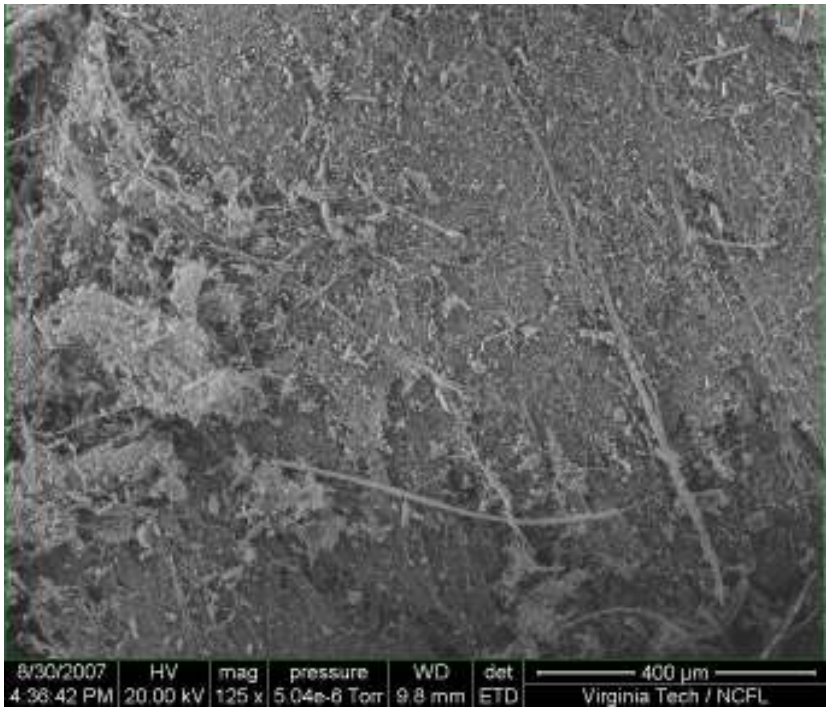

Figure 2-27: Microstructure of ISM-Charred ARI-2750 Specimen 1 (125x)

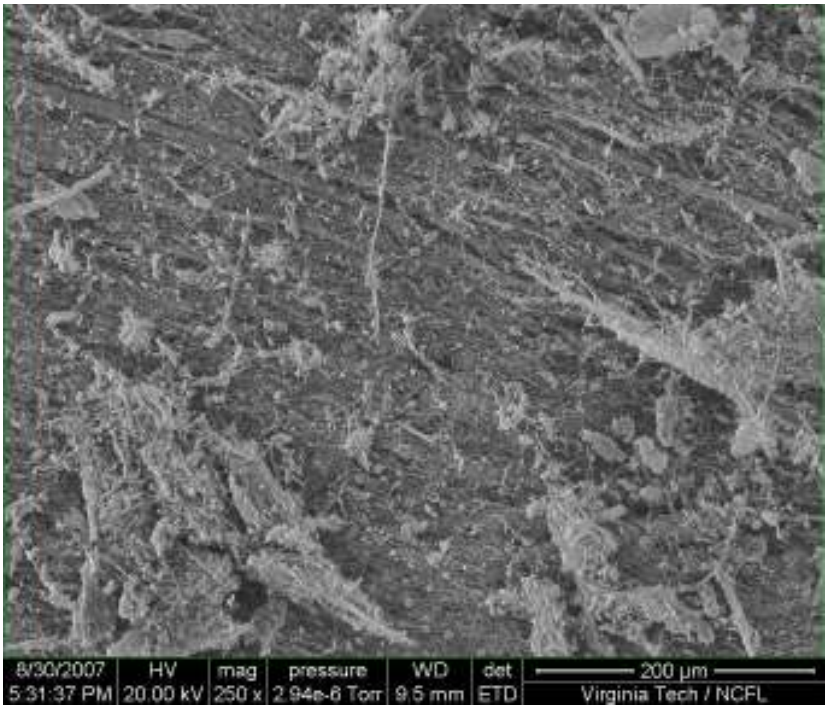

Figure 2-28: Microstructure of ISM-Charred ARI-2750 Specimen 5 (250x)

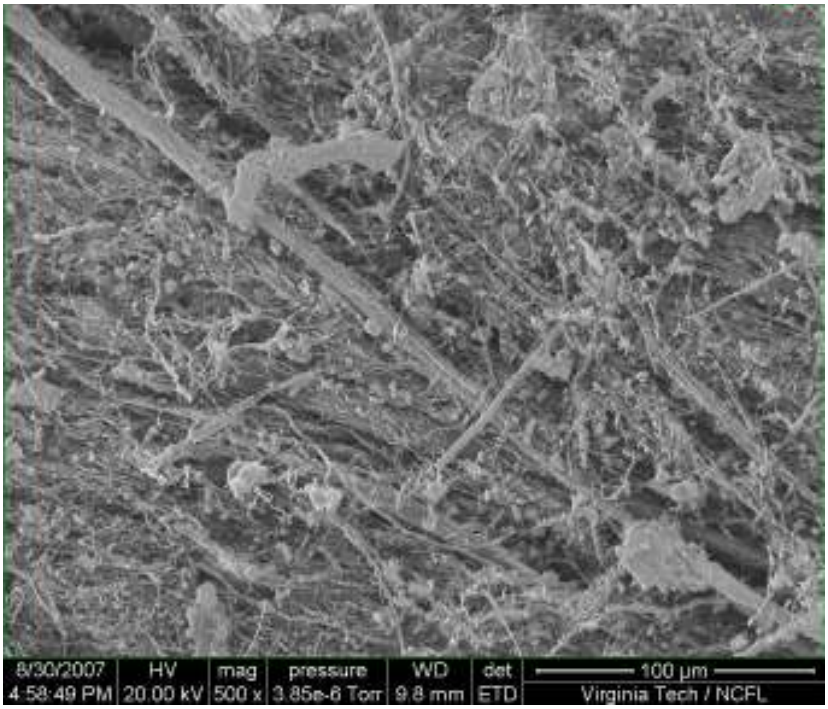

Figure 2-29: Microstructure of ISM-Charred ARI-2750 Specimen 2 (500x)

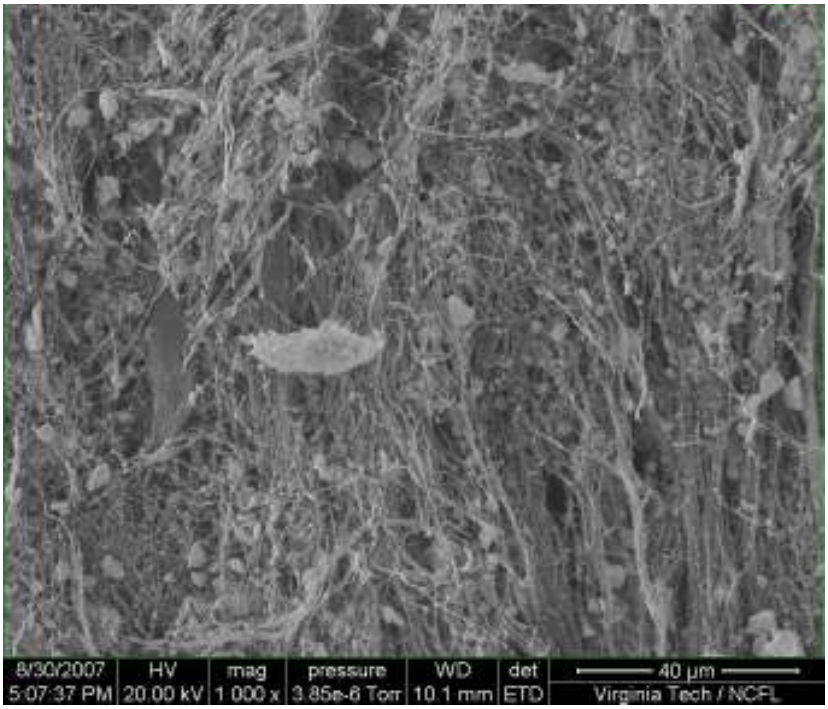

Figure 2-30: Microstructure of ISM-Charred ARI-2750 Specimen 3 (1000x)

These figures again show the clear distinction in fiber sizes included in this material, as well as the tangled fiber network and the particle reinforcements throughout.

### Compositional changes

For a chart of composition results as obtained by EDS for each material, as well as a comparison of these results to the virgin compositions, see the attached Appendix B (ITAR restricted).

*The full set of micrographs taken for this study is included below in Appendix C, including some images of virgin microstructures from polished material specimens.*

## *Mechanical Testing*

### Testing setup

Because the failure loads for the small samples used in this work were expected to be very low, the shear testing was initially performed on a TA Instruments Q-800 DMA fixture. Early tests showed that the loads at failure for these materials were between 2 and 5 N, well within the 18-N capacity of this machine. The test parameters were determined from analysis of these practice tests. First, a preload force of 0.1 N was applied, followed by compressing the specimens at a rate of 0.2 N/min and measuring the deflection of the DMA clamp. Specimens were monitored to observe when failure took place.

Full testing proceeded as charred specimens became available. ARI-2750 specimens were first, with two longitudinal (L) specimens and three transverse (T) specimens. All failed within the machine's capacity. Two L and three T specimens of ARI-2718 were then tested, followed by two L and two T of ARI-2719. In total, five T and three L of ARI-2750, seven L and eight T of ARI-2719, and thirteen L and twelve T of ARI-2718 were tested before equipment malfunctions, conference travels, and a medical leave delayed further mechanical testing for three months.

The second series of testing finished the remainder of the ARI-2718 specimens; all failed below 5 N of load. The remainder of T specimens of ARI-2750 followed, again with all failing within the DMA capacity. The first L specimen of this material tested, though, failed at 11.5 N, much higher than any previous specimen. The next two were also unusually strong, and the fourth specimen actually survived the 18-N maximum load for the machine. Because the tests were now running too long, the ramp rate was increased to 0.4 N/min. Two of the next five specimens tested also survived. A single ARI-2719 L specimen was tested and also survived. In searching for an explanation for the increase in strengths from the earlier tests, it was discovered that while testing for this work was on hold, the facilities manager in charge of the DMA determined that the calibration was very incorrect; recalibration occurred without alerting anyone who had been testing in recent months. Once this was established, results from the earlier tests were thrown out and a new test frame with a higher load capacity was sought.

The remainder of the tests took place on an Instron 5867 test frame, shown in Figure 2-31 below.

Figure 2-31: Instron 5867 Test Fixture

The compression clamps were machined from aluminum specifically for this study; they are shown closer in Figure 2-32.

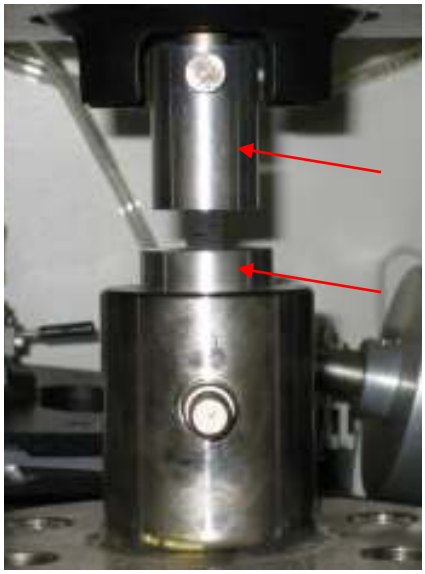

Figure 2-32: Machined Aluminum Compression Clamps

Initially, the 0.4 N/min ramp rate from the DMA was used as the controlling parameter for the Instron, but the frame was unable to maintain a load-controlled compression when the specimens would start to break. The load would drop too fast for the screws to increase it to the necessary amount, so the frame would frantically cycle up and down to try to compensate, thus destroying the specimen. Looking at the crosshead speed during testing revealed that a controlling parameter of 0.025 mm/min would approximate the loading produced by the 0.4 N/min rate.

## Results

Figure 2-33 and Table 2-2 below present the average shear strength values measured for each material, along with error bars representing one standard deviation.

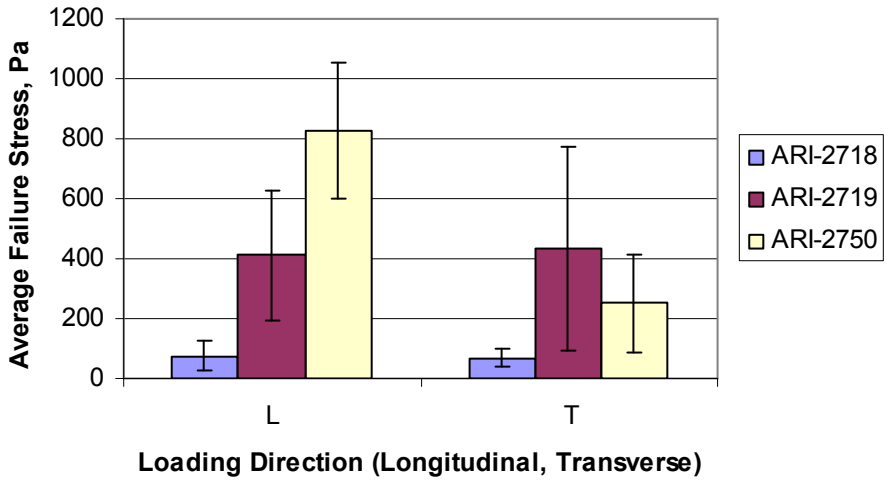


Figure 2-33: Average Shear Strength Measurements

Table 2-2: Average Shear Strength Measurements

| Material | Average Shear Strength | |
|---|---|---|
| | Longitudinal | Transverse |
| ARI-2718 | 75.8 ± 51 | 69.5 ± 31 |
| ARI-2719 | 412 ± 220 | 432 ± 340 |
| ARI-2750 | 826 ± 230 | 237 ± 160 |

For these numbers, specimens that were judged to have failed incorrectly were not included in the average strength calculations. This poor breakage refers to specimens not breaking between the notches, poorly-fabricated specimens (too warped to generate good shearing, notches not reaching the center of the specimen or overshooting the center, etc.), or any other observation during testing that signifies that the test on that material poorly reflects the actual material behavior. Full results for these tests are included below in Appendix D.

## *Thermal Property Testing*

For these tests, square specimens were cut from the original panels so as to be large enough in area that the panel thickness could be used as the probing depth. After making room-temperature measurements on a Kapton-enclosed sensor, it was discovered

that there are no high-temperature sensors, which are enclosed in mica, that are small enough to accurately measure any specimens cut from the provided panels. As the panels provided were already thicker than most produced by Aerojet, the elevated-temperature measurements were abandoned, though room-temperature measurements were still taken.

## Testing setup

As mentioned above, squares were cut from the original panels, about 4 cm on a side, to be used in the HotDisk measurements. These specimens were charred alongside those for the shear testing. ARI-2732 was not included in this series of tests due to the inability to produce specimens of sufficient size and integrity, as described above. Practice runs were performed on each of the materials to determine what combination of test parameters for a given material produces the most reproducible results. For all materials, the power output was set to 10 mW, a recommended setting for polymer materials. The only real adjustment among materials, therefore, was the measuring time, which was set to the following values after the practice runs:

Table 2-3: HotDisk Measuring Time by Material

| Material | ARI-2718 | ARI-2719 | ARI-2750 |
|---|---|---|---|
| Measuring Time, s | 7.5 | 10.0 | 5.0 |

## Results

Five measurements were made for each material, from which the average values below were calculated (error bars represent one standard deviation).

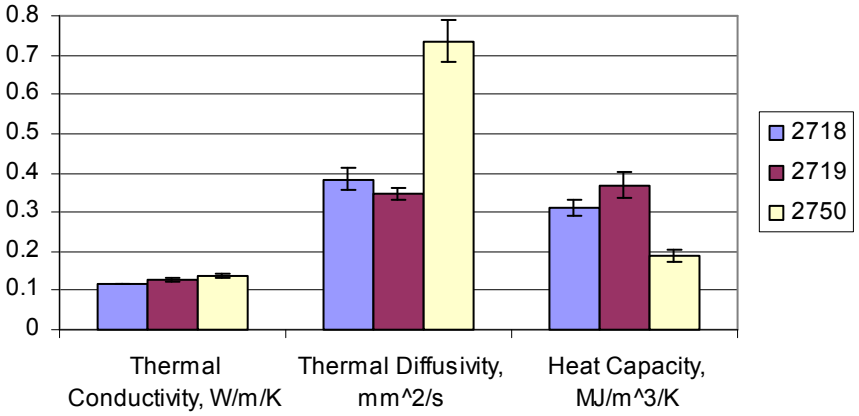


Figure 2-34: Average Thermal Property Measurements

Table 2-4: Average Thermal Property Measurements

| Material | ARI-2718 | ARI-2719 | ARI-2750 |
|---|---|---|---|
| Thermal Conductivity, W/m/K | 0.119 ± 0.001 | 0.127 ± 0.006 | 0.138 ± 0.004 |
| Thermal Diffusivity, $mm^2/s$ | 0.384 ± 0.027 | 0.347 ± 0.017 | 0.735 ± 0.055 |
| Heat Capacity, $MJ/m^3/K$ | 0.311 ± 0.022 | 0.368 ± 0.033 | 0.188 ± 0.015 |

As expected by the similar compositions, the thermal properties of ARI-2718 and ARI-2719 are very similar. ARI-2750 has a similar value of thermal conductivity, a higher thermal diffusivity, and a reduced heat capacity compared with these two materials.

The thermal conductivity measurements here are low compared to published values of other EPDM composites, which report conductivities between about 0.275 and 0.375 W/m-K.[4,19] These materials are not identical to any tested in this work, though. No published thermal diffusivity values were found, and densities were not calculated to allow these heat capacity values to be compared to published specific heat measurements.

# Chapter 3: Discussion and Conclusions

## *Microstructural Comparison*

There are few clear differences between the microstructures of ARI-2718 and ARI-2719. The main visible difference is probably the condition of the matrix material, as shown in Figure 3-1and Figure 3-2 below.

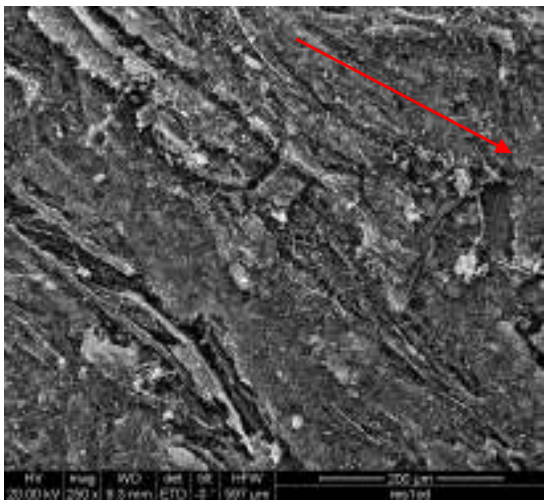

Specimen L20

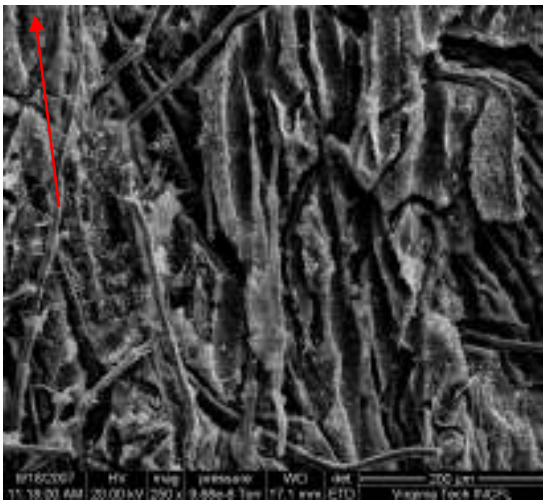

Specimen T11

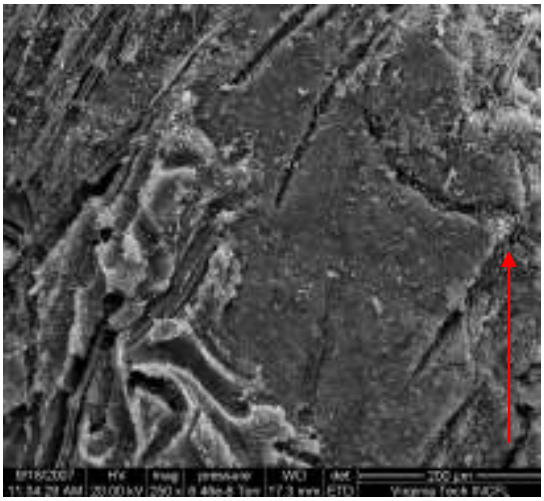

Specimen T14

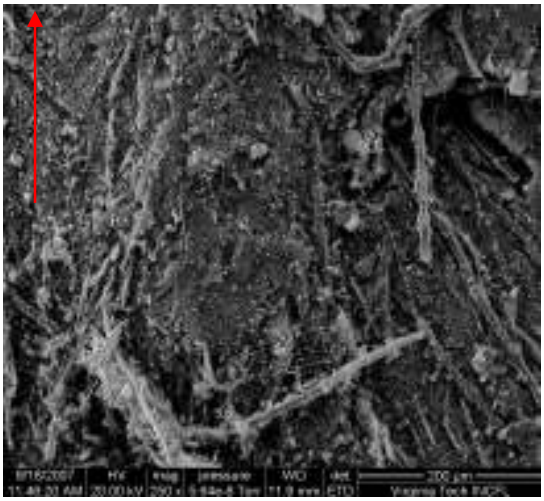

Specimen T18

Figure 3-1: Microstructures of ARI-2718 (250x)

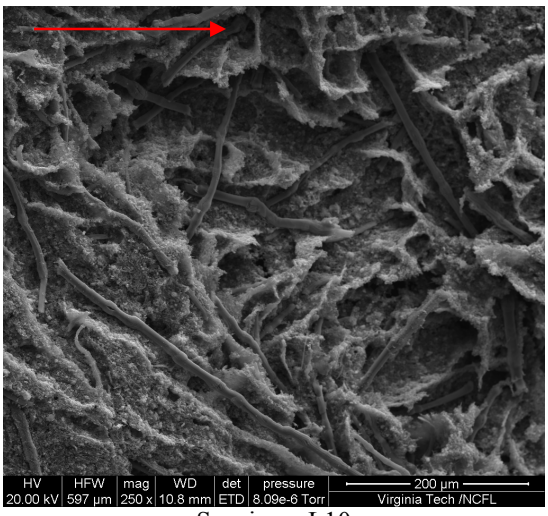


Specimen L10

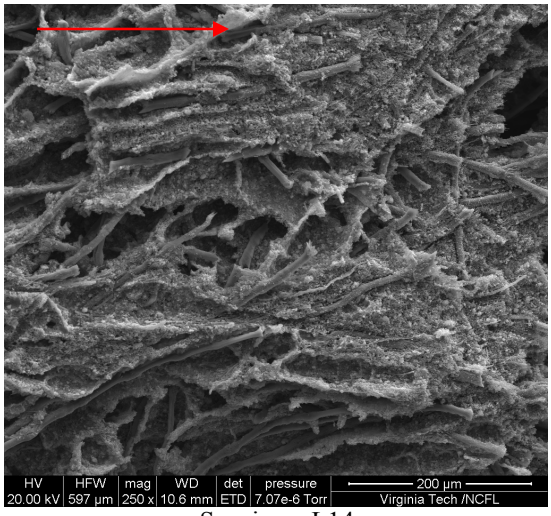


Specimen L14

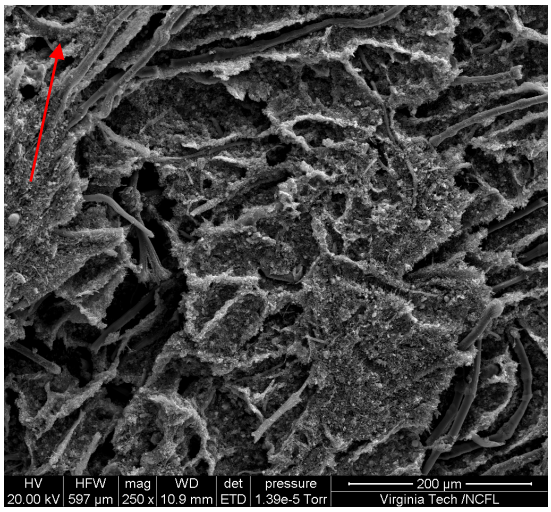


Specimen T11

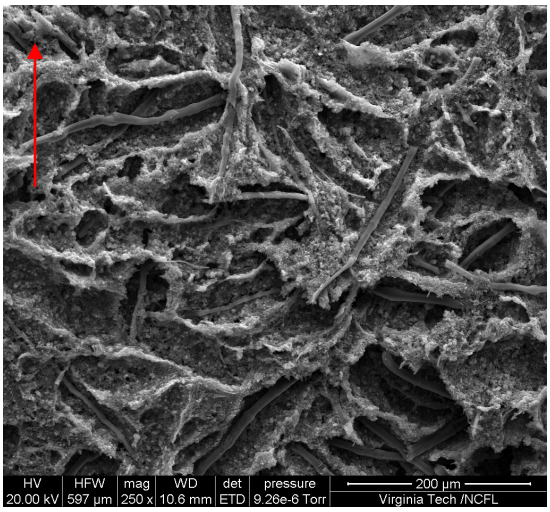


Specimen T18

Figure 3-2: Microstructures of ARI-2719 (250x)

The charred matrix in the ARI-2719 seems to be more porous than that of the ARI-2718. The ARI-2718 also seemed to have more matrix area "intact," similar to that shown in the microstructure of specimen T14. Initially, it appeared that there may be a difference in fiber failure behavior between these materials. Further research showed that there was no statistically significant difference between the fiber failures in ARI-2718 and ARI-2719 and that the fiber failure in both materials was consistent with the literature.[20-22]

The matrix material is also a key difference between ARI-2718/2719 and ARI-2750; figures 3-3, 3-4, and 3-5 illustrate this difference.

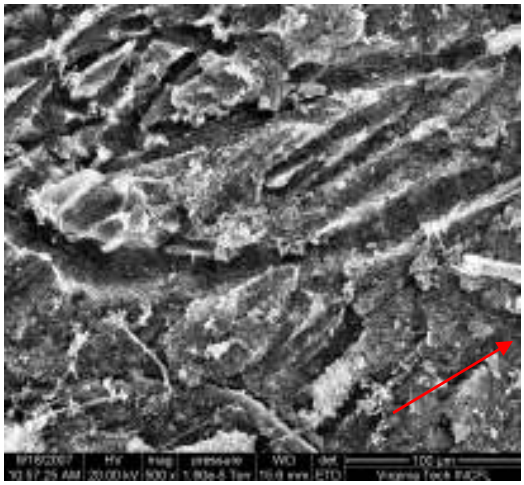

Specimen L4

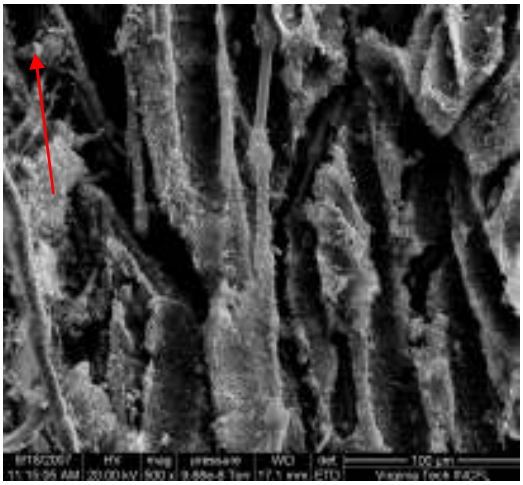

Specimen T11

Figure 3-3: Microstructures of ARI-2718 (500x)

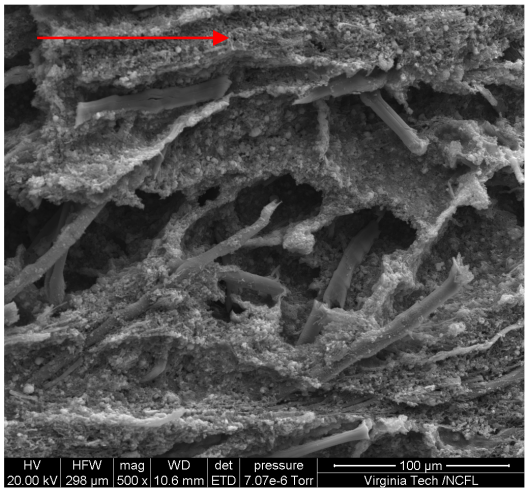


Specimen L14

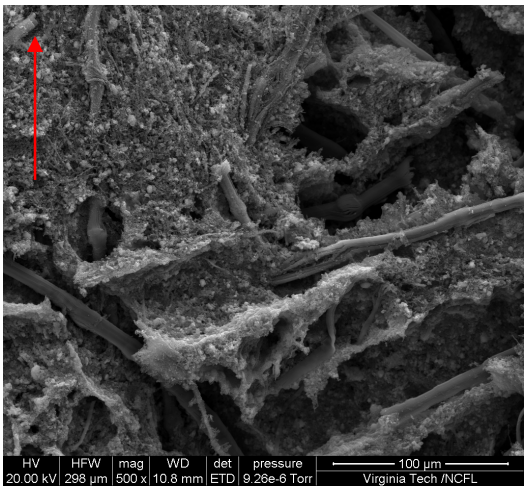


Specimen T18

Figure 3-4: Microstructures of ARI-2719 (500x)

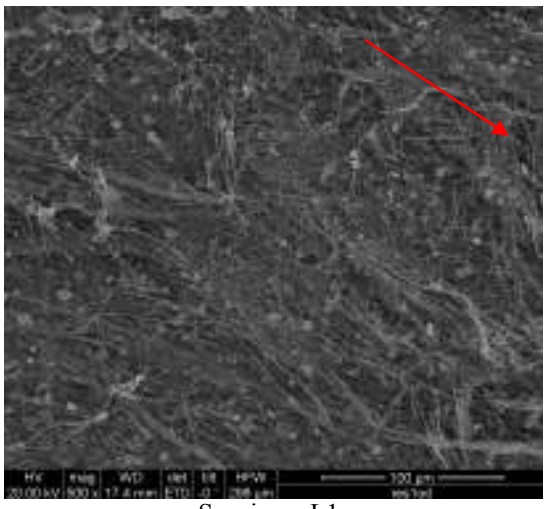

Specimen L1

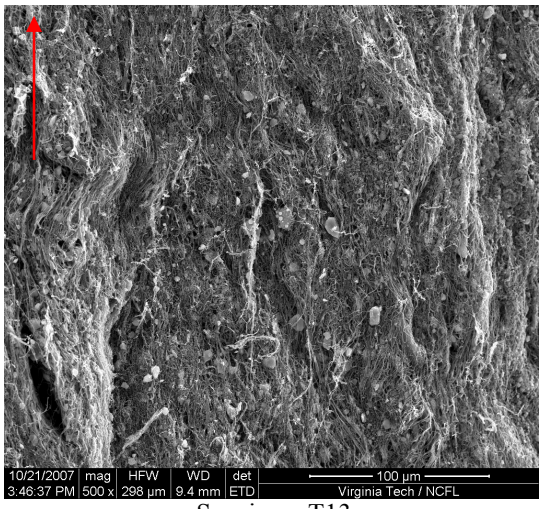


Specimen T13

Figure 3-5: Microstructures of ARI-2750 (500x)

While there is a clear difference between fiber and matrix in the ARI-2718 and ARI-2719, the matrix in ARI-2750 is less clearly discernible. Figure 3-6 shows the ARI-2750 microstructure at a higher magnification.

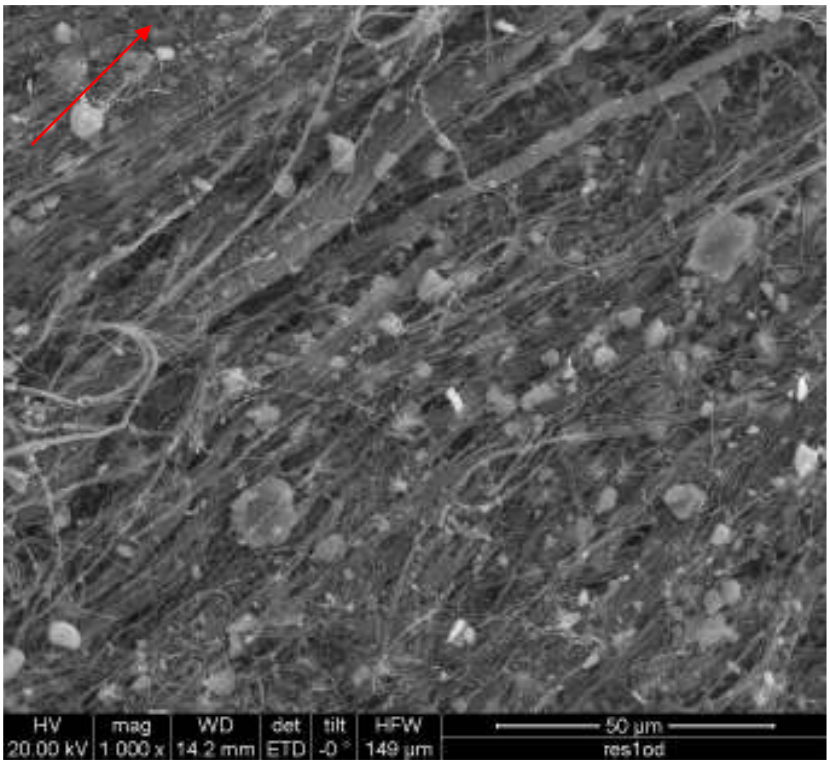

Figure 3-6: Microstructure of ARI-2750 (1000x)

The matrix material in the ARI-2750 seems to exist only in small, crumbled pieces, compared to the larger fragments visible in ARI-2718 and ARI-2719. Another major difference in ARI-2750 is the fact that the fiber reinforcements in this material are in a blend of two different sizes, clearly shown in Figure 3-6 above, compared to the uniform fiber size in ARI-2718 and ARI-2719.

One of the objectives of this project was to compare the microstructure of the charred ARI-2750 material to that taken from Aerojet's insulation screening motor. Since there are no available fracture surfaces for the ISM-charred ARI-2750, the microstructures cannot be directly compared to one another, but should be sufficient to

verify that the furnace procedure described above produced material reasonably similar to that produced in the ISM. Figures 3-7 and 3-8 below show the microstructures of the two materials.

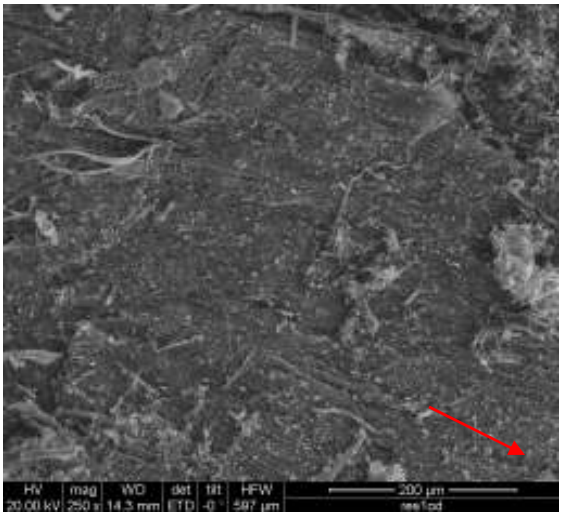


Specimen L6

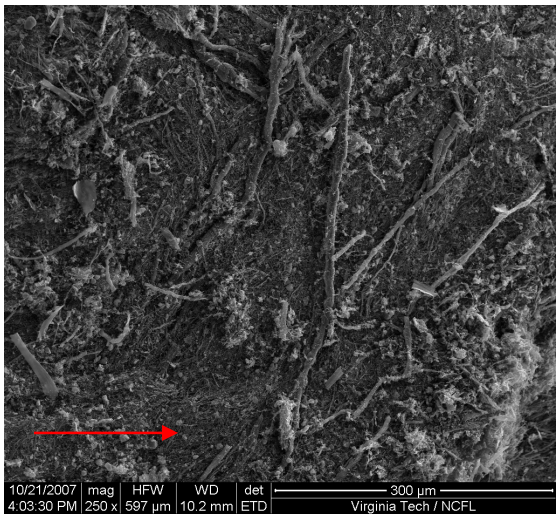


Specimen L11

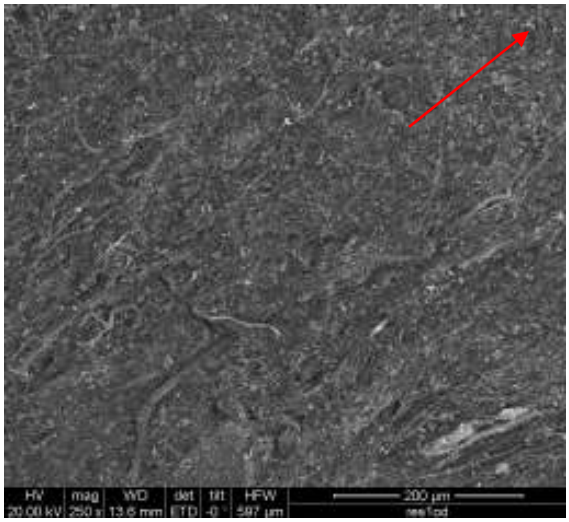


Specimen T1

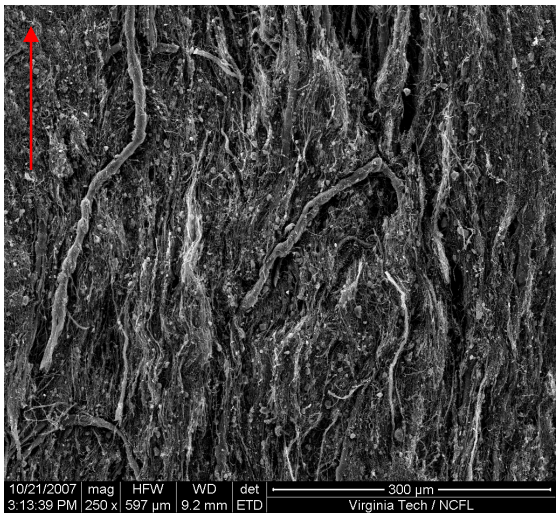


Specimen T13

Figure 3-7: Microstructures of ARI-2750 (250x)

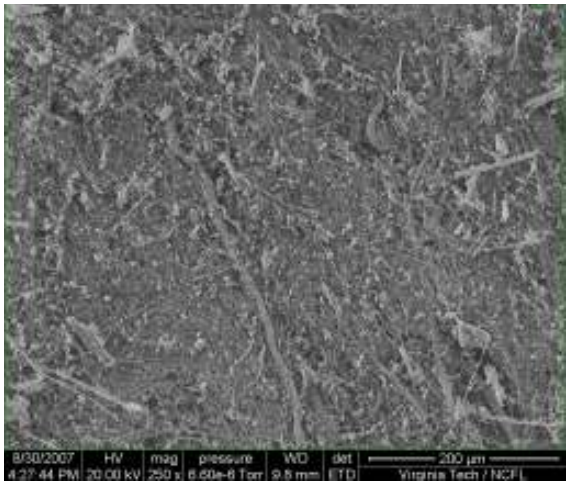
Specimen 1

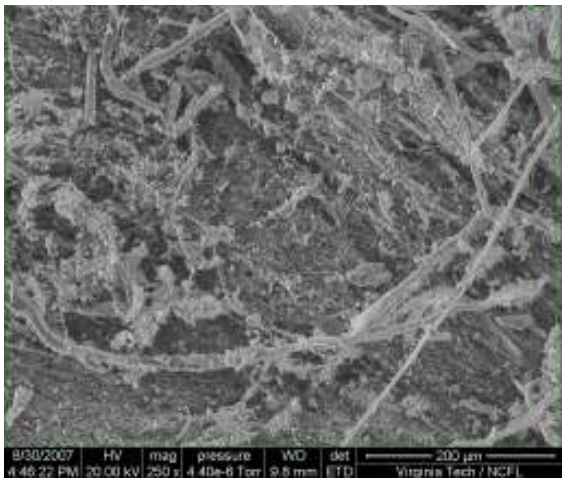
Specimen 2

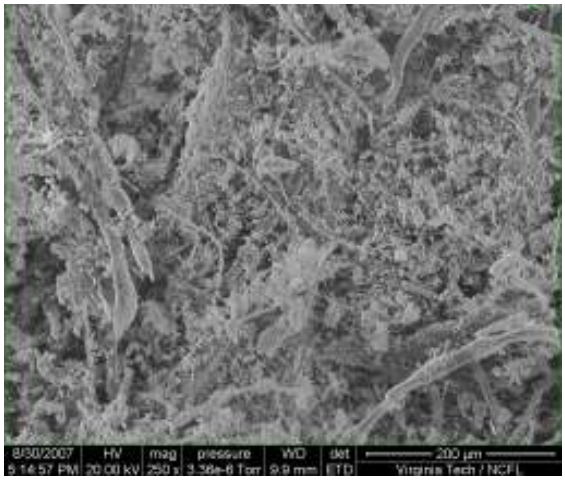
Specimen 3

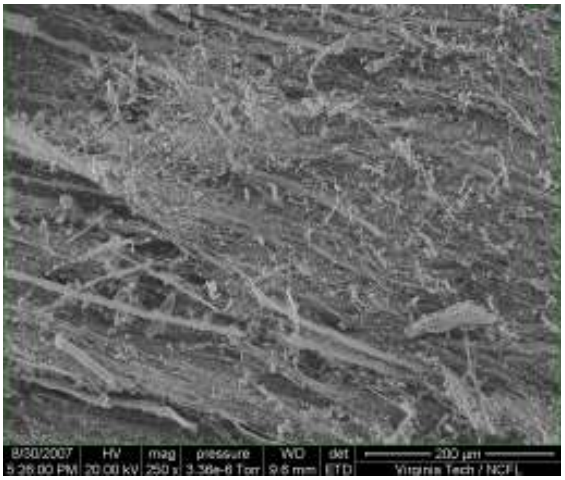
Specimen 5

Figure 3-8: Microstructures of ISM-Charred ARI-2750 (250x)

These microstructures of these two materials are very similar to each other. The ISM material, upon delivery, had split basically into layers planar to the original material panel. Some evidence of this splitting can be seen in some of the micrographs in Appendix C, but it does not represent any significant difference in microstructure between the furnace-charred and ISM-charred ARI-2750. Another insignificant difference is what appears to be an increase in debris present in the ISM-charred material. This probably arose from transport and storage of the material, which took place inside a large plastic bag, allowing powdered remnants of the material to collect on the larger sections of material. These two small differences aside, the microstructure of ARI-2750

seems consistent for the two charring procedures, thereby confirming that the furnace charring procedure produced material physically comparable to that which may occur during actual rocket motor operation.

### *Shear Strength Comparison*

The ARI-2718 and ARI-2719 materials show no statistical effect of loading direction on shear strengths, unlike the ARI-2750. ARI-2719 is much stronger than the ARI-2718 in both directions, and it is stronger when loaded transverse to the orientation direction than the ARI-2750 is. The strongest material overall is the longitudinally-loaded ARI-2750.

### *Structure-Property Correlations*

The high sensitivity of the ARI-2750 strength values to loading direction most likely relates to the microstructural differences described above. As shown previously in Figure 3-6, the fibers in ARI-2750 are very aligned with very little visible matrix material remaining after char. Since the majority of remaining material is oriented fibers, it follows that the properties will strongly depend on the angle between the loading direction and the fibers' orientation. The ARI-2718/2719, with less-aligned fibers and more matrix material remaining after charring, should be better able to transfer load throughout the material, reducing the directional sensitivity of the materials' shear strengths.

Though made of very similar materials, the ARI-2719 was much stronger in shear than the ARI-2718. No clear reason behind this was found through either microstructural or compositional analysis. The change in strength may result from the extra number of cycles through the calender when processing ARI-2719 compared to ARI-2718, affecting

the orientation of the material. The constituent materials, supplied by different vendors for ARI-2718 and ARI-2719, may respond very differently to charring in terms of mechanical properties (fiber strength, etc.); this could also affect the overall mechanical behavior. The first round of microscopy showed that there might be a difference in fiber failure mechanisms in the two materials, but more detailed analysis did not produce any conclusive results for this project.

No clear impact of particle shape, size, or concentration could be determined from looking at the failure surfaces of these materials. A separate test schedule controlling all other variables would be necessary to investigate the influence of these factors.

## *Conclusions*

A furnace procedure was developed to simulate the charring that happens to insulating materials in solid rocket motors during operation. A comparison of ARI-2750 samples charred with this procedure to the same material charred in an Aerojet test motor showed no significant difference in microstructure or elemental composition. This verified that materials produced with the charring process developed herein could be used to reasonably represent those produced during actual rocket motor operation.

In this work's tests, the ARI-2750 demonstrated the highest shear strength after charring, though only when loaded along the material orientation induced during processing. The shear strength when loaded transverse to the material orientation was less than 30% of the longitudinal shear strength; this is likely caused by the high fiber alignment observed in the ARI-2750 microstructure. These fibers can only bear load along their axis, and without any fibers in transverse directions, the load is borne almost entirely by the remnants of the matrix material.

The ARI-2719 was strongest when loaded transverse to the material orientation, due probably to less-oriented fibers and a greater amount of residual matrix compared to the ARI-2750. The fibers in ARI-2719, being less aligned than in ARI-2750, would be better able to handle load transferred to them through the matrix.

The ARI-2718, though compositionally very similar to the ARI-2719, showed much lower shear strengths in both directions than the ARI-2719. No clear microstructural or compositional explanation for this could be determined under the scope of this work. Additional testing focusing on isolating specific elements of the materials, such as charred fiber strength or particle size, may be able to identify further correlations between shear strength and microstructure.

All objectives of this project were thus met, though no microstructural analysis or shear strength measurements could be made for ARI-2732, since shear specimens machined from this material did not survive the charring process. The shear strength measurements and their relation to the material morphology, as discussed herein, will hopefully allow for improved modeling and design of thermal insulation systems for solid rocket motors. From the results of this experiment, the best microstructure to produce a charred material with superior shear strength in one direction would be one that has very aligned fibers in a matrix that survives the charring procedure in large fragments. If the charred shear strength cannot be too low in the transverse direction, then the fiber alignment should be reduced and the matrix should still survive in larger proportions.

## *Lessons Learned and Future Work*

The first lesson learned in this project was about the sensitivity of the materials to heating rate during char. 1 °C/min is probably the fastest effective rate, and even that may be too fast for ARI-2732. Also, the tube used for charring should be significantly long enough so as to prevent too much heat from reaching the tape sealing the ends, which reduces the tape's effectiveness. For the mechanical tests, the warping that occurs during char makes some specimens difficult to accurately compress. To address this, machining the overall panel thickness to a more uniform measurement and being extremely cautious to cut right angles throughout the specimen fabrication may allow for a second ceramic platform to be placed on top of specimens as they char. This second platform should prevent some, if not all, of the warping by holding the top of the specimens in place. There were also several less-successful means of machining the shear test specimens from the panel before reaching the method detailed in Chapter 1, which definitely seemed to be the most effective.

Initial studies into performing tensile tests revealed, as was expected, that strips of the charred material were too fragile to be held directly in the DMA film tension grips; the same is probably true for Instron grips. Tensile test specimens likely would need to be potted at the ends to be successfully tested. The larger the specimen involved, the more beneficial a slow heating rate may be, since there would be more material in which a flaw could develop; conversely, the increased material volume would also reduce the impact of a flaw of any given size compared to a smaller specimen, possibly implying smaller specimens being more sensitive to char rate. A simple experiment could determine which phenomenon dominates the material behavior in this circumstance.

One obvious direction to proceed with this research is to develop a method for performing tensile tests on the charred materials, further characterizing their mechanical properties. Similar work could even be done for individual fibers used in these materials, studying their individual char strength, or using single-fiber composites to test the integrity of the fiber-matrix interface after char. Research could also determine the effect of increased or decreased fiber orientation within a given material system, both to optimize processing procedures and to estimate the effects of varying fiber orientation through a given panel of material. Early attempts to quantify the fiber orientation of the virgin material did not reveal any easy way to determine the amount of orientation. SEM imaging of cut surfaces did not show any real orientation, and reflected light microscopy could not differentiate between fiber and matrix in any way that could lead to quantitative analysis of the fibers' orientation. One method suggested was to freeze the virgin material in liquid nitrogen, then fracture it in the frozen state and study the fracture surfaces; due to time constraints, this method could not be attempted during this work. Finally, some study into the effect of particle reinforcement shape and/or size could help determine any effect these factors may have on material performance.

# References


1. Umholtz, P.D. "The History of Solid Rocket Propulsion and Aerojet," AIAA Technical Paper 99-2927, 1999.
2. Koo, J.H.; Stretz, H.; Bray, A.; Weispfenning, J.; Luo, Z.P.; Blanski, R.; Ruth, P. "Nanostructured Materials for Rocket Propulsion System: Recent Progress," AIAA Technical Paper 2003-1769, 2003.
3. Shorr, M. "Motor Design" in Solid Rocket Technology, Shorr, M.; Zaehringer, A.J.; Eds. John Wiley & Sons: New York, 1967.
4. Hender, D.R.; Roots, A.L.; Litzinger, G.E. "Thermal Response Characterization of a Microballoon Loaded Silicone Rubber," AIAA Technical Paper 83-1472, 1983.
5. Spear, G.B. "The Role of Chemical Reactions and Mechanical Erosion in Aerothermal Modeling of External Insulations," AIAA Technical Paper 90-1868, 1990.
6. Nelson, D.S.; Prince, A.S. "An Experimental Method for Evaluating the Char Tenacity of Fiber-Reinforced Insulation Materials," AIAA Technical Paper 94-3184, 1994.
7. Crump, J.K.; Amy, A.T. "Flight Amplified Erosion of Head End Internal Insulation," AIAA Technical Paper 91-1851, 1991.
8. Bradley, W. "Internal Insulation for Multiple Restart Motors," AIAA Technical Paper 68-500, 1968.
9. Annicelli, R.A. "Next generation EPDMS for auto, wire and cable," *Rubber World*, February 2004, p. 15-17.
10. Caveny, L.H.; Geisler, R.L.; Ellis, R.A.; Moore, T.L. "Solid Rocket Enabling Technologies and Milestones in the United States," *Journal of Propulsion and Power*, V.19, No.6, 2003, p.1038-1066.
11. Grythe, K.F.; Hansen, F.K.; Olsen, T. "Adhesion in Solid Propellant Rocket Motors," *The Journal of Adhesion*, V.83, 2007, p.223-254.
12. Canaud, C.; Visconte, L.L.Y.; Sens, M.A.; Nunes, R.C.R. "Dielectric Properties of Flame Resistant EPDM Composites," *Polymer Degradation and Stability*, V.70, 2000, p.259-262.
13. Schneider, P.J.; Dolton, T.A.; Reed, G.W. "Mechanical Erosion of Charring Ablators in Ground-Test and Re-Entry Environments," AIAA Technical Paper 66-424, 1966.
14. Potts, R.L. "Application of Integral Methods to Ablation Charring Erosion, A Review," *Journal of Spacecraft and Rockets*, V.32, No.2, 1995, p.200-209.
15. Milos, F.S.; Marschall, J. "Thermochemical Ablation Model for TPS Materials with Multiple Surface Constituents," AIAA Technical Paper 94-2042, 1994.
16. Smith, S.L.; Spear, G.B.; Cornwell, M.D. "Statistical Monte Carlo Prediction for Thermal Reliability," AIAA Technical Paper 94-3183, 1994.
17. HotDisk. "Introduction to TPS Technology.", September 11, 2007, <http://www.hotdisk.se>.
18. McPherson, D. Aerojet, Culpeper, VA. Personal communication, 2007.
19. Yezzi, C.A.; Moore, B.B. "Characterization of Kevlar/EPDM Rubbers for use as Rocket Motor Case Insulators," AIAA Technical Paper 86-1489, 1986.

20. Morgan, R.J.; Allred, R.E. “Aramid Fiber Reinforcements,” in Composites Technology, Stuart M. Lee, Ed. CRC Press, 1989, p. 143-166.
21. Cheng, M.; Chen, W.; Weerasooriya, T. “Mechanical Properties of Kevlar ® KM2 Single Fiber,” *Journal of Engineering Materials and Technology*, V.127, 2005, p. 197-203.
22. Wang, L.; Tiju, W.C.; Teh, S.F.; He, C.; Liu, T. “Fracture and Toughening Behavior of Aramid Fiber / Epoxy Composites,” *Polymer Composites*, V.26, 2005, p. 333-342.

# Appendix A: Virgin Compositions (ITAR Restricted)

*Due to the ITAR restriction, this section is not available to the general public. For access to this information, please contact Dr. Scott Case, Virginia Tech*.

# Appendix B: Charred Compositions (ITAR Restricted)

*Due to the ITAR restriction, this section is not available to the general public. For access to this information, please contact Dr. Scott Case, Virginia Tech*.

# Appendix C: Additional Micrographs

Charred ARI-2718 Micrographs

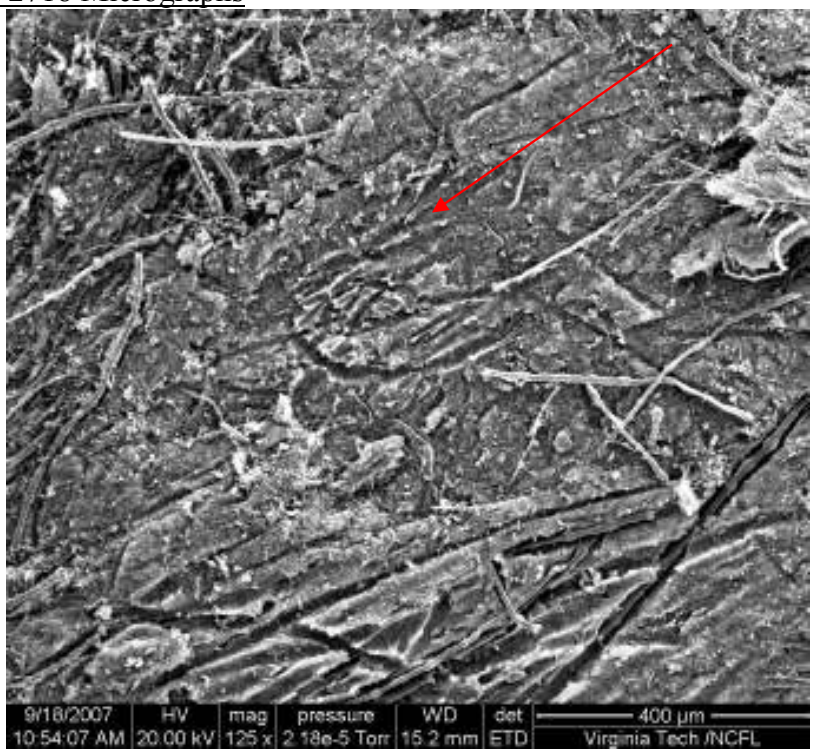


Figure C-1: ARI-2718 Specimen L4 Location A (125x)


Figure C-2: ARI-2718 Specimen L4 Location A (250x)

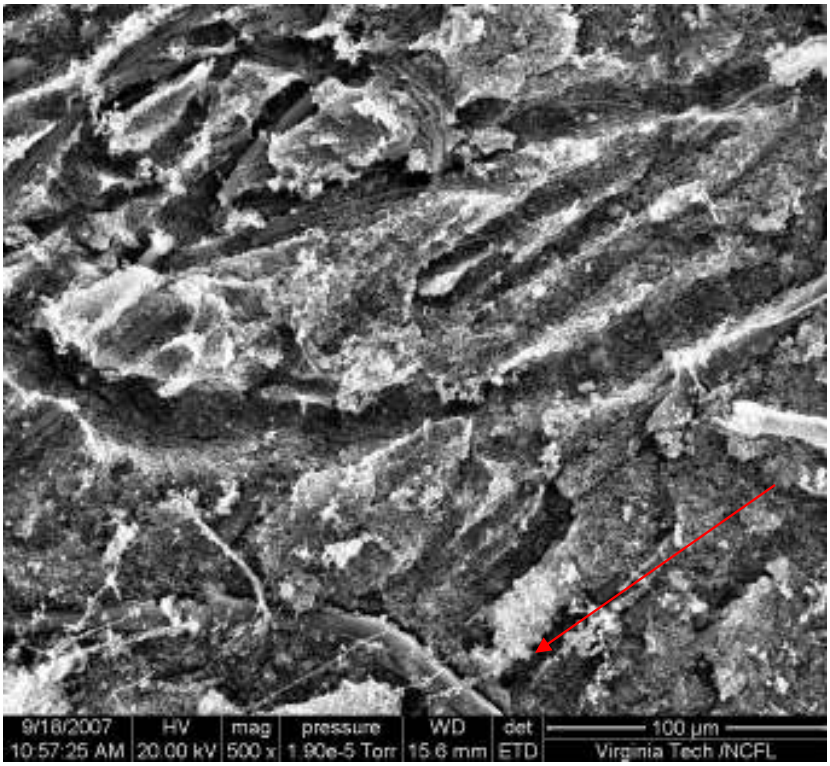

Figure C-3: ARI-2718 Specimen L4 Location A (500x)

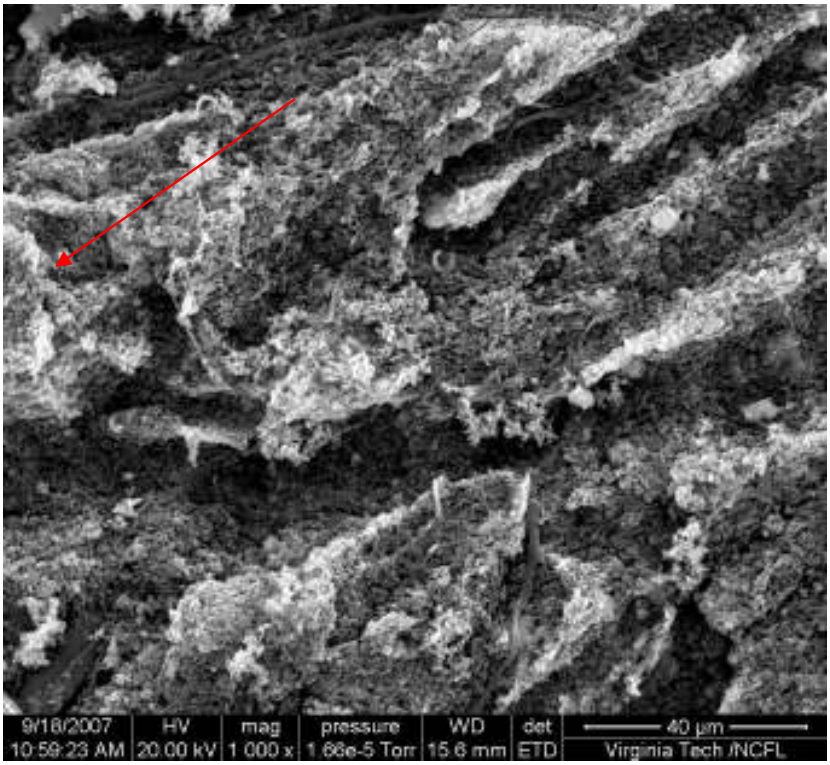

Figure C-4: ARI-2718 Specimen L4 Location A (1000x)

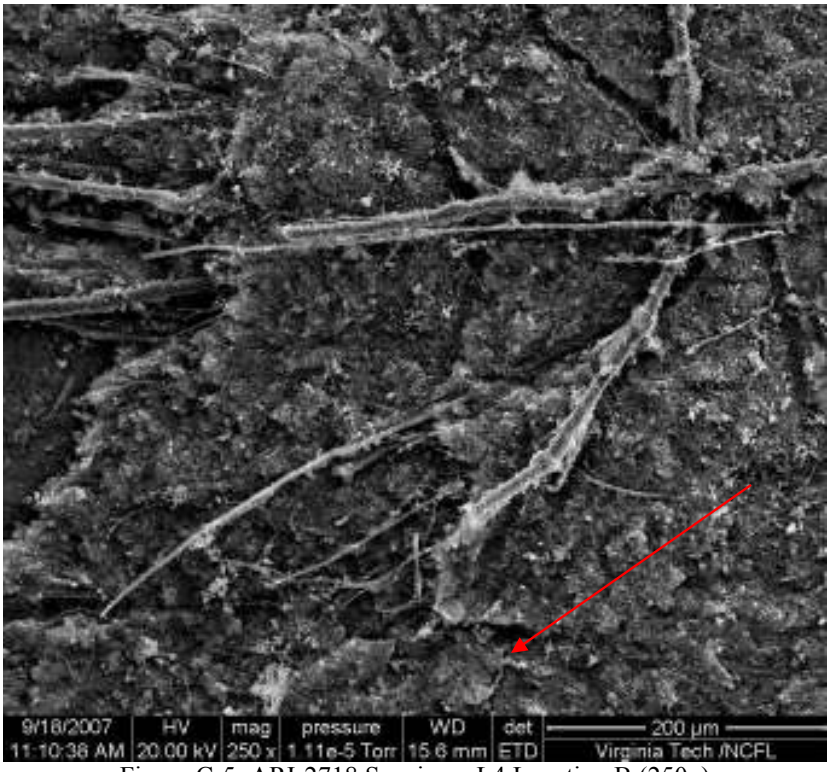

Figure C-5: ARI-2718 Specimen L4 Location B (250x)

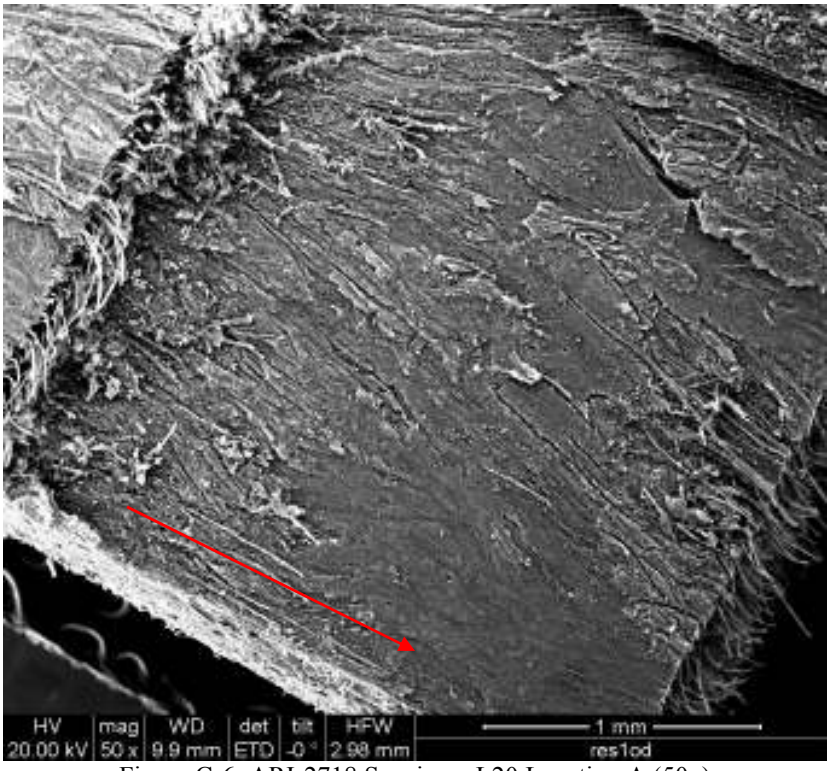

Figure C-6: ARI-2718 Specimen L20 Location A (50x)

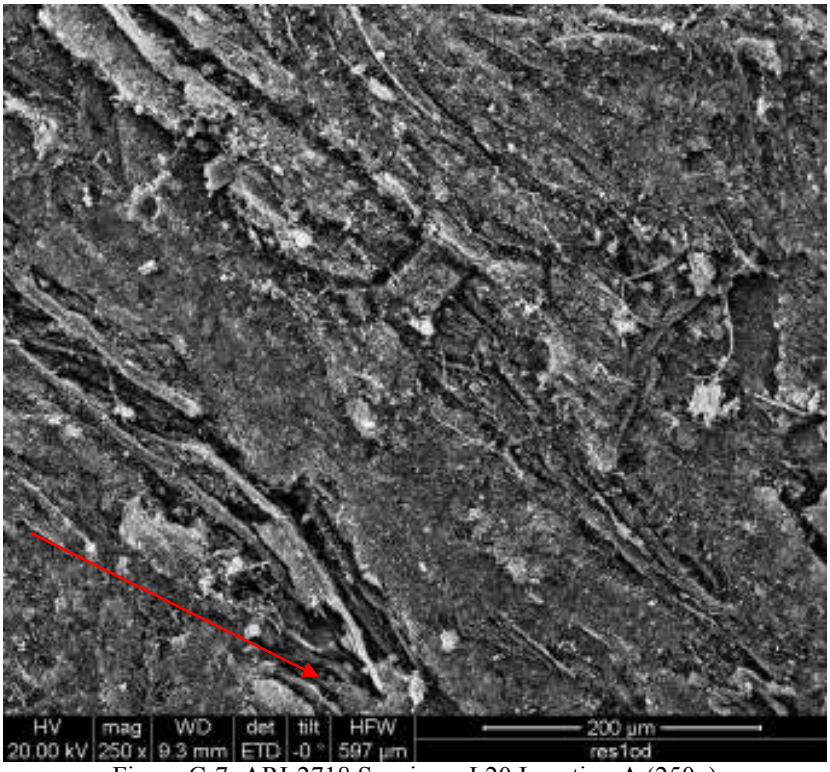

Figure C-7: ARI-2718 Specimen L20 Location A (250x)

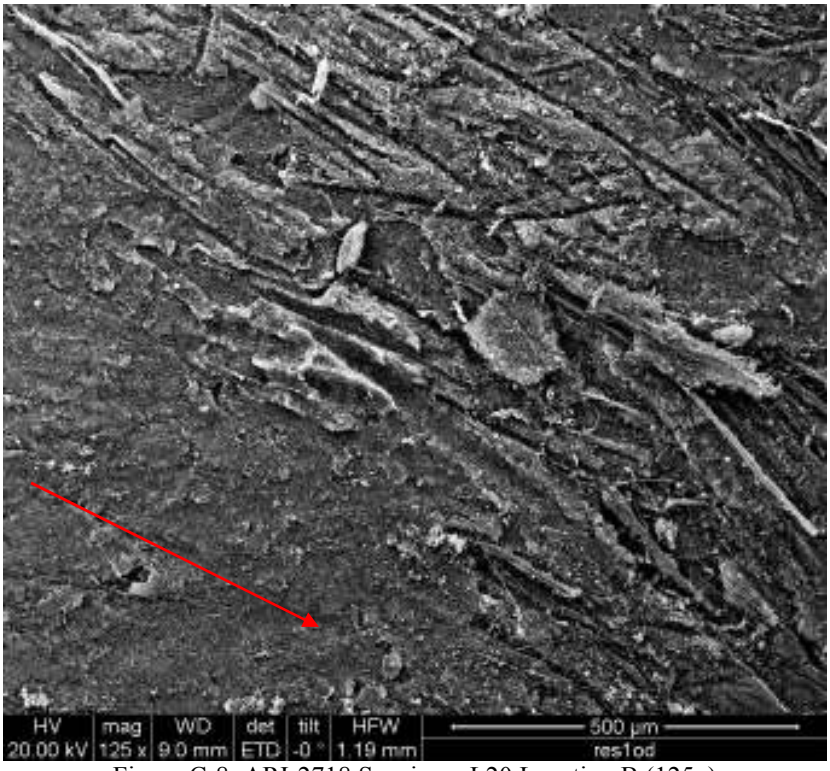

Figure C-8: ARI-2718 Specimen L20 Location B (125x)

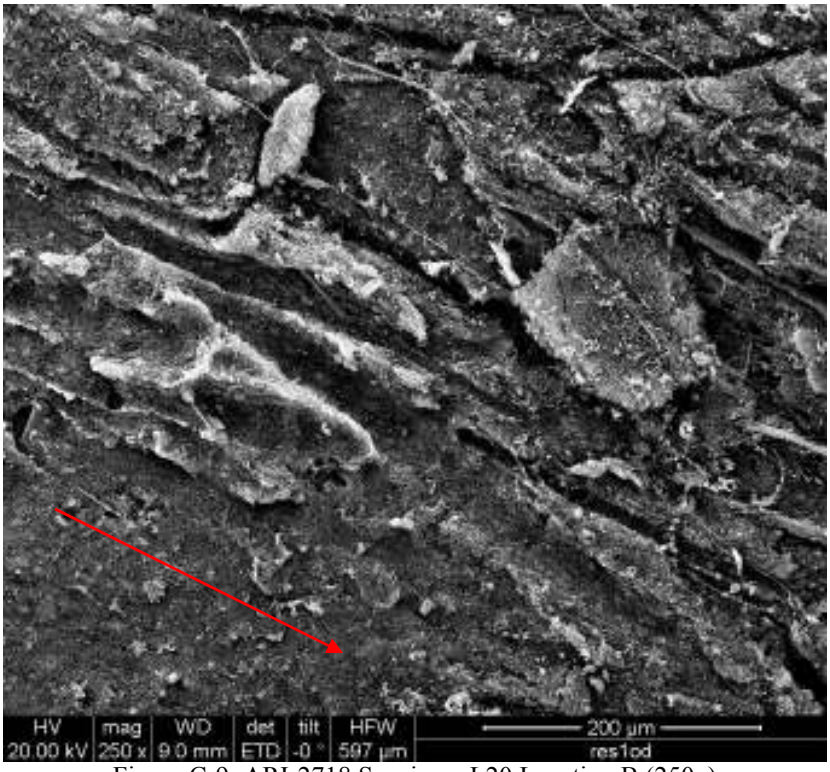

Figure C-9: ARI-2718 Specimen L20 Location B (250x)

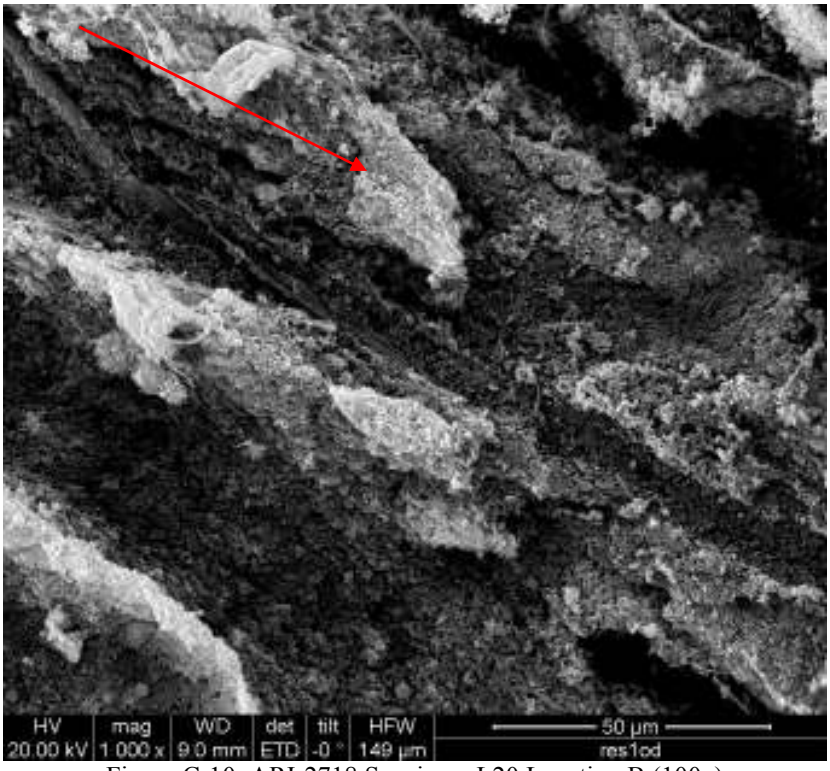

Figure C-10: ARI-2718 Specimen L20 Location B (100x)

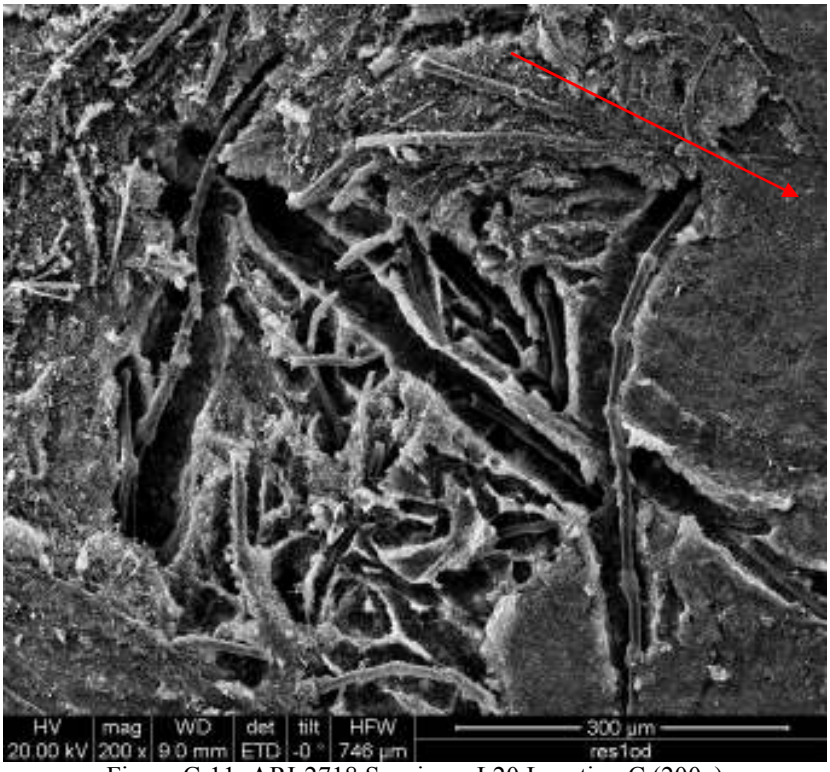

Figure C-11: ARI-2718 Specimen L20 Location C (200x)

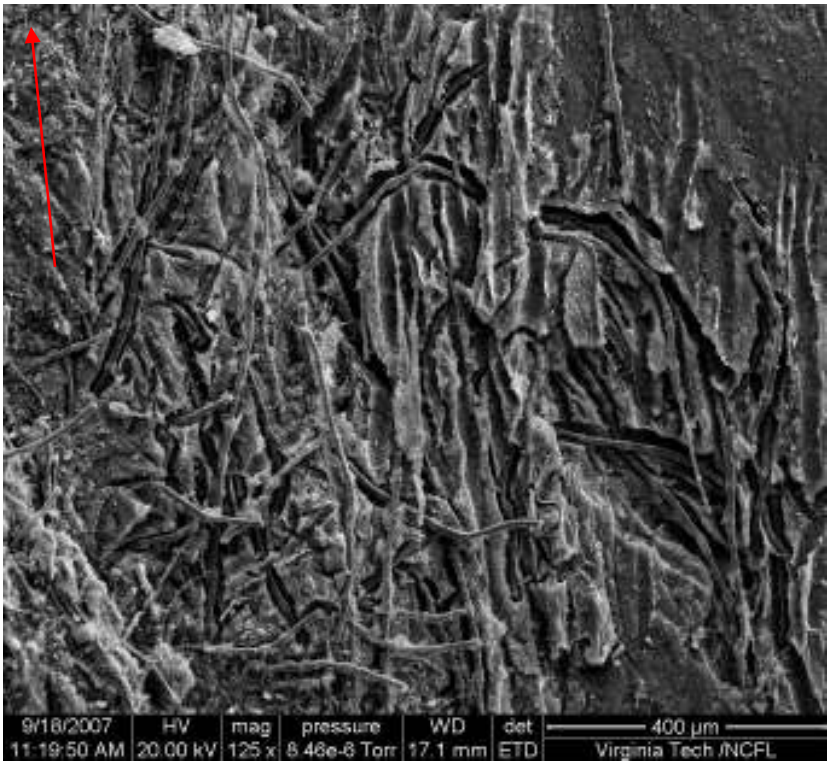

Figure C-12: ARI-2718 Specimen T11 Location A (125x)

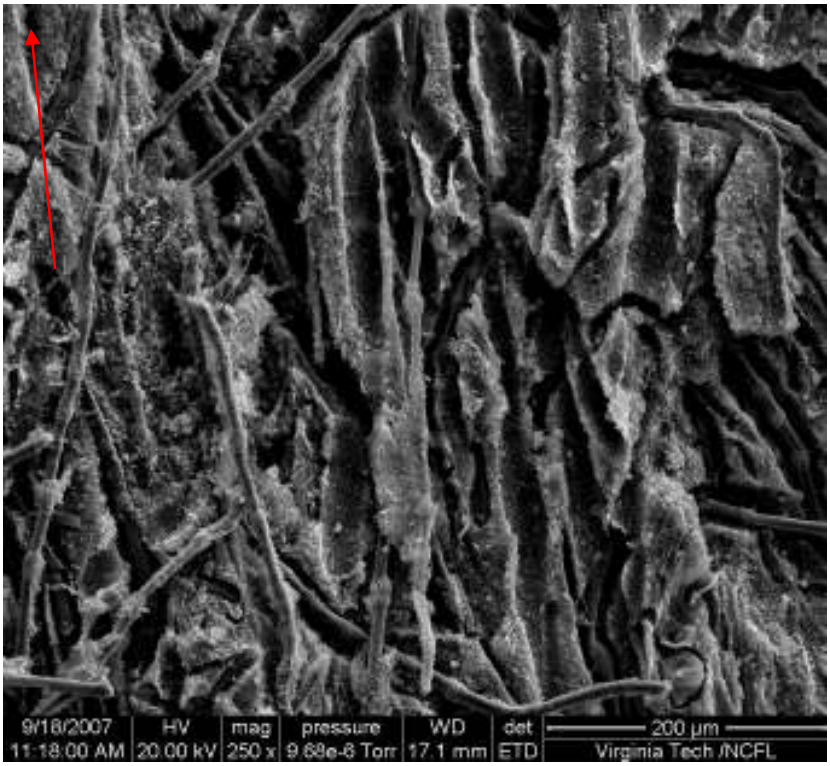

Figure C-13: ARI-2718 Specimen T11 Location A (250x)

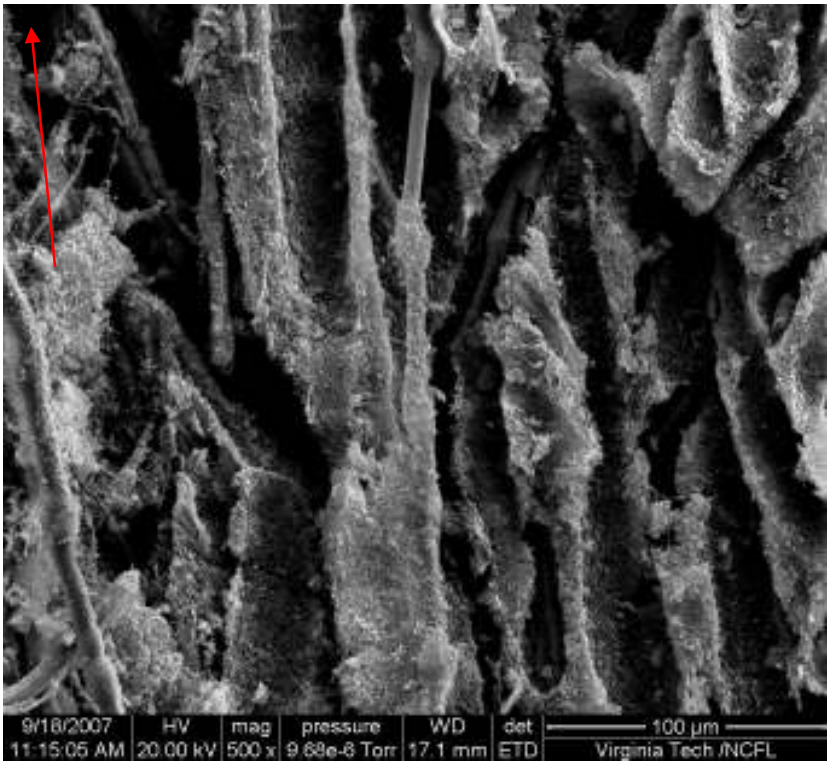

Figure C-14: ARI-2718 Specimen T11 Location A (500x)

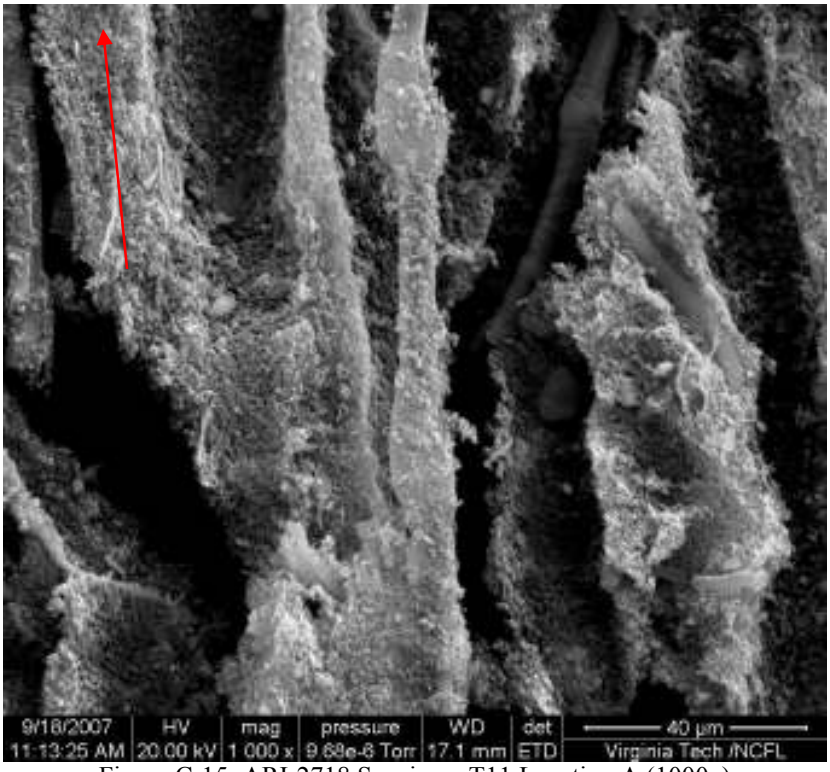

Figure C-15: ARI-2718 Specimen T11 Location A (1000x)

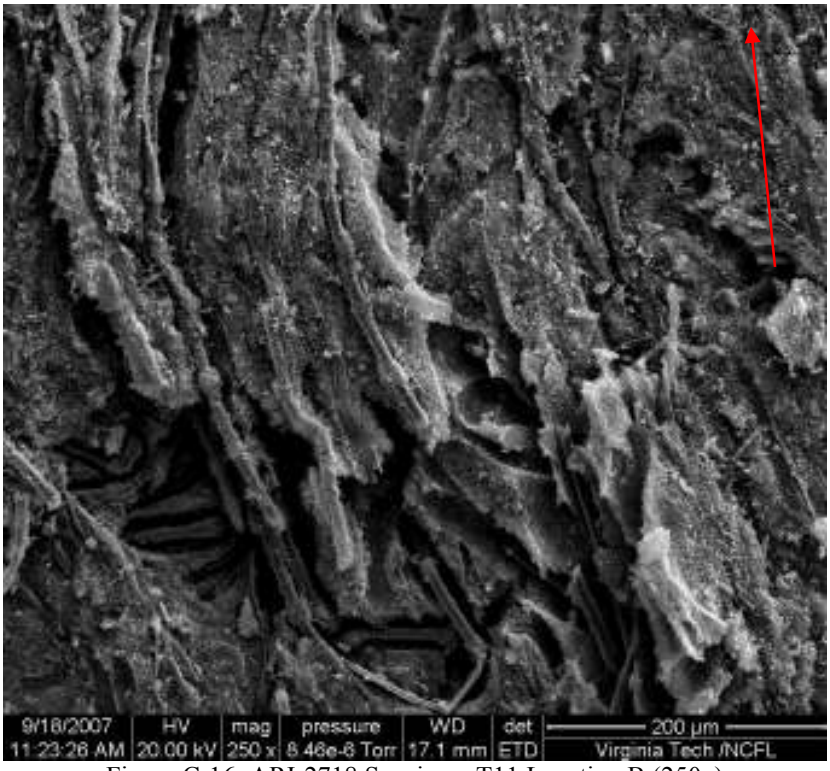

Figure C-16: ARI-2718 Specimen T11 Location B (250x)

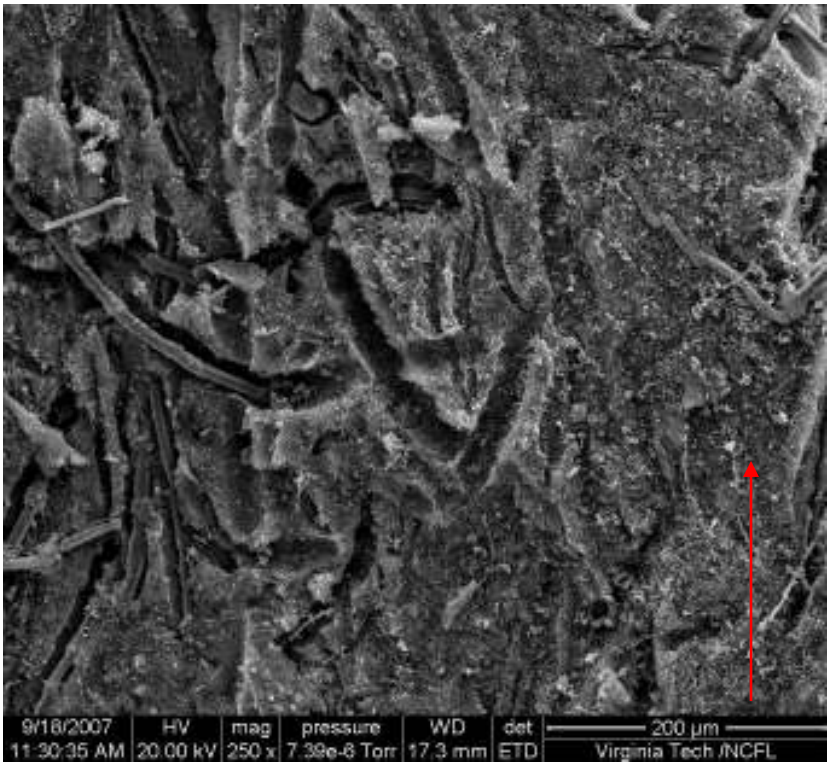

Figure C-17: ARI-2718 Specimen T14 Location A (250x)

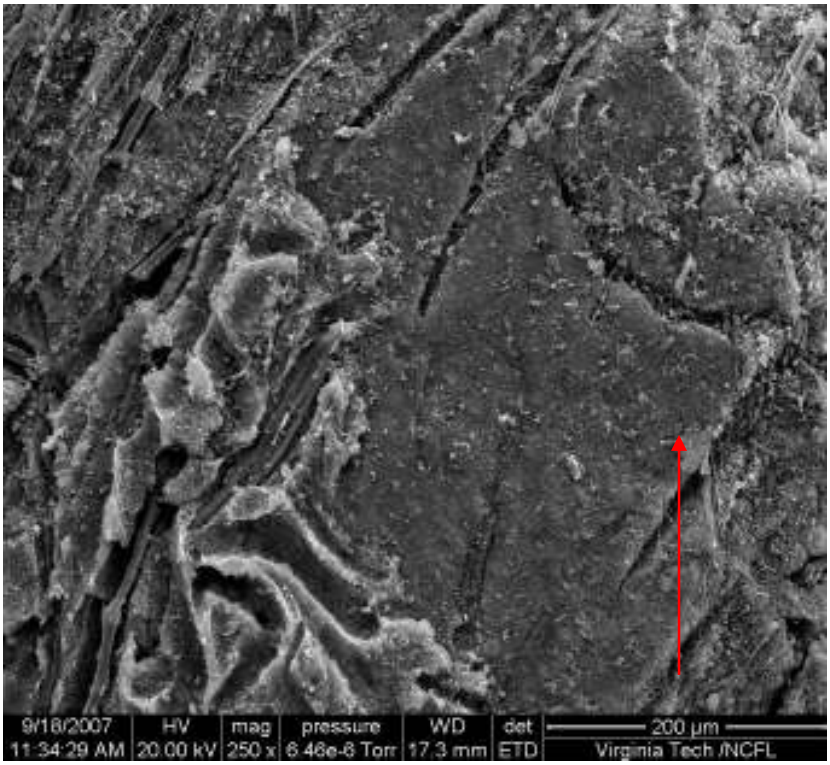

Figure C-18: ARI-2718 Specimen T14 Location B (250x)

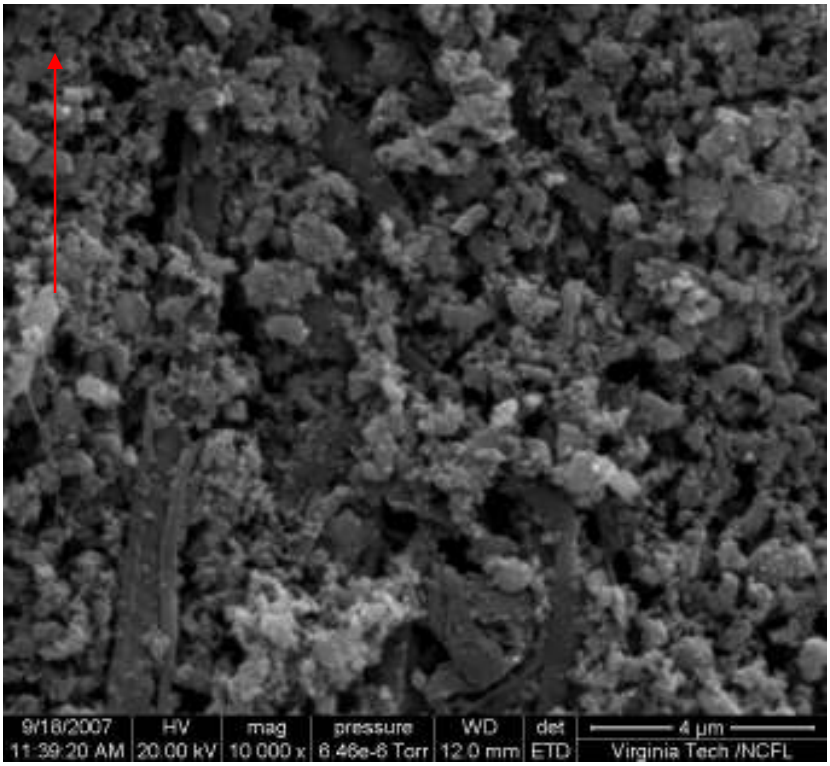

Figure C-19: ARI-2718 Specimen T14 Location B (10kx)

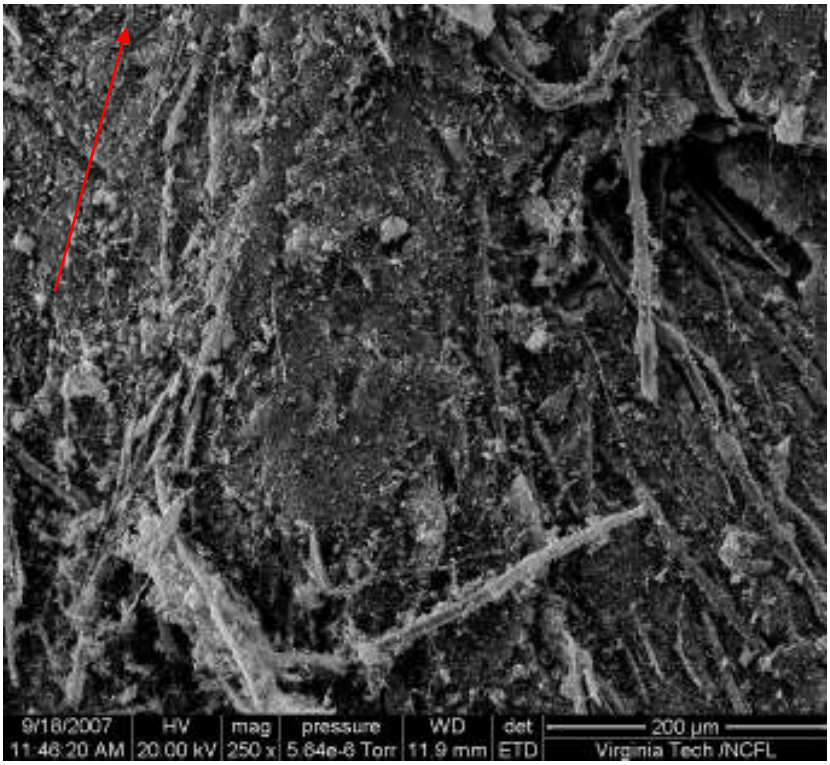

Figure C-20: ARI-2718 Specimen T18 Location A (250x)

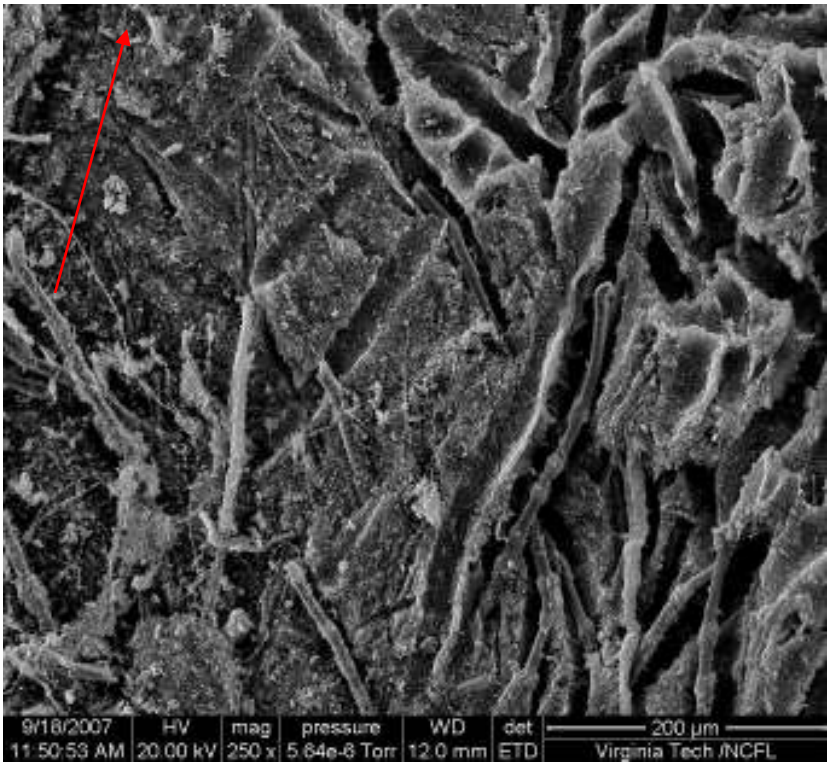

Figure C-21: ARI-2718 Specimen T18 Location B (250x)

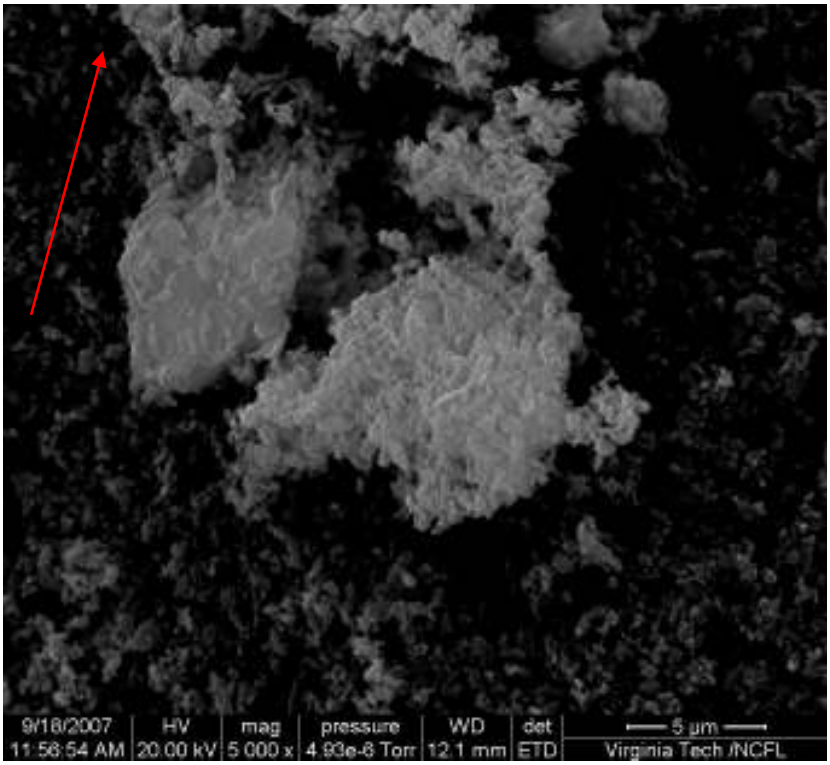

Figure C-22: ARI-2718 Specimen T18 Location C (5000x)

Charred ARI-2719 Micrographs

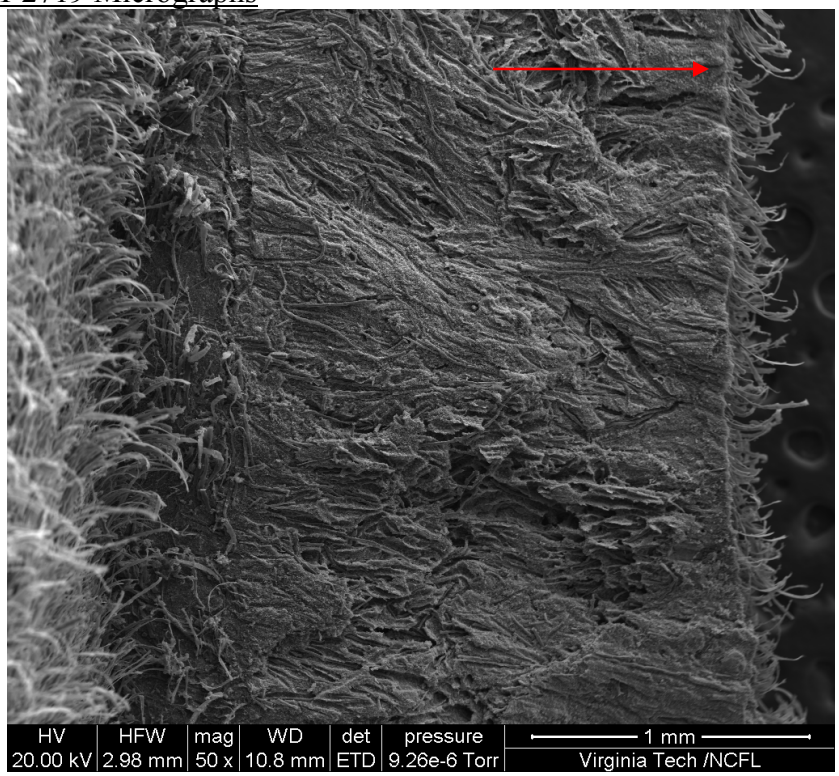


Figure C-23: ARI-2719 Specimen L10 Location A (50x)

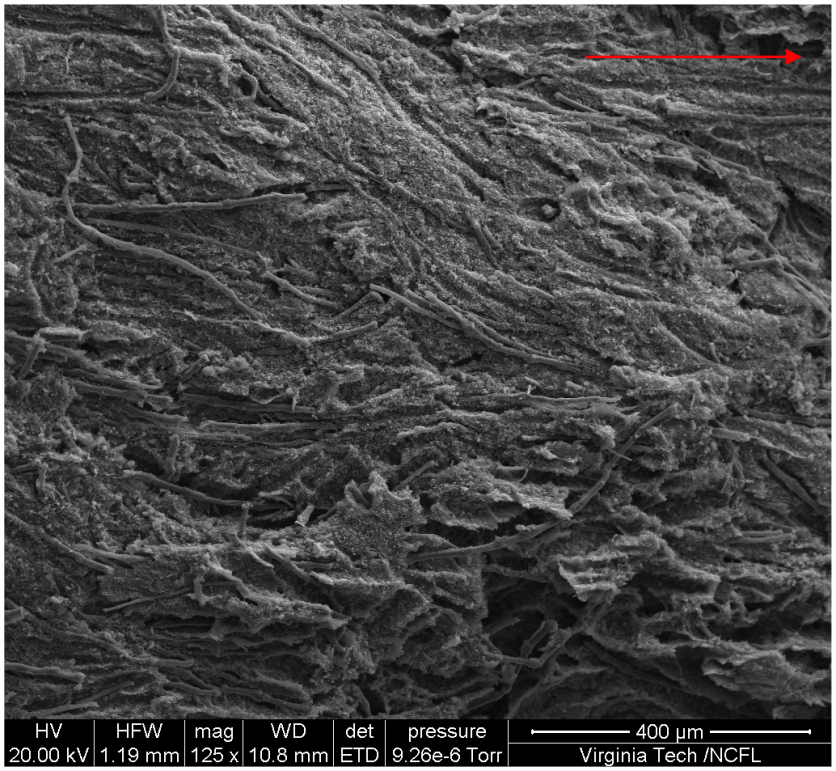


Figure C-24: ARI-2719 Specimen L10 Location A (125x)

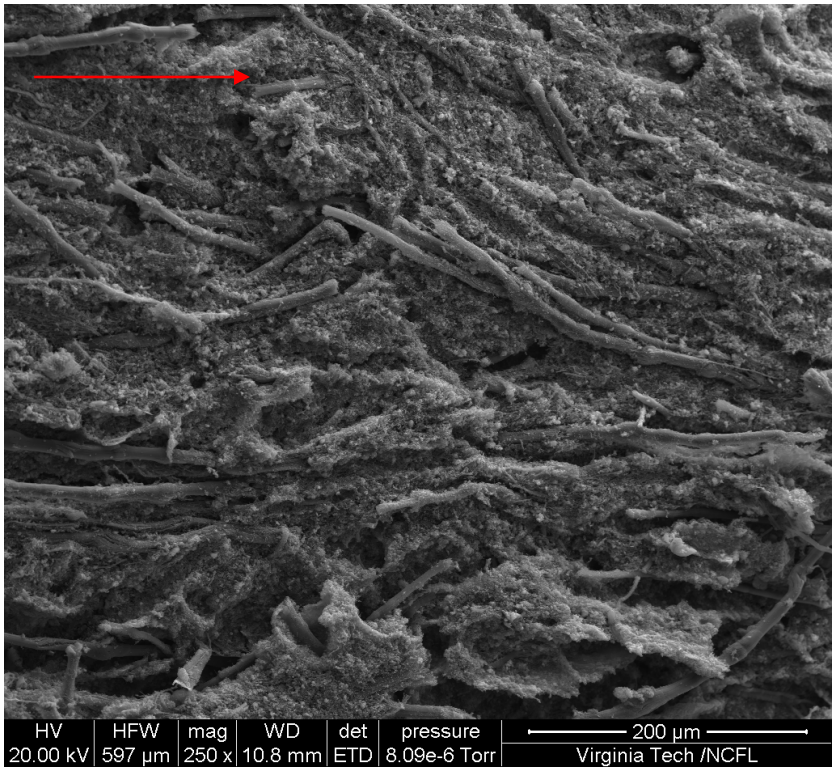

Figure C-25: ARI-2719 Specimen L10 Location A (250x)

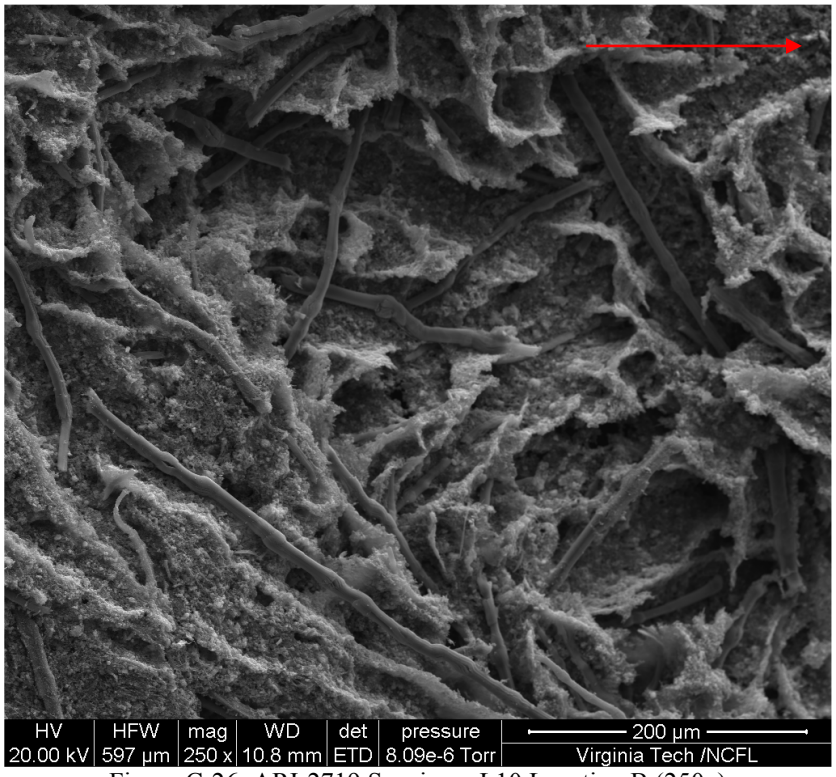

Figure C-26: ARI-2719 Specimen L10 Location B (250x)

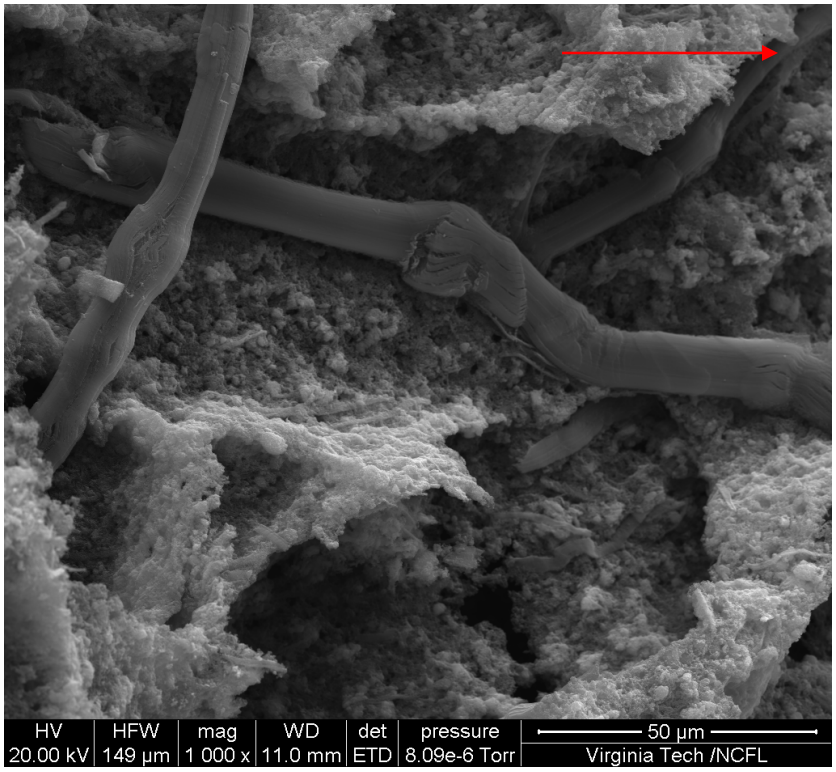

Figure C-27: ARI-2719 Specimen L10 Location B (1000x)

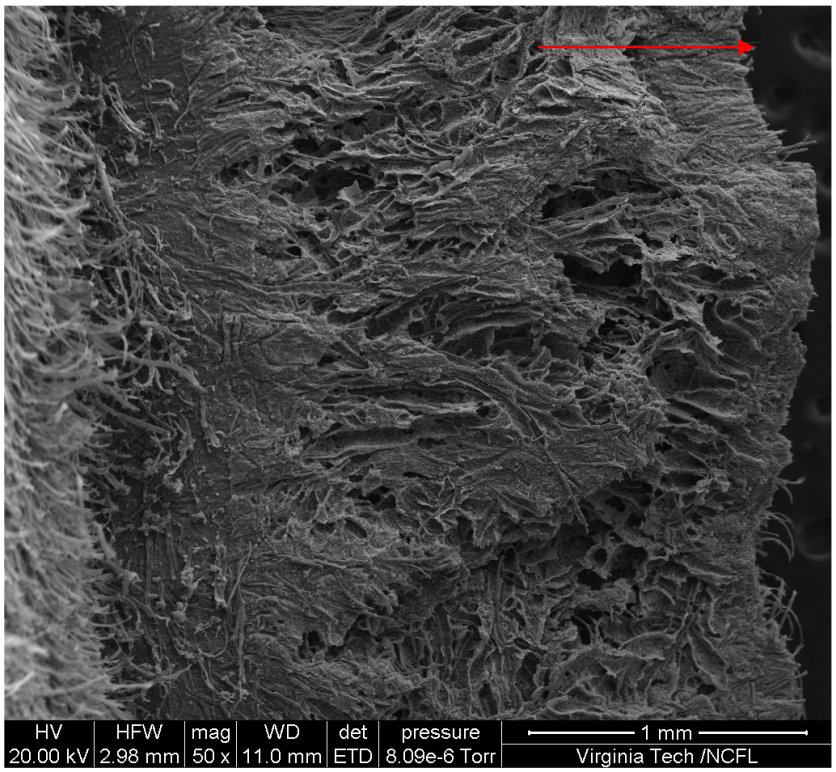

Figure C-28: ARI-2719 Specimen L14 Location A (50x)

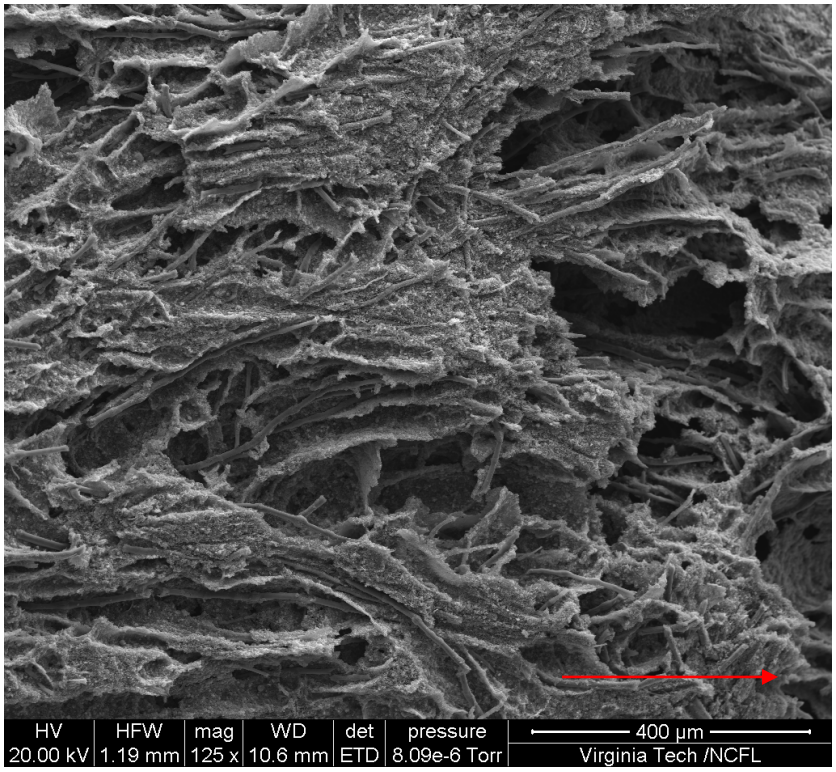

Figure C-29: ARI-2719 Specimen L14 Location A (125x)

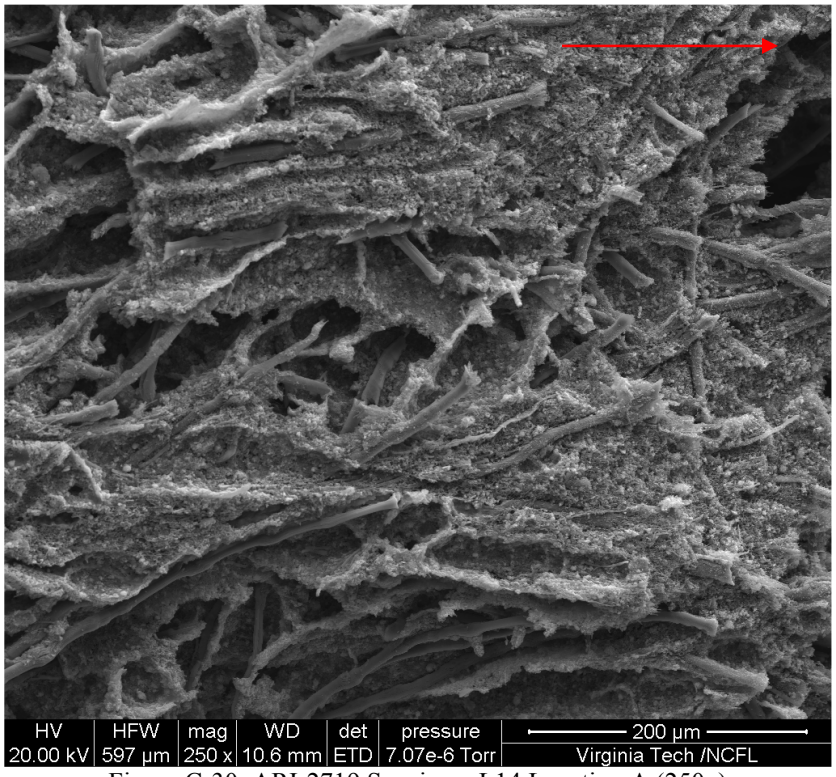

Figure C-30: ARI-2719 Specimen L14 Location A (250x)

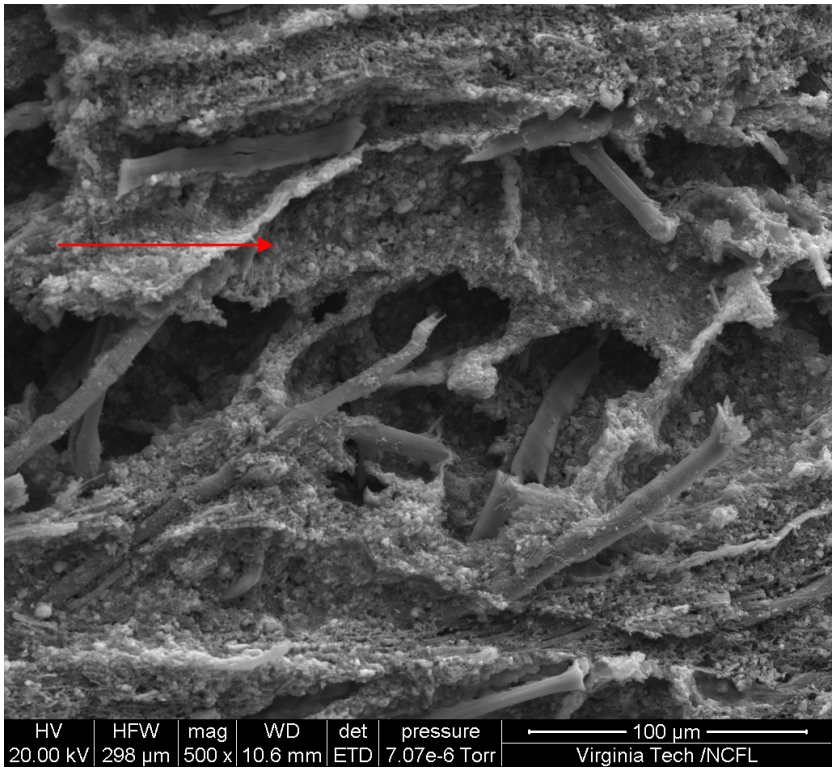

Figure C-31: ARI-2719 Specimen L14 Location A (500x)

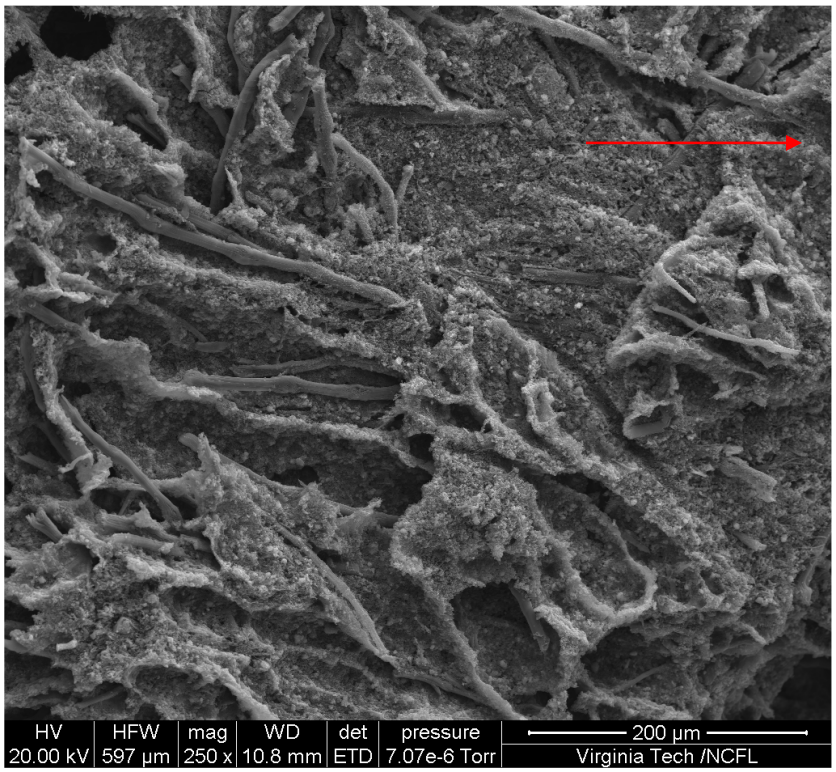

Figure C-32: ARI-2719 Specimen L14 Location B (250x)

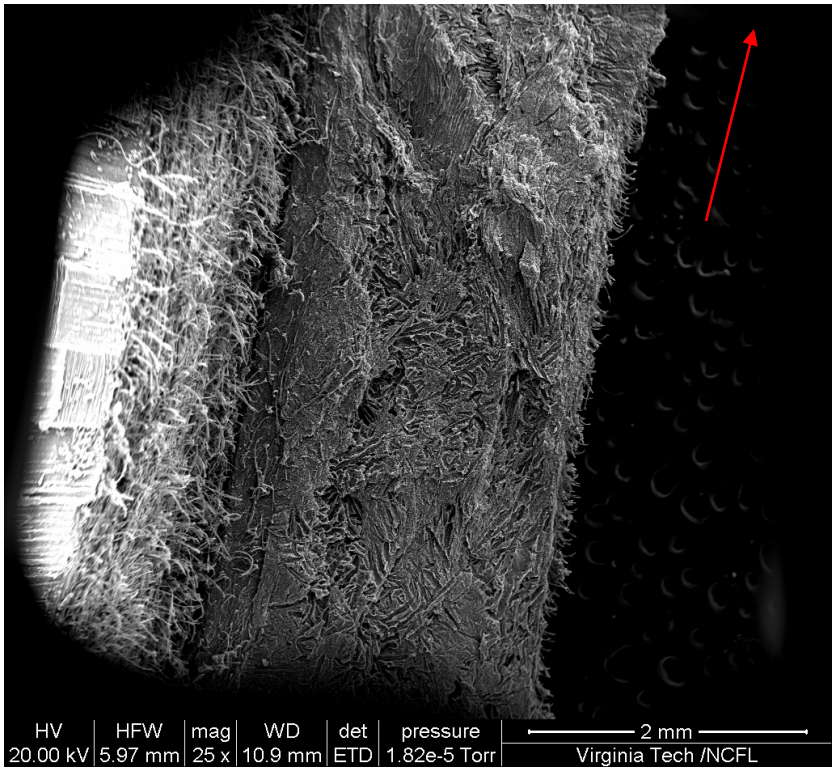

Figure C-33: ARI-2719 Specimen T11 Location A (25x)

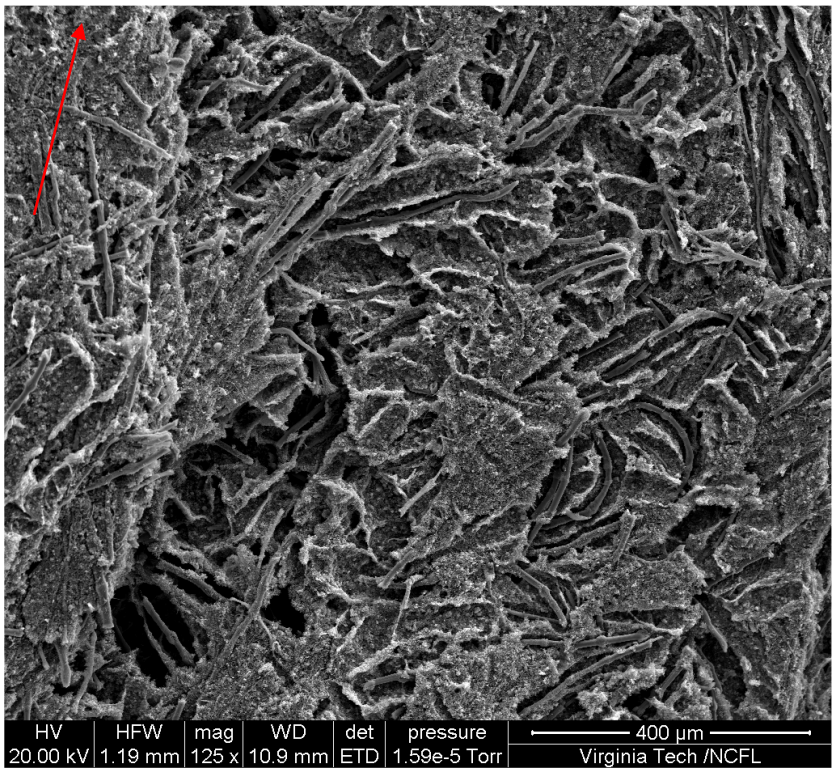

Figure C-34: ARI-2719 Specimen T11 Location A (125x)

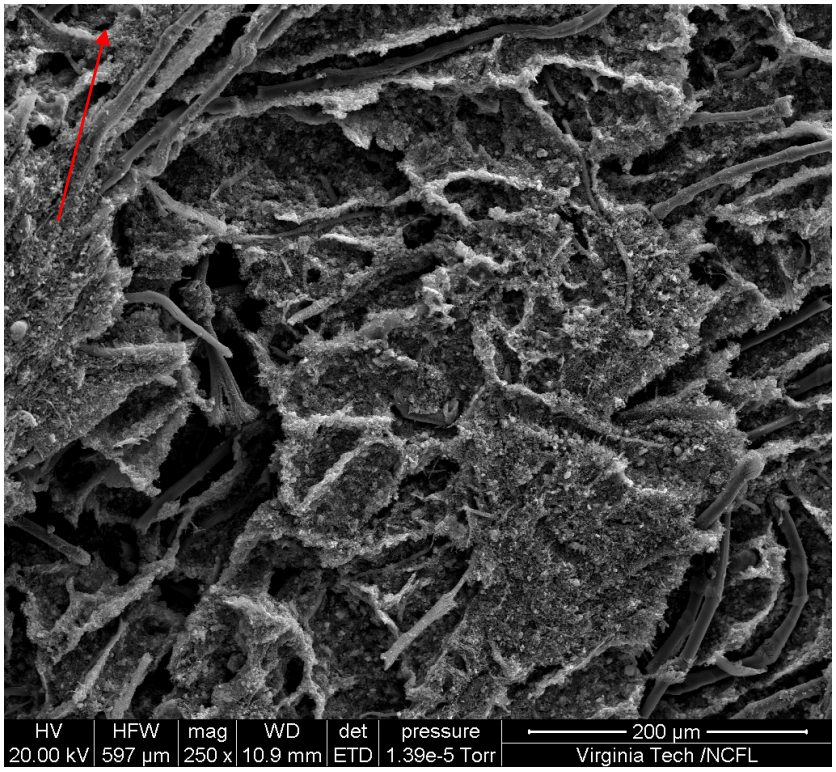

Figure C-35: ARI-2719 Specimen T11 Location A (250x)

Figure C-36: ARI-2719 Specimen T11 Location A (1000x)

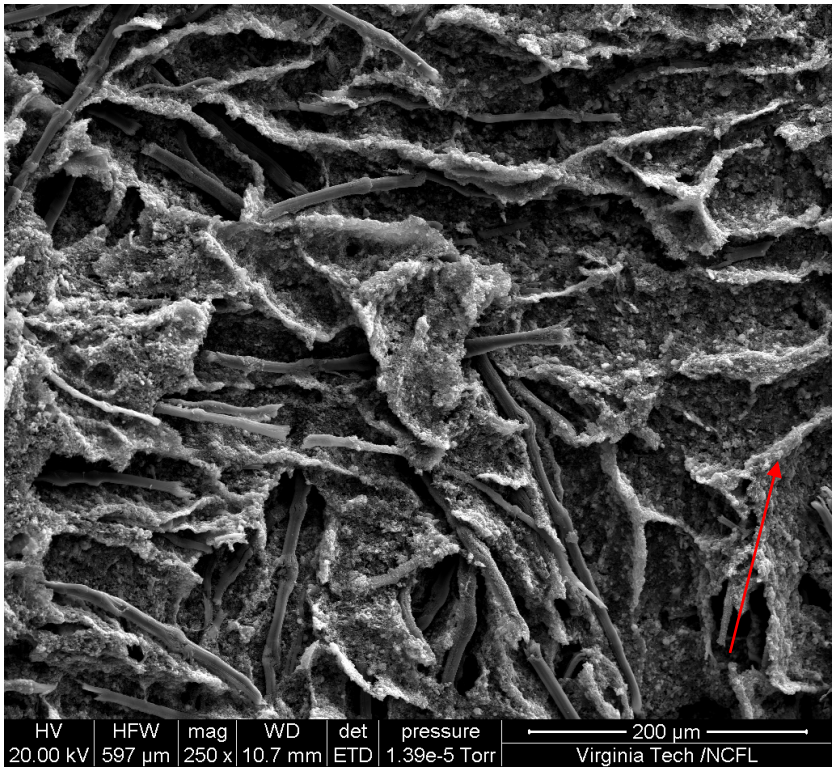

Figure C-37: ARI-2719 Specimen T11 Location B (250x)

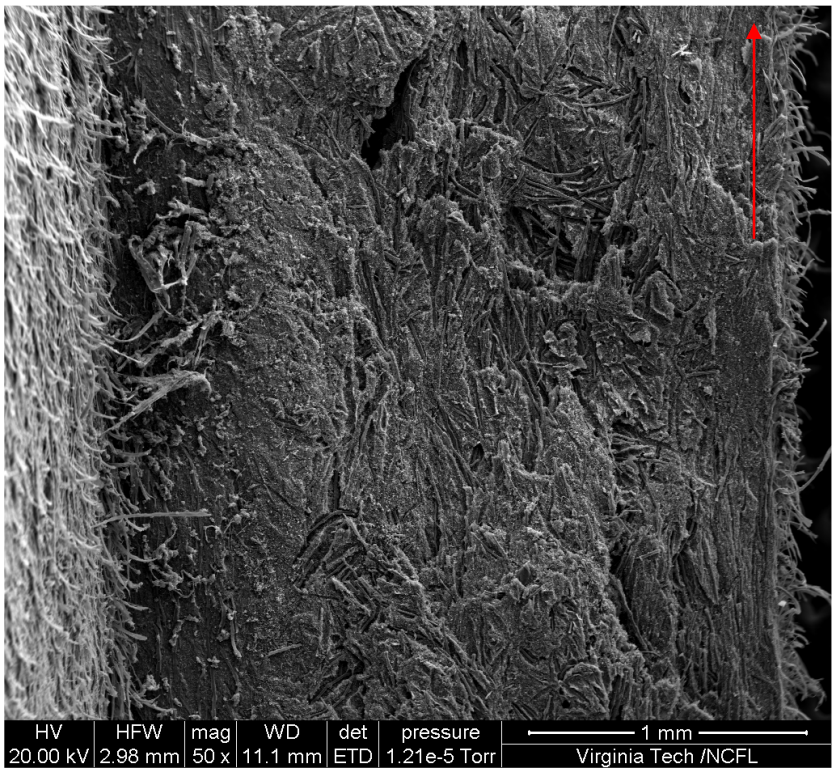

Figure C-38: ARI-2719 Specimen T15 Location A (50x)

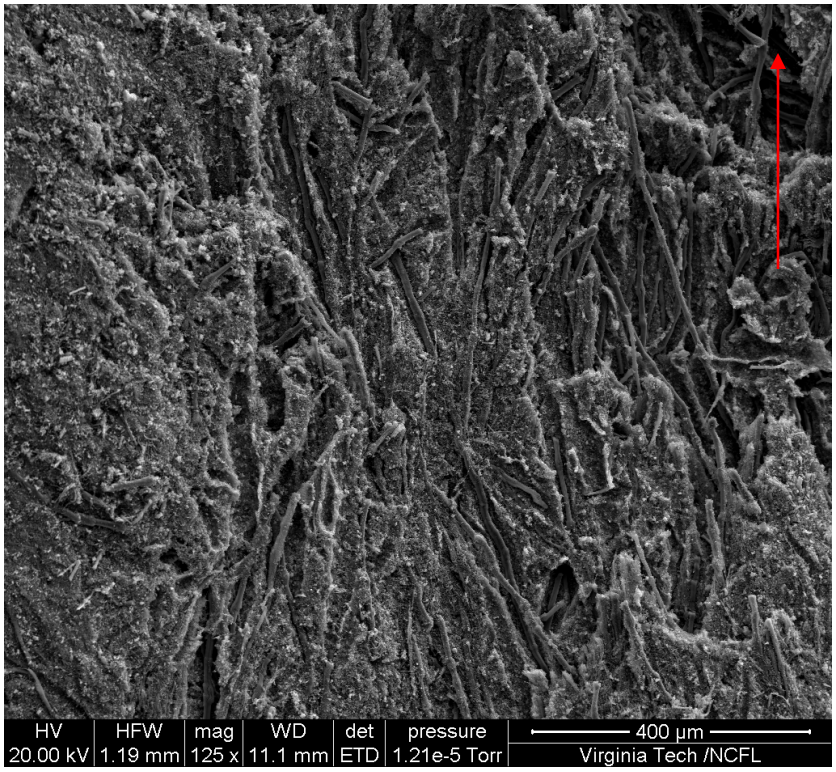

Figure C-39: ARI-2719 Specimen T15 Location A (125x)

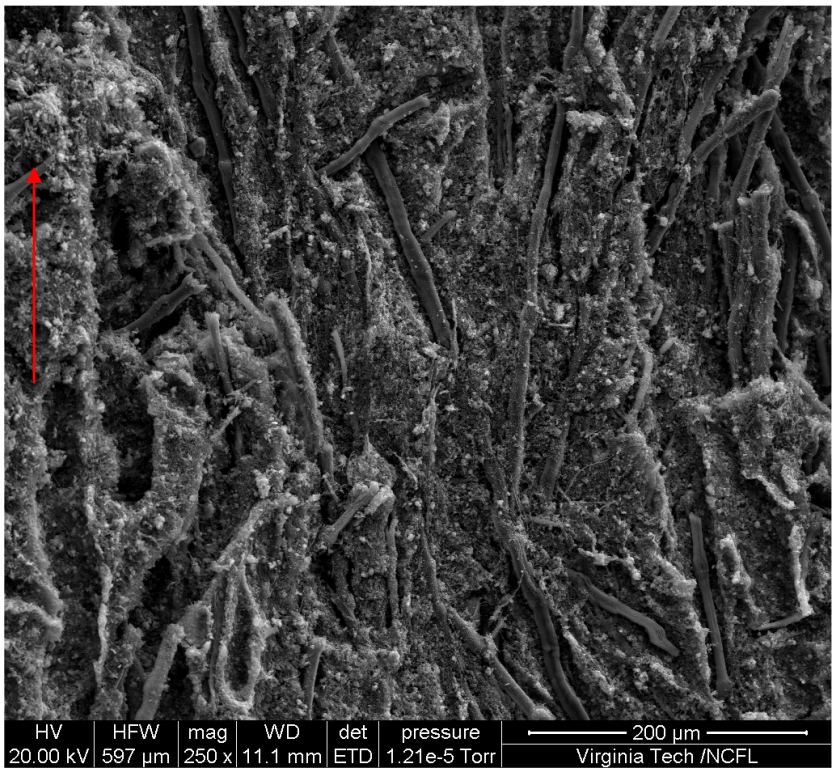

Figure C-40: ARI-2719 Specimen T15 Location A (250x)

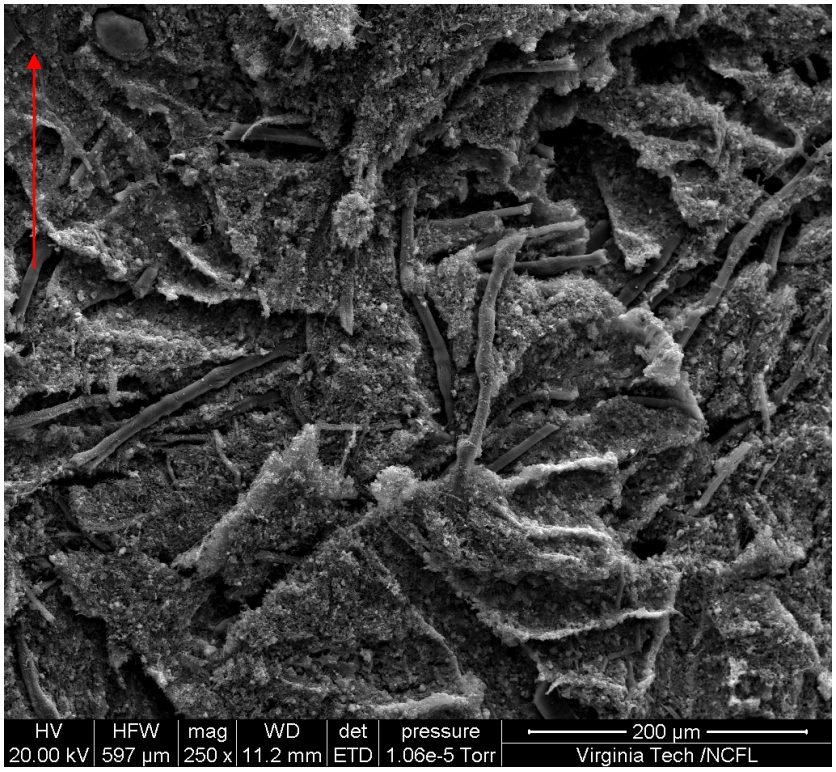

Figure C-41: ARI-2719 Specimen T15 Location B (250x)

Figure C-42: ARI-2719 Specimen T15 Location B (1000x)

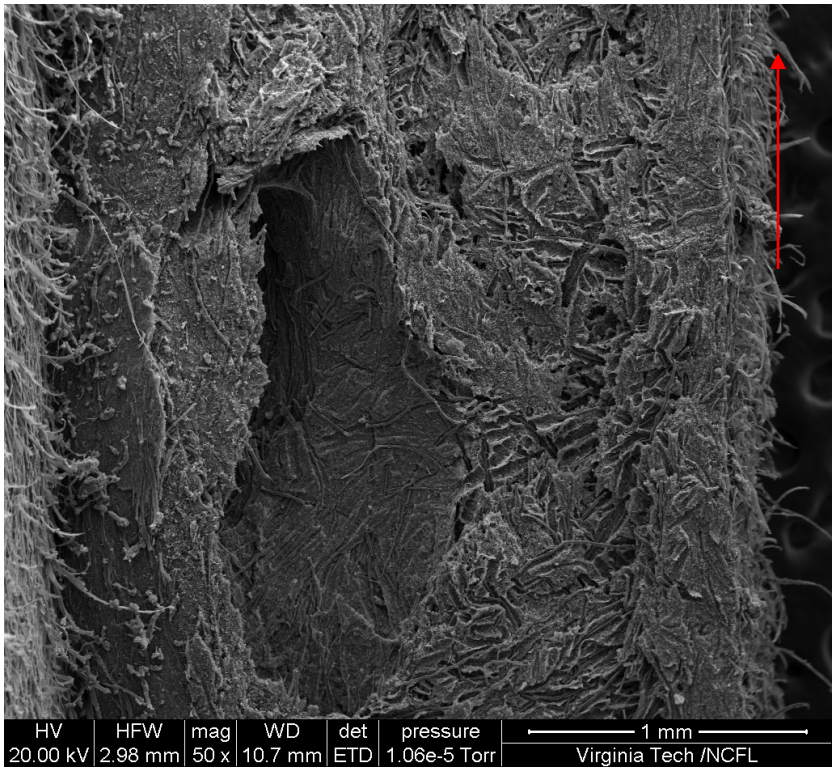

Figure C-43: ARI-2719 Specimen T18 Location A (50x)

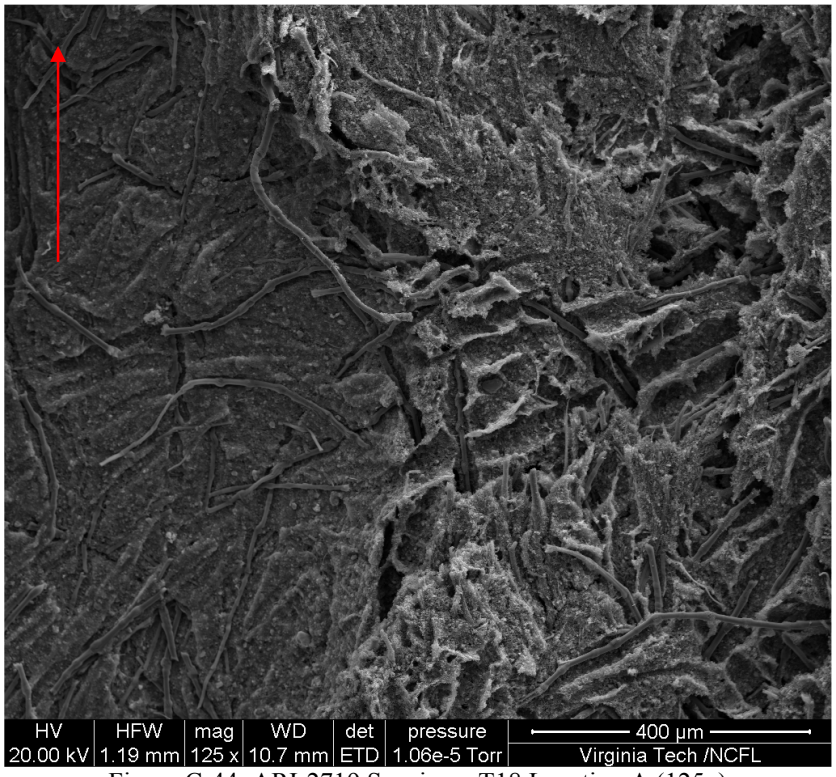

Figure C-44: ARI-2719 Specimen T18 Location A (125x)

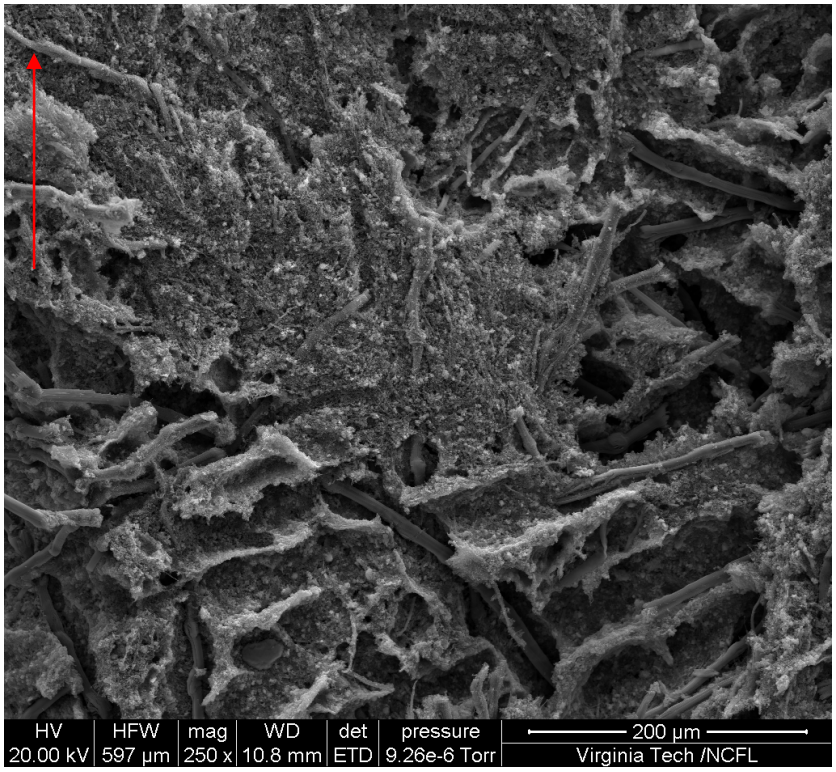

Figure C-45: ARI-2719 Specimen T18 Location A (250x)

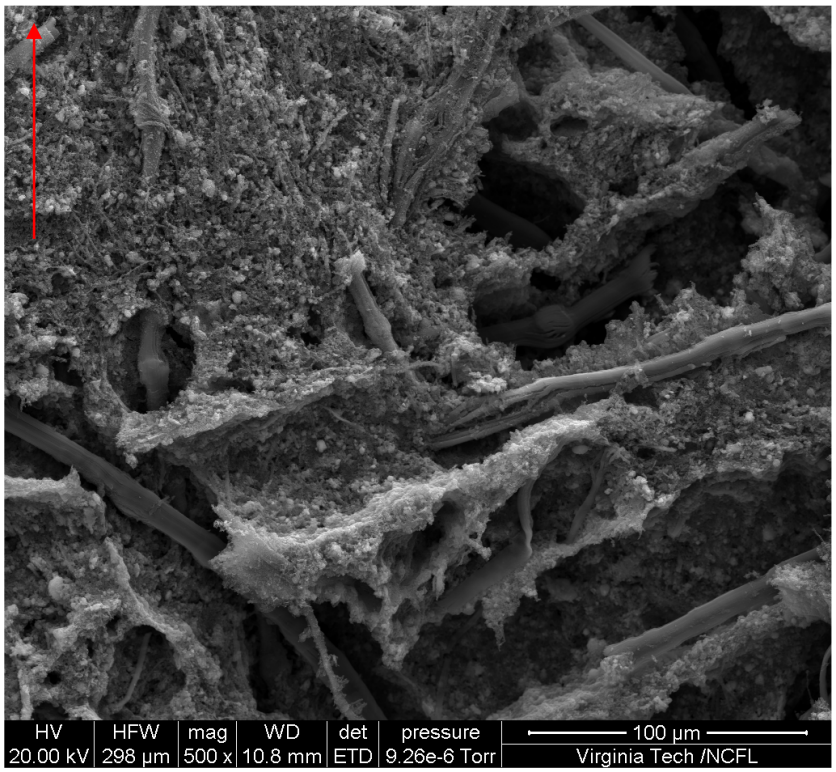

Figure C-46: ARI-2719 Specimen T18 Location A (500x)

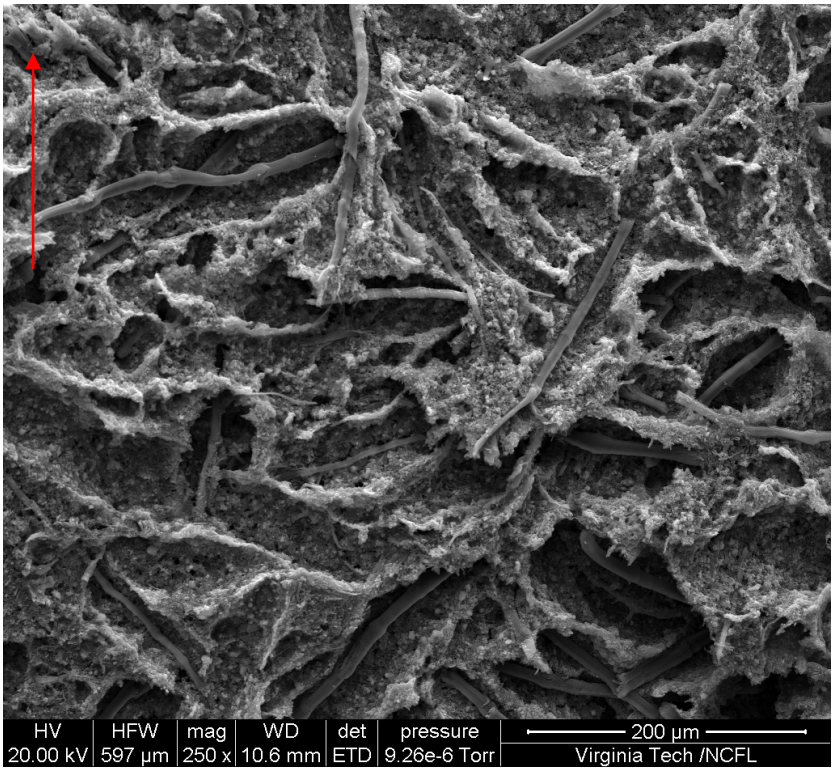

Figure C-47: ARI-2719 Specimen T18 Location B (250x)

Charred ARI-2732 Micrographs

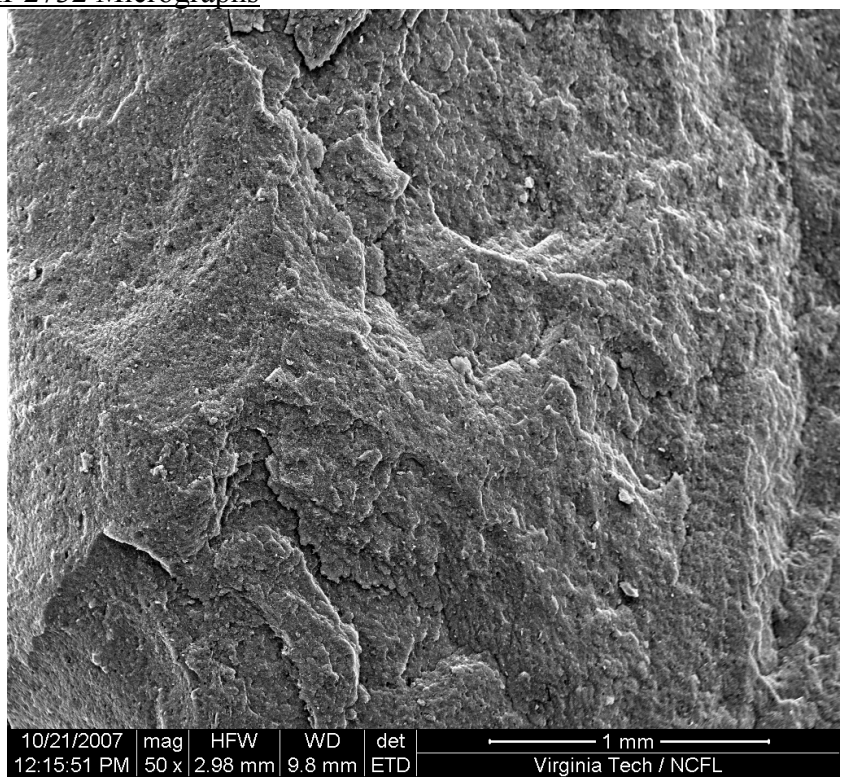


Figure C-48: ARI-2732 Specimen 1 Location A (50x)

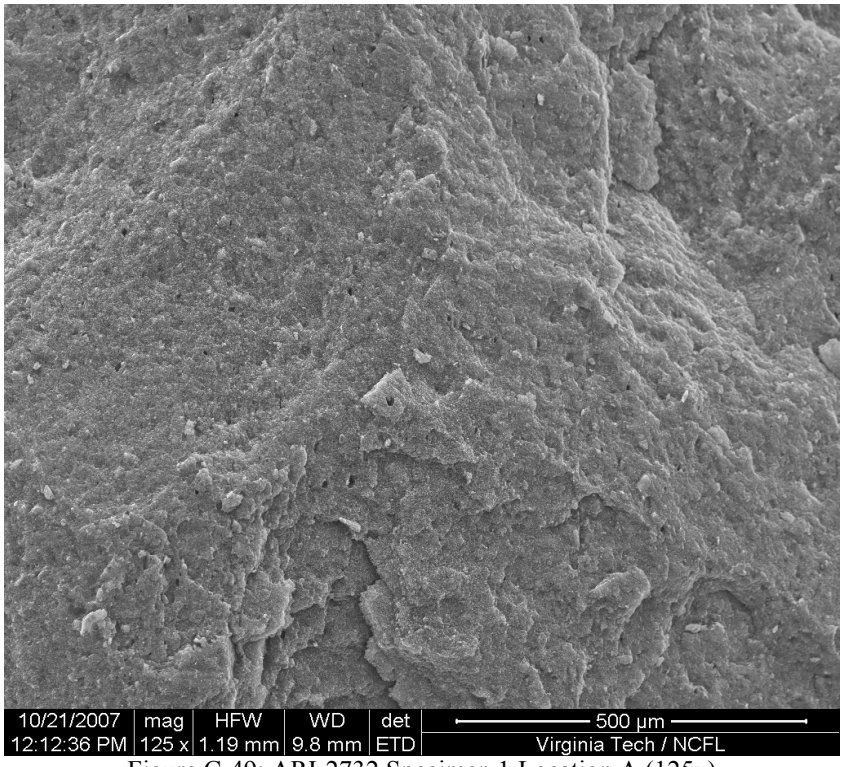


Figure C-49: ARI-2732 Specimen 1 Location A (125x)

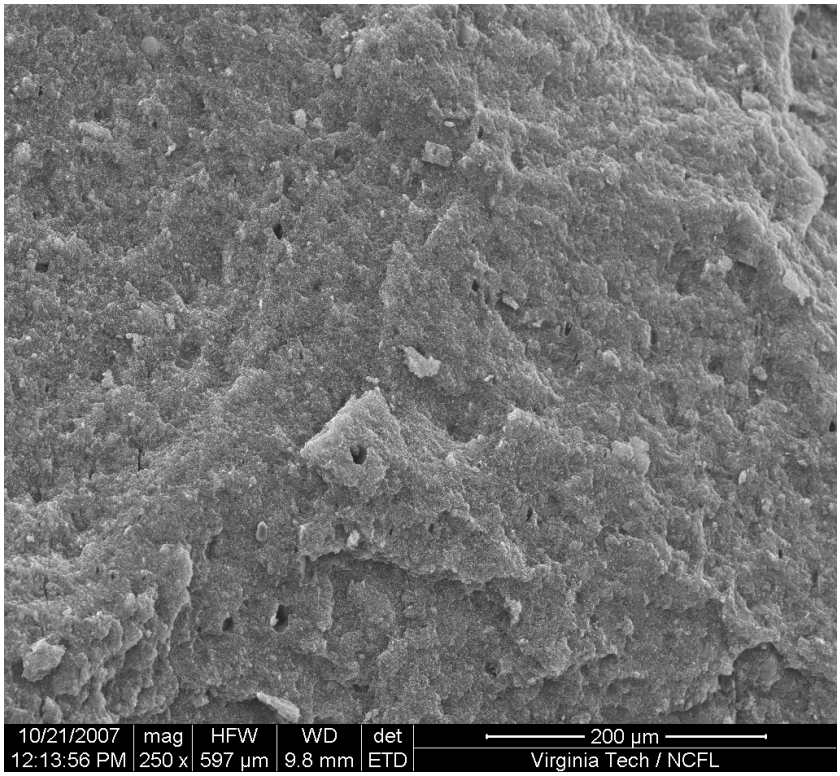

Figure C-50: ARI-2732 Specimen 1 Location A (250x)

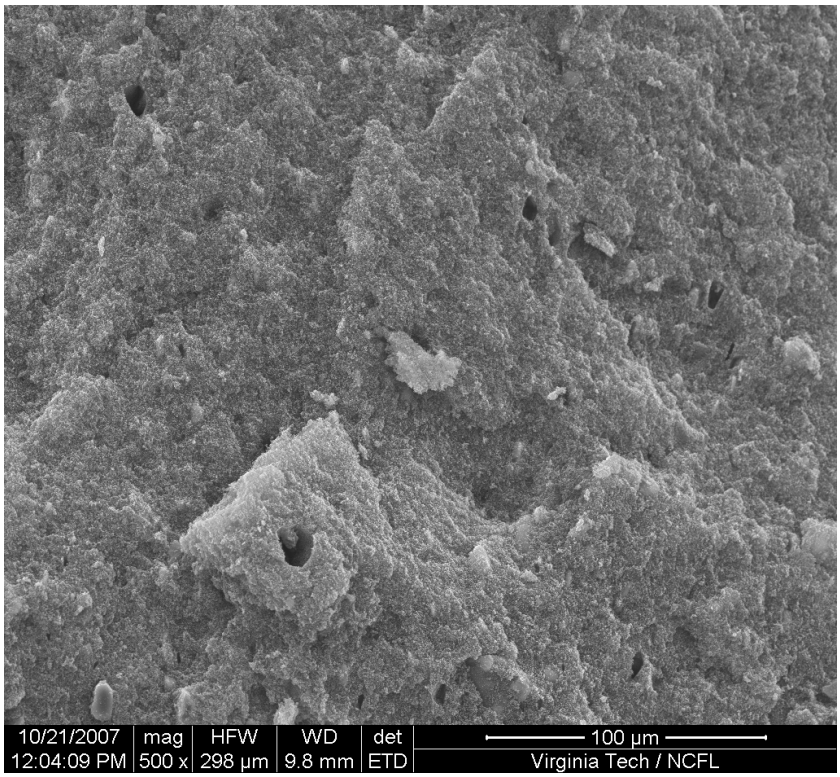

Figure C-51: ARI-2732 Specimen 1 Location A (500x)

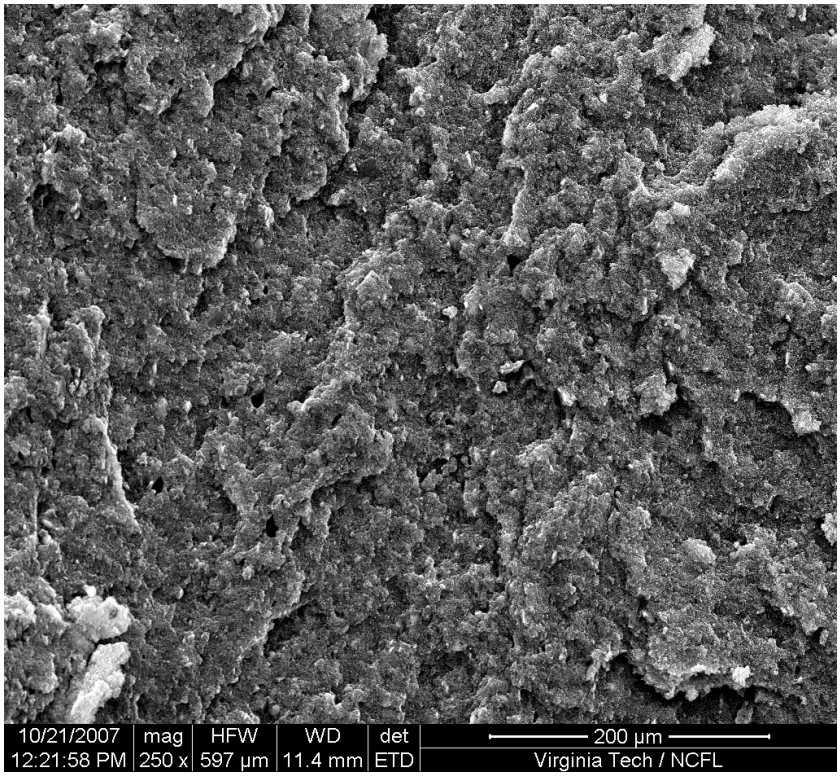

Figure C-52: ARI-2732 Specimen 1 Location B (250x)

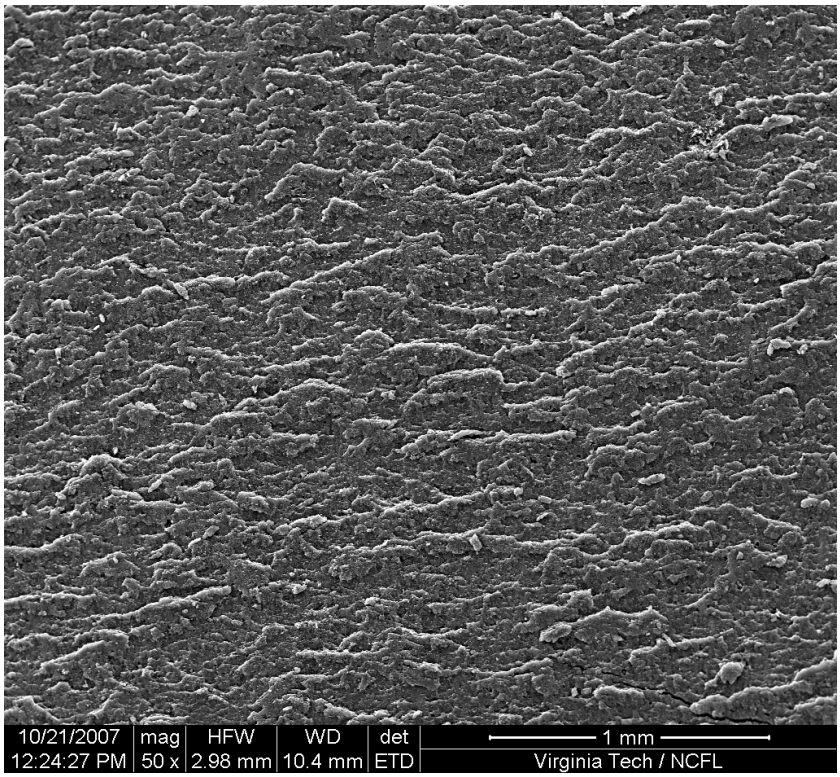

Figure C-53: ARI-2732 Specimen 2 Location A (50x)

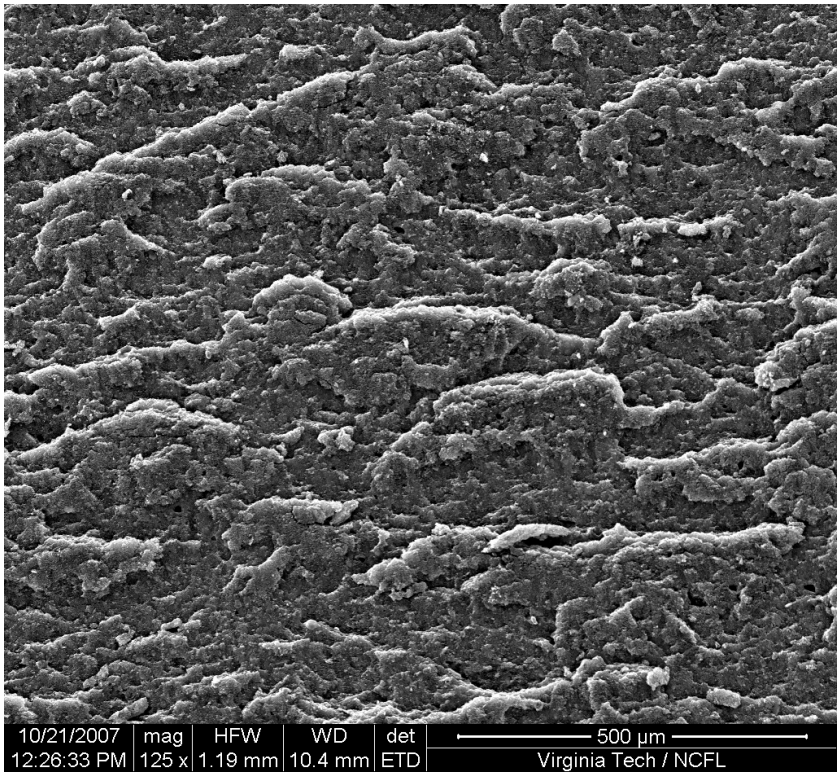

Figure C-54: ARI-2732 Specimen 2 Location A (125x)

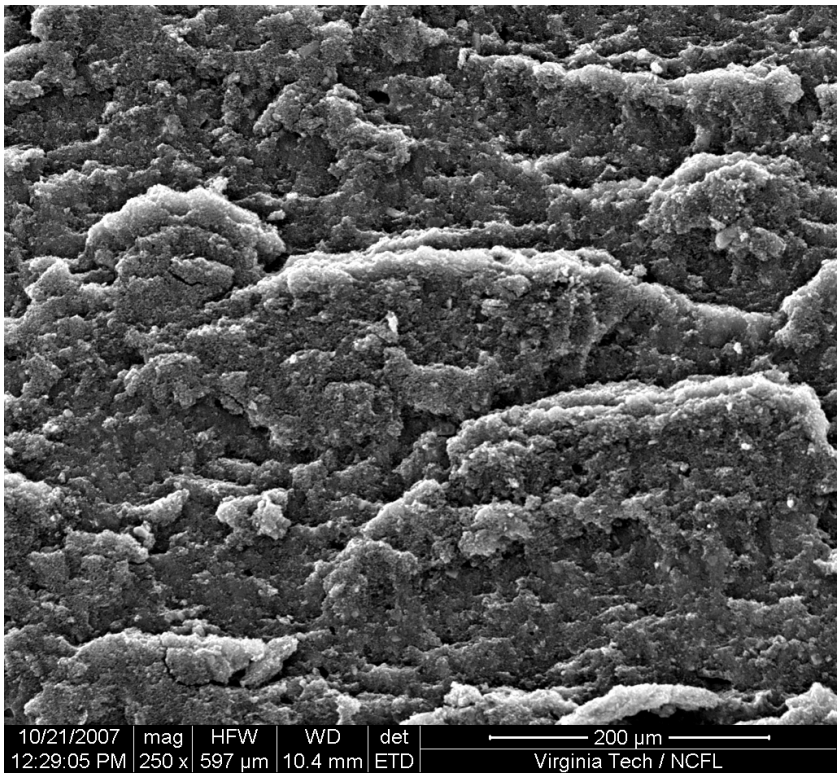

Figure C-55: ARI-2732 Specimen 2 Location A (250x)

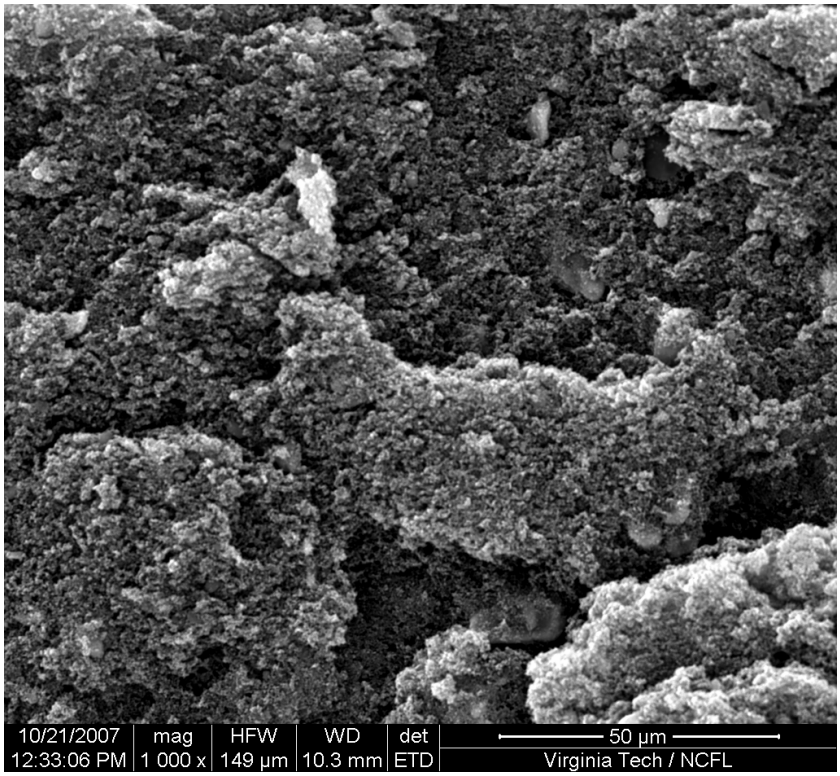

Figure C-56: ARI-2732 Specimen 2 Location A (1000x)

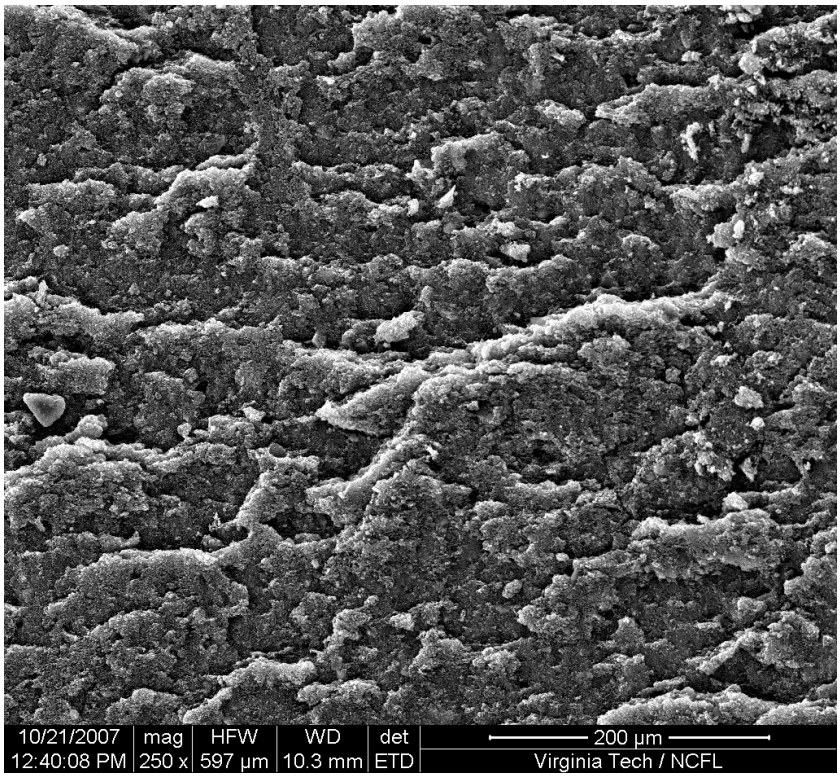

Figure C-57: ARI-2732 Specimen 2 Location B (250x)

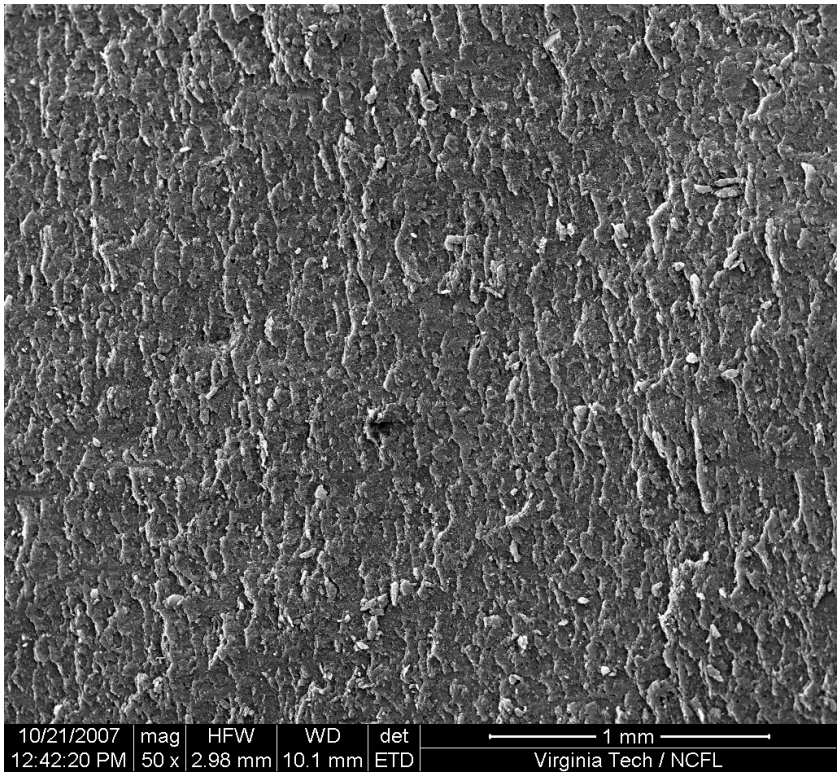

Figure C-58: ARI-2732 Specimen 3 Location A (50x)

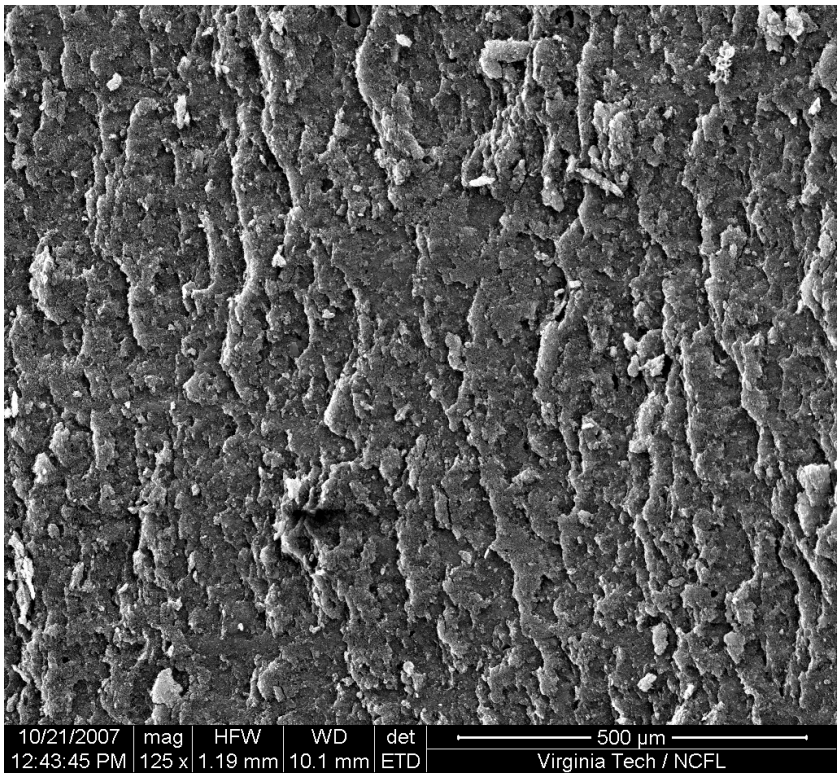

Figure C-59: ARI-2732 Specimen 3 Location A (125x)

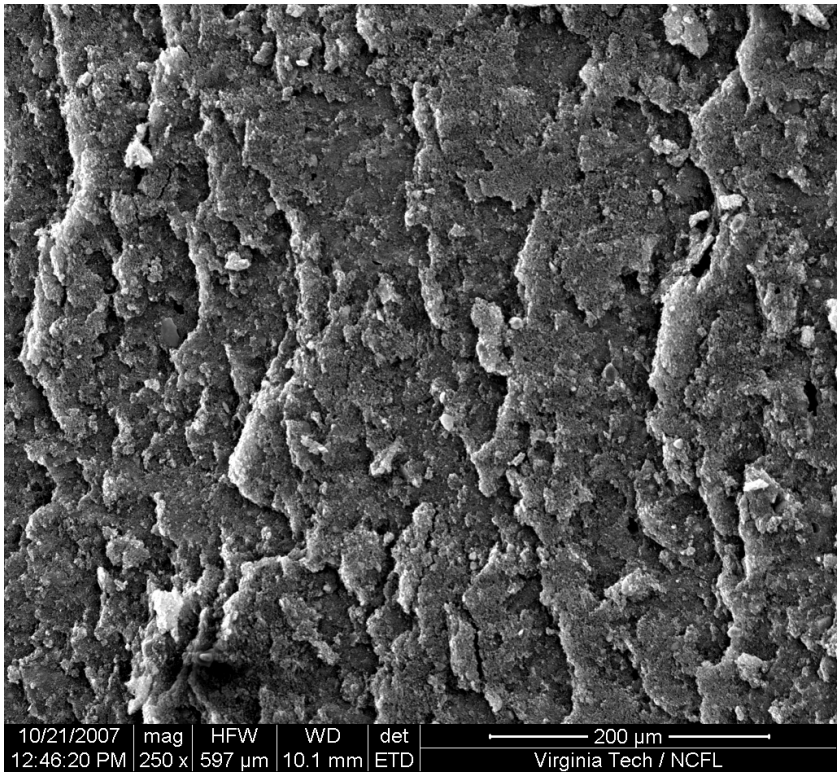

Figure C-60: ARI-2732 Specimen 3 Location A (250x)

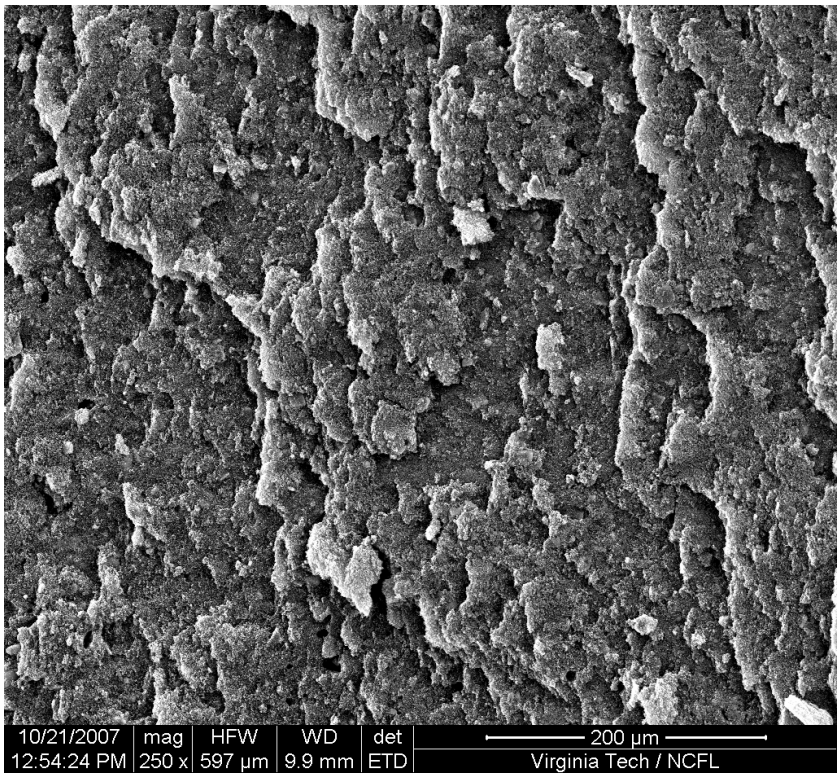

Figure C-61: ARI-2732 Specimen 3 Location B (250x)

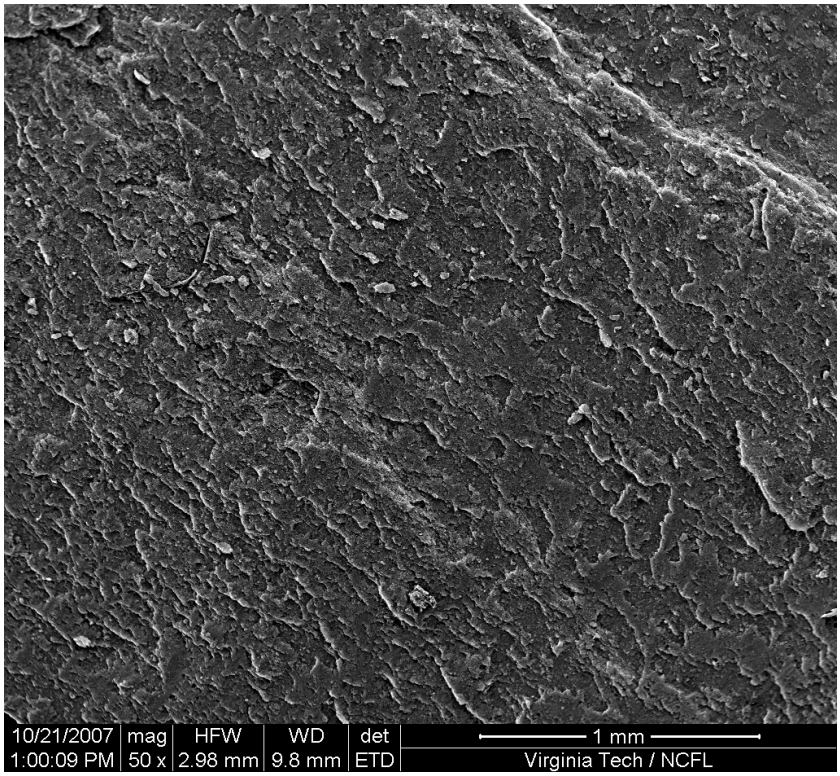

Figure C-62: ARI-2732 Specimen 4 Location A (50x)

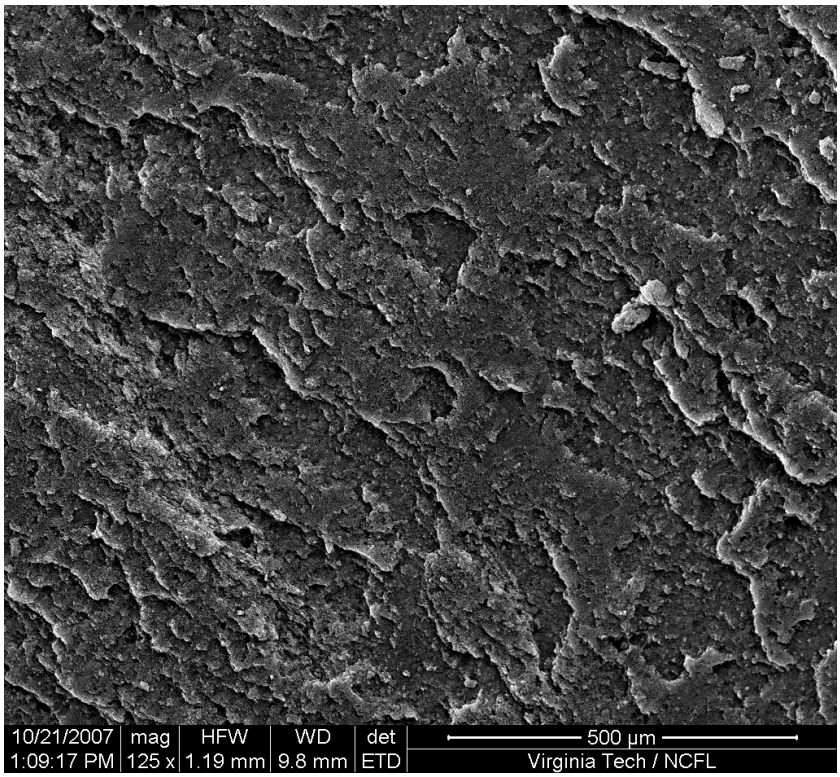

Figure C-63: ARI-2732 Specimen 4 Location A (125x)

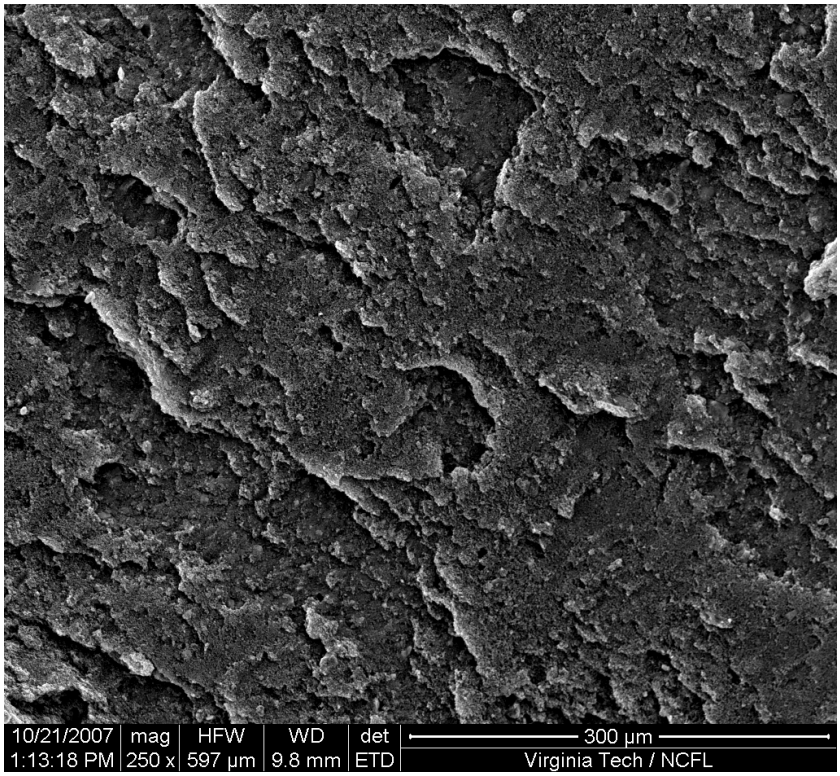

Figure C-64: ARI-2732 Specimen 4 Location A (250x)

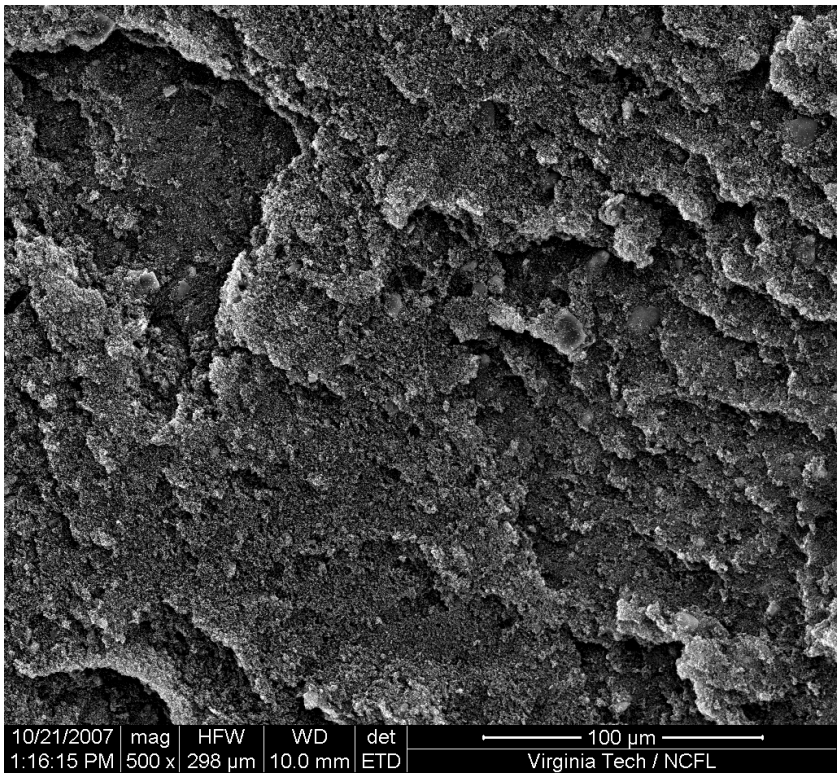

Figure C-65: ARI-2732 Specimen 4 Location A (500x)

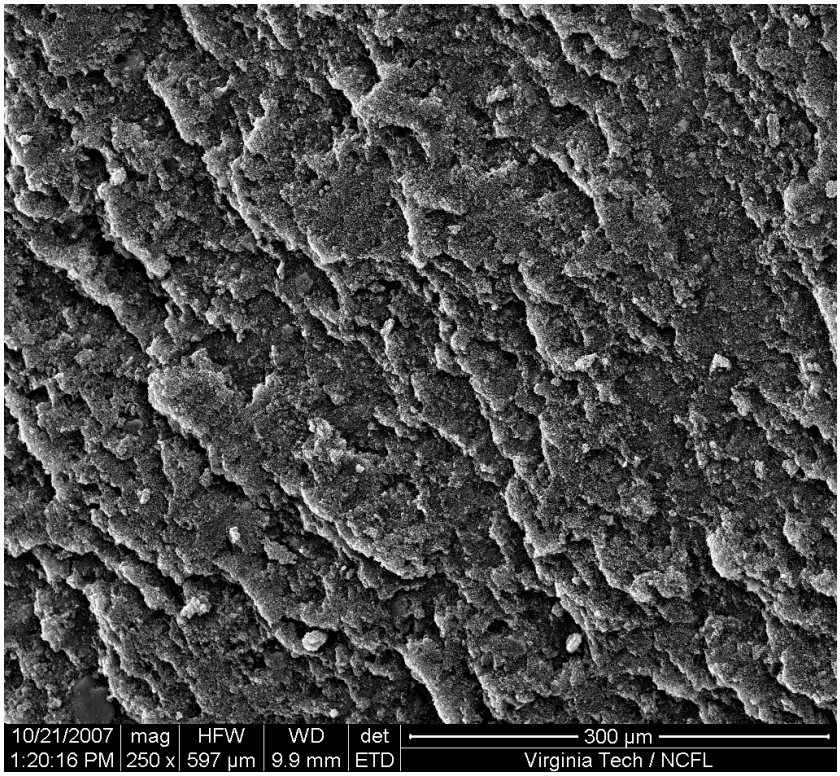

Figure C-66: ARI-2732 Specimen 4 Location B (250x)

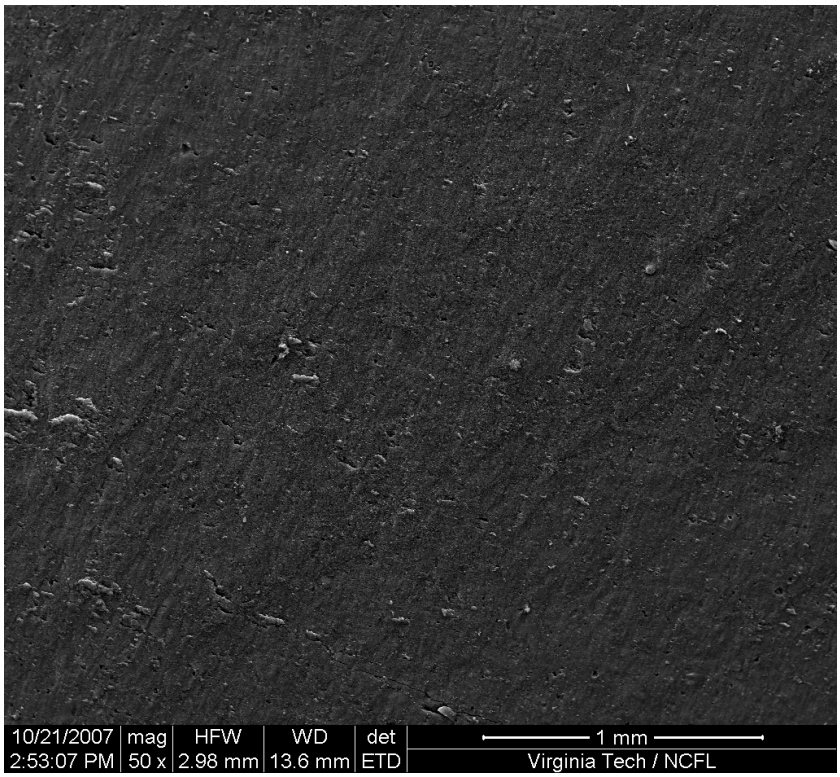

Figure C-67: ARI-2732 Specimen 5 Location A (50x)

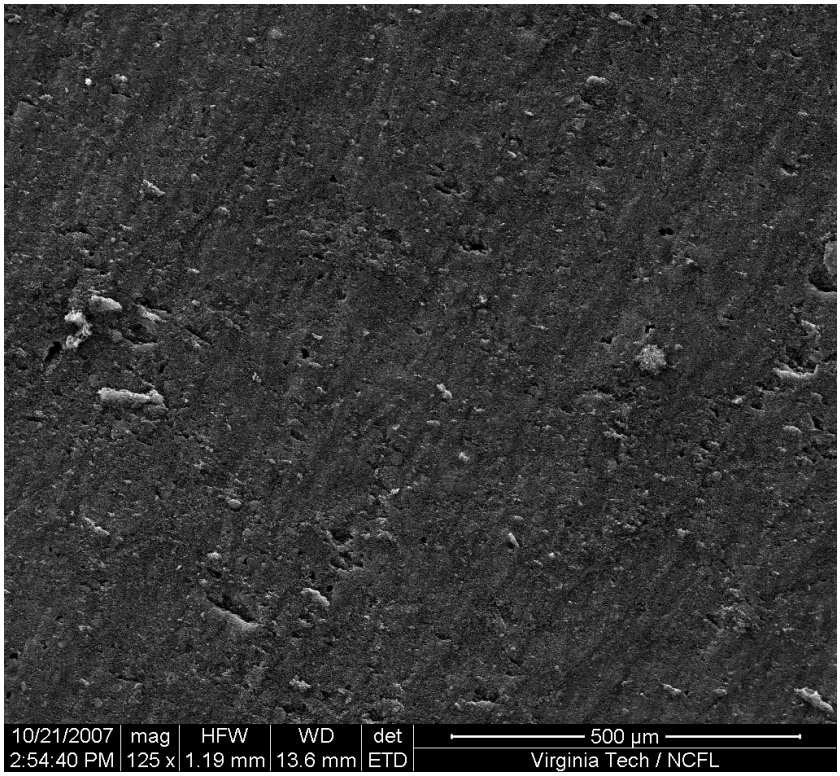

Figure C-68: ARI-2732 Specimen 5 Location A (125x)

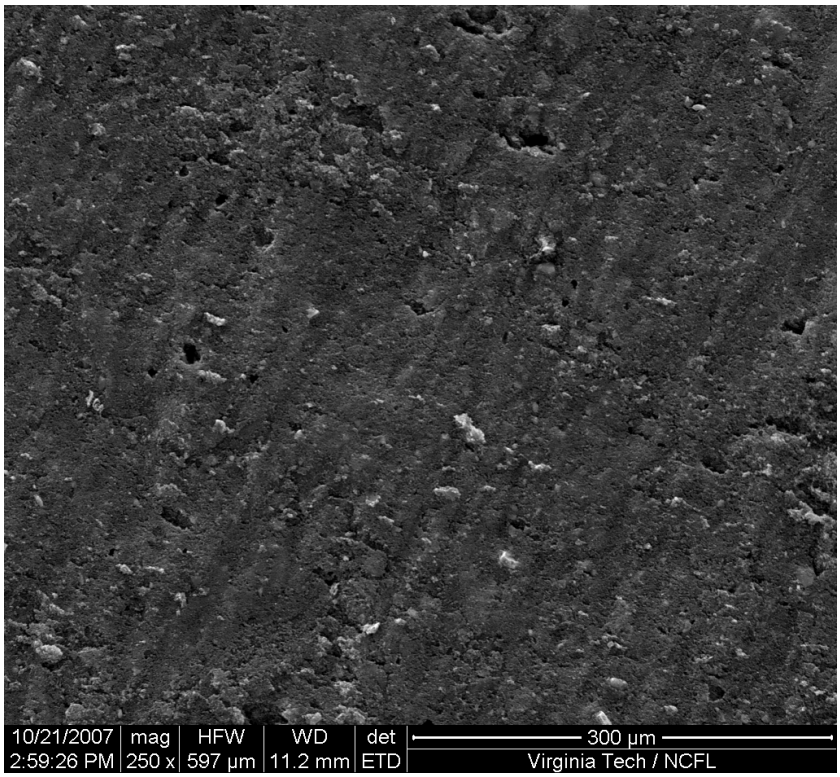

Figure C-69: ARI-2732 Specimen 5 Location A (250x)

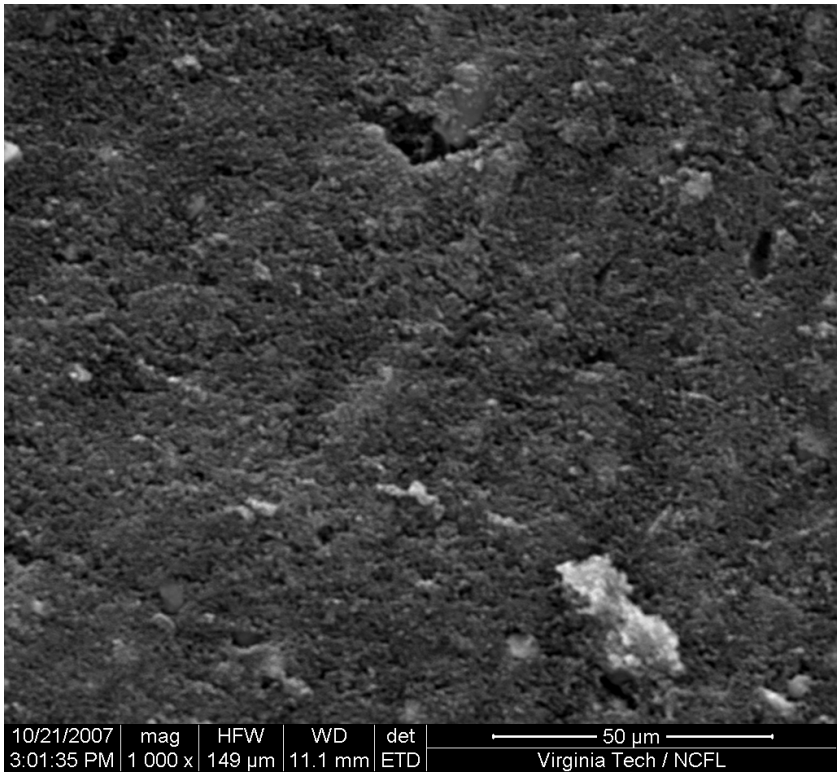

Figure C-70: ARI-2732 Specimen 5 Location A (1000x)

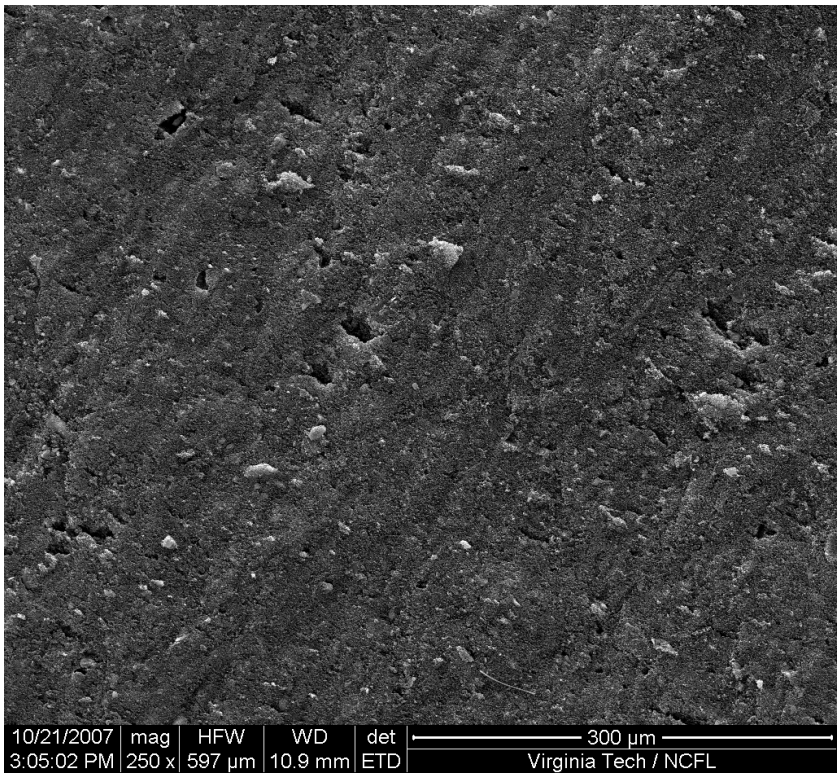

Figure C-71: ARI-2732 Specimen 5 Location B (250x)

Charred ARI-2750 Micrographs

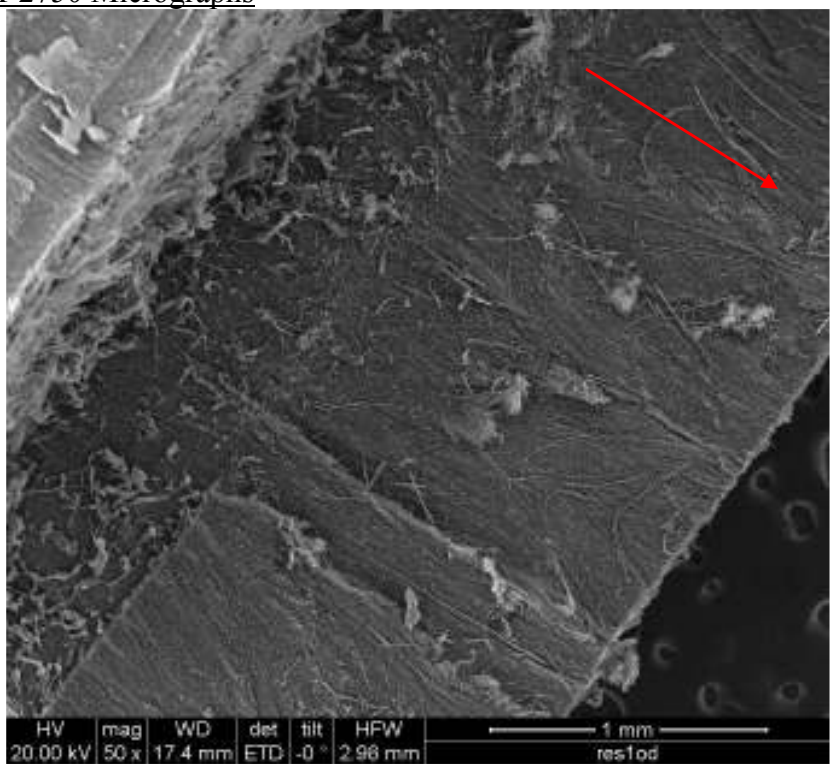

Figure C-72: ARI-2750 Specimen L1 Location A (50x)

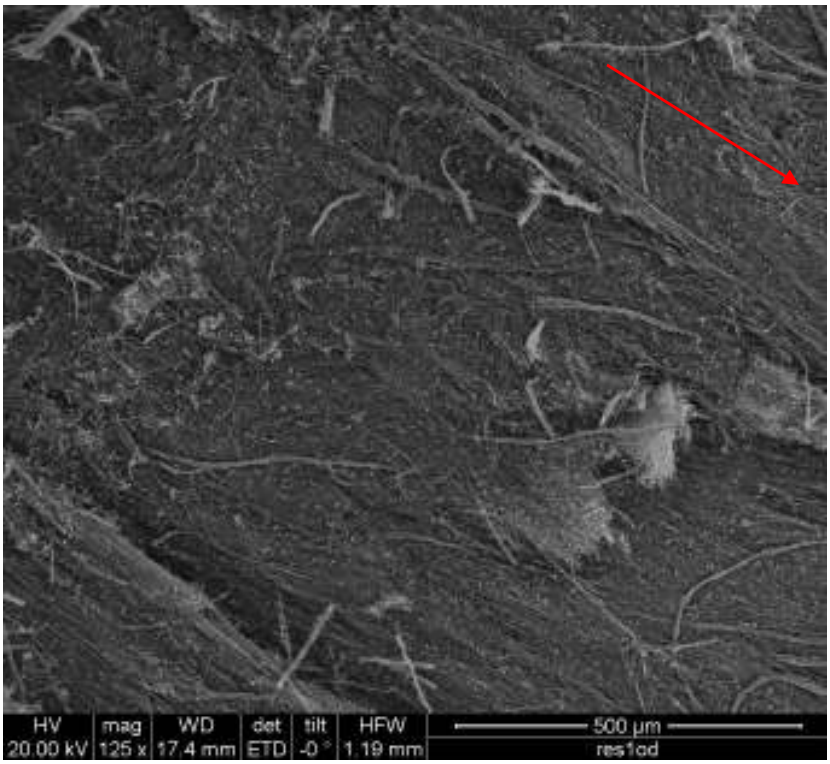

Figure C-73: ARI-2750 Specimen L1 Location A (125x)

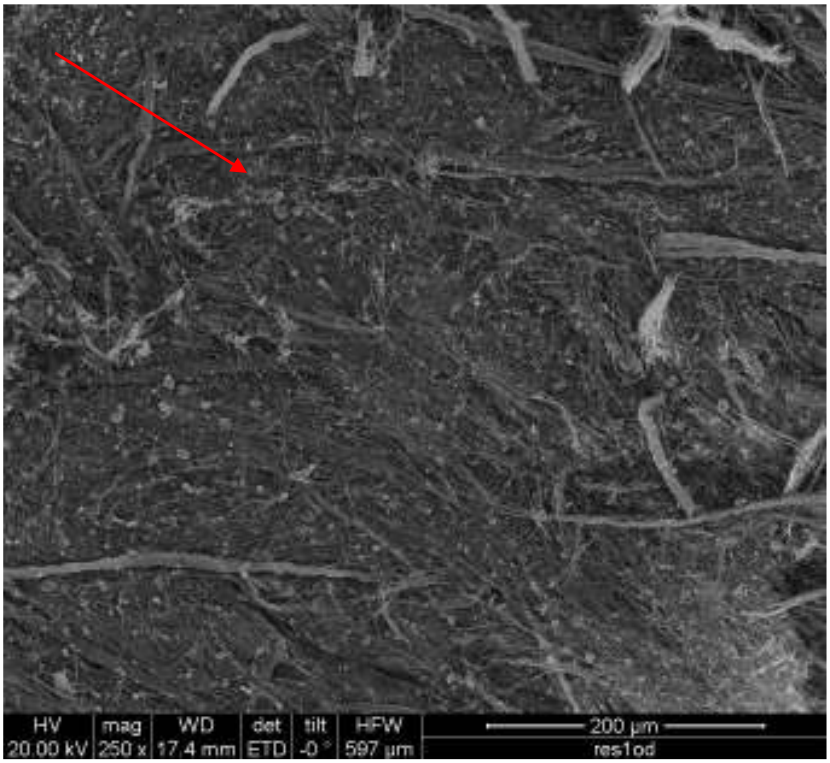

Figure C-74: ARI-2750 Specimen L1 Location A (250x)

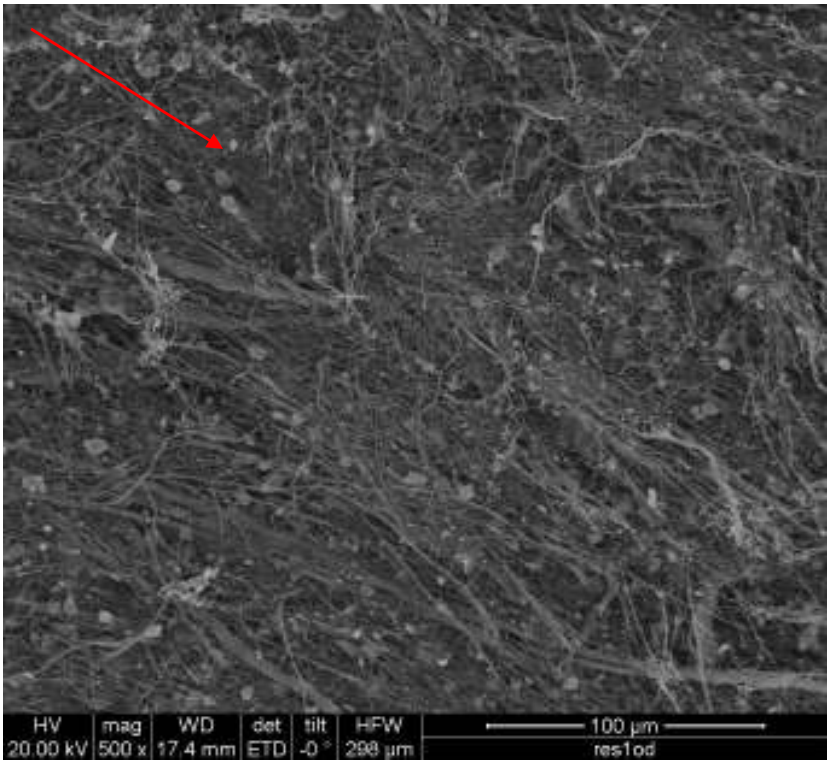

Figure C-75: ARI-2750 Specimen L1 Location A (500x)

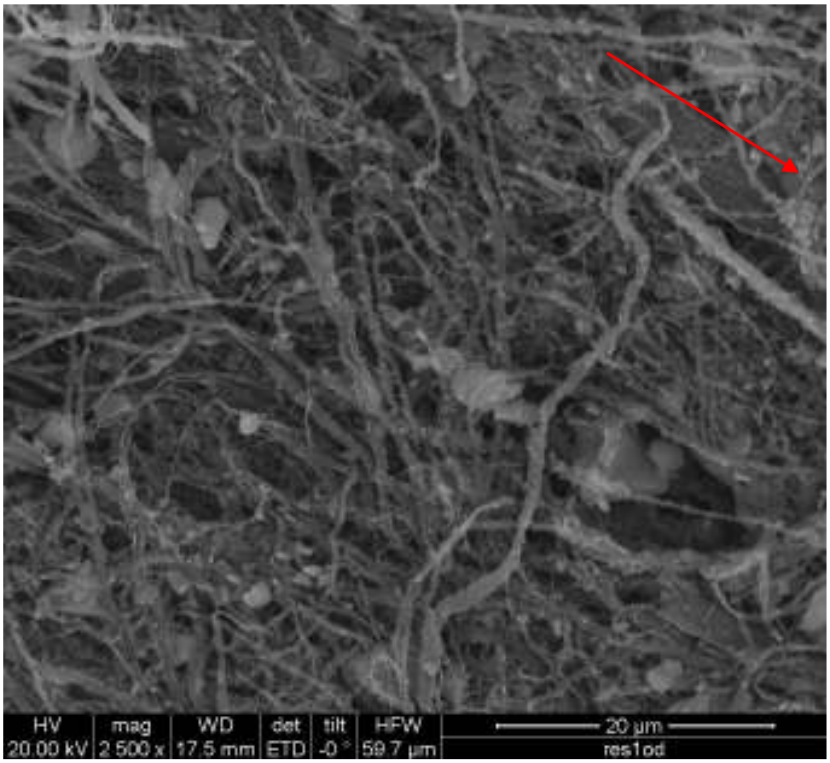

Figure C-76: ARI-2750 Specimen L1 Location A (2500x)

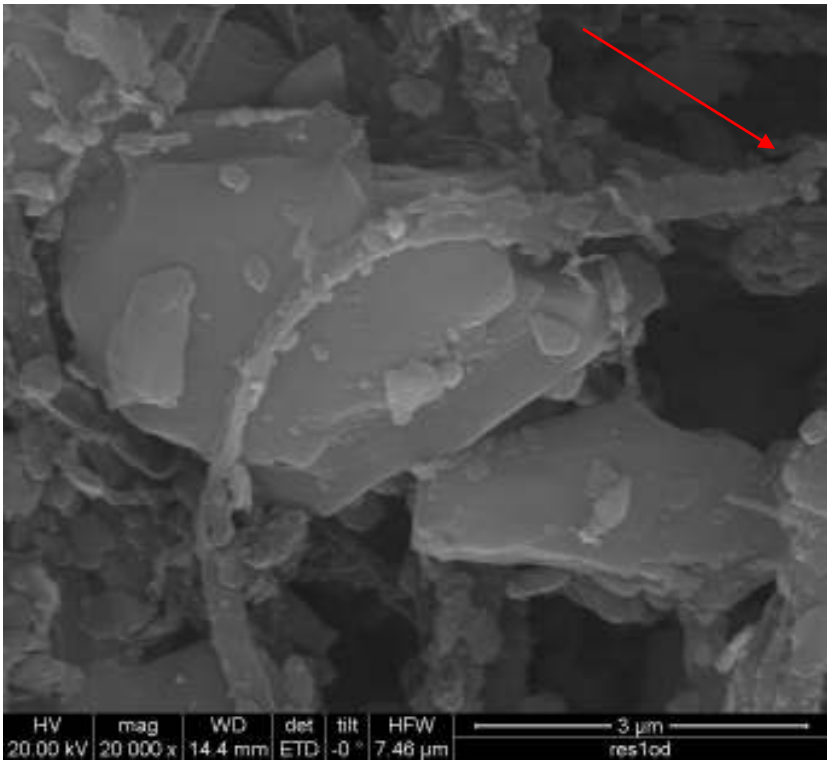

Figure C-77: ARI-2750 Specimen L1 Location A (20kx)

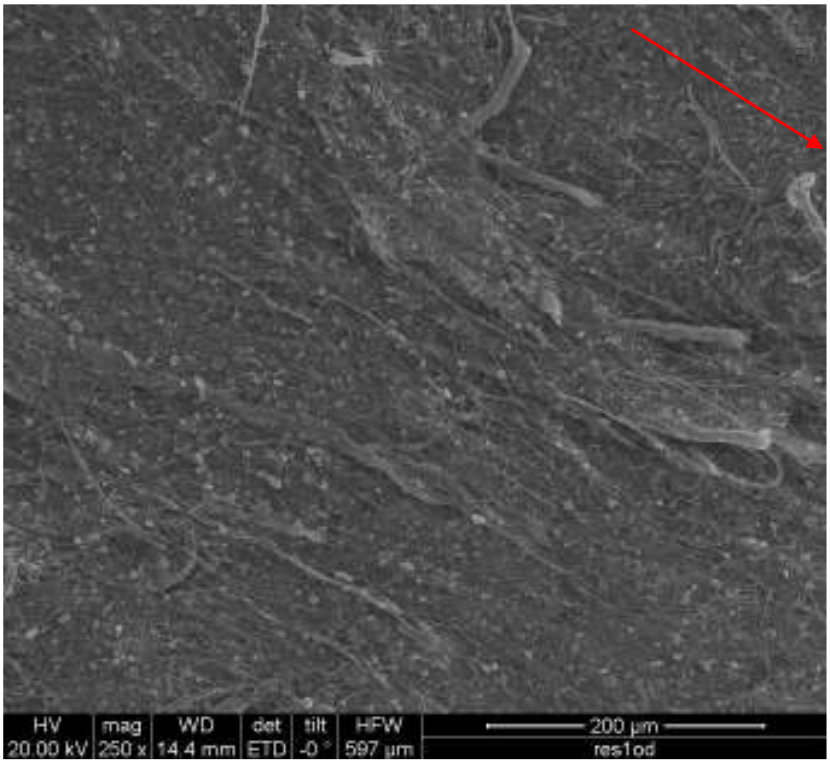

Figure C-78: ARI-2750 Specimen L1 Location B (250x)

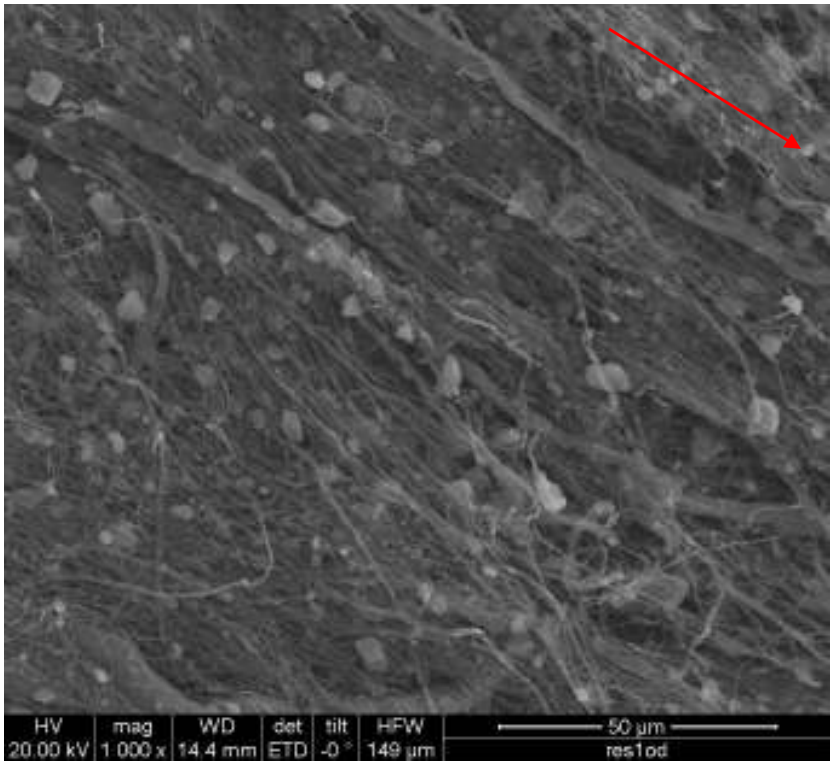

Figure C-79: ARI-2750 Specimen L1 Location B (1000x)

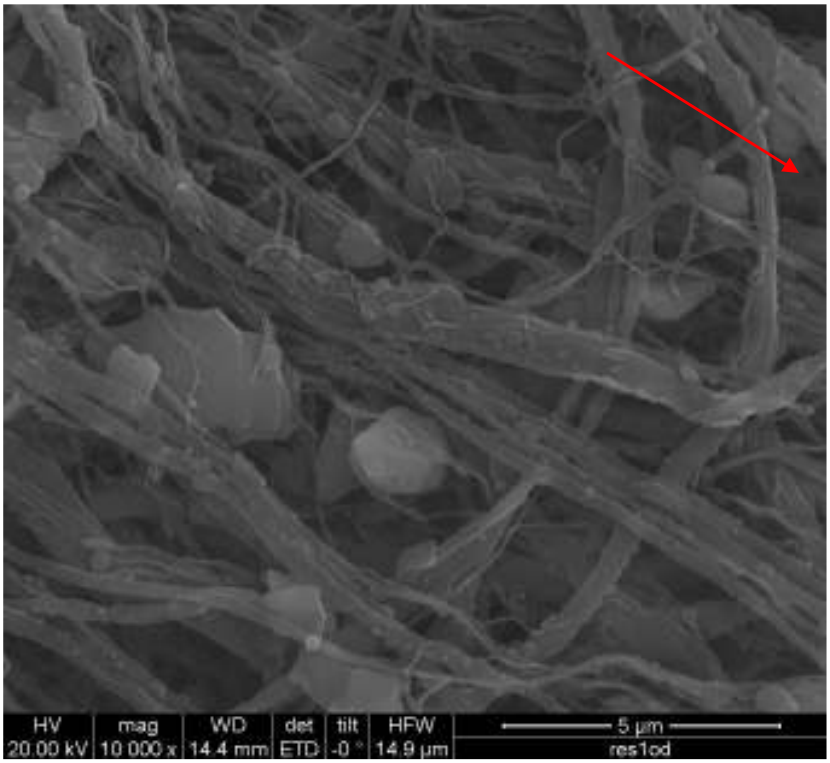

Figure C-80: ARI-2750 Specimen L1 Location B (10kx)

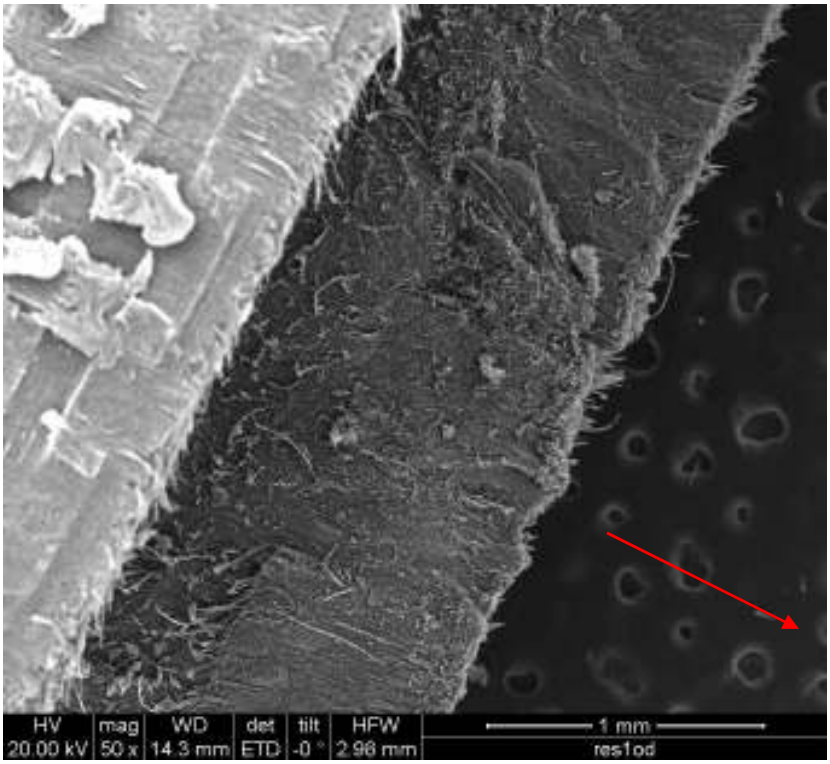

Figure C-81: ARI-2750 Specimen L6 Location A (50x)

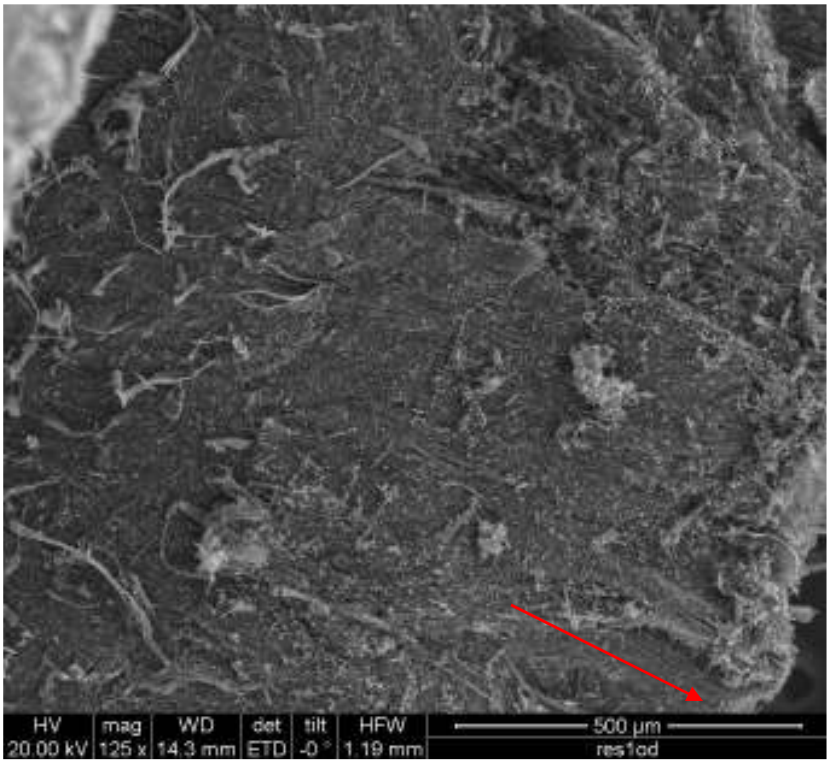

Figure C-82: ARI-2750 Specimen L6 Location A (125x)

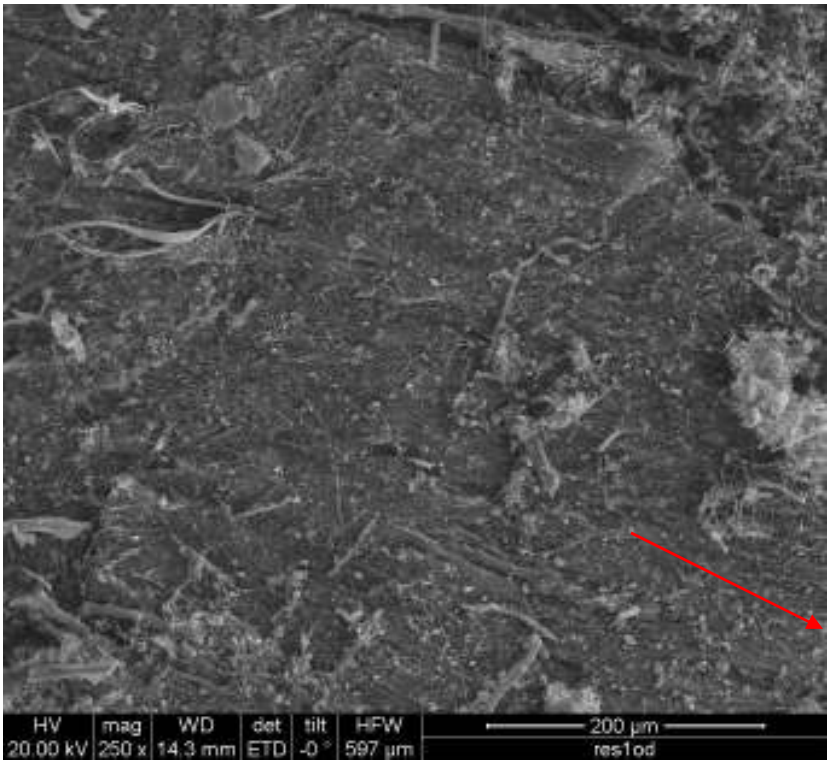

Figure C-83: ARI-2750 Specimen L6 Location A (250x)

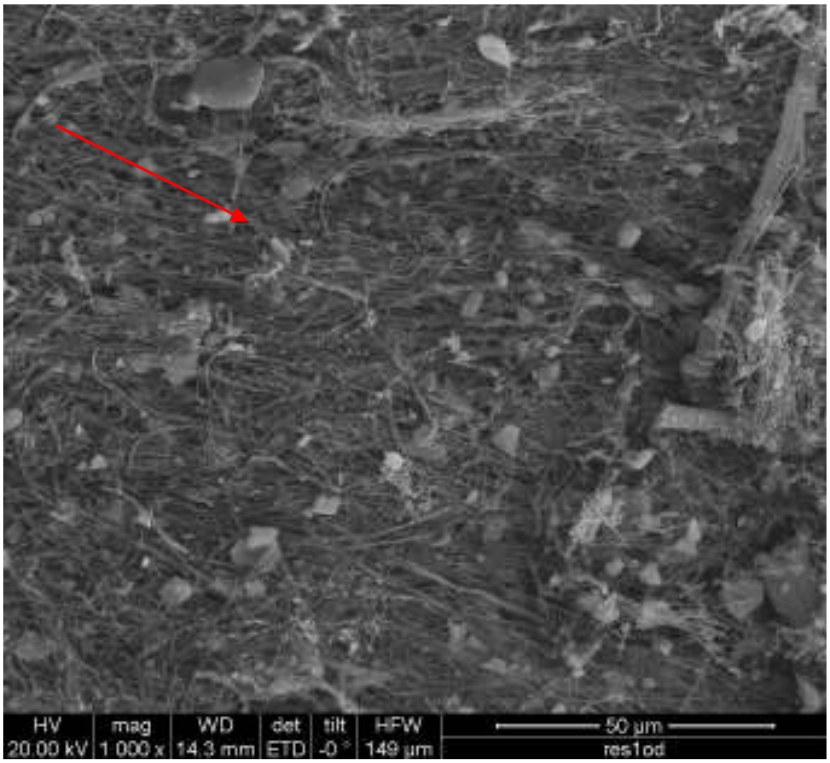

Figure C-84: ARI-2750 Specimen L6 Location A (1000x)

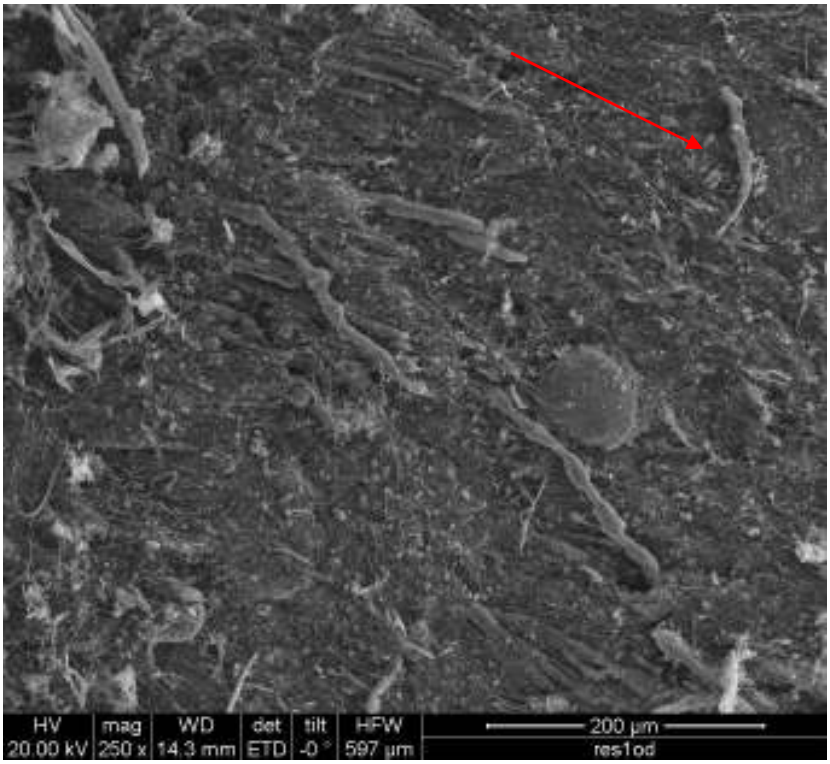

Figure C-85: ARI-2750 Specimen L6 Location B (250x)

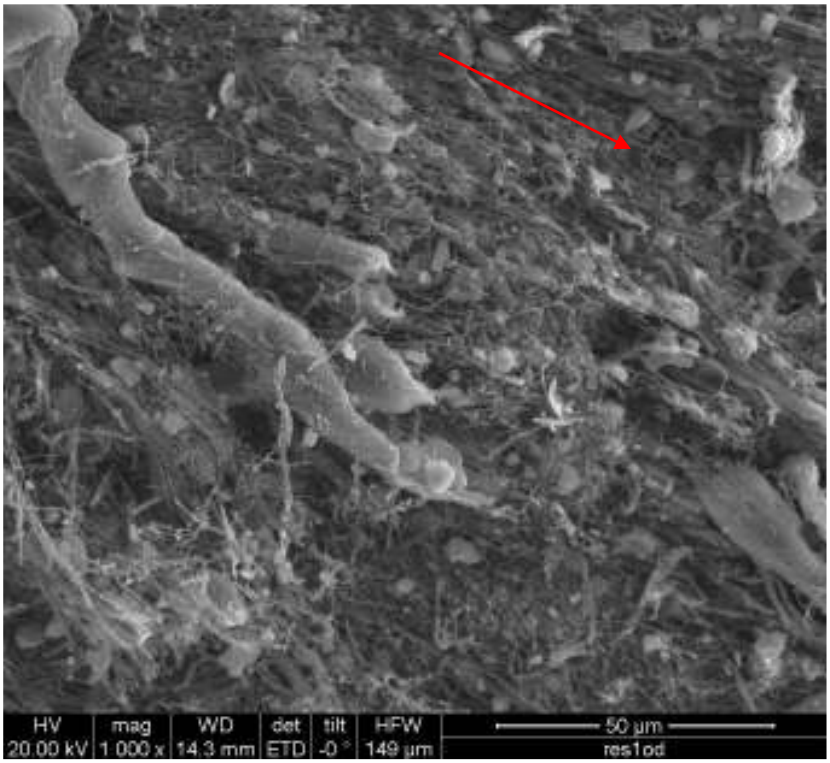

Figure C-86: ARI-2750 Specimen L6 Location B (1000x)

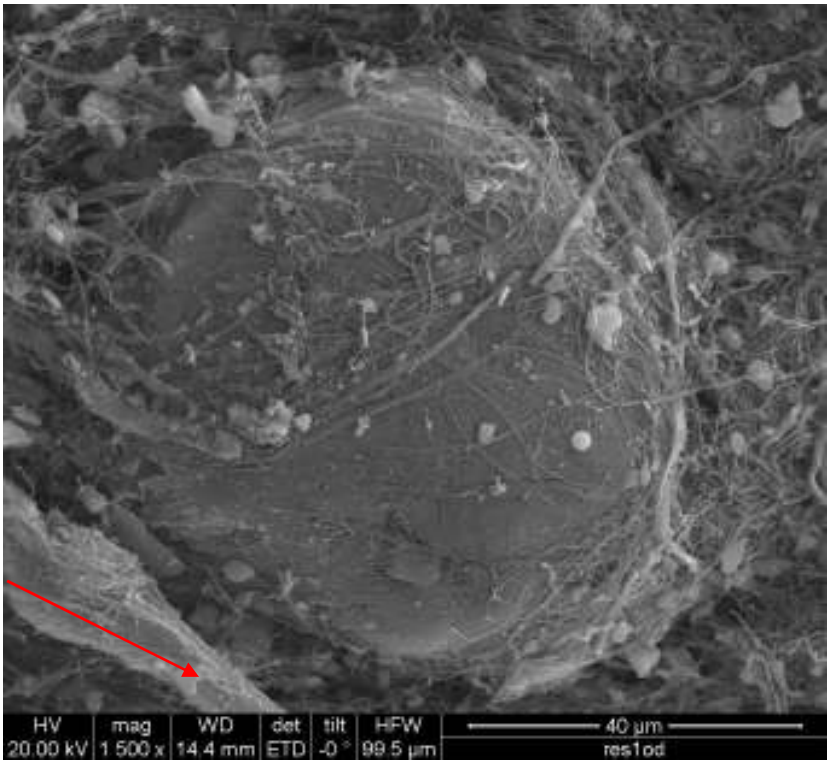

Figure C-87: ARI-2750 Specimen L6 Location C (1500x)

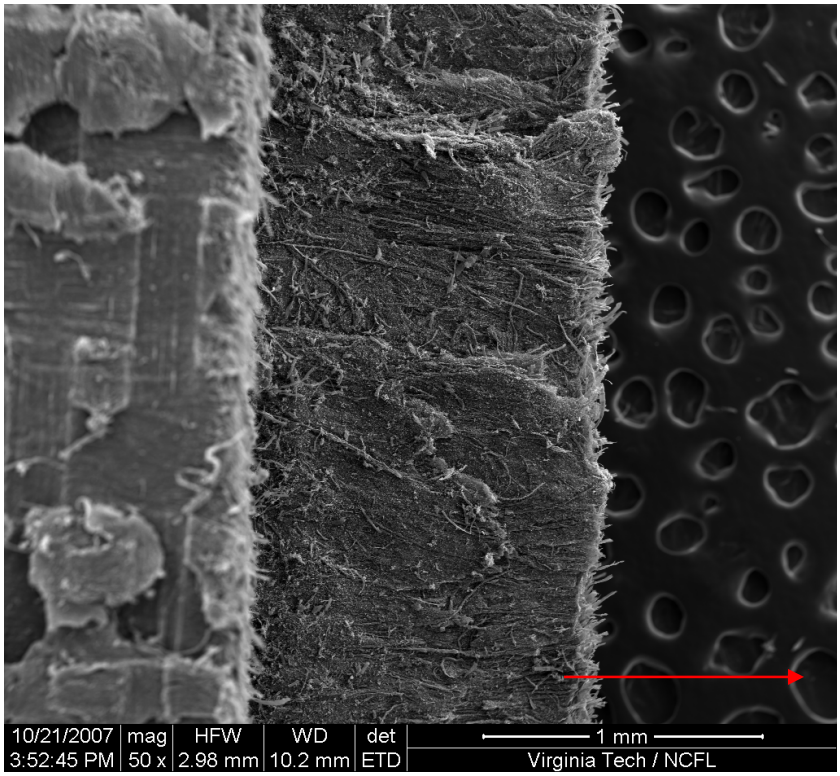

Figure C-88: ARI-2750 Specimen L11 Location A (50x)

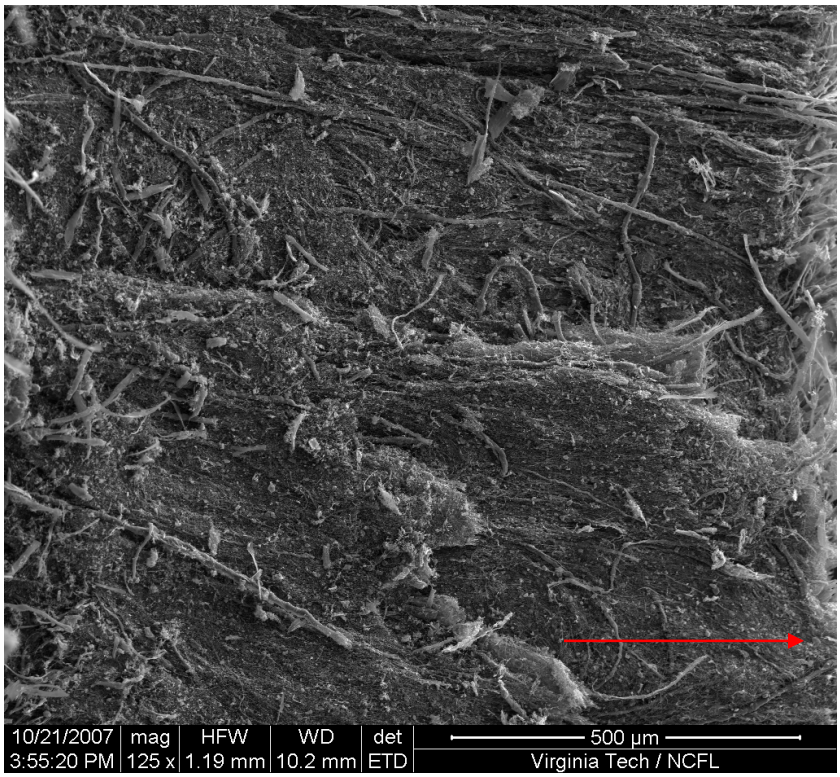

Figure C-89: ARI-2750 Specimen L11 Location A (125x)

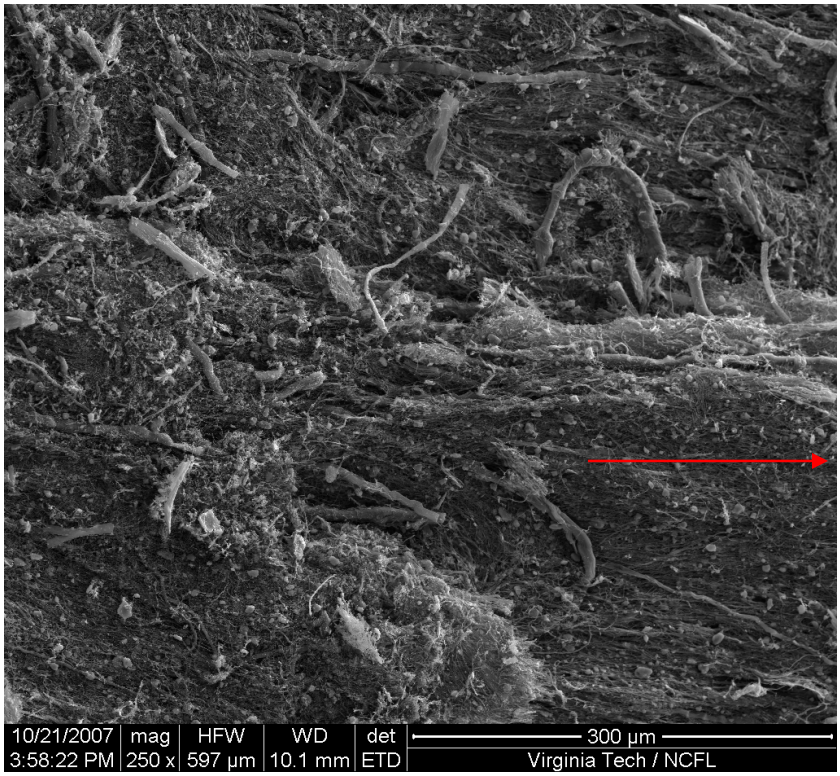

Figure C-90: ARI-2750 Specimen L11 Location A (250x)

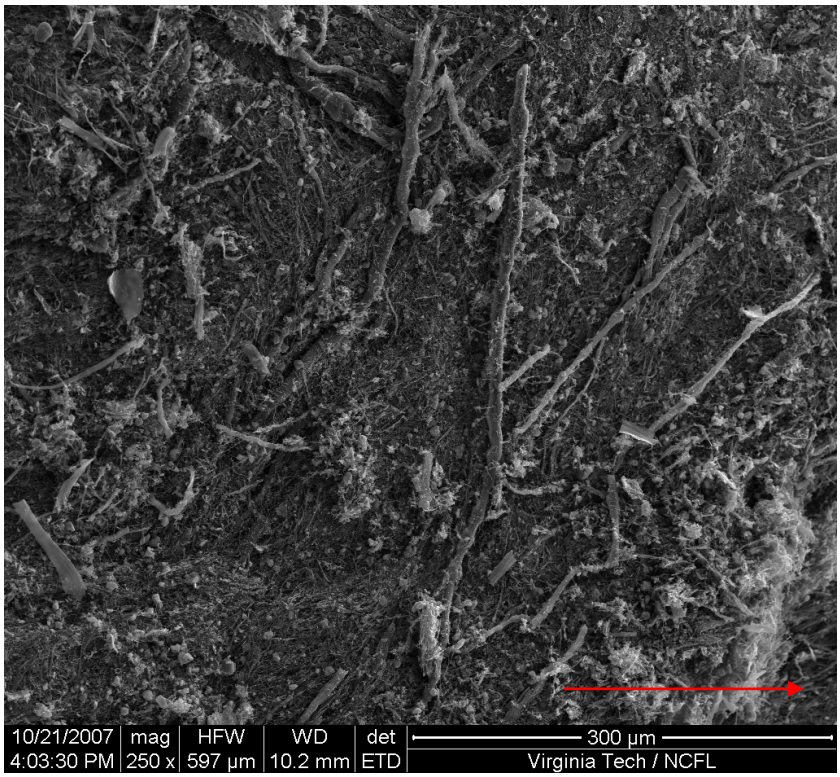

Figure C-91: ARI-2750 Specimen L11 Location B (250x)

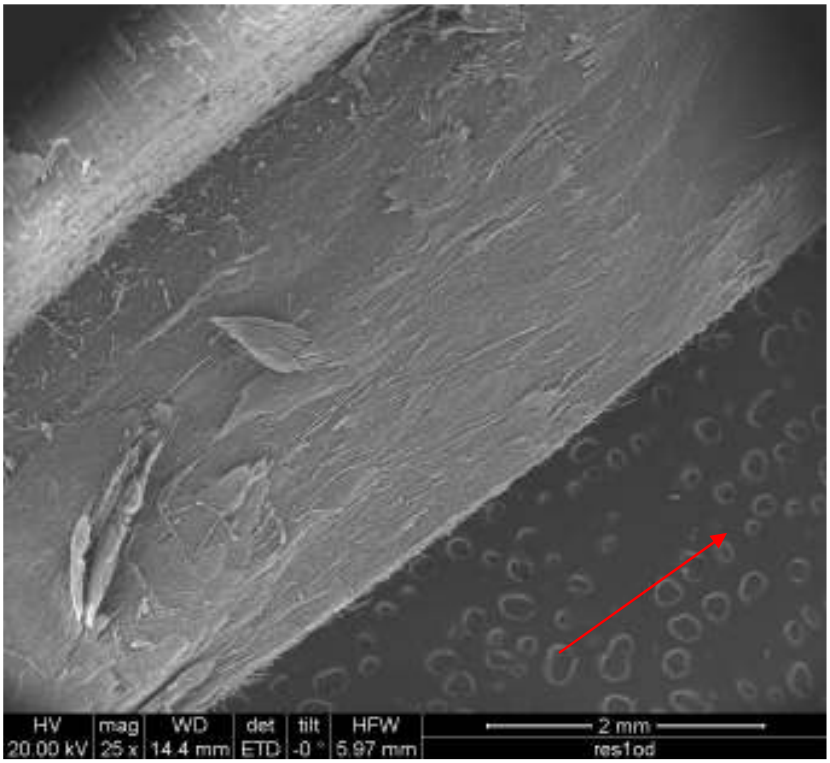

Figure C-92: ARI-2750 Specimen T1 Location A (25x)

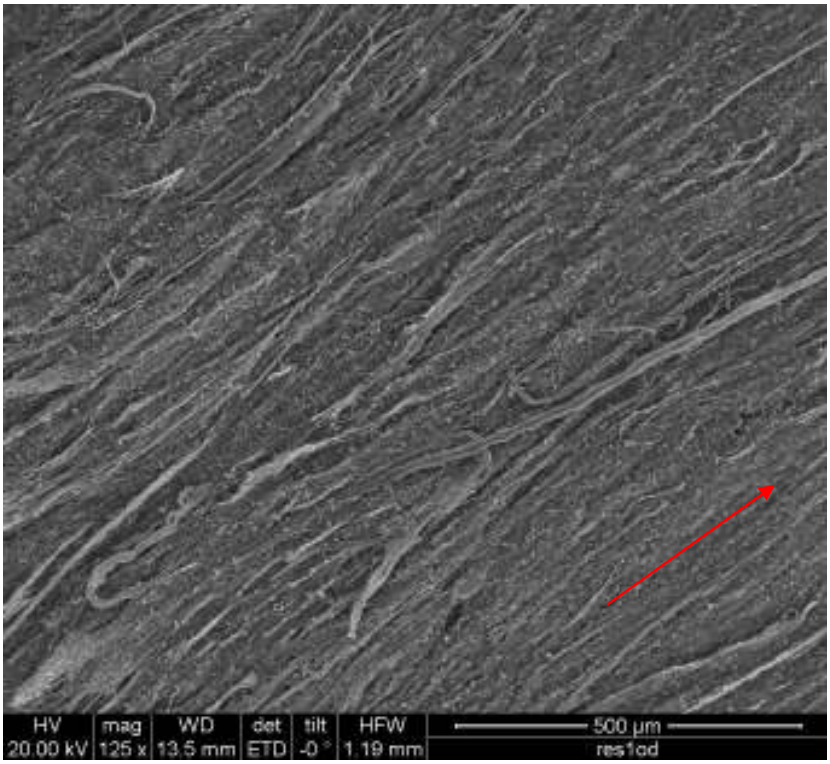

Figure C-93: ARI-2750 Specimen T1 Location A (125x)

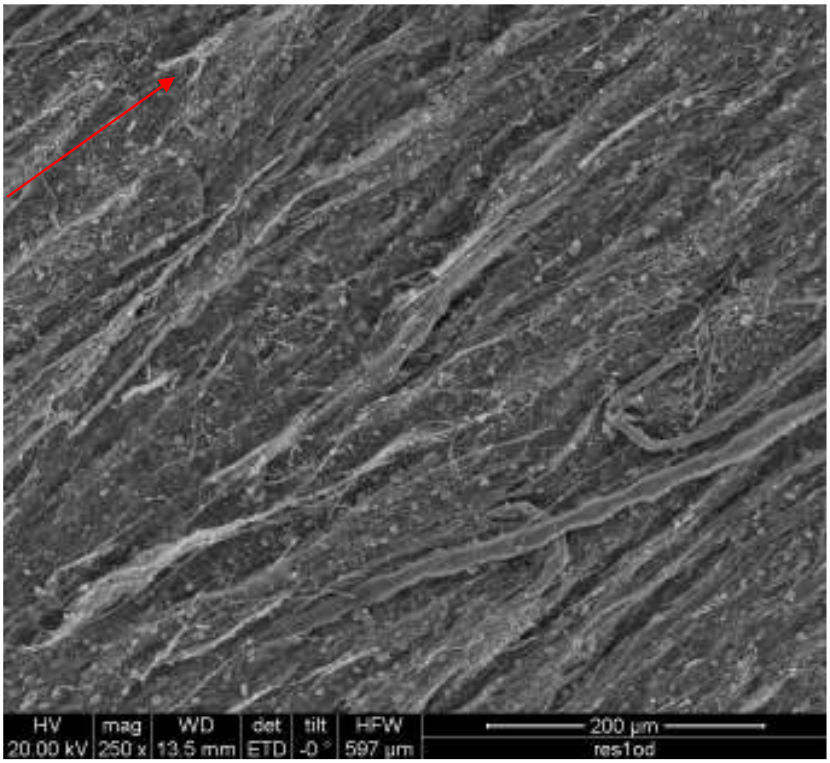

Figure C-94: ARI-2750 Specimen T1 Location A (250x)

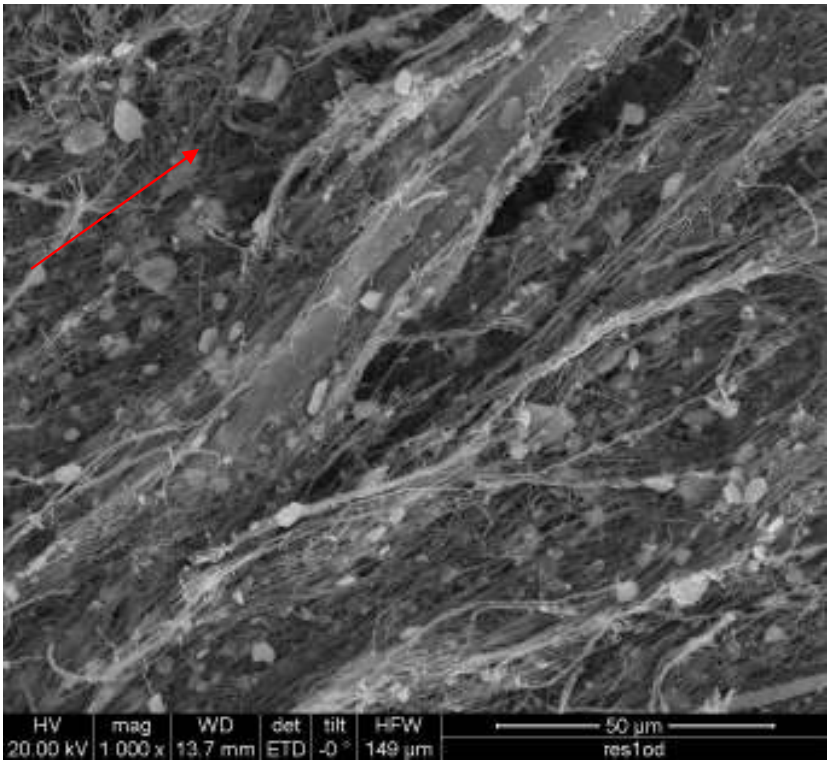

Figure C-95: ARI-2750 Specimen T1 Location A (1000x)

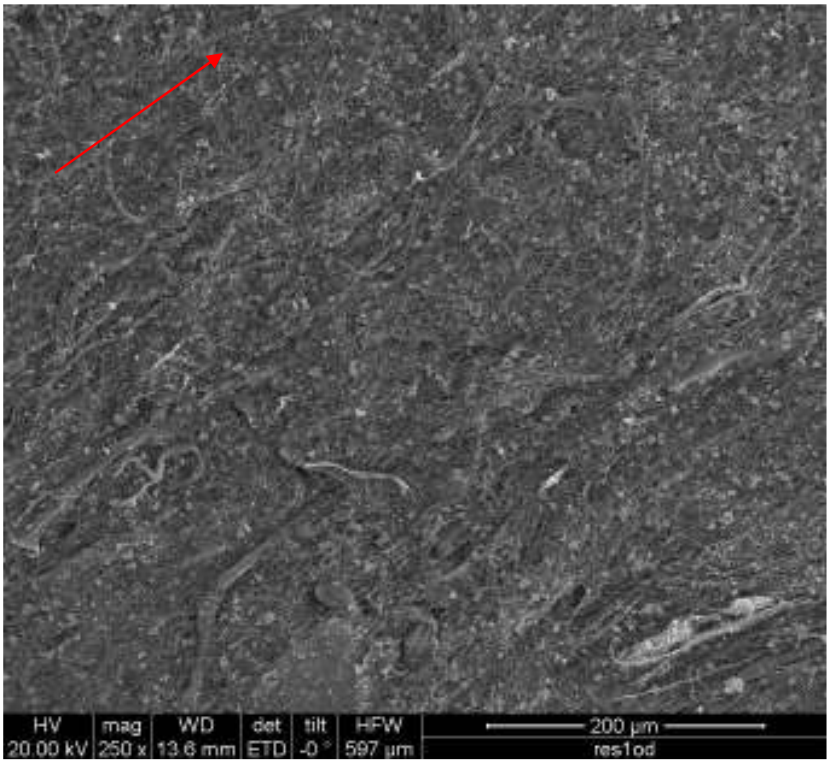

Figure C-96: ARI-2750 Specimen T1 Location B (250x)

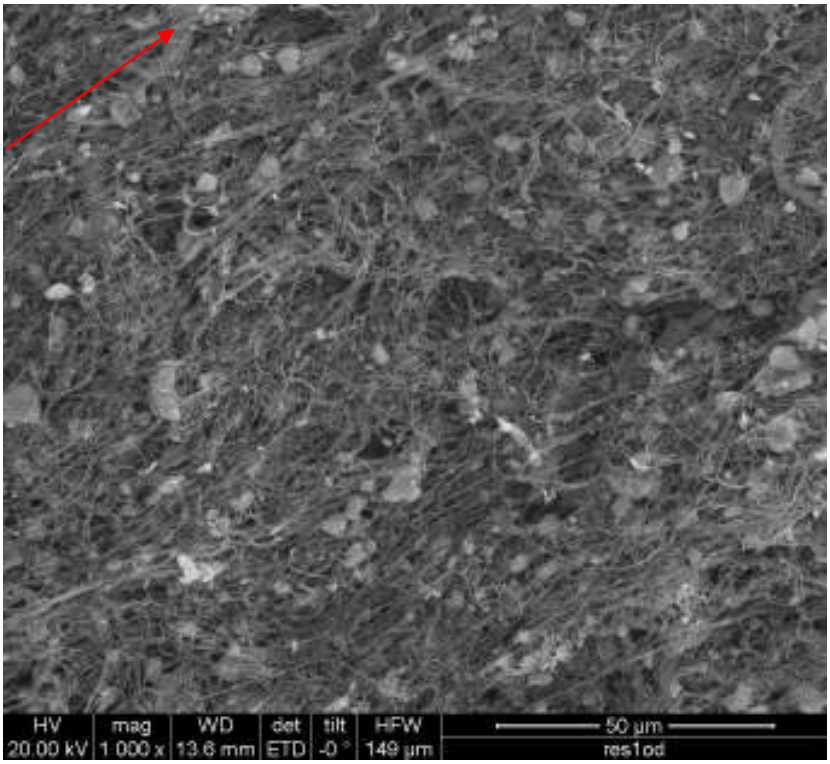

Figure C-97: ARI-2750 Specimen T1 Location B (1000x)

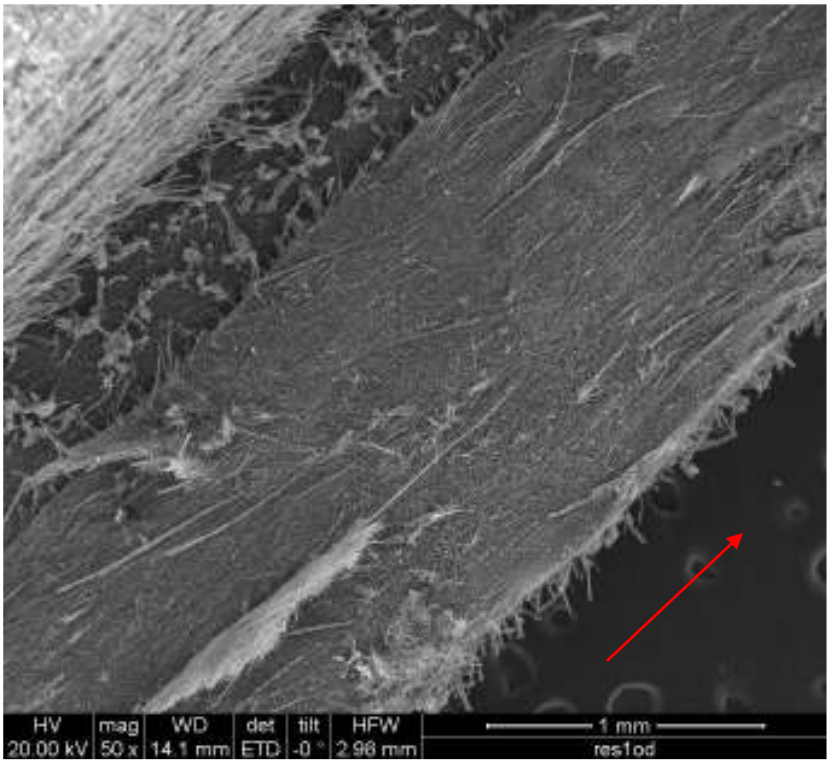

Figure C-98: ARI-2750 Specimen T5 Location A (50x)

Figure C-99: ARI-2750 Specimen T5 Location A (125x)

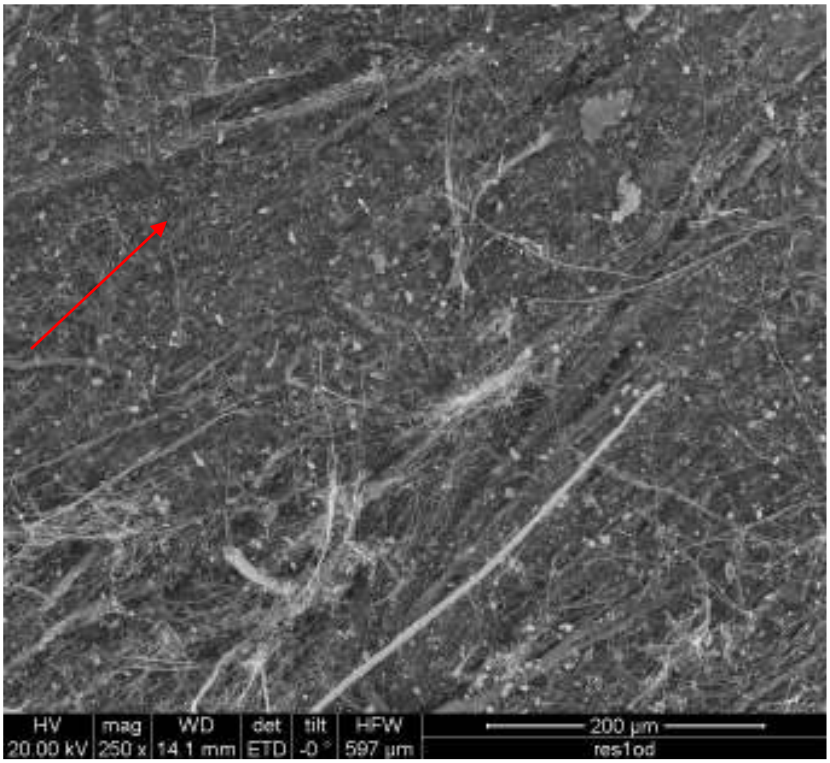

Figure C-100: ARI-2750 Specimen T5 Location A (250x)

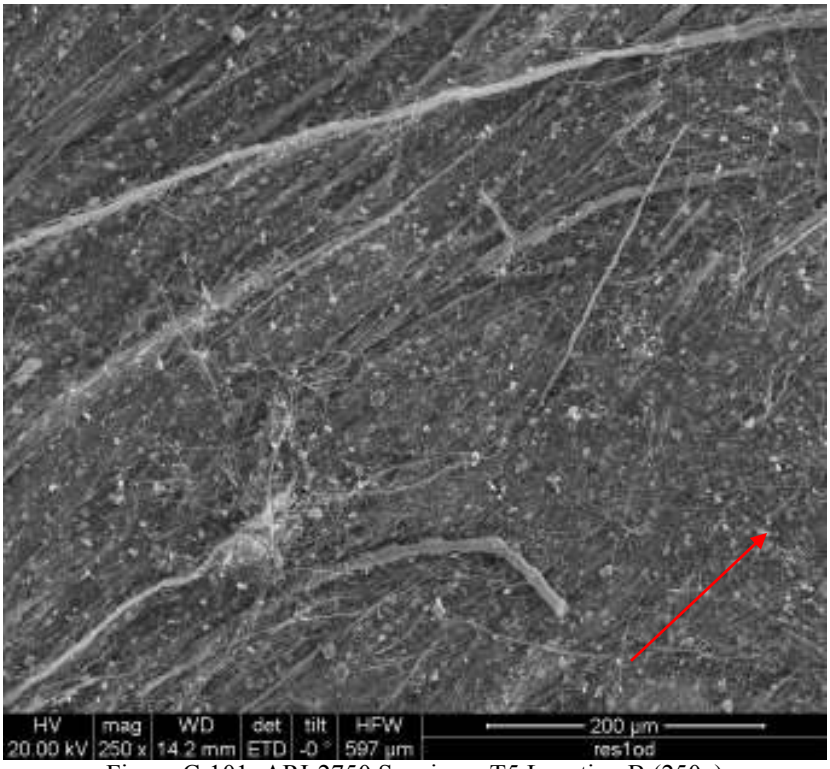

Figure C-101: ARI-2750 Specimen T5 Location B (250x)

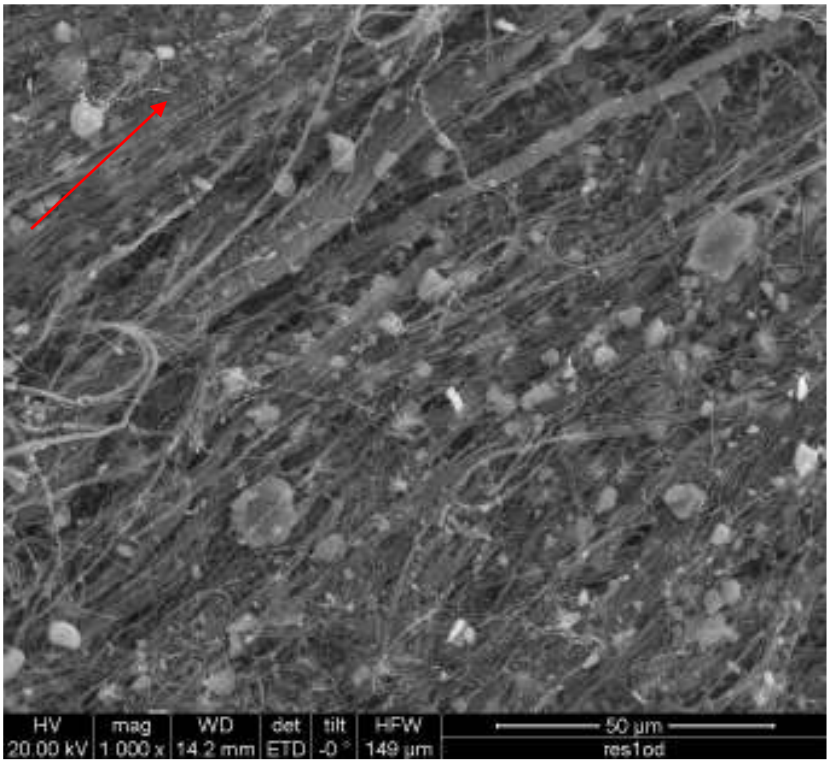

Figure C-102: ARI-2750 Specimen T5 Location B (1000x)

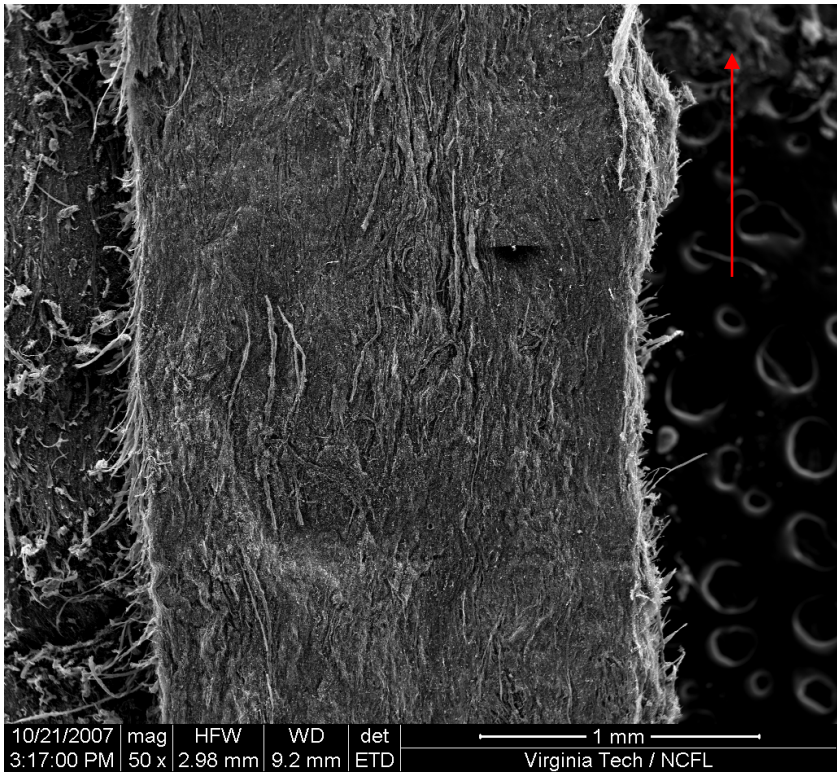

Figure C-103: ARI-2750 Specimen T13 Location A (50x)

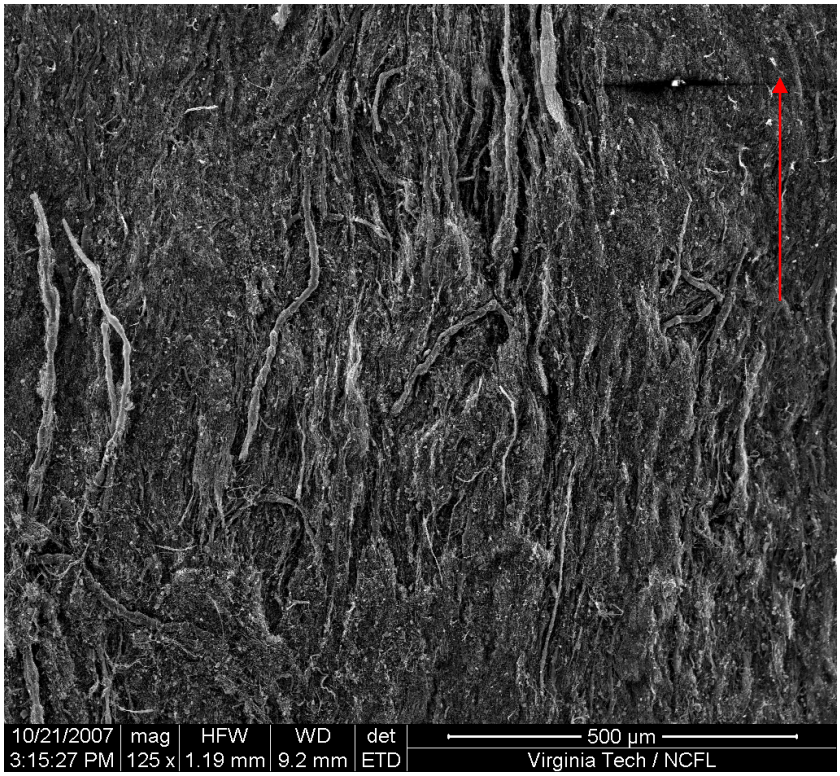

Figure C-104: ARI-2750 Specimen T13 Location A (125x)

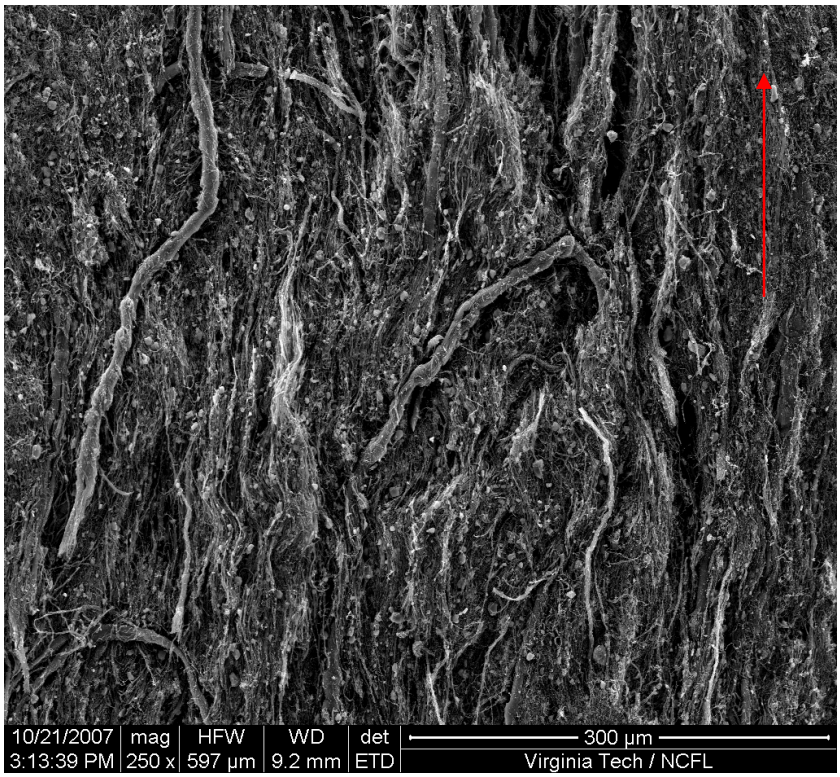

Figure C-105: ARI-2750 Specimen T13 Location A (250x)

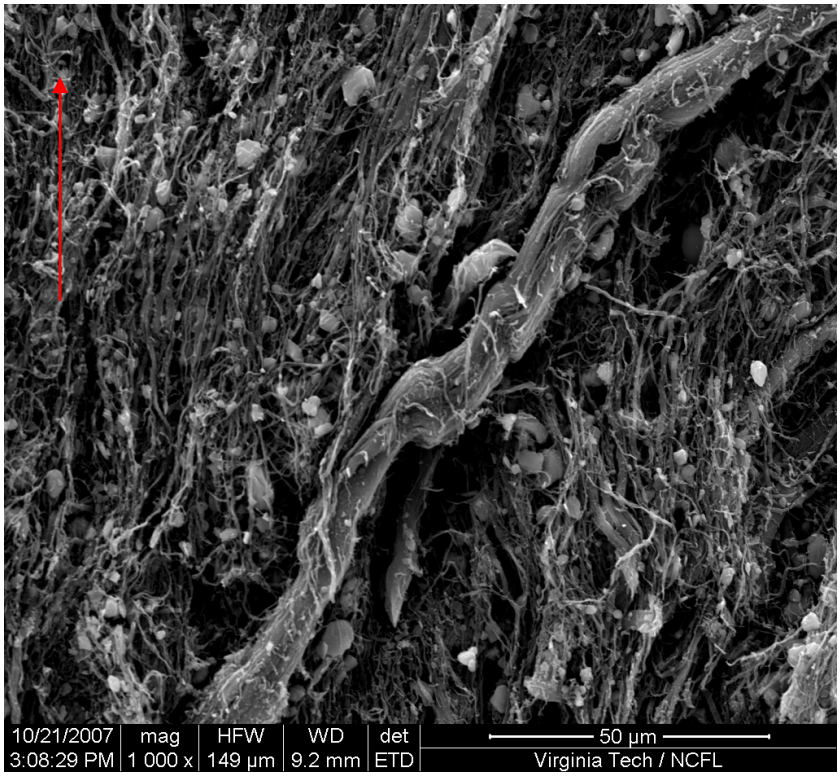

Figure C-106: ARI-2750 Specimen T13 Location A (1000x)

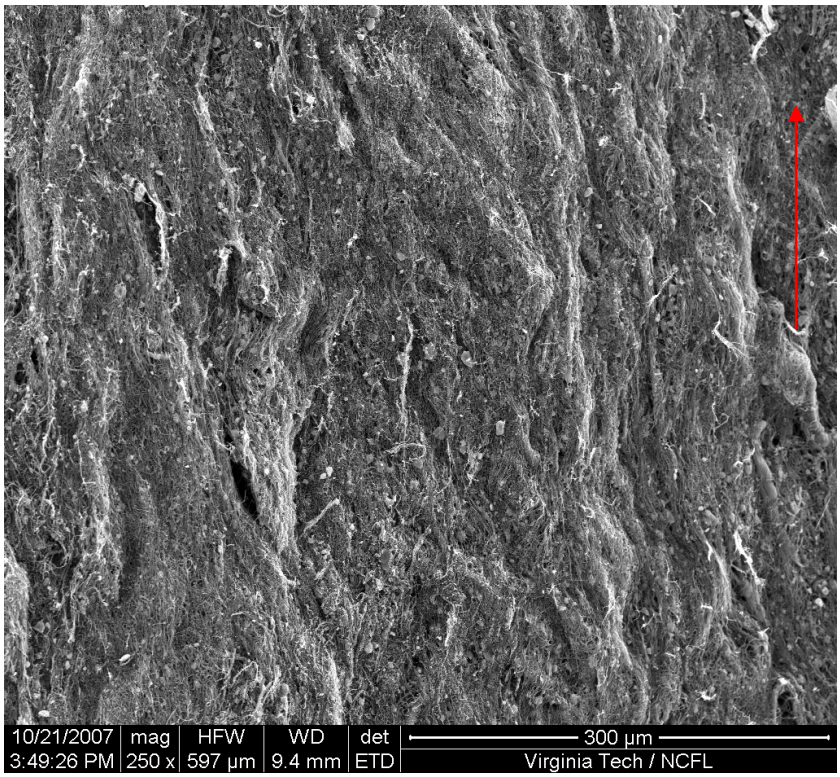

Figure C-107: ARI-2750 Specimen T13 Location B (250x)

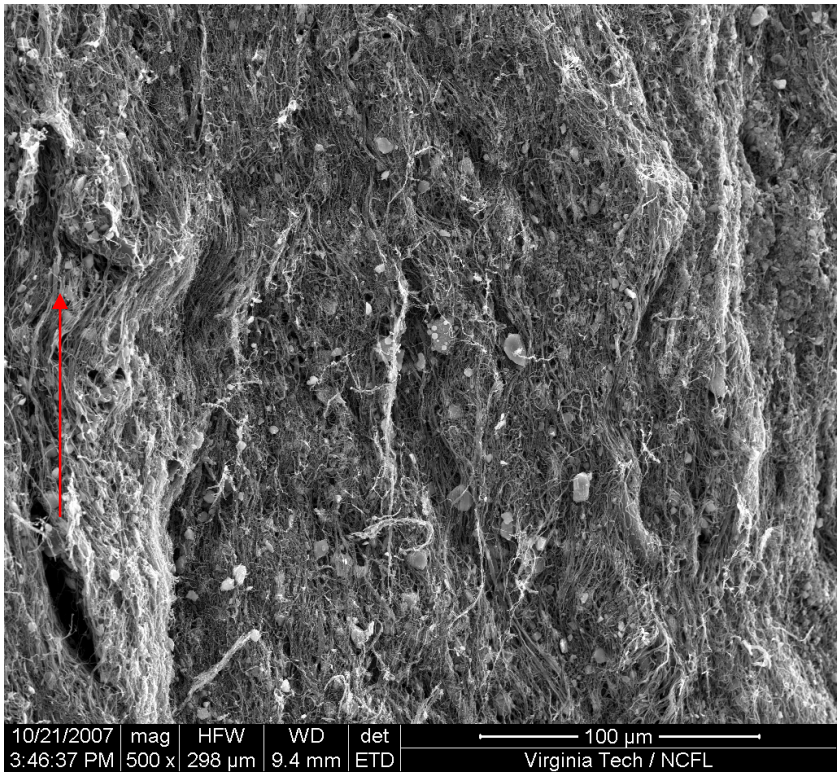

Figure C-108: ARI-2750 Specimen T13 Location B (500x)

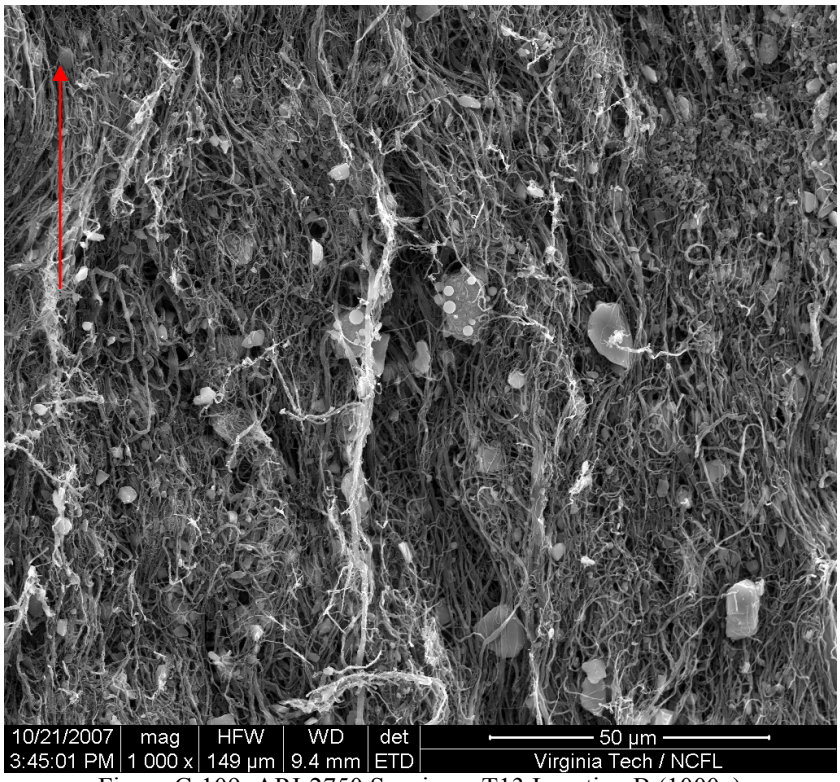

Figure C-109: ARI-2750 Specimen T13 Location B (1000x)

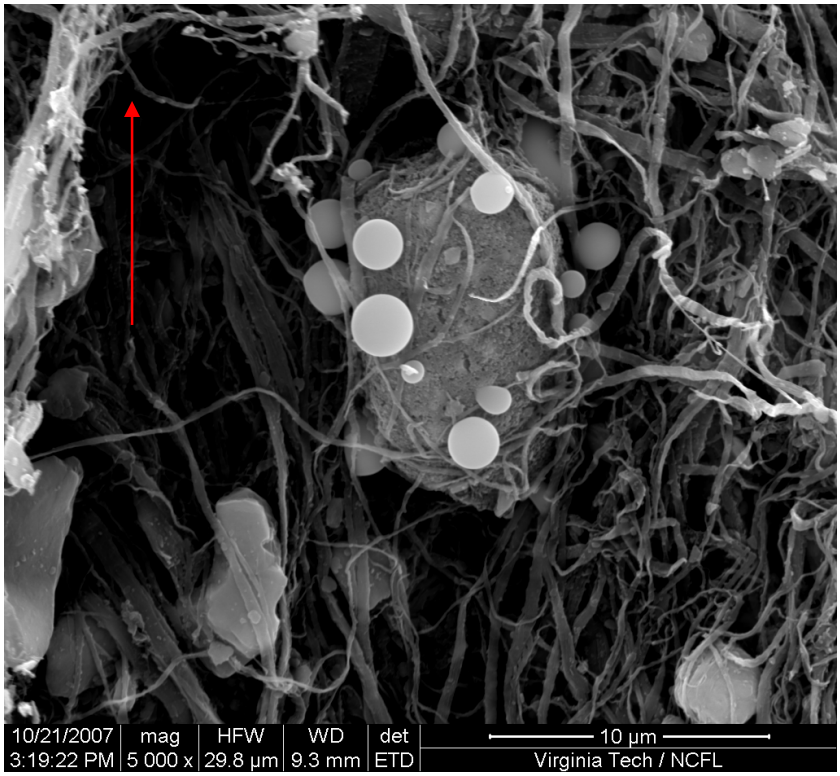

Figure C-110: ARI-2750 Specimen T13 Location B (5000x)

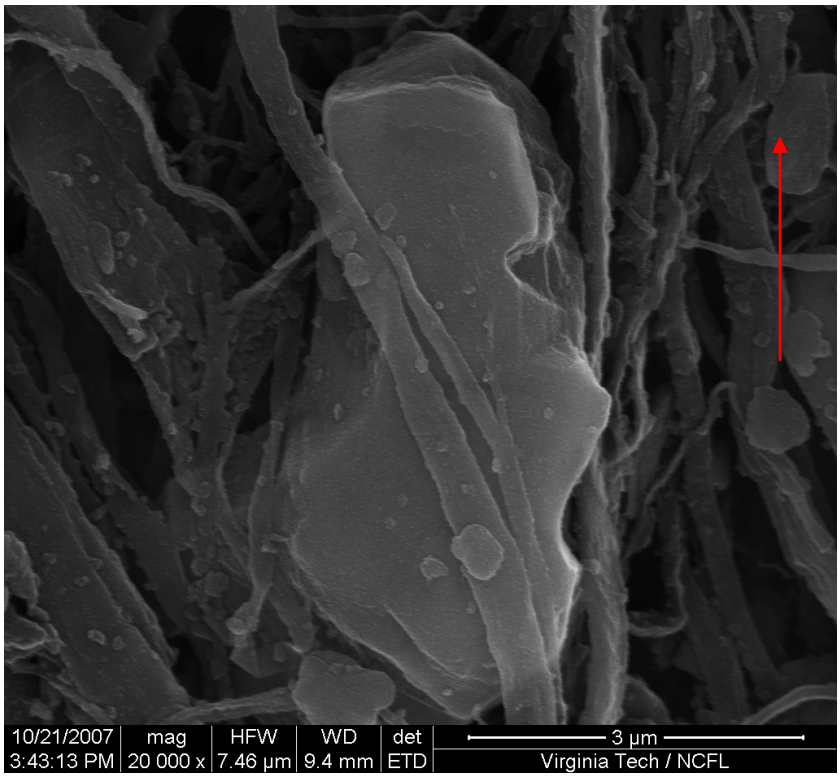

Figure C-111: ARI-2750 Specimen T13 Location B (20kx)

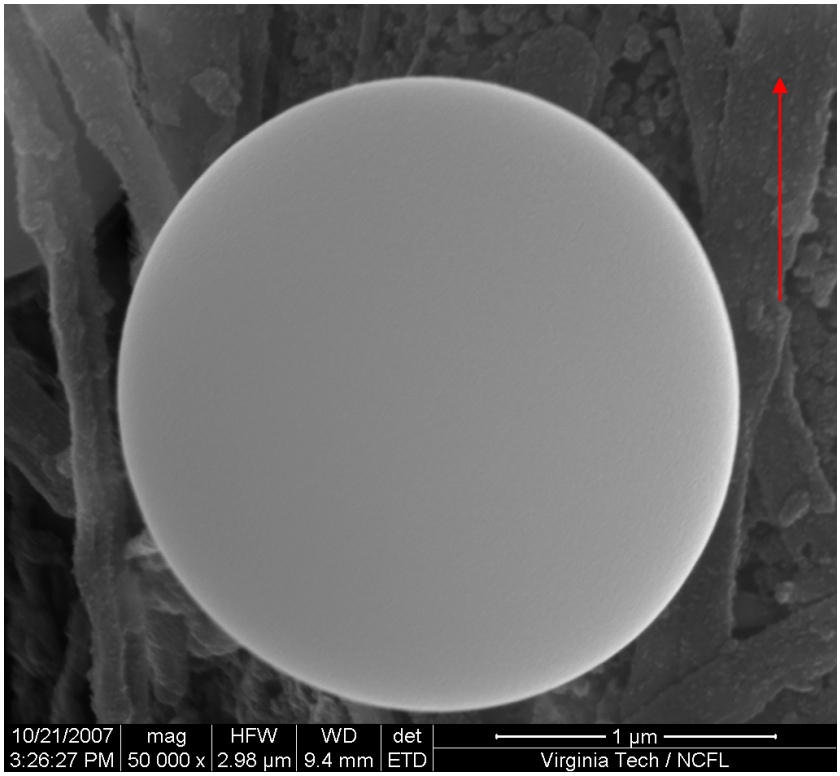

Figure C-112: ARI-2750 Specimen T13 Location B (50kx)

ISM-Charred ARI-2750 Micrographs

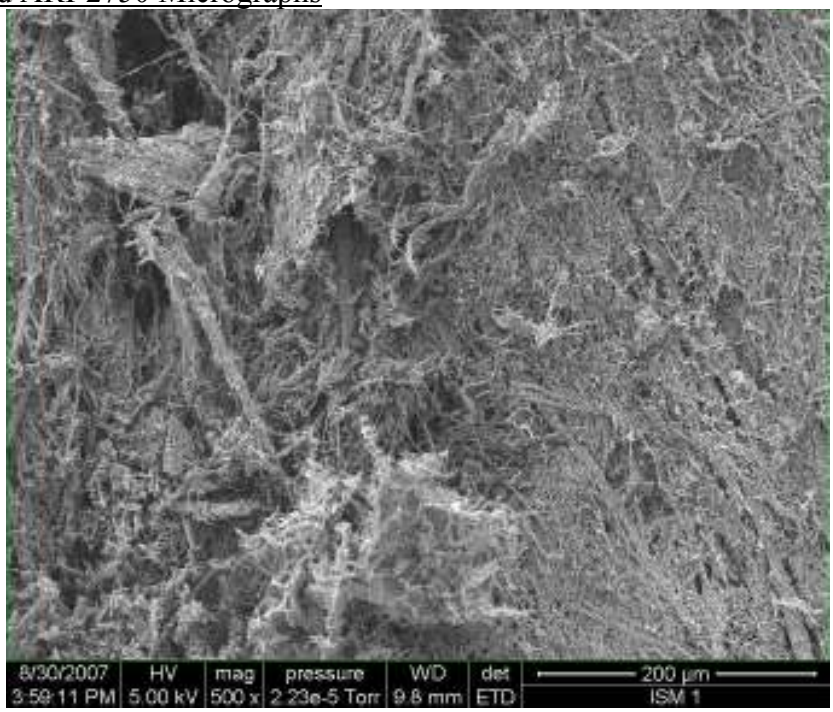


Figure C-113: ISM-Charred ARI-2750 Specimen 1 Location A (250x)

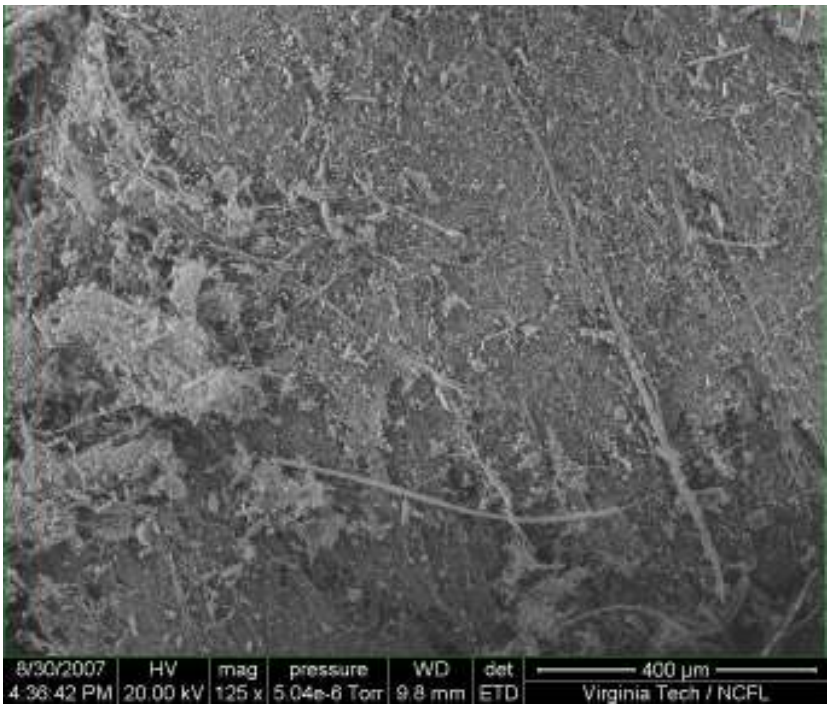


Figure C-114: ISM-Charred ARI-2750 Specimen 1 Location B (125x)

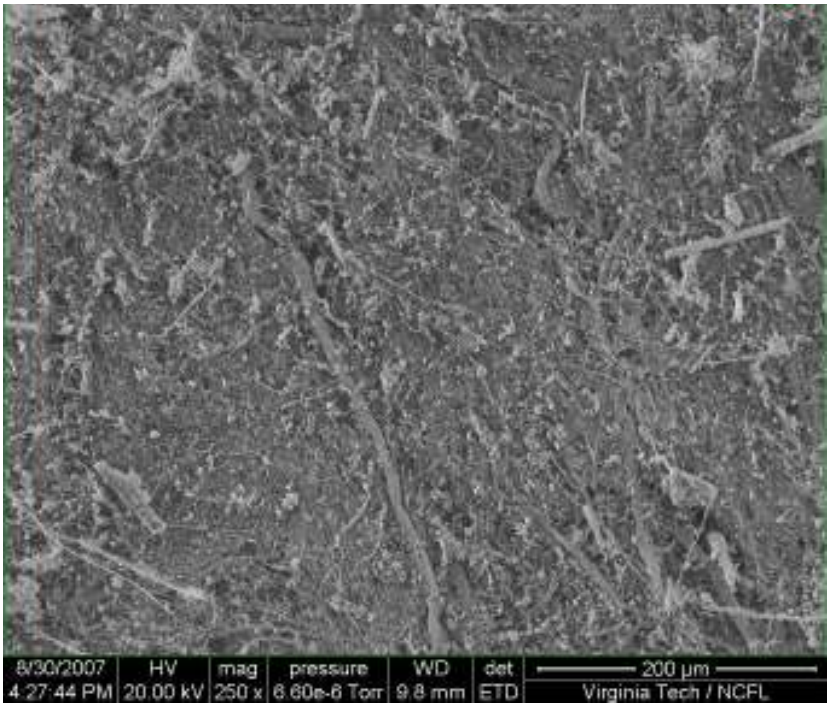

Figure C-115: ISM-Charred ARI-2750 Specimen 1 Location B (250x)

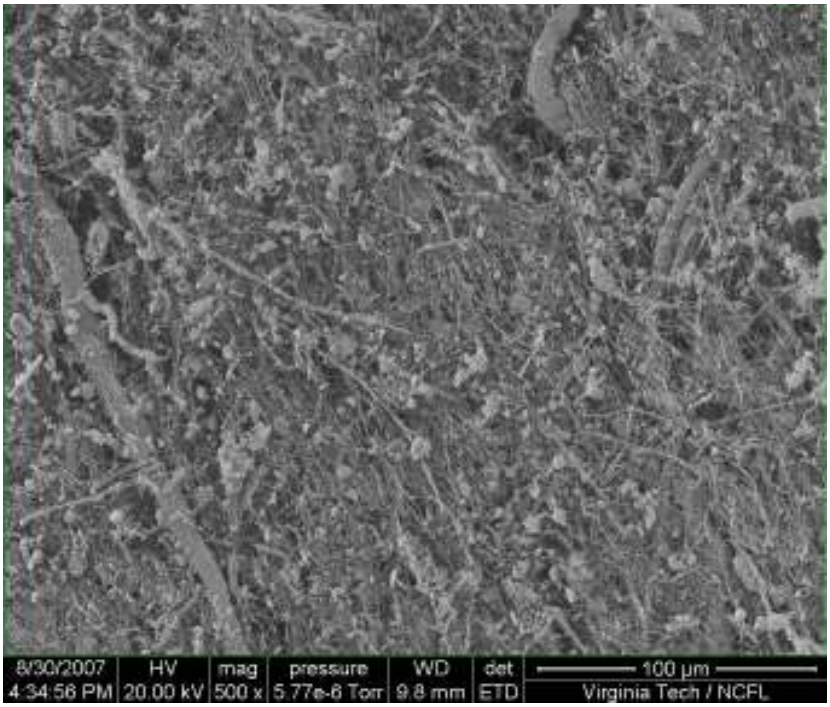

Figure C-116: ISM-Charred ARI-2750 Specimen 1 Location B (500x)

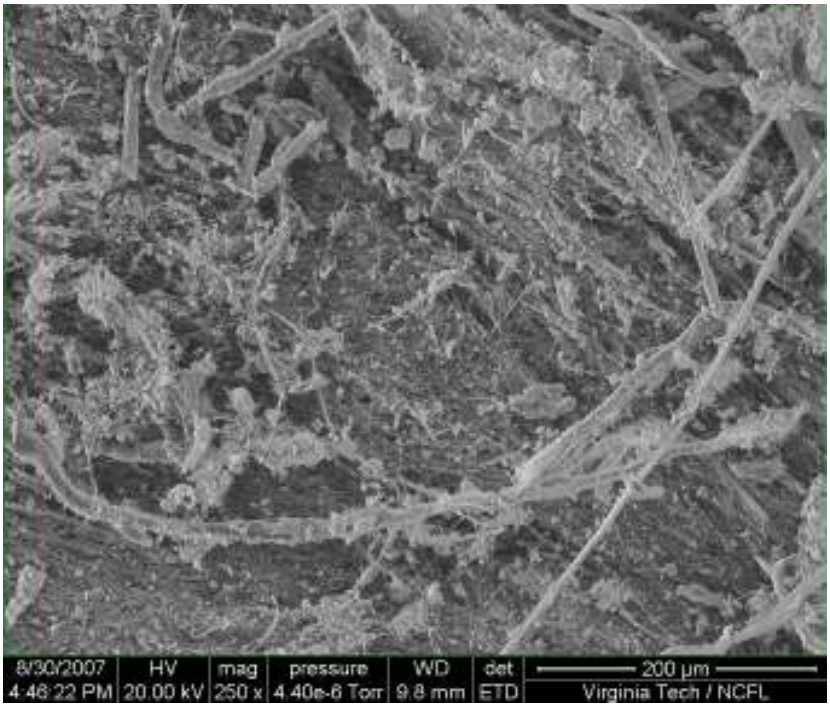

Figure C-117: ISM-Charred ARI-2750 Specimen 2 Location A (250x)

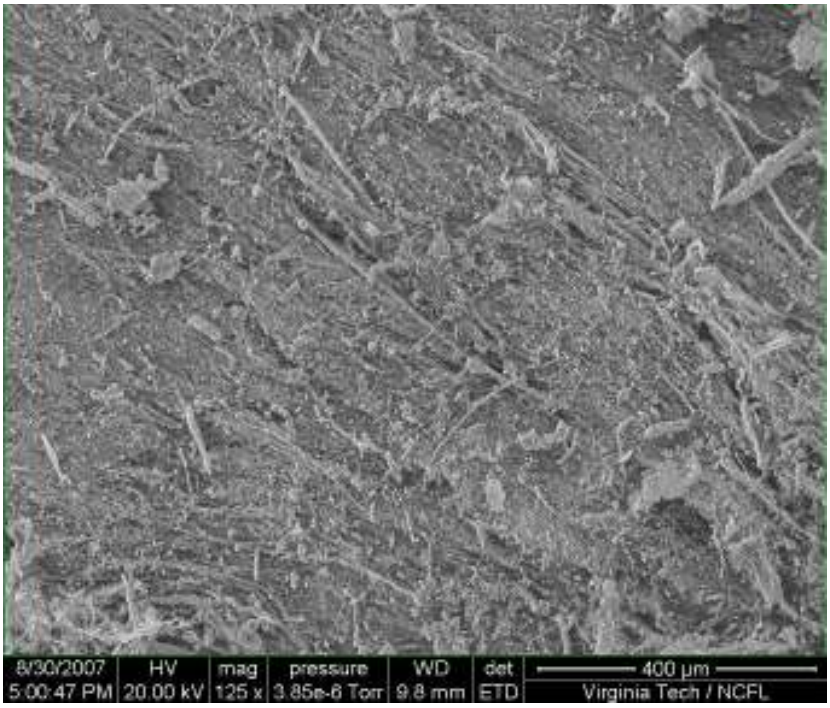

Figure C-118: ISM-Charred ARI-2750 Specimen 2 Location B (125x)

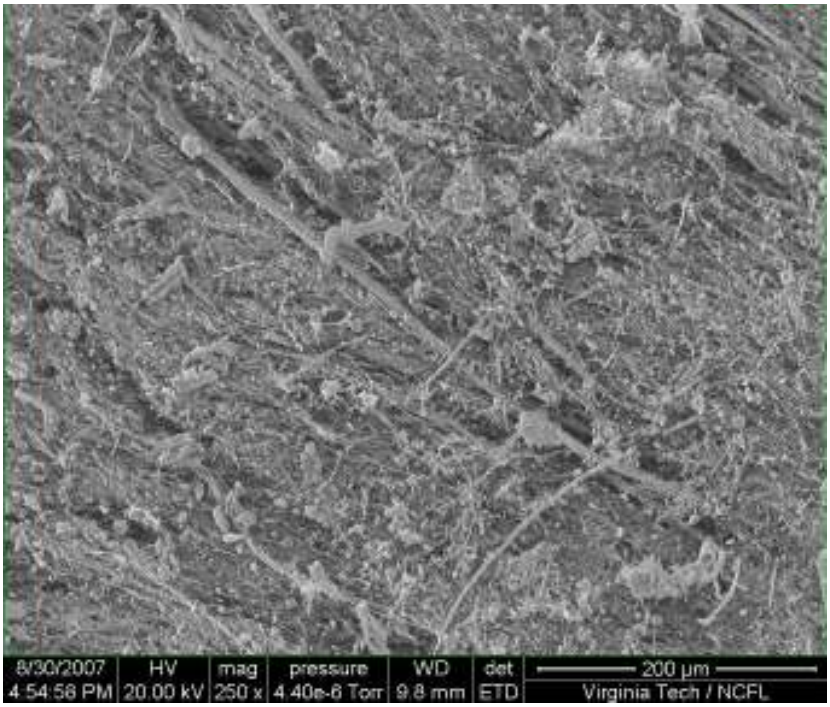

Figure C-119: ISM-Charred ARI-2750 Specimen 2 Location B (250x)

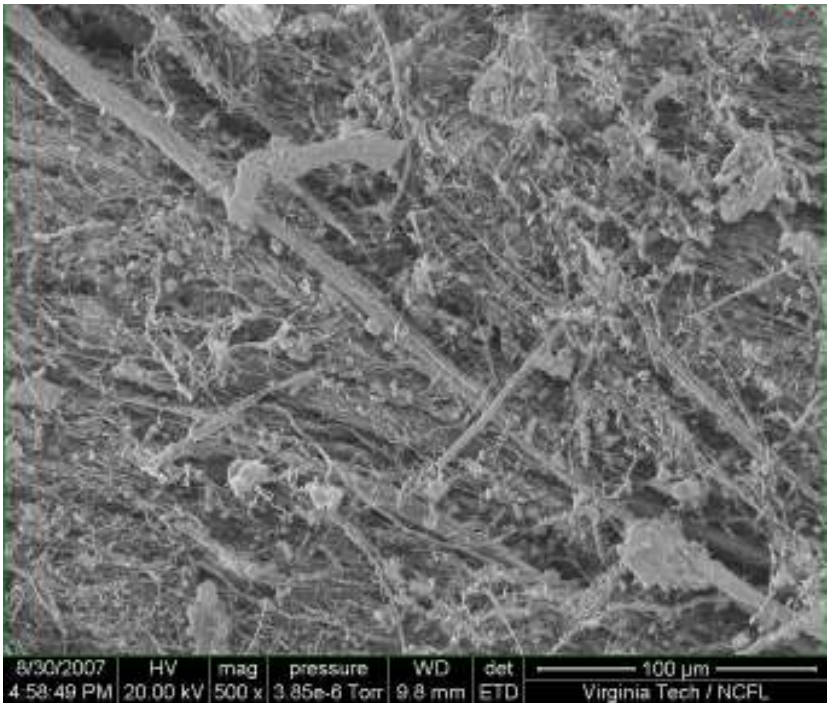

Figure C-120: ISM-Charred ARI-2750 Specimen 2 Location B (500x)

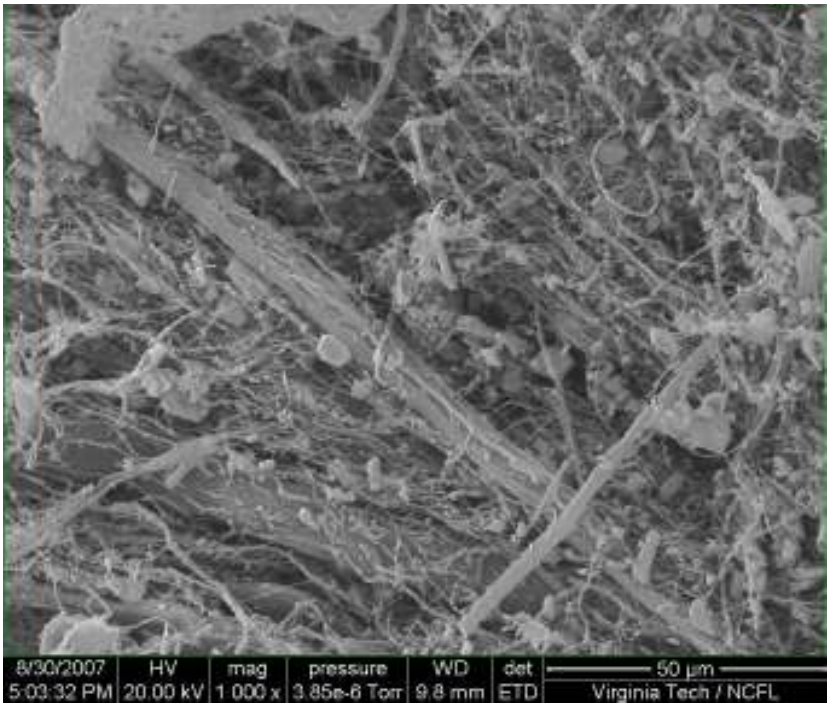

Figure C-121: ISM-Charred ARI-2750 Specimen 2 Location B (1000x)

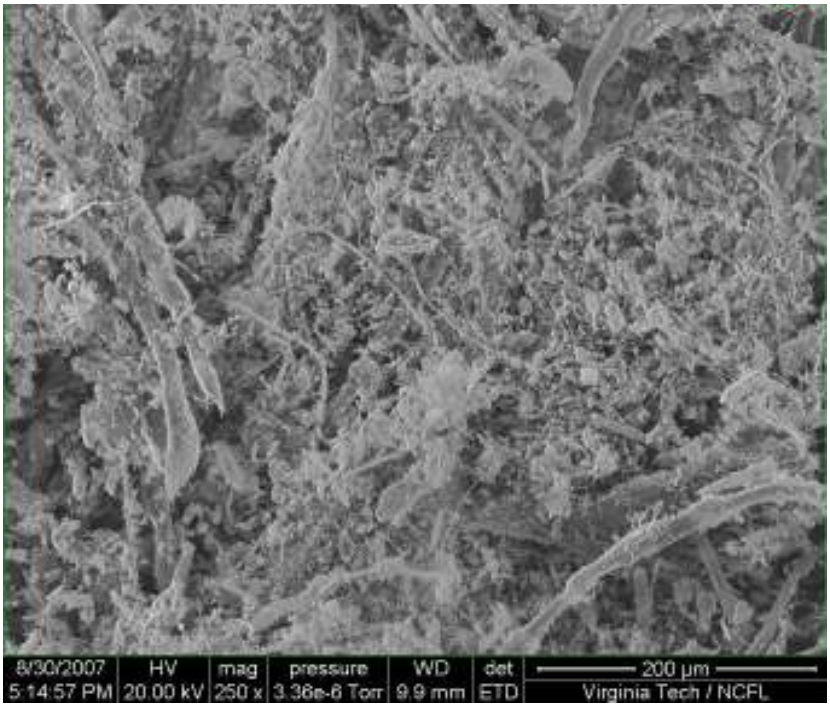

Figure C-122: ISM-Charred ARI-2750 Specimen 3 Location A (250x)

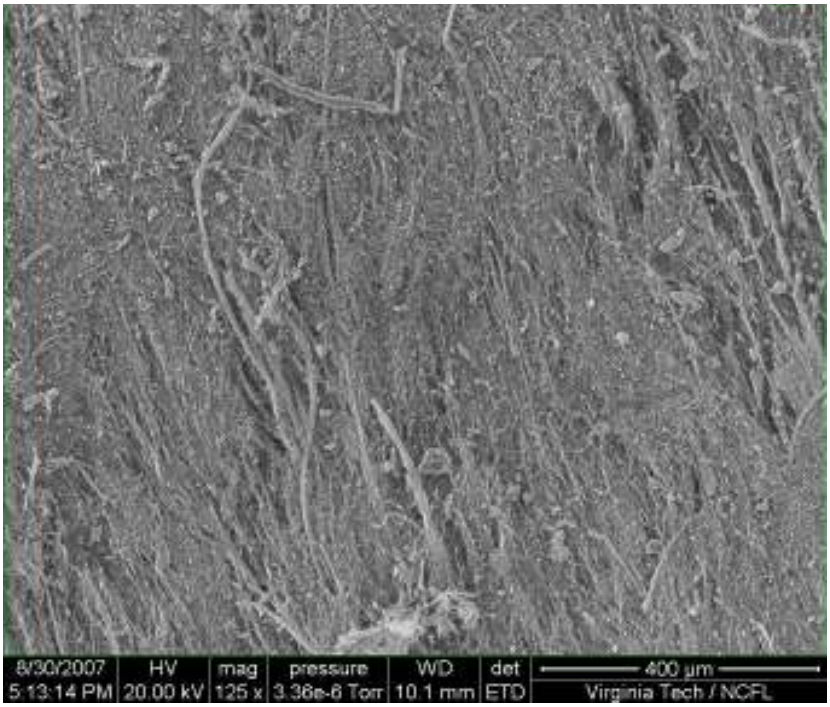

Figure C-123: ISM-Charred ARI-2750 Specimen 3 Location B (125x)

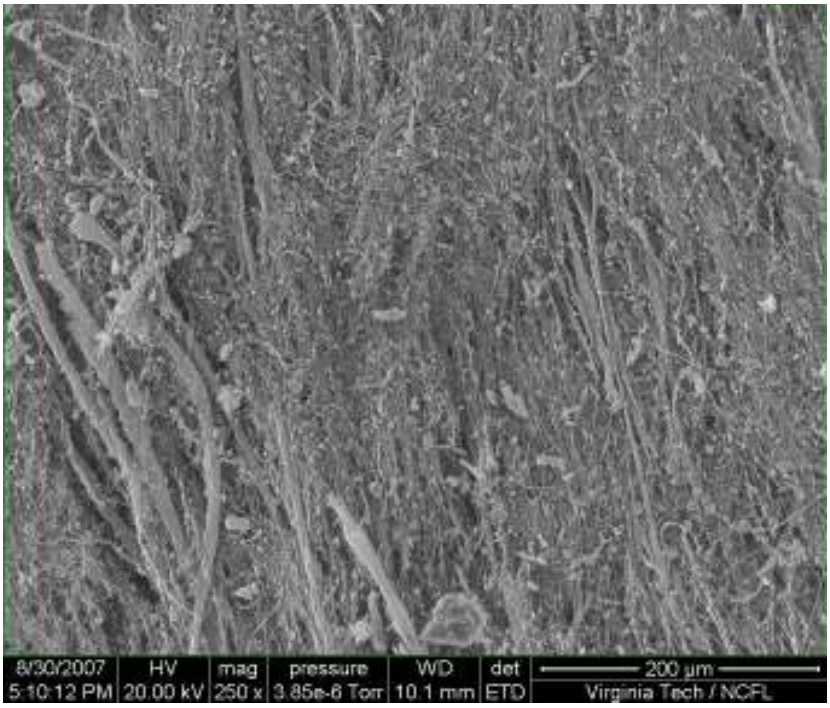

Figure C-124: ISM-Charred ARI-2750 Specimen 3 Location B (250x)

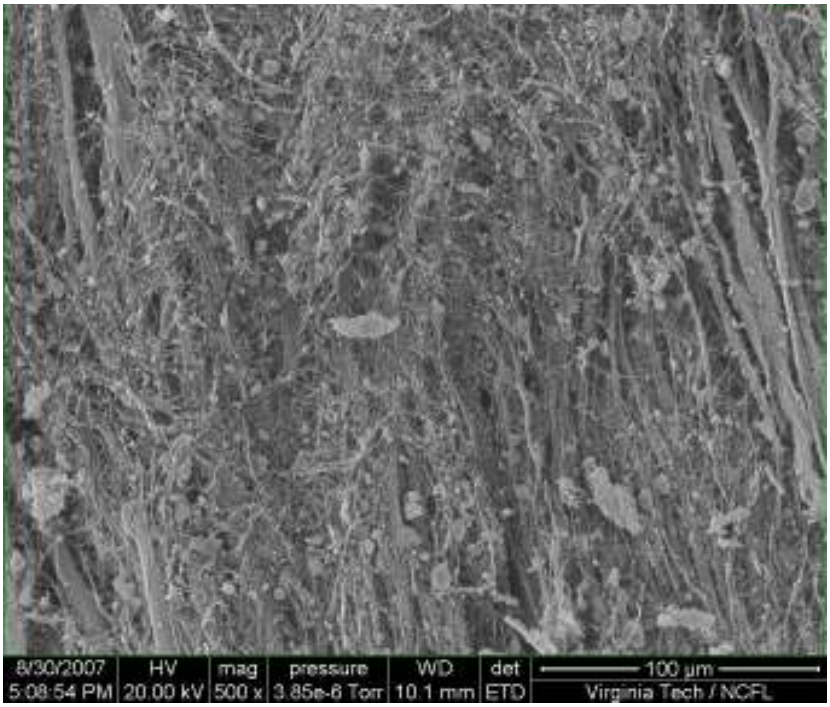

Figure C-125: ISM-Charred ARI-2750 Specimen 3 Location B (500x)

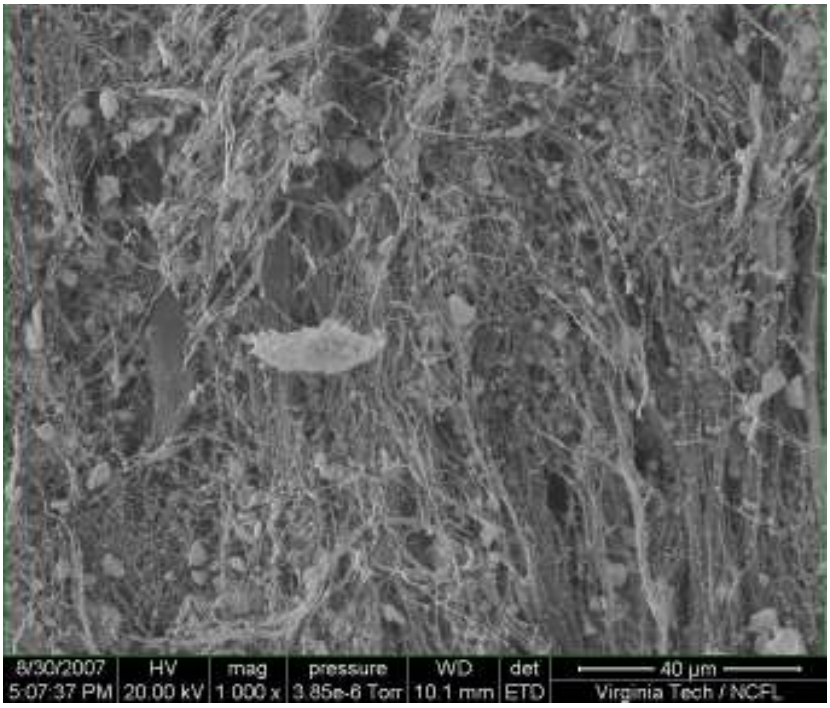

Figure C-126: ISM-Charred ARI-2750 Specimen 3 Location B (1000x)

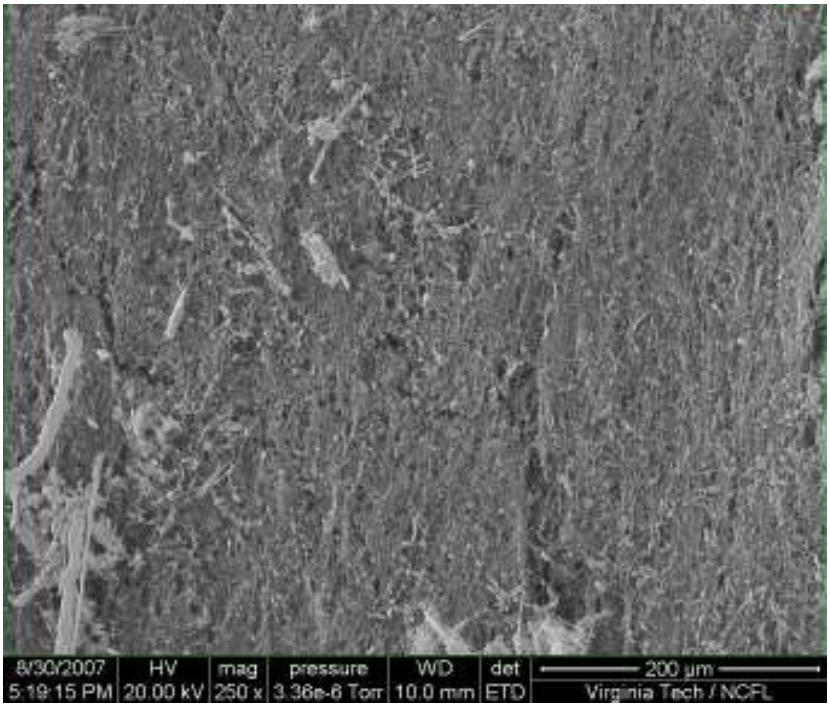

Figure C-127: ISM-Charred ARI-2750 Specimen 4 Location A (250x)

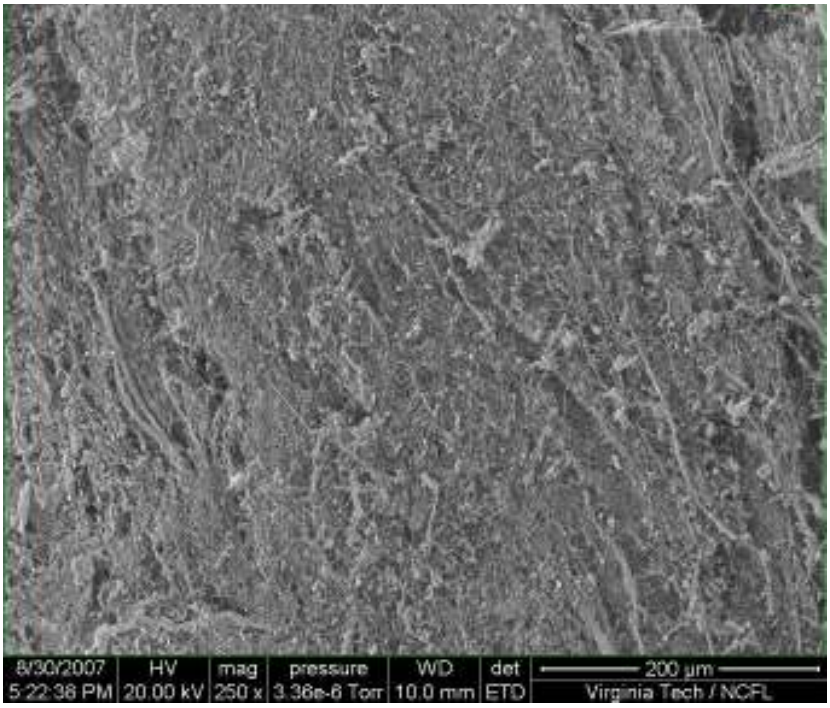

Figure C-128: ISM-Charred ARI-2750 Specimen 4 Location B (250x)

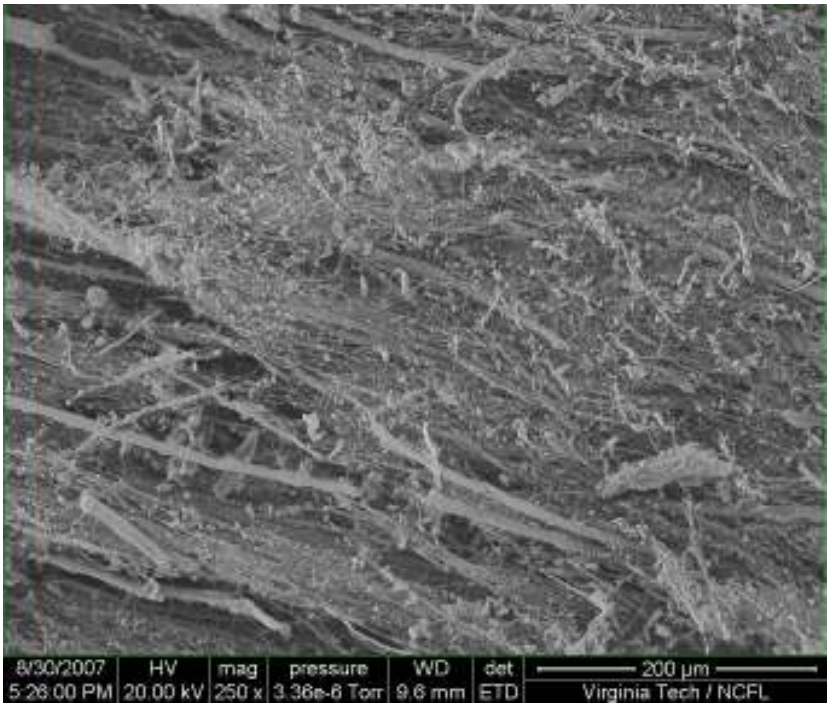

Figure C-129: ISM-Charred ARI-2750 Specimen 5 Location A (250x)

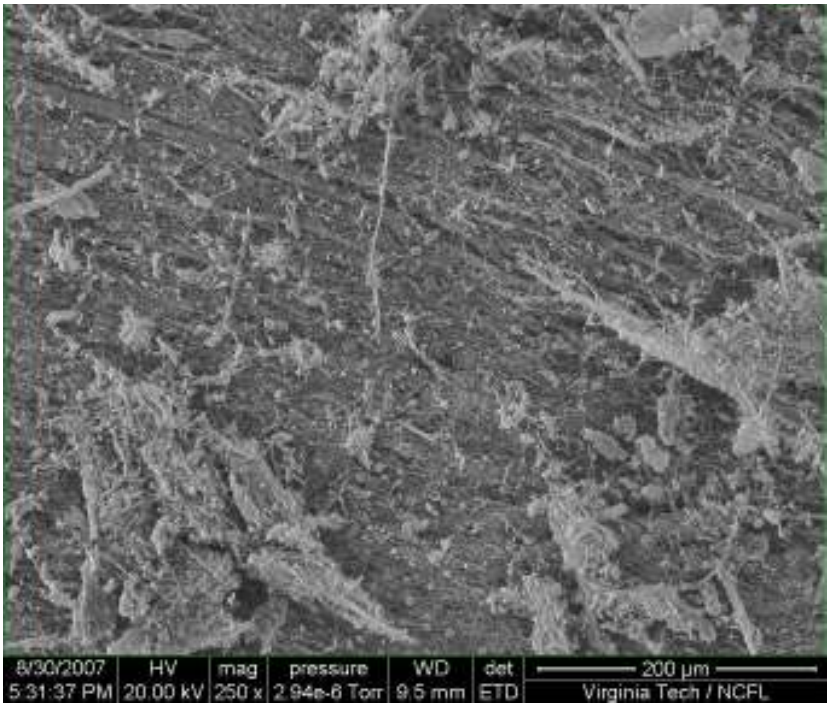

Figure C-130: ISM-Charred ARI-2750 Specimen 5 Location B (250x)

Virgin ARI-2718 Micrographs

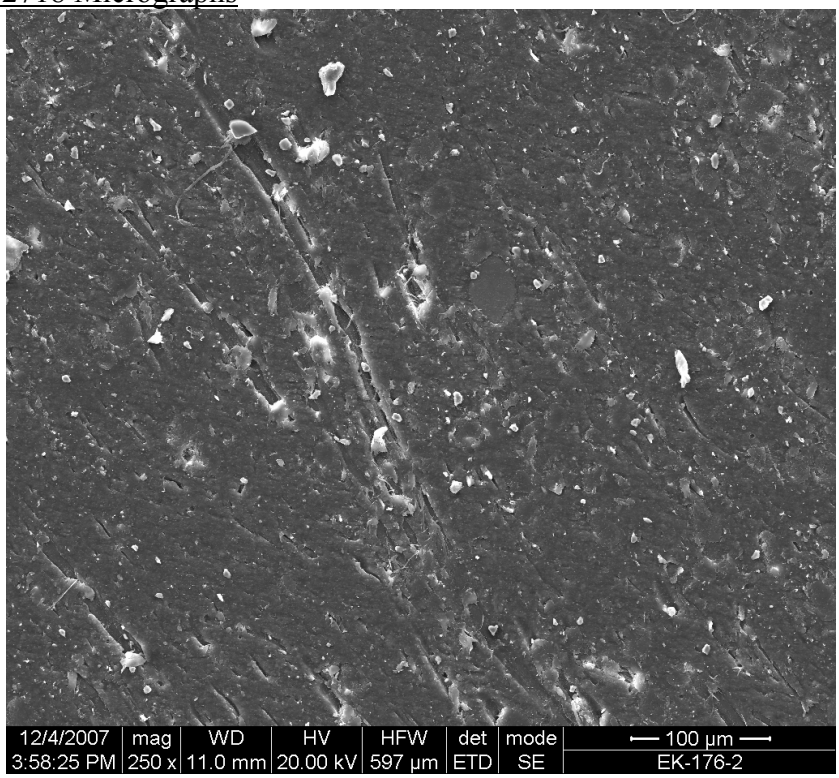

Figure C-131: Virgin ARI-2718 Location A (250x)

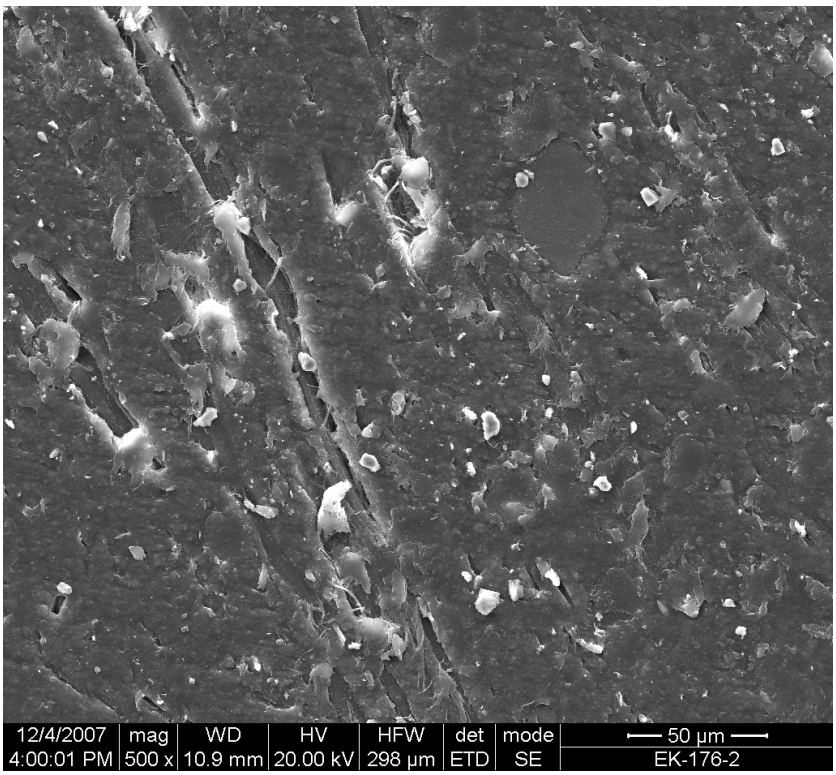

Figure C-132: Virgin ARI-2718 Location A (500x)

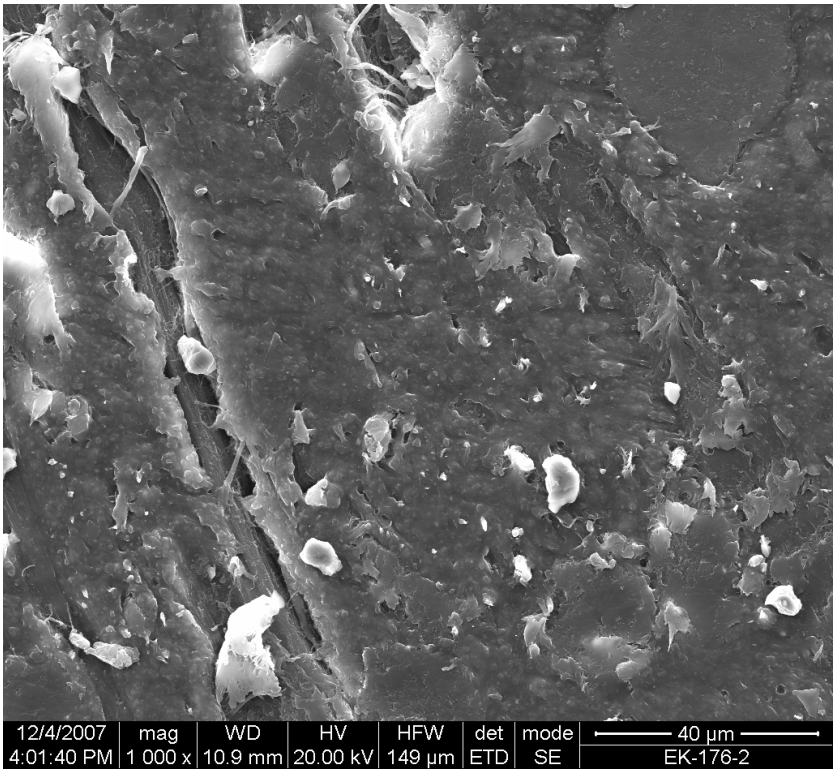

Figure C-133: Virgin ARI-2718 Location A (1000x)

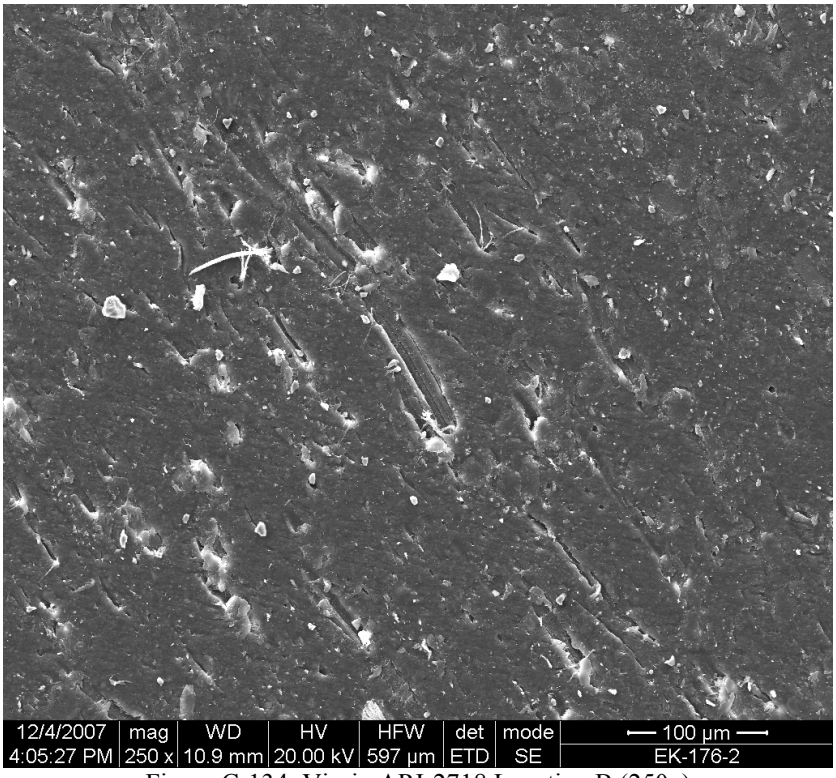

Figure C-134: Virgin ARI-2718 Location B (250x)

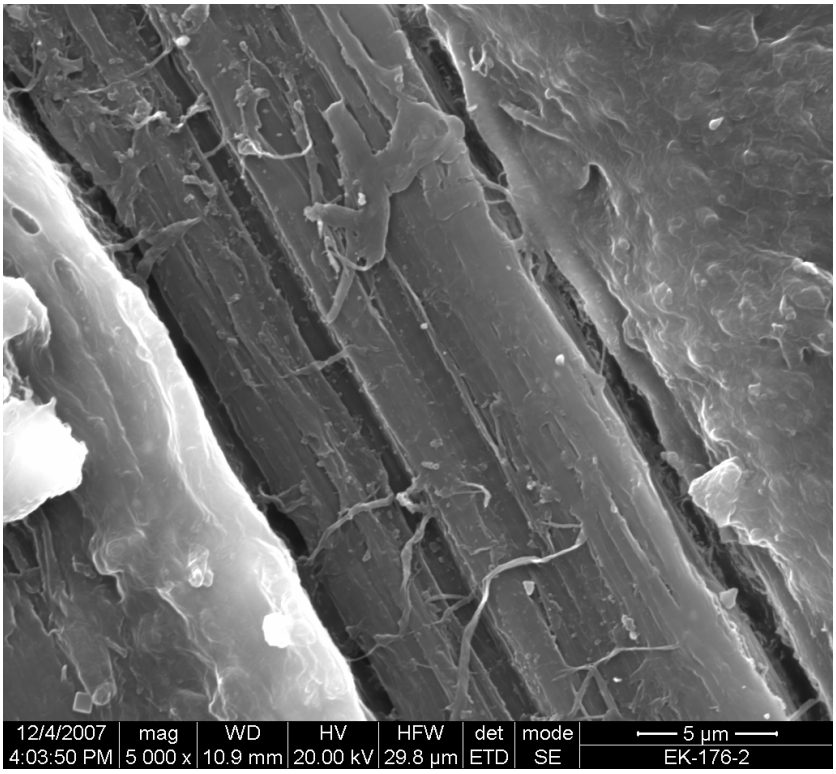

Figure C-135: Virgin ARI-2718 Location B (5000x)

Virgin ARI-2719 Micrographs

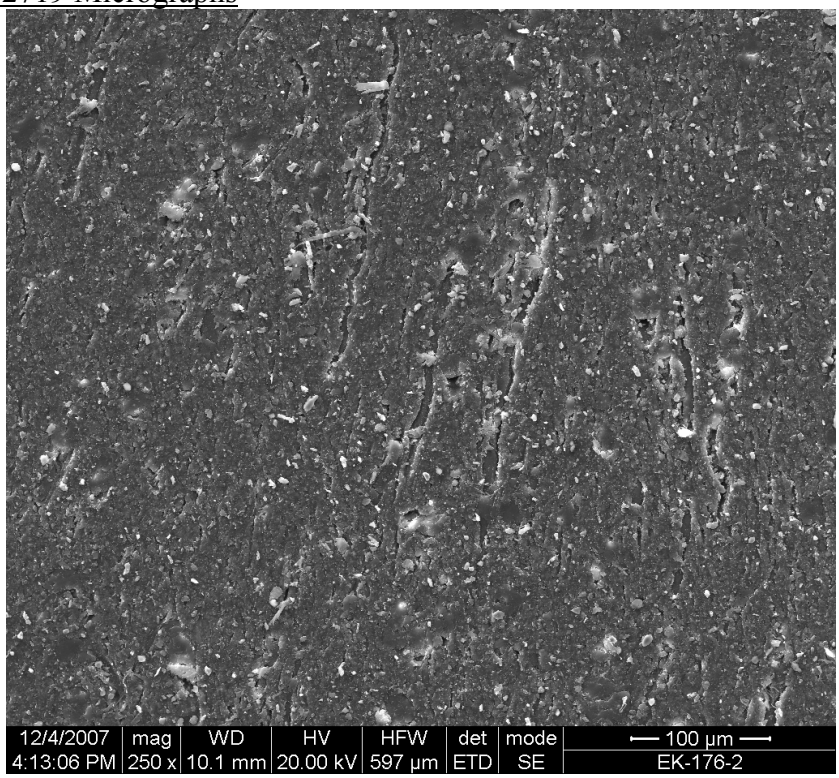

Figure C-136: Virgin ARI-2719 Location A (250x)

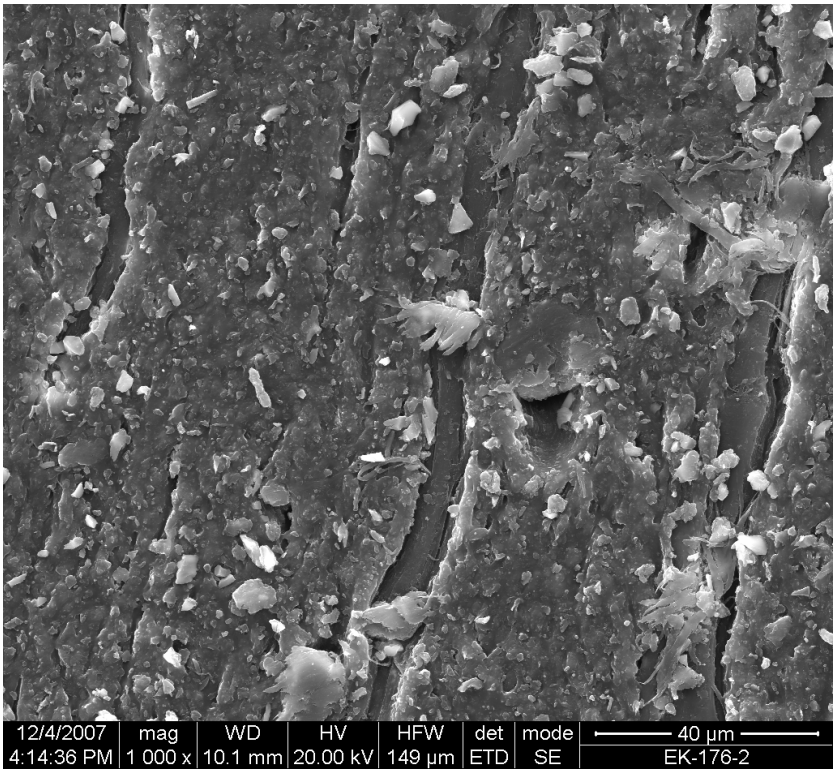

Figure C-137: Virgin ARI-2719 Location A (1000x)

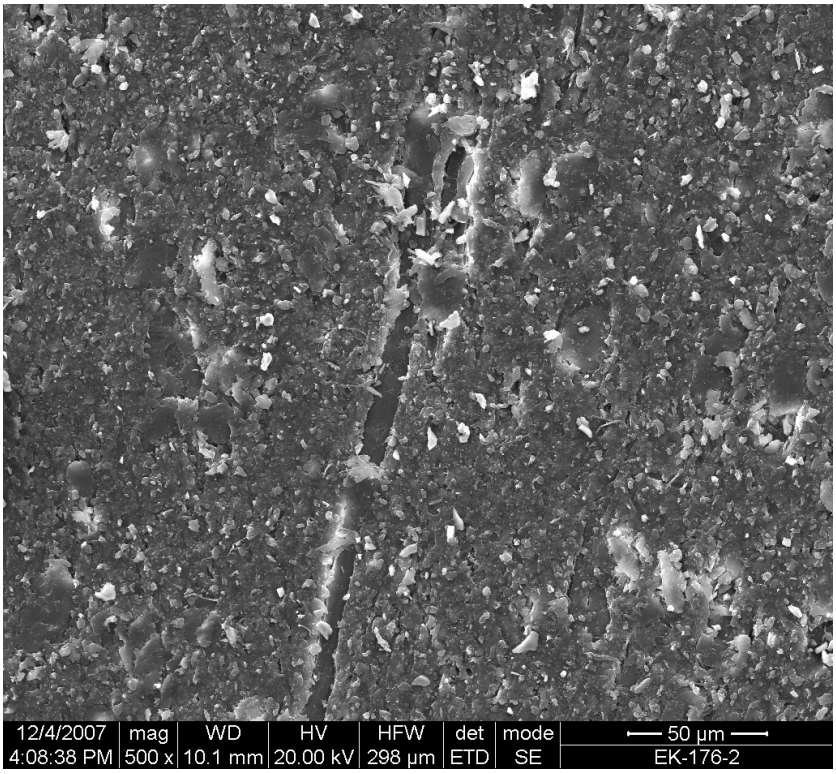

Figure C-138: Virgin ARI-2719 Location B (500x)

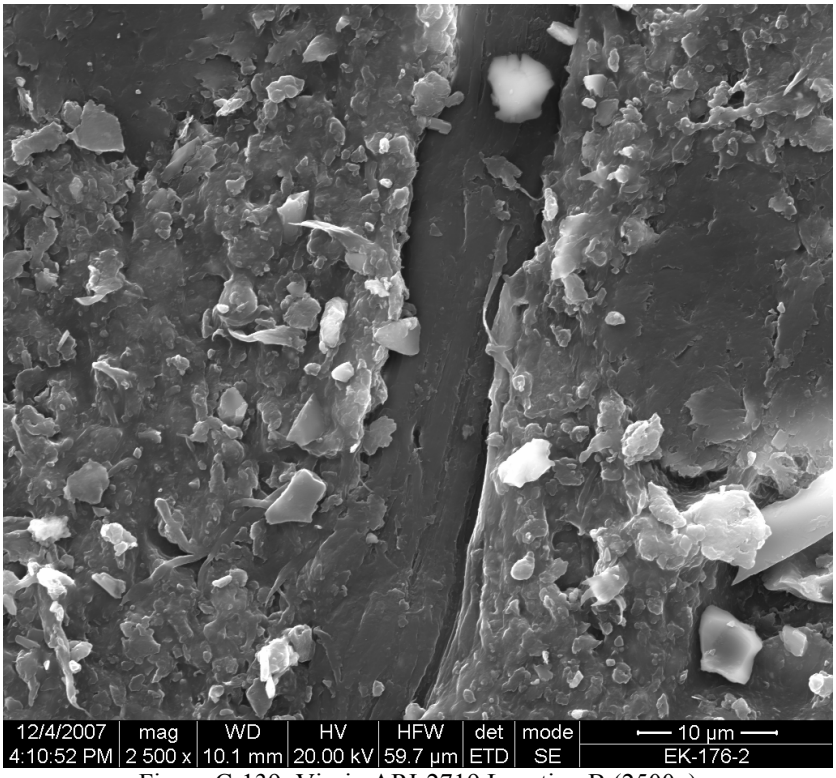

Figure C-139: Virgin ARI-2719 Location B (2500x)

Virgin ARI-2732 Micrographs

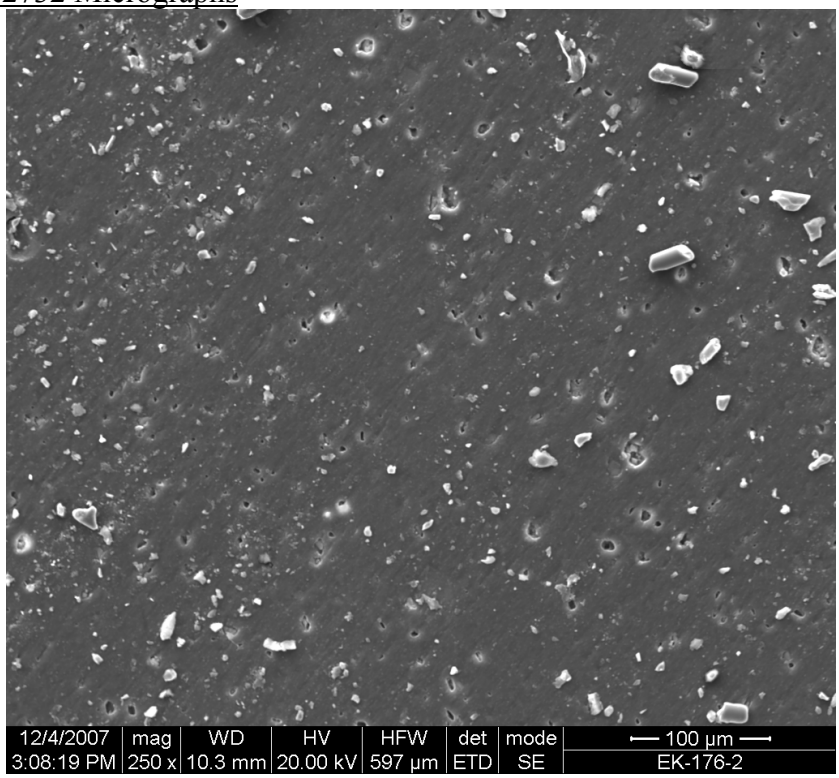


Figure C-140: Virgin ARI-2732 Location A (250x)

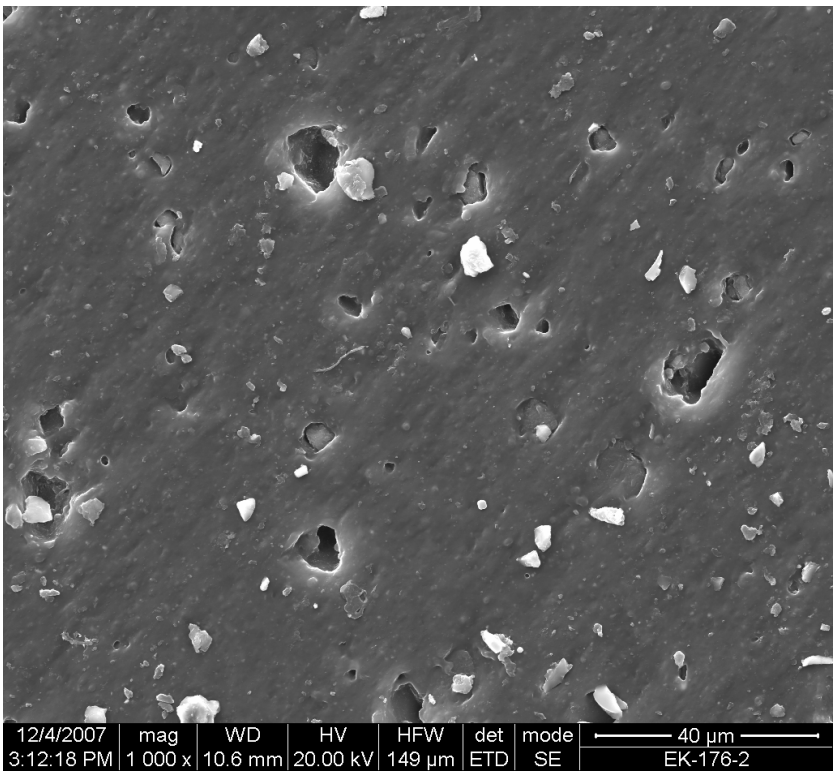


Figure C-141: Virgin ARI-2732 Location B (1000x)

Virgin ARI-2750 Micrographs

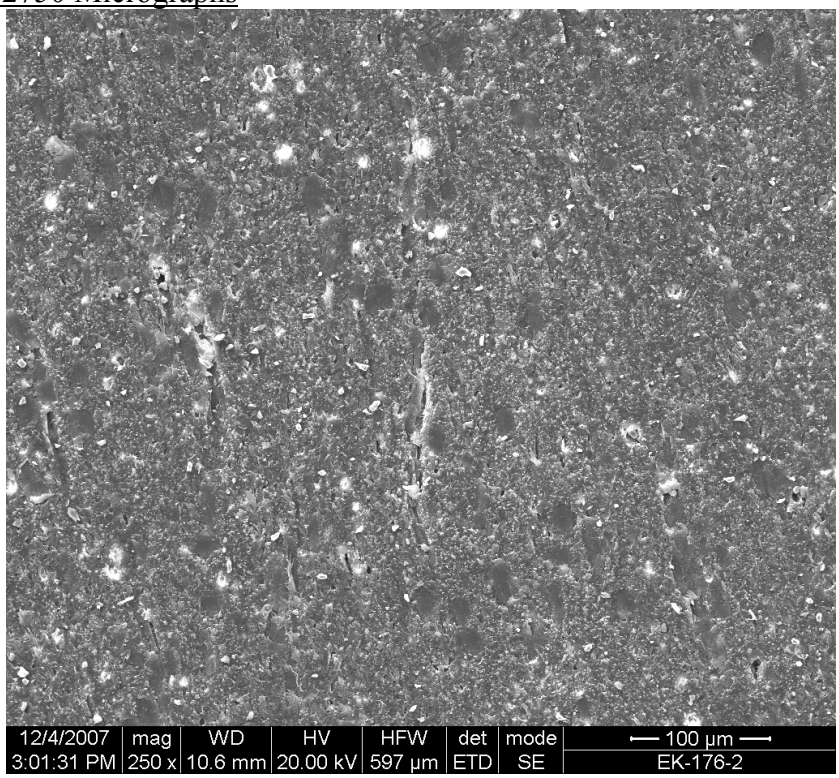


Figure C-142: Virgin ARI-2750 Location A (250x)

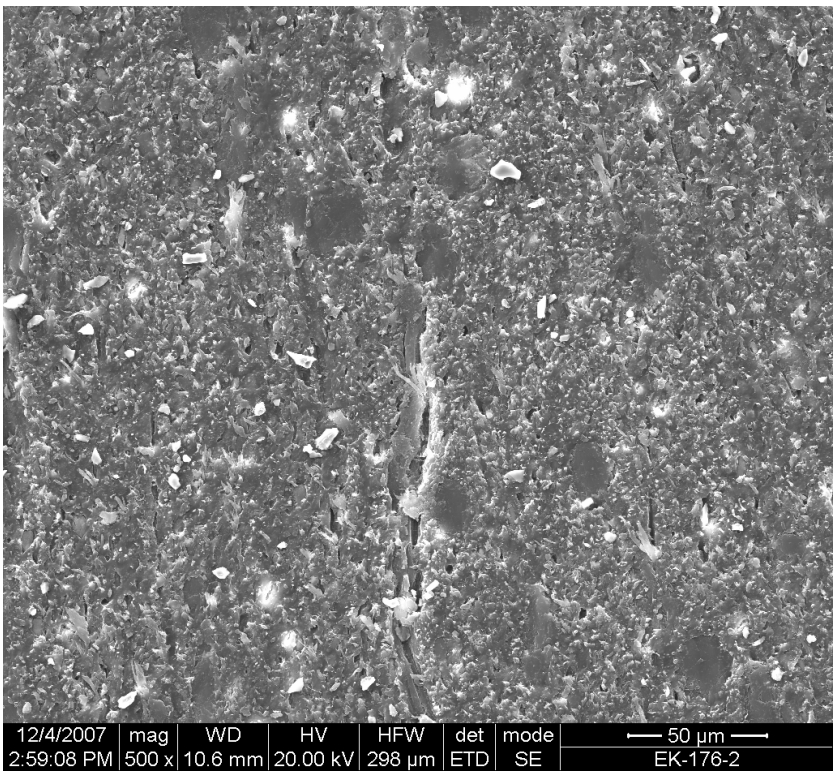


Figure C-143: Virgin ARI-2750 Location A (500x)

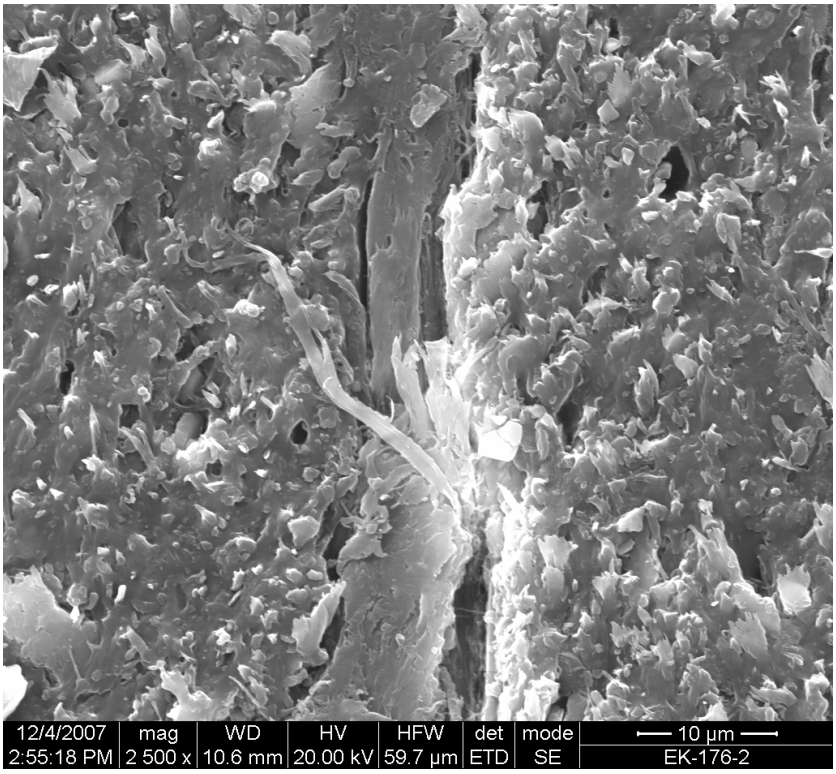

Figure C-144: Virgin ARI-2750 Location A (2500x)

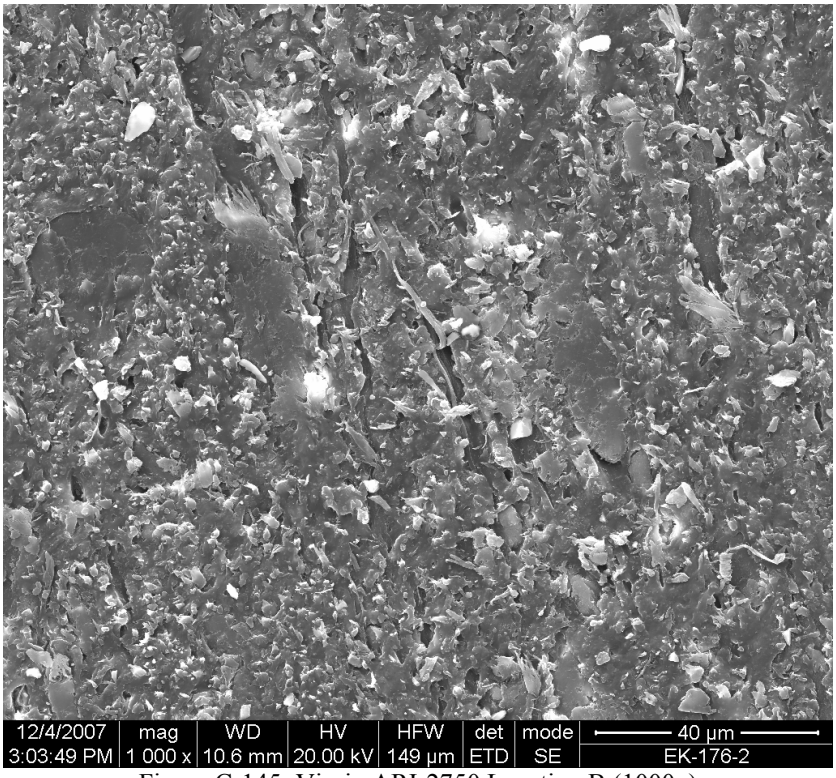

Figure C-145: Virgin ARI-2750 Location B (1000x)

# Appendix D: Complete Shear Testing Results

The following tables and figure present the measurements and data for all specimens tested in this work, except for those tested on the DMA prior to recalibration. Samples are identified first by their four-digit numerical designation, then by "L" or "T" for longitudinal or transverse, and finally the number of the specimen of those conditions (for example, 2718-L26 would be the 26$^{th}$ specimen of ARI-2718 tested longitudinally to the nominal orientation direction). Samples whose data is in italics were deemed unfit for including in the above calculations and were edited out. The notes column contains short factors noticed before, during, or after testing and may relate to why individual specimens were edited out.

ARI-2718 Results

Table D-1: ARI-2718 Longitudinal Shear Test Data

| Sample | Failure Load, N | l, mm | w, mm | h, mm | t, mm | $\tau$, Pa | Notes |
|---|---|---|---|---|---|---|---|
| 2718-L14 | 4.18 | 11.79 | 6.70 | 8.87 | 2.07 | 171.4 | |
| 2718-L15 | 0.808 | 11.31 | 6.60 | 9.06 | 2.04 | 35.0 | |
| 2718-L16 | 2.82 | 11.96 | 6.63 | 8.72 | 1.87 | 125.9 | |
| 2718-L17 | 1.089 | 10.32 | 6.62 | 9.10 | 2.15 | 49.1 | |
| 2718-L19 | 1.014 | 11.67 | 6.62 | 9.02 | 1.94 | 44.8 | |
| 2718-L20 | 1.557 | 11.38 | 6.57 | 8.81 | 1.99 | 68.8 | |
| 2718-L21 | 0.301 | 11.40 | 6.57 | 8.83 | 2.08 | 12.69 | Slight warp |
| 2718-L22 | *9.49* | *11.47* | *6.94* | *9.52* | *2.13* | *388* | *Outlier* |
| 2718-L23 | *10.72* | *11.76* | *6.94* | *9.36* | *2.20* | *414* | *Outlier* |
| 2718-L24 | 1.331 | 11.11 | 6.72 | 9.38 | 2.13 | 56.2 | |
| 2718-L25 | 3.97 | 12.24 | 6.63 | 9.43 | 2.18 | 148.9 | |
| 2718-L26 | *5.56* | *11.53* | *6.67* | *9.38* | *2.30* | *210* | *Broke wrong* |
| 2718-L27 | *5.33* | *11.73* | *6.74* | *9.50* | *2.05* | *222* | *Broke wrong* |
| 2718-L28 | 0.936 | 11.92 | 6.67 | 9.50 | 2.05 | 38.3 | Slight warp |
| 2718-L29 | 0.969 | 11.87 | 6.63 | 9.36 | 2.03 | 40.2 | |
| 2718-L30 | 1.746 | 11.10 | 6.72 | 9.37 | 2.03 | 77.5 | |
| 2718-L31 | 2.10 | 11.41 | 6.78 | 9.51 | 2.11 | 87.0 | |
| 2718-L32 | *5.25* | *11.51* | *6.76* | *9.47* | *2.14* | *213* | *Broke wrong* |

Table D-2: ARI-2718 Longitudinal Shear Test Edited Results

| | Failure Load, N | l, mm | w, mm | h, mm | t, mm | τ, Pa |
|---|---|---|---|---|---|---|
| Mean | 1.727 | 11.54 | 6.65 | 9.12 | 2.05 | 75.8 |
| Median | 1.210 | 11.67 | 6.63 | 9.06 | 2.05 | 56.2 |
| Standard Deviation | 1.259 | 0.526 | 0.0655 | 0.292 | 0.0852 | 50.8 |
| Coefficient of Variation | 0.729 | 0.0456 | 0.00985 | .0320 | 0.0415 | .670 |

Table D-3: ARI-2718 Longitudinal Shear Test Unedited Results

| | Failure Load, N | l, mm | w, mm | h, mm | t, mm | τ, Pa |
|---|---|---|---|---|---|---|
| Mean | 3.29 | 11.53 | 6.70 | 9.23 | 2.08 | 133.5 |
| Median | 1.921 | 11.52 | 6.67 | 9.37 | 2.08 | 82.3 |
| Standard Deviation | 3.02 | 0.425 | 0.1085 | 0.279 | 0.0992 | 118.3 |
| Coefficient of Variation | 0.918 | 0.0369 | 0.01621 | 0.03 | 0.0476 | 0.886 |

Table D-4: ARI-2718 Transverse Shear Test Data

| Sample | Failure load, N | l, mm | w, mm | h, mm | t, mm | τ, Pa | Notes |
|---|---|---|---|---|---|---|---|
| 2718-T13 | 1.489 | 11.50 | 6.59 | 8.74 | 1.92 | 67.4 | Slight warp |
| 2718-T15 | 1.755 | 9.56 | 6.60 | 8.64 | 1.89 | 97.2 | |
| 2718-T16 | 1.659 | 10.17 | 6.64 | 8.43 | 1.55 | 105.3 | |
| 2718-T17 | *2.42* | *10.32* | *6.68* | *8.79* | *2.19* | *107.0* | *Broke wrong* |
| 2718-T18 | *1.074* | *12.62* | *6.64* | *8.67* | *1.84* | *46.3* | *Broke wrong* |
| 2718-T19 | *1.083* | *11.14* | *6.65* | *8.73* | *3.17* | *30.7* | *Thick gauge, slight warp, broke wrong* |
| 2718-T20 | *1.150* | *11.25* | *6.41* | *8.80* | *3.16* | *32.4* | *Thick gauge, slight warp, broke wrong* |
| 2718-T23 | *5.35* | *10.55* | *6.73* | *9.54* | *2.14* | *237* | *Broke wrong* |
| 2718-T24 | .920 | 11.13 | 6.74 | 9.62 | 2.03 | 40.7 | |
| 2718-T25 | 2.05 | 11.75 | 6.92 | 9.61 | 2.22 | 78.6 | Slight warp |
| 2718-T26 | 0.679 | 12.07 | 6.81 | 9.54 | 2.03 | 27.7 | Slight warp |
| 2718-T27 | *8.79* | *11.41* | *6.86* | *9.68* | *2.06* | *374* | *Oxygen?* |
| 2718-T28 | *0.937* | *9.92* | *7.02* | *9.68* | *2.17* | *43.5* | *Warped, broke wrong* |
| 2718-T29 | *5.83* | *11.50* | *6.73* | *9.53* | *2.05* | *247* | *Broke wrong* |
| 2718-T30 | *5.96* | *11.55* | *6.82* | *9.63* | *2.03* | *254* | *Broke wrong* |
| 2718-T31 | *10.23* | *11.70* | *6.86* | *9.71* | *2.11* | *414* | *Broke wrong* |
| 2718-T32 | *11.05* | *11.58* | *6.84* | *9.63* | *1.98* | *482* | *Oxygen?* |

Table D-5: ARI-2718 Transverse Shear Test Edited Results

| | Failure Load, N | l, mm | w, mm | h, mm | t, mm | τ, Pa |
|---|---|---|---|---|---|---|
| Mean | 1.425 | 11.03 | 6.72 | 9.10 | 1.940 | 69.5 |
| Median | 1.574 | 11.32 | 6.69 | 9.14 | 1.975 | 73.0 |
| Standard Deviation | 0.524 | 0.973 | 0.1313 | 0.550 | 0.223 | 30.7 |
| Coefficient of Variation | 0.367 | 0.0882 | 0.01954 | 0.0605 | 0.1152 | 0.442 |

Table D-6: ARI-2718 Transverse Shear Test Unedited Results

| | Failure Load, N | l, mm | w, mm | h, mm | t, mm | τ, Pa |
|---|---|---|---|---|---|---|
| Mean | 3.67 | 11.29 | 6.73 | 9.49 | 2.24 | 243 |
| Median | 1.755 | 11.40 | 6.78 | 9.63 | 2.07 | 246 |
| Standard Deviation | 3.51 | 0.423 | 0.1671 | 0.341 | 0.454 | 185 |
| Coefficient of Variation | 0.955 | 0.0375 | 0.0248 | 0.0360 | 0.202 | 0.762 |

## ARI-2719 Results

Table D-7: ARI-2719 Longitudinal Shear Test Data

| Sample | Failure load, N | l, mm | w, mm | h, mm | t, mm | τ, Pa | Notes |
|---|---|---|---|---|---|---|---|
| 2719-L8 | *15.14* | *11.76* | *7.77* | *10.50* | *1.83* | *704* | *Bubbling, slight warp, broke wrong* |
| 2719-L9 | *6.17* | *12.51* | *7.57* | *10.63* | *2.03* | *243* | *Slight warp, broke wrong* |
| 2719-L10 | 14.81 | 12.16 | 7.72 | 10.50 | 2.27 | 537 | |
| 2719-L11 | 5.12 | 12.34 | 7.61 | 10.53 | 1.99 | 208 | |
| 2719-L12 | 11.16 | 12.74 | 7.70 | 10.55 | 1.97 | 445 | |
| 2719-L13 | *21.2* | *11.70* | *7.70* | *10.51* | *1.99* | *908* | *Bubbling, broke wrong* |
| 2719-L14 | 20.4 | 11.64 | 7.62 | 10.73 | 2.05 | 856 | Bubbling, slight warp |
| 2719-L15 | *33.9* | *13.71* | *7.73* | *10.62* | *1.79* | *1381* | *Bubbling, broke wrong* |
| 2719-L16 | 12.37 | 12.80 | 7.74 | 10.51 | 1.91 | 506 | Bubbling, slight warp |
| 2719-L17 | *40.5* | *13.15* | *7.62* | *10.54* | *1.99* | *1548* | *Bubbling, broke wrong* |
| 2719-L18 | 5.27 | 11.37 | 6.83 | 9.48 | 2.18 | 213 | Bubbling |
| 2719-L19 | *1.754* | *11.85* | *7.18* | *9.44* | *2.09* | *70.8* | *Slight warp, outlier* |
| 2719-L20 | 4.75 | 10.65 | 6.49 | 9.31 | 1.89 | 236 | Bubbling, slight warp |
| 2719-L21 | *10.88* | *11.41* | *6.92* | *9.48* | *2.05* | *465* | *Bubbling, broke wrong* |
| 2719-L22 | *5.83* | *12.01* | *7.19* | *9.35* | *1.91* | *254* | *Bubbling, broke wrong* |
| 2719-L23 | 8.76 | 11.39 | 6.86 | 9.36 | 1.83 | 420 | |
| 2719-L24 | *9.88* | *10.80* | *6.92* | *9.31* | *1.78* | *514* | *Broke wrong* |
| 2719-L25 | 5.86 | 11.78 | 7.05 | 9.41 | 1.79 | 278 | Bubbling |
| 2719-L26 | 3.87 | 11.27 | 6.81 | 9.39 | 1.93 | 177.8 | Slight warp |
| 2719-L27 | *0.717* | *11.18* | *6.90* | *9.10* | *1.90* | *33.8* | *Broke wrong* |
| 2719-L28 | 13.77 | 11.55 | 6.66 | 9.24 | 1.82 | 655 | Slight warp |

Table D-8: ARI-2719 Longitudinal Shear Test Edited Results

| | Failure Load, N | l, mm | w, mm | h, mm | t, mm | $\tau$, Pa |
|---|---|---|---|---|---|---|
| Mean | 9.65 | 11.79 | 7.19 | 9.91 | 1.966 | 412 |
| Median | 8.76 | 11.64 | 7.05 | 9.48 | 1.930 | 420 |
| Standard Deviation | 5.31 | 0.659 | 0.488 | 0.632 | 0.1506 | 216 |
| Coefficient of Variation | 0.550 | 0.0559 | 0.0678 | 0.0637 | 0.0766 | 0.524 |

Table D-9: ARI-2719 Longitudinal Shear Test Unedited Results

| | Failure Load, N | l, mm | w, mm | h, mm | t, mm | $\tau$, Pa |
|---|---|---|---|---|---|---|
| Mean | 12.00 | 11.89 | 7.27 | 9.93 | 1.952 | 507 |
| Median | 9.88 | 11.76 | 7.19 | 9.48 | 1.93 | 445 |
| Standard Deviation | 10.09 | 0.766 | 0.430 | 0.626 | 0.1308 | 398 |
| Coefficient of Variation | 0.841 | 0.0644 | 0.0592 | 0.0631 | 0.0670 | 0.784 |

Table D-10: ARI-2719 Transverse Shear Test Data

| Sample | Failure load, N | l, mm | w, mm | h, mm | t, mm | $\tau$, Pa | Notes |
|---|---|---|---|---|---|---|---|
| 2719-T10 | *24.7* | *14.58* | *7.51* | *10.54* | *1.69* | *1001* | *Bubbling, broke wrong* |
| 2719-T11 | 9.83 | 13.32 | 7.54 | 10.74 | 1.86 | 397 | Warped |
| 2719-T12 | 4.22 | 12.40 | 7.67 | 10.47 | 1.90 | 179.1 | Warped |
| 2719-T13 | 9.00 | 12.50 | 7.66 | 10.46 | 1.57 | 459 | Bubbling |
| 2719-T14 | 6.29 | 12.26 | 7.63 | 10.49 | 1.96 | 262 | Bubbling, slight warp |
| 2719-T15 | 11.43 | 12.11 | 7.55 | 10.54 | 1.64 | 575 | Bubbling, slight warp |
| 2719-T16 | 4.37 | 13.06 | 7.57 | 10.43 | 1.75 | 191.4 | Bubbling, slight warp |
| 2719-T17 | *28.3* | *13.32* | *7.63* | *10.40* | *1.64* | *1294* | *Bubbling, broke wrong* |
| 2719-T18 | 13.37 | 12.20 | 7.60 | 10.54 | 1.78 | 616 | Bubbling, slight warp |
| 2719-T19 | 28.1 | 13.04 | 7.62 | 10.56 | 1.84 | 1171 | Bubbling |
| 2719-T20 | *12.21* | *12.25* | *7.54* | *10.58* | *1.57* | *635* | *Warped, broke wrong* |
| 2719-T21 | *1.113* | *11.60* | *7.07* | *9.32* | *1.63* | *58.9* | *Bubbling, slight warp, broke wrong* |
| 2719-T22 | 1.763 | 11.74 | 7.06 | 9.39 | 1.87 | 80.3 | Bubbling, slight warp |
| 2719-T23 | *11.12* | *12.82* | *6.94* | *9.47* | *1.80* | *482* | *Bubbling, broke wrong* |
| 2719-T24 | 2.77 | 11.29 | 7.02 | 9.46 | 1.78 | 137.8 | Oxygen?, bubbling |
| 2719-T25 | 7.91 | 11.26 | 7.14 | 9.17 | 1.92 | 366 | Slight warp |
| 2719-T26 | 19.50 | 12.18 | 7.08 | 9.57 | 1.84 | 870 | Bubbling |
| 2719-T27 | *2.31* | *13.08* | *7.10* | *9.23* | *1.72* | *102.7* | *Bubbling, warped, broke wrong* |
| 2719-T28 | 20.4 | 12.82 | 6.78 | 9.59 | 1.70 | 935 | Bubbling, slight warp |
| 2719-T29 | 2.63 | 11.80 | 6.94 | 9.43 | 1.74 | 127.9 | Bubbling, slight warp |
| 2719-T30 | 2.65 | 12.84 | 7.37 | 9.65 | 1.80 | 114.6 | Oxygen?, bubbling, slight warp |

Table D-11: ARI-2719 Transverse Shear Test Edited Results

| | Failure Load, N | l, mm | w, mm | h, mm | t, mm | $\tau$, Pa |
|---|---|---|---|---|---|---|
| Mean | 9.61 | 12.32 | 7.35 | 10.03 | 1.80 | 432 |
| Median | 7.91 | 12.26 | 7.54 | 10.43 | 1.80 | 366 |
| Standard Deviation | 7.79 | 0.627 | 0.309 | 0.563 | 0.1059 | 339 |
| Coefficient of Variation | 0.810 | 0.0509 | 0.0421 | 0.0561 | 0.0589 | 0.784 |

Table D-12: ARI-2719 Transverse Shear Test Unedited Results

| | Failure Load, N | l, mm | w, mm | h, mm | t, mm | τ, Pa |
|---|---|---|---|---|---|---|
| Mean | 10.66 | 12.50 | 7.33 | 10.00 | 1.76 | 479 |
| Median | 9.00 | 12.40 | 7.51 | 10.40 | 1.78 | 397 |
| Standard Deviation | 8.76 | 0.784 | 0.299 | 0.574 | 0.1124 | 382 |
| Coefficient of Variation | 0.822 | 0.0627 | 0.0407 | 0.0573 | 0.0638 | 0.798 |

## ARI-2750 Results

Table D-13: ARI-2750 Longitudinal Shear Test Data

| Sample | Failure load, N | l, mm | w, mm | h, mm | t, mm | τ, Pa | Notes |
|---|---|---|---|---|---|---|---|
| 2750-L6 | 11.51 | 12.28 | 6.18 | 8.80 | 1.11 | 844 | |
| 2750-L7 | 12.97 | 12.91 | 5.78 | 8.74 | 0.92 | 1092 | |
| 2750-L8 | 9.59 | 11.14 | 6.35 | 8.74 | 0.89 | 967 | |
| 2750-L9 | *18* | *11.17* | *6.39* | *9.43* | *1.84* | *876* | *Survived DMA* |
| 2750-L10 | *10.08* | *11.12* | *7.13* | *9.55* | *1.82* | *498* | *Broke wrong* |
| 2750-L11 | 9.89 | 12.39 | 6.48 | 8.75 | 0.99 | 806 | Slight warp |
| 2750-L12 | *7.39* | *11.56* | *7.53* | *9.37* | *1.78* | *359* | *Slight warp, broke wrong* |
| 2750-L13 | *18* | *12.13* | *7.36* | *9.39* | *2.03* | *731* | *Broke wrong, survived DMA* |
| 2750-L14 | *18* | *11.24* | *7.35* | *9.49* | *1.62* | *989* | *Cracked, survived DMA* |
| 2750-L15 | 14.15 | 11.25 | 7.28 | 9.44 | 1.84 | 684 | Cycling |
| 2750-L16 | 5.99 | 12.76 | 6.36 | 8.76 | 0.79 | 594 | Slight warp, cycling |
| 2750-L17 | 17.62 | 11.11 | 6.81 | 9.46 | 1.90 | 835 | Cycling |
| 2750-L18 | *22.9* | *10.87* | *6.84* | *9.42* | *1.84* | *1144* | *Broke wrong* |
| 2750-L19 | 8.35 | 10.61 | 6.42 | 8.77 | 0.97 | 812 | |
| 2750-L20 | *32.0* | *12.31* | *7.09* | *9.25* | *1.76* | *1479* | *Broke wrong* |
| 2750-L21 | *4.51* | *11.86* | *7.59* | *9.36* | *1.87* | *203* | *Broke wrong* |
| 2750-L22 | *10.69* | *10.89* | *6.68* | *9.39* | *2.01* | *488* | *Broke wrong* |
| 2750-L23 | *7.96* | *11.26* | *7.11* | *9.47* | *1.87* | *378* | *Broke wrong* |
| 2750-L24 | 10.80 | 11.23 | 7.08 | 9.42 | 1.81 | 531 | |
| 2750-L25 | *37.9* | *12.30* | *7.61* | *8.99* | *1.87* | *1648* | *Broke wrong* |
| 2750-L26 | *4.09* | *11.97* | *6.54* | *8.78* | *1.24* | *276* | *Warped* |
| 2750-L27 | 19.85 | 11.43 | 6.86 | 9.43 | 1.88 | 924 | |
| 2750-L28 | 25.7 | 11.28 | 7.58 | 9.06 | 2.28 | 998 | |

Table D-14: ARI-2750 Longitudinal Shear Test Edited Results

| | Failure Load, N | l, mm | w, mm | h, mm | t, mm | τ, Pa |
|---|---|---|---|---|---|---|
| Mean | 13.31 | 11.67 | 6.65 | 9.03 | 1.40 | 826 |
| Median | 11.51 | 11.25 | 6.48 | 8.8 | 1.11 | 834 |
| Standard Deviation | 4.67 | 0.762 | 0.425 | 0.341 | 0.454 | 228 |
| Coefficient of Variation | 0.351 | 0.0653 | 0.0639 | 0.0377 | 0.325 | 0.275 |

Table D-15: ARI-2750 Longitudinal Shear Test Unedited Results

| | Failure Load, N | l, mm | w, mm | h, mm | t, mm | τ, Pa |
|---|---|---|---|---|---|---|
| Mean | 14.69 | 11.61 | 6.89 | 9.19 | 1.61 | 789 |
| Median | 11.51 | 11.28 | 6.86 | 9.37 | 1.82 | 812 |
| Standard Deviation | 8.64 | 0.645 | 0.513 | 0.312 | 0.441 | 359 |
| Coefficient of Variation | 0.588 | 0.0555 | 0.0745 | 0.0339 | 0.275 | 0.455 |

Table D-16: ARI-2750 Transverse Shear Test Data

| Sample | Failure load, N | l, mm | w, mm | h, mm | t, mm | τ, Pa | Notes |
|---|---|---|---|---|---|---|---|
| 2750-T4 | 1.328 | 10.94 | 7.14 | 8.39 | 2.12 | 57.3 | |
| 2750-T5 | 1.557 | 10.32 | 6.39 | 8.67 | 1.49 | 101.2 | |
| 2750-T7 | 2.35 | 11.44 | 7.08 | 8.52 | 2.05 | 100.3 | |
| 2750-T8 | 2.30 | 11.40 | 7.44 | 8.83 | 1.78 | 113.3 | Small precrack |
| 2750-T9 | 1.672 | 11.51 | 6.70 | 8.29 | 2.10 | 69.2 | Slight warp |
| 2750-T10 | *0.358* | *9.22* | *6.18* | *8.58* | *2.16* | *17.97* | *Slight warp, bad break* |
| 2750-T11 | 5.32 | 10.54 | 7.14 | 8.93 | 1.55 | 326 | |
| 2750-T12 | 5.63 | 9.97 | 3.74 | 8.94 | 2.18 | 259 | |
| 2750-T13 | 1.175 | 11.20 | 7.73 | 8.72 | 1.68 | 62.5 | |
| 2750-T14 | *3.35* | *11.18* | *7.43* | *8.95* | *1.79* | *167.5* | *Broke wrong* |
| 2750-T15 | *3.34* | *10.70* | *7.83* | *8.90* | *1.81* | *172.5* | *Broke wrong* |
| 2750-T16 | 5.01 | 10.13 | 6.86 | 8.89 | 1.72 | 287 | |
| 2750-T17 | 8.73 | 10.76 | 7.14 | 9.16 | 1.83 | 443 | |
| 2750-T18 | 9.34 | 11.43 | 7.01 | 9.04 | 2.02 | 405 | |
| 2750-T19 | 11.39 | 11.65 | 7.27 | 9.12 | 1.98 | 494 | Slight warp |
| 2750-T20 | 6.32 | 11.86 | 7.13 | 9.05 | 1.75 | 305 | |
| 2750-T21 | 11.05 | 11.75 | 7.60 | 9.21 | 1.96 | 480 | |
| 2750-T22 | *8.71* | *11.26* | *7.53* | *9.14* | *1.95* | *397* | *Slight warp, broke wrong* |

Table D-17: ARI-2750 Transverse Shear Test Edited Results

| | Failure Load, N | l, mm | w, mm | h, mm | t, mm | τ, Pa |
|---|---|---|---|---|---|---|
| Mean | 5.23 | 11.06 | 6.88 | 8.84 | 1.87 | 250 |
| Median | 5.17 | 11.30 | 7.14 | 8.91 | 1.90 | 273 |
| Standard Deviation | 3.69 | 0.624 | 0.967 | 0.287 | 0.218 | 164.6 |
| Coefficient of Variation | 0.706 | 0.0564 | 0.1405 | 0.0325 | 0.1163 | 0.658 |

Table D-18: ARI-2750 Transverse Shear Test Unedited Results

| | Failure Load, N | l, mm | w, mm | h, mm | t, mm | τ, Pa |
|---|---|---|---|---|---|---|
| Mean | 4.94 | 10.96 | 6.96 | 8.85 | 1.88 | 237 |
| Median | 4.18 | 11.19 | 7.14 | 8.92 | 1.89 | 216 |
| Standard Deviation | 3.59 | 0.705 | 0.912 | 0.271 | 0.205 | 160.3 |
| Coefficient of Variation | 0.726 | 0.0643 | 0.1310 | 0.0306 | 0.1087 | 0.678 |

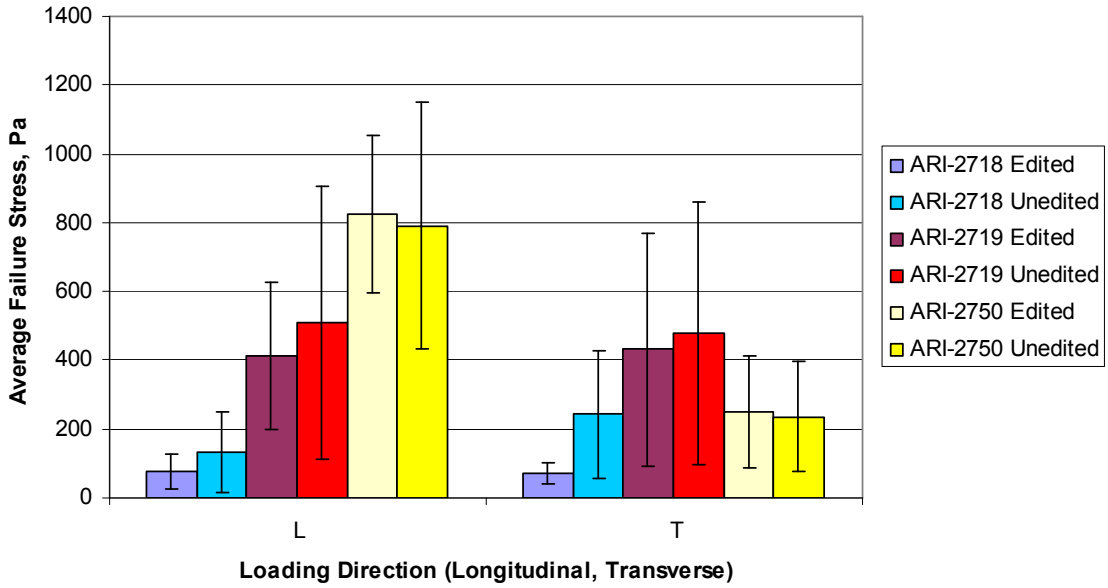


Figure D-1: Unedited Shear Strength Test Results

The only material to show any significant change in average strength was the ARI-2718, which showed an increase in strength when considering the results edited out above. Data scatter for all three materials is increased in the unedited results.

# Vita

Steven Kyriakides was born in Richmond, Virginia, and lived in nearby Chesterfield County until leaving to attend Virginia Tech in August of 2002. While earning his Bachelor's Degree in Materials Science & Engineering, he was actively involved in several ensembles in the Virginia Tech Music department, performing, arranging, and composing for them throughout his undergraduate and graduate careers. He spent one summer as a research assistant with the Virginia Tech Chemistry department's Summer Undergraduate Research Program, funded by NSF, under the guidance of Dr. Scott Case, and spent another as a Materials Engineering Intern at Ford Motor Company in Dearborn, Michigan. Graduating with his B.S in 2006, Steven continued his education at Virginia Tech under the Materials Science & Engineering department's five-year B.S. / M.S. program, again with Dr. Case.